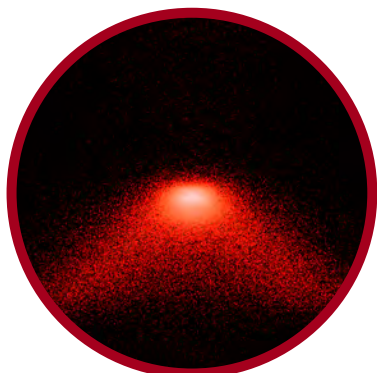


PhD Thesis

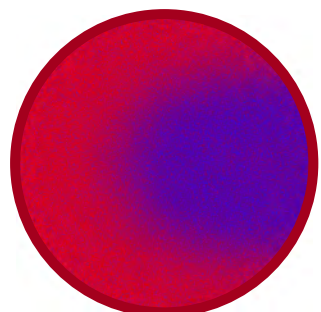


# Superradiant Lasers Based on Strontium-88

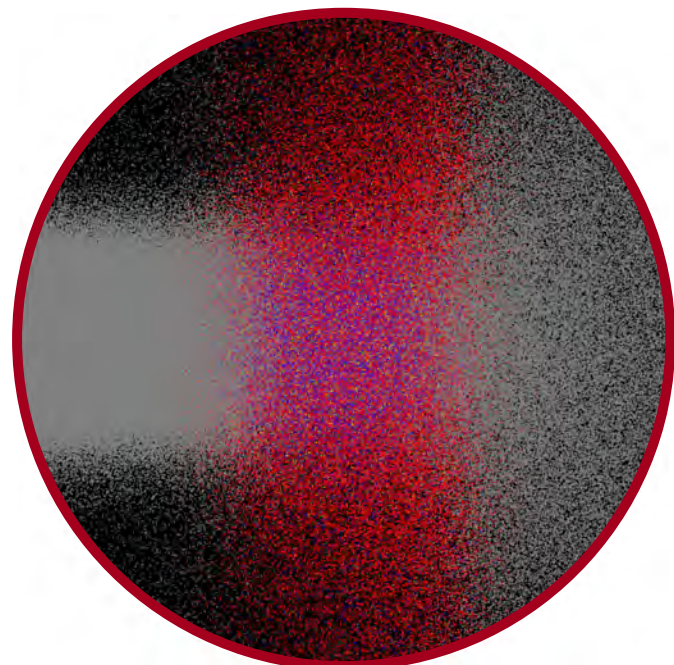
This thesis has been submitted to the PhD School of  
The Faculty of Science, University of Copenhagen



Mikkel Tang



Niels Bohr Institute  
November 7, 2022





PhD Thesis

# Superradiant Lasers Based on Strontium-88

**Author:** Mikkel Tang

**Advisor:** Jörg Helge Müller

Quantum Metrology Group  
Niels Bohr Institute  
November 7, 2022

## Abstract

In superradiant lasers the emitted light has a frequency determined mainly by atoms, as opposed to ordinary lasers, where mechanical parts have a large influence. And while mechanical parts are hard to replicate and control exactly, the universal properties of atoms are ideal to use as references for precision measurements. In this sense, photons emitted by an atom are a "frequency ruler" which we can compare other photon frequencies to. Therefore superradiant lasers are a promising technology within quantum metrology, as the best frequency references today are limited by tiny thermal disturbances in mechanical mirrors. And even though frequency is the quantity we can measure most accurately, it can also be used as proxy for many other quantities, such as length or gravitational acceleration. Therefore a wide range of areas such as timekeeping, geopositioning and geodesy may benefit from the development of superradiant lasers. Today, this is still an emerging technology, confined to big machines in research labs.

In this thesis we investigate superradiant lasing in different settings, using the 7.48 kHz-wide  $^1S_0$ - $^3P_1$  electronic transition in strontium. This magnitude of linewidth implies that superradiant lasing is relatively easy and less technically demanding to realize, compared to on the much narrower transitions which are considered in other labs. Similarly, a relatively high power can be realized. The drawback is that narrower transitions may allow for a narrower laser linewidth and lower sensitivity to mechanical disturbances, quantified by the cavity pulling coefficient.

The first system we consider is an experimental setup at the University of Copenhagen. Here a cloud of atoms is trapped and cooled to mK temperatures using a magneto-optical trap (MOT). The atoms are then coherently pumped to  $^3P_1$  before emitting a laser pulse into an optical cavity. In experiments and numerical simulations we investigate how the atom number, their finite temperature, and the cavity detuning influence the pulse dynamics. The parameters place this system within the superradiant crossover regime, where phase information within both the atoms and the cavity field have a large impact on the dynamics. We find a reduction in cavity pulling by up to a factor 4 when considering the full pulse spectrum. Within a range of detunings, the peak frequency of the spectrum also becomes immune to local variations. In addition we find a good agreement between the numerical simulations and experimental results. This also provides some verification of the models of other systems presented in this thesis. These share many features with the pulsed model, but are used predictively.

The setup was upgraded to cool atoms to  $\mu$ K temperatures, including a system to control the MOT coil currents on the ms-timescale, which was crucial to achieve a low atom loss. These improvements to the setup are also presented in the thesis. In the new crossover regime at  $\mu$ K, atoms phase-synchronize to a higher degree, and cavity pulling is reduced by up to a factor 56. However, due to the short pulse duration when using coherent pumping, the pulse linewidth is limited to hundreds of kHz. We use numerical simulations to investigate pulses in another new regime with incoherent repumping, which is now being realized in the lab. Here we also determine the impact of photon recoils from repumping on the temperature and cloud expansion, and in turn the pulse dynamics and spectra. These suggest a linewidth of a few hundred Hz may be realized. This appears most viable at small cavity detunings, or possibly at a finite detuning with a fine-tuning of atom cloud parameters. We have also determined the lasing threshold for fully continuous lasing in the system, which ranges on the order of  $10^9$  atoms/s. Realizing this may require more extensive changes to the setup.

The second system we consider is a hot beam superradiant lasing machine at the University of Amsterdam. Here a beam of strontium atoms from an oven is transversely laser-cooled to a few mK and then pumped incoherently to  ${}^3\text{P}_1$  right before passing through an optical cavity. We describe parts of the experimental machine and numerical simulations of pumping and superradiant lasing within it. Simulations of pumping are also used to investigate the prospects of a velocity selection scheme. This reduces the final temperature, but also flux, of  ${}^3\text{P}_1$  atoms.

The simple architecture of the hot beam machine allows for a very high atom flux. As a result, hundreds of nW emitted power is expected if the lasing threshold near  $\sim 2 \cdot 10^{12}$  atoms/s is overcome. Cavity pulling is suppressed by a factor  $\sim 20\text{--}30$ , with velocity-selection contributing a 10-25% improvement. A simple estimate suggests a linewidth of 9.4 Hz can be reached by this system. The impact of different physical effects is investigated in simulations. One effect is the relativistic Doppler shift, which affects all the atoms differently. These cause net shifts in the lasing frequency of hundreds of Hz, and also affect the variations in frequency fluctuations at different cavity detunings. We also investigate the effect of variations in temperature, decoherence from stray light, requirements for the velocity selection stage, and the frequency-dependency of the cavity pulling effect. Finally, we present the characteristics of absorption and amplification for a wide range of atom fluxes if a laser beam is input into the optical cavity.

The final system we consider is based on a  $\mu\text{K}$  beam of atoms, transported in a dipole guide. This atom source has been realized at the University of Amsterdam, but is here considered in the context of superradiant lasing. We assume atoms are continually repumped as they propagate through the cavity mode. The model includes all Zeeman-levels involved in pumping, photon recoils, state-dependent optical potentials, and coherent effects from two pumping lasers. A stochastic master equation and quantum jumps are used in the model to capture the thermal effects from repumping within state-dependent optical potentials. In the literature, stationary two-level atoms are often considered in models of superradiant lasers, with a greatly simplified treatment of pumping. Therefore our approach also has broader relevance when considering superradiant lasing schemes which rely on repumping within optical potentials.

Hundreds of pW may be realized in the cold beam system, and each atom may emit up to  $\sim 40$  photons into the cavity before heating up and escaping. Cavity pulling is suppressed by a factor  $\sim 50\text{--}100$ , which is favorable compared to the hot beam system. On the other hand, a crude estimate of the linewidth yields 82 Hz, inferior to the hot beam estimate. An optical lattice may reduce cavity pulling further, but introduces significant light shift variations on pumping transitions. Repumping laser frequencies affect a net shift in the lasing frequency, but variations are suppressed by over two orders of magnitude. Similarly, intensities do affect a net shift, which also varies with parameters such as atom flux. However we find there are regimes where the net shift in lasing frequency is zero, and is also locally independent of the atom flux. Over-all, the hot beam system has many advantages compared to this approach, especially in terms of experimental simplicity. On the other hand, for narrower transitions, a setting similar to the cold beam system is more viable for realizing superradiant lasing.

## Resumé

Det udsendte lys fra superradiante lasere har en frekvens, der primært bestemmes af atomer, i modsætning til almindelige lasere, hvor mekaniske dele har en stor indflydelse. Og mens mekaniske dele er svære at genskabe og kontrollere præcist, er atomers universelle egenskaber ideelle til at bruge som referencer til præcisionsmålinger. Her er fotonerne fra et atom et slags ”frekvens-målebånd”, man kan sammenligne andre foton-frekvenser med. Derfor er superradiante lasere en lovende teknologi inden for kvantemetrologi, efter som de bedste frekvensreferencer i dag begrænses af små termiske fluktuationer i mekaniske spejle. Og selvom frekvens er den fysiske størrelse, vi kan måle mest nøjagtigt, kan den også bruges indirekte til at måle andre størrelser, som afstand eller tyngdeacceleration. Derfor kan et bredt udsnit af områder, som tidstaging, geopositionering og geodæsi, drage nytte af udviklingen af superradiante lasere. Den dag i dag er superradiante lasere stadig en fremvoksende teknologi, begrænset til store maskiner i laboratorier.

I denne afhandling undersøger vi superradiant lasing i forskellige sammenhænge, hvor den 7.48 kHz-bredde  $^1S_0$ - $^3P_1$  elektronovergang i strontium bruges. Denne størrelse af linjebredde gør, at superradiant lasing er relativt nemt og mindre teknisk krævende at realisere, sammenlignet med på de langt smallere overgange, som overvejes i andre laboratorier. Det gør også, at en relativt høj emitteret effekt kan opnås. Ulempene er til gengæld, at en smallere overgang kunne give en smallere linjebredde af laseren, og mindre følsomhed overfor mekaniske forstyrrelser, hvilket beskrives matematisk af cavity pulling-koefficienten.

Det første system, vi undersøger, er et eksperimentelt apparat på Københavns Universitet. Her fanges en sky af atomer og køles til  $\mu\text{K}$ -temperaturer vha. en magneto-optisk fælde (MOT). Derefter pumpes atomerne koherent til  $^3P_1$ , hvorefter de udsender en laserpuls i en optisk kavitet. Vha. eksperimenter og numeriske simulationer undersøger vi hvordan antallet af atomer, deres temperatur, og kavitetens detuning har indflydelse på puls-dynamikken. Systemets parametre gør, at pulsernes opførsel passer med det superradiante crossover regime, hvor faseinformationen i både atomerne og kavitetsfeltet har stor indflydelse på dynamikken. Vi finder at cavity pulling reduceres med op til en faktor 4, når vi betragter hele pulspektrum. Inden for et interval af detunings er toppen af pulsens spektrum også immun overfor små ændringer i detuning. Derudover finder vi god overensstemmelse mellem numeriske simulationer og forsøgsresultater. Dette giver også en hvis verifikation af modellerne af de andre systemer, som er præsenteret i afhandlingen. De har mange fællestræk med modellen af pulserne, men bruges til forudsigtigheder under nye betingelser.

Forsøgsopstillingen blev opgraderet for at køle atomer til  $\mu\text{K}$ -temperaturer, inklusiv et system til at styre strømmen i MOT-spolerne på ms-tidsskala, hvilket var vigtigt for at opnå et lavt tab af atomer. Disse forbedringer af opstillingen er også præsenteret i afhandlingen. I det nye crossover regime ved  $\mu\text{K}$  fase-synkroniserer atomerne i højere grad, og cavity pulling er reduceret op til en faktor 56. Linjebredden af pulserne er dog begrænset til hundredes af kHz pga. den korte varighed, når atomerne pumpes koherent. Vha. numeriske simulationer undersøger vi pulser i et andet regime med inkoherent repumping, som nu realiseres i laboratoriet. Her undersøger vi også hvordan foton-impulser har indflydelse på temperaturen og udvidelsen af atomskyen, og dette i sidste ende påvirker dynamik og spektra af laserpulserne. Ud fra simulationerne er det realistisk at opnå en linjebredde på nogle hundrede Hz. Dette er mest realistisk for lille kavitsdetuning, men måske også ved en betydelig detuning, hvis atomskyens parametre kan fin-tunes. Vi har også bestemt tærsklen for at realisere lasing i et helt kontinuert system, som ligger omkring  $10^9$  atomer/s. At realisere dette kan dog kræve betydelige ændringer i forsøgsopstillingen.

Det andet system, vi undersøger, er en superradiant lasing-maskine baseret på en varm atomstråle. Denne er bygget på Amsterdam Universitet. Atomstrålen udsendes fra en ovn og køles først transverst til få mK, og derefter pumpes atomerne inkoherent til  $^3P_1$  lige inden, de passerer igennem en optisk kavitet. Vi beskriver dele af det eksperimentelle apparat, pumpeprocessen og superradiant lasing i systemet. Simulationerne af pumpe-processen bliver også brugt til at undersøge indvirkningen af en metode til hastigheds-udvælgelse. Denne kan sænke den endelige temperatur, men også flux, af  $^3P_1$ -atomer.

En meget høj atomflux kan opnås pga. maskinens simple arkitektur. Pga. dette kan en effekt på hundredesvis af nW forventes, hvis lasing-tærsklen omkring  $\sim 2 \cdot 10^{12}$  atoms/s kan overkommes. Cavity pulling undertrykkes med en faktor  $\sim 20\text{-}30$ , og heraf bidrager hastigheds-udvælgelse med en forbedring på 10-25%. Ifølge et simpelt estimat kan en linjebredde på 9.4 Hz opnås i dette system. I simulationer undersøger vi indvirkningen fra forskellige fysiske effekter. En effekt er den relativistiske dopplerforskydning, som påvirker alle atomerne forskelligt. Dette giver en forskydning i laserens frekvens på hundredesvis af Hz, og påvirker også hvordan frekvensfluktuationer varierer ved forskellig kavitets-detuning. Vi undersøger også indvirkningerne af temperatur-aændringer, dekoherens fra forstyrrende lys, krav til hastighedsudvælgelsen, og frekvensafhængigheden af cavity pulling-effekten. Derudover præsenterer vi karakteristika for absorption og forstærkning, som kan opnås ved forskellige størrelsesordnere af atomflux, hvis laserlys sendes ind i kavitten.

Det sidste system vi betragter er baseret på en stråle af  $\mu\text{K}$ -kolde atomer, der transporteres i en dipol-fælde. Denne atomkilde er realiseret på Amsterdam Universitet, men her betragtes dens potentielle i forbindelse med superradiant lasing. Vi antager, at atomerne pumpes vedvarende, imens de propagerer igennem kavitten. Vores model inkluderer alle Zeeman-niveauer, der er involveret i pumpningen, foton-impulser, tilstandsafhængige optiske potentiader, og koherente effekter fra to pumpe-lasere. I modellen bruger vi en stokastisk master equation og diskrete kvantespring til at tage højde for de termiske effekter fra at pumpe atomerne i tilstandsafhængige optiske potentiader. I modeller af superradiante lasere i litteraturen betragter man ofte stationære atomer med to energetilstande, hvor pumpningen behandles meget simplificeret. Derfor har vores tilgang også generel relevans for superradiante lasere, der er baseret på at pumpe atomer i optiske potentiader.

Hundredesvis af pW kan opnås i systemet baseret på den kolde atomstråle, og hvert atom kan udsende op til  $\sim 40$  fotoner i kavitten, før de opvarmes og flyver væk. Cavity pulling undertrykkes med en faktor  $\sim 50\text{-}100$ , hvilket er en fordel ift. maskinen baseret på en varm atomstråle. Til gengæld giver et simpelt estimat af linjebredden 82 Hz, hvilket er ringere. Et optisk gitter kan muligvis reducere cavity pulling yderligere, men vil også give store light shift-variationer på pumpeovergangene. Pumpelaserne frekvens indvirker også på en forskydning af laserfrekvensen, men variationer er undertrykt med over to størrelsesordnere. Forskydningen påvirkes ligeledes af pumpelaserne intensitet, men også af atomfluks. Vi finder dog at der er regimer, hvor forskydningen er nul, og den samtidig er lokalt uafhængig af atomflux. Alt i alt har maskinen baseret på den varme atomstråle mange fordele sammenlignet med denne tilgang, specielt pga. dens simple konstruktion. På smallere overgange i atomer er det til gengæld mere realistisk at opnå superradiant lasing i systemer, som minder om den kolde atomstråle.

# Contents

<b>Abstract</b>	<b>i</b>
<b>Symbols and abbreviations</b>	<b>vii</b>
<b>Acknowledgements</b>	<b>ix</b>
<b>Publications</b>	<b>xi</b>
<b>1 Introduction to quantum metrology and superradiant lasers</b>	<b>1</b>
1.1 Quantum metrology . . . . .	1
1.2 Strontium . . . . .	2
1.3 Atomic clocks, optical cavities and lasers . . . . .	3
1.4 Superradiant lasers . . . . .	6
1.5 Thesis overview . . . . .	12
<b>2 Theory for superradiant lasing and numerical treatment</b>	<b>13</b>
2.1 Cavity quantum electrodynamics . . . . .	14
2.2 The stochastic master equation . . . . .	21
2.3 Coherent pumping vs rate equations . . . . .	24
2.4 Transitions between Zeeman sublevels . . . . .	26
2.5 Heating . . . . .	27
2.6 Cavity field phase and spectral information . . . . .	28
2.7 Atom group approximation and performance considerations . . . . .	32
<b>3 Atom cloud machine for superradiant laser pulses</b>	<b>35</b>
3.1 Laser systems for the atom cloud machine . . . . .	36
3.2 Magneto-optical trap . . . . .	39
3.3 Implementation of second stage MOT cooling . . . . .	47
3.4 Experimental routines . . . . .	59
<b>4 Superradiant crossover pulses from a mK atom cloud</b>	<b>67</b>
4.1 Setup and numerical model . . . . .	67
4.2 Lasing pulse dynamics and phase behavior . . . . .	68
4.3 Lasing regimes and scaling with atom number . . . . .	71
4.4 Lasing pulses in a detuned cavity . . . . .	74
4.5 Cavity-detuning dependency and pulling . . . . .	80
<b>5 Superradiant lasing in the upgraded atom cloud machine</b>	<b>85</b>
5.1 Crossover pulses from atoms at $\mu\text{K}$ temperatures . . . . .	85
5.2 Simulations of quasi-continuous superradiance . . . . .	88
5.3 Requirements for steady-state superradiance . . . . .	94
<b>6 Machine for continuous superradiant lasing at UvA</b>	<b>95</b>
6.1 Monitor cavities . . . . .	95
6.2 The science cavity . . . . .	96
6.3 The superradiant lasing machine . . . . .	100
6.4 Simulations of pumping and velocity selection stages . . . . .	104

<b>7 Superradiant lasing from a hot atom beam</b>	<b>111</b>
7.1 Numerical model . . . . .	111
7.2 Performance of the SRLM . . . . .	115
7.3 Sensitivity to cavity fluctuations . . . . .	123
7.4 Absorption and driven lasing . . . . .	126
<b>8 Superradiant lasing from a cold atom beam</b>	<b>129</b>
8.1 Numerical model . . . . .	131
8.2 Spatial variations in the lasing region . . . . .	138
8.3 Output power, cavity pulling and linewidth . . . . .	140
8.4 Sensitivity to repumping laser variations . . . . .	142
8.5 Optical lattice . . . . .	144
<b>9 Conclusion and outlook</b>	<b>147</b>
<b>Appendices</b>	<b>151</b>
A.1 Tapered Amplifier power . . . . .	151
A.2 Beam profile for pumping mK atom cloud . . . . .	151
A.3 Crossover pulses in mK ensembles for high atom numbers . . . . .	152
A.4 Pulse spectrum dependency on cloud temperature . . . . .	153
A.5 Beam profile for pumping $\mu$ K atom cloud . . . . .	153
A.6 Pure and crossover pulses in the $\mu$ K regime . . . . .	153
A.7 Light shifts on pumping transitions from optical lattice . . . . .	154
A.8 Simulations of lasing in the Sr2 Machine at UCPH . . . . .	155
<b>List of Figures</b>	<b>156</b>
<b>List of Tables</b>	<b>158</b>
<b>Bibliography</b>	<b>159</b>

## Symbols and abbreviations

### Abbreviations

AOM	- Acousto-optic modulator
(C)QED	- (Cavity) quantum electrodynamics
CoM	- Center of mass
CPU	- Central processing unit
ECDL	- External cavity diode laser
EOM	- Electro-optic modulator
EPS	- Expanded polystyrene
FSR	- Free spectral range (of cavity)
GPU	- Graphics processing unit
GUI	- Graphical user interface
MFT	- Mean field theory
MOSFET	- Metal–oxide–semiconductor field-effect transistor
MOT	- Magneto-optical trap
(N)PS(D)	- (Normalized) power spectrum/spectral density
PI(D)	- Proportional-integral(-differential) (circuit)
PDH	- Pound-Drever-Hall (technique)
RAM	- Random access memory
RF	- Radio frequency
SME	- Stochastic master equation
SRLM	- Superradiant lasing machine
SWAP	- Sawtooth-wave adiabatic passage
TA	- Tapered amplifier
TEM	- Transverse electromagnetic mode
UvA	- University of Amsterdam (Universiteit van Amsterdam)
UCPH	- University of Copenhagen

### Symbols

$a$	- Cavity field annihilation operator; acceleration
$a^\dagger$	- Cavity field creation operator
$B, \mathbf{B}$	- Magnetic field strength/vector
$c$	- Speed of light, 299792458 m/s
$c_g$	- Clebsch-Gordan coefficient
$C$	- Cooperativity; capacitance
$E$	- Energy
$f, f^\dagger$	- Filter cavity field annihilation/creation operators
$F$	- Cavity finesse; force
$g, g_f$	- Angular coupling rate of (atom/filter cavity) to the science cavity
$\hbar$	- Planck's constant/reduced Planck's constant
$H$	- Hamiltonian operator
$I$	- Intensity; current
$k, \mathbf{k}$	- Wavenumber/wave vector
$L$	- Cavity length (between mirrors); inductance
$m$	- Mass
$n$	- Number of cavity photons; photon number operator; column density
$N$	- Number of atoms
$o$	- Operator
$p$	- Momentum
$P$	- Power
$P_{out}, P_{out}^S$	- Cavity output power (total/single side)
$q, q^\dagger$	- annihilation/creation operators

---

$r$	- Radius; distance
$\mathbf{r}$	- Position vector
$R$	- Resistance
$t$	- Time
$T$	- Temperature; end time
$U$	- Voltage
$v, \mathbf{v}$	- Velocity/velocity vector
$w$	- Repumping rate (angular frequency)
$W$	- Cavity waist radius
$x$	- Position coordinate, along atom propagation axis (if applicable)
$y$	- Position coordinate, along repumping laser beam axis (if applicable)
$z$	- Position coordinate along cavity axis
$\alpha$	- Polarizability
$\gamma$	- Atomic decay rate/FWHM transition linewidth (angular frequency); Lorentz factor
$\Gamma$	- Characteristic FWHM bandwidth (angular frequency)
$\delta_{ij}$	- Angular frequency difference; $\delta_{ij} = \omega_i - \omega_j$
$\delta_L$	- Shift in lasing frequency with respect to the unperturbed transition; $\delta_L = \omega_L - \omega_E$
$\Delta$	- Change/shift in the subsequent quantity
$\mathcal{E}$	- Emf
$\eta$	- Driving rate of driving laser
$\kappa$	- Cavity power dissipation rate/FWHM linewidth (angular frequency)
$\lambda$	- Wavelength
$\nu, \omega$	- Frequency (ordinary/angular)
$\rho$	- Density operator/matrix/matrix element
$\sigma$	- Atomic spin operator; standard deviation; cross section
$\tau$	- Characteristic time
$\phi$	- Phase
$\Phi$	- Flux
$\chi$	- Rabi frequency (angular)
$\psi$	- State
$\Omega$	- Generalized Rabi frequency (angular); collective atom-cavity coupling rate

**Subscript notation for atomic levels, frequencies, etc.** $^1\text{S}_0$ :  $g$ ,  $^3\text{P}_0$ :  $n$ ,  $^3\text{P}_1$ :  $(i, e, u)$ ,  $^3\text{S}_1$ :  $(x, y, z)$ ,  $^3\text{P}_2$ :  $(p, q, r, s, t)$  ( $m_J$  from - to +)

Capital letters denote the unperturbed transition (but including potential Zeeman-shifts).

$c$	- Cavity resonance
$d$	- Driving laser (cavity input beam) resonance
$f$	- Filter cavity resonance
$li, lx$	- Pumping laser (689 nm $\sigma^-$ transition/688 nm $\pi$ transition)
$L$	- The superadiant laser

## Acknowledgements

This thesis is based on my slightly over 3 years of work in the quantum metrology lab<sup>1</sup> at the University of Copenhagen (UCPH), including my half year secondment at the University of Amsterdam (UvA). Here I want to thank all the people who I have worked with, and who also contributed greatly to the setups and results presented in this thesis. Surely if I had started in an empty lab without supervisors and co-workers, there would have been a lot less interesting physics to present.

**Jan W. Thomsen** was my supervisor during the first half of my PhD, but also during my master's thesis in the same group. I first got to know Jan from his impressive and motivating lectures during the optics and atomic physics courses. And from the lab, I also know Jan's great enthusiasm for atomic physics. Jan introduced me to many of the lab routines that are necessary for our setups to work, such as laser injection. I have also enjoyed our many physics discussions.

**Jörg H. Müller** became my supervisor during the second half of my PhD. As Jan, he also brings enthusiasm to the lab, and offers a wealth of knowledge to students, ranging from experimental techniques and analog electronics to the similarity between the physics of stars and atom clouds in a magneto-optical trap (MOT). In addition to all the advice on experimental issues, I have also enjoyed our discussions of superradiant lasing, which have helped to identify relevant physical effects and include them in the numerical models. Finally, I want to thank Jörg for giving advice on thesis writing.

From the start of my PhD, I worked on the "Sr1" machine, where we trap a mK strontium MOT cloud and use it for interactions with an optical cavity mode. This was first in collaboration with **Stefan A. Schäffer**, **Bjarke T. R. Christensen**, **Martin R. Henriksen** and **Asbjørn A. Jørgensen**. I learned a lot of the concrete lab-work techniques from them, and their work on the setup and experiments was also crucial for the results on pulsed superradiance presented in the thesis. Stefan and Bjarke are also responsible for a huge part of the past work building up the initial Sr1 setup. The collaboration on the Sr1 setup with Stefan began already during my master's thesis, and in Amsterdam we arrived again at almost the same time to work on the hot beam superradiant lasing machine. In addition to all the experimental techniques I have learned from Stefan, we have also had many discussions about superradiant lasing (often with Jan, Jörg and other group members), which has helped to consider the numerical models in this thesis from different angles and refining them. In addition I want to thank Stefan for reading through and giving insightful comments on some chapters from the thesis.

Later, **Sofus L. Kristensen** and **Eliot Bohr** joined Sr1 as PhD students. We collaborated on upgrading the machine to cool atoms to  $\mu\text{K}$  temperatures. This pursuit allowed us to experience the occasional mercilessness of experimental physics, as the rapid ramping of the current in our big MOT coils would be a challenge haunting our setup for a long time. Despite these challenges I am happy to have worked with them and appreciate their big interest and excitement for physics. Fortunately we could begin to appreciate the physics more after celebrating our first  $\mu\text{K}$  atom cloud. Sofus and Eliot have put much effort into upgrading many different parts of the Sr1 machine, also including a new oven and some new laser systems. These are not presented in this thesis in detail, but were important for realizing the experiments at  $\mu\text{K}$  temperatures. I also want to thank them for reading and giving useful comments on a couple of thesis chapters.

---

<sup>1</sup>Website: [nbi.ku.dk/english/research/quantum-optics-and-photonics/quantum-metrology/](http://nbi.ku.dk/english/research/quantum-optics-and-photonics/quantum-metrology/)

**JyunKai Lin**, and later **Julian Robinson-Tait** and **Valentin P. Cambier**, also joined our group during my PhD. They primarily worked on the "Sr2" setup for interrogating a continuous strontium beam. Still, they would often lend a helping hand to Sr1, whether for making MOT coils, or to adjust some piezo while we run between all the other knobs, trying to keep up with optimizing the setup during our struggles with entropy. I have enjoyed working in group with them and following their exciting improvements to the strontium beamline.

Several students also worked on projects on the Sr1 setup. **Mantas Ambroza** built a setup for his master project to finally lock those athletic repumper resonances we always struggled with taming. **Maria S. V. Larsen** worked on the Sr1 setup for her master project and contributed to our final realization of  $\mu\text{K}$  cooling. In addition to her experimental work, she also dived into the theory of atom-light interactions and simulations. Here I was very lucky, as she spotted a mistake in one of my equations. **Andrea S. Eriksen** also contributed to our laser system for  $\mu\text{K}$  cooling during her bachelor project. **Jens Kinch** worked on setting up the initial absorption imaging system and determining the cloud temperature. He also deserves a big thanks for allowing us to exploit his graphics card and sacrifice FPS for numerical simulations before we had a dedicated simulation computer. **Jonathan G. Elsborg** and **Kasper Pedersen** also improved the imaging system further during their bachelor projects.

Outside the lab I would also like to thank **Michael Heide Bernt** and the rest of the technical workshop at UCPH for all their advice and help with designing and making many important components for the Sr1 setup.

Beyond UCPH I would also like to thank the people from the iqClock consortium<sup>2</sup>. In this international collaboration I have mainly been involved in what became the hot beam superradiant lasing machine at the University of Amsterdam. At the beginning we had regular online meetings discussing possible designs and numerical simulations of continuous superradiance. I enjoyed the discussions with **Florian Schreck**, **Shayne Bennetts** and others from the Amsterdam group, whose expertise in atomic beams and machinery guided the project, **Georgy Kazakov** from TU Wien who contributed with advice on numerical modeling, and **Christoph Hotter** and the rest of the group of **Helmut Ritsch** at the University of Innsbruck, contributing their expertise in quantum theory and even making independent checks of the model for our pulsed experiments at UCPH. Christoph has also shown great interest in the Sr1 setup and come up with new, interesting ideas for us to explore.

Later I also got to know the iqClock team and Strontium quantum gases group<sup>3</sup> at the University of Amsterdam better, now in the context of our lab work on the hot beam machine. It was exciting to follow the vacuum chamber's journey, hatching from its bubble wrap, consuming our components and growing into a full machine beast over the course of six months. Especially **Shayne**, **Francesca Famà** and **Sheng Zhou** helped me get started in the new lab and become increasingly familiar with where all the different components were hidden. I also got to work with **Camila B. Silva**, **Zeyuan Zhang**, **Stefan**, **Benjamin Pasquiou** and **Florian**. They made many contributions to the hot beam project that are not presented in this thesis. I am also thankful for all the techniques I learned from them during my time in the lab.

---

<sup>2</sup>Website: [www.iqclock.eu](http://www.iqclock.eu)

<sup>3</sup>Website: [strontiumbec.com](http://strontiumbec.com)

## Publications

- [54] S. A. Schäffer, **M. Tang**, M. R. Henriksen, A. A. Jørgensen, B. T. R. Christensen, and J. W. Thomsen, Lasing on a narrow transition in a cold thermal strontium ensemble, Phys. Rev. A **101**, 013819 (2020)

In this publication we present an experimental realization of lasing pulses in the superradiant crossover regime from a mK strontium ensemble prepared by coherent pumping. The lasing dynamics and behavior of the output power is presented, both for varying numbers of atoms and cavity detuning. Corresponding results from a numerical model are shown, which agree well with experiments. The role of atoms moving at different velocities in the pulse dynamics is also investigated in simulations. The content of this publication is covered in Chapter 4.

I developed the numerical simulations, performed data analysis, and contributed to the setup, experiments and manuscript.

- 
- [59] **M. Tang**, S. A. Schäffer, A. A. Jørgensen, M. R. Henriksen, B. T. R. Christensen, J. H. Müller, and J. W. Thomsen, Cavity-immune spectral features in the pulsed superradiant crossover regime, Phys. Rev. R **3**, 033258 (2021)

Here we report experimental studies of the spectral properties and phase behavior of lasing pulses from the mK strontium ensemble. Results from numerical simulations covering the same regime are also presented. The role of the thermal velocity distribution is also analyzed using the numerical model. We find cavity pulling can be reduced by up to a factor 4 in the system. Within a particular range of cavity detunings, the peak frequency of the laser spectrum becomes locally immune to variations in detuning. The content is covered in Chapter 4.

I was the main author of the manuscript, developed the numerical simulations, performed data analysis, and contributed to the setup and experiments.

- 
- [84] **M. Tang**, S. A. Schäffer, and J. H. Müller, Prospects of a superradiant laser based on a thermal or guided beam of Sr-88, under review with Phys. Rev. A (2022)

This manuscript presents numerical simulations in two different approaches to achieve continuous superradiant lasing on the kHz-wide transition in strontium. One is based on a machine being developed at the University of Amsterdam. It uses a hot atomic beam, which is transversely cooled to a few mK. Here hundreds of nW may be achieved, and cavity pulling can be reduced by a factor 20-30. The other system assumes an ultracold atom source demonstrated at UvA is used for realizing the laser. Here hundreds of pW can be achieved, and cavity pulling reduced by a factor 50-100. These two approaches are covered in Chapters 7 and 8, respectively.

I was the main author of the manuscript and developed the numerical simulations.

# Introduction to quantum metrology and superradiant lasers

## 1.1 Quantum metrology

Quantum metrology<sup>1</sup> is a field of science that deals with precision measurements based on quantum physics. Technologies advanced within the field of quantum metrology include atomic clocks [1, 2], lasers with ultra-stable frequencies [3, 4, 5] and systems based on ultracold atoms in optical cavities [6]. These are used as tools in many areas at the frontier of science, such as in gravitational wave detection [7], geodesy [8, 9], geopositioning [10] and quantum simulation [11]. Improvements to the precision of the very best tools may also uncover new realms of physics [12, 13], similarly to how microscopes and telescopes enabled us to discover new aspects of the universe beyond the limitations of the naked eye.

The quantity we can measure most precisely and accurately<sup>2</sup> is time, and its inverse, frequency. Today's state-of-the-art atomic clocks can reach a fractional uncertainty at the level of  $10^{-18}$  [9, 14, 15, 16, 17, 18] - smaller than the magnitude of a second relative to the age of the universe.

Centuries ago time was measured using mechanical clocks, for example by counting how many times an arm swung back and forth. These clocks had limited accuracy because the mechanics inevitably vary, so that two mechanical clocks will never have the exact same arm length and behave exactly the same. That causes the clocks to get out of sync - the arm in one might swing 60 times in the same time interval another one swings 61 times. Using atomic transitions was a big step forward for clocks, because two atoms of the same isotope will behave in the same way under the same conditions. The impact of "conditions" might sound disappointing at first, but can be controlled extremely well compared to the factors influencing e.g. mechanical clocks.

---

<sup>1</sup>Quantum metrology should not be confused with the study of quantum subways. Also not with quantum meterology, which would be dealing with quantum weather forecasts.

<sup>2</sup>Precision refers to how small a spread can be obtained in measurements of a given quantity (small statistical uncertainty). Accuracy refers to how close the measured values are compared to a known reference on average (small systematic uncertainty/bias).

### 1.1.1 Atomic pendula

The discrete states of atoms are connected by transitions, which enable them to be used as "pendula" for clocks and measurements, instead of mechanical arms. A state describes an atom's physical quantities at a given time, such as the angular momentum of the nucleus and electrons. The state can be changed by interactions, and we will only be dealing with electromagnetic interactions between photons and the outermost electrons of atoms. For example an atom can absorb a photon, which can cause one of its electrons to e.g. jump to an orbit further from the nucleus. In this excited state with higher energy, it may emit a photon, reversing the process.

Because the electrons cannot simply have a stable orbit at any arbitrary distance from the nucleus or arbitrary angular momentum, the states are discrete, and a very specific amount of energy  $E$  is needed by the photon to cause these jumps. This leads to one important quantity - the transition frequency  $\nu = E/h$ , where  $h$  is Planck's constant. In this thesis we will work in angular units most of the time, where we have  $\omega = E/\hbar$ . These atomic transition frequencies serve as natural alternatives to oscillation frequencies of mechanically constructed pendula. Interactions do not last infinitely long, so the Fourier limit tells us that the transitions cannot be infinitely well-defined spectrally. Instead there is a span of photon frequencies that can cause a given transition, defining a second important quantity - the transition linewidth  $\gamma$  (in angular units). This characterizes the natural span by the full-width at half-maximum (FWHM) of a Lorentzian curve around the transition frequency, and is the inverse of the characteristic spontaneous decay time  $1/\gamma$  back from the excited state.

## 1.2 Strontium

As an example of an interesting atom for metrology we can consider strontium, which we will be working with in this thesis (specifically  $^{88}\text{Sr}$ ).  $^{88}\text{Sr}$  is the most abundant isotope of strontium in nature at 82.58(1)% by mass [19, p. 2], but  $^{87}\text{Sr}$  at 7.00(1)% is also of great metrological interest.  $^{88}\text{Sr}$  has no nuclear spin, which gives it a simpler level structure compared to other isotopes and makes it easier to work with. As an alkaline earth atom, strontium has two electrons in the outermost shell, which gives it a structure of electronic transitions that is particularly useful in quantum metrology. A selection of energy levels and transitions for strontium is shown in Fig. 1.1. The levels refer to the electrons in the outermost shell in the Russel-Saunders notation  $^{2S+1}L_J$  [20, p. 81]. Here  $S$  is the total spin quantum number of the two electrons (as they are spin 1/2 particles,  $S$  can be either 0 or 1).  $L$  represents the orbital angular momentum quantum numbers by letters from spectroscopic notation ( $S$  means 0,  $P$  means 1 and  $D$  means 2).  $J$  denotes the total angular momentum quantum number from the spin-orbit coupling.

Each level can be further divided into  $2J + 1$  states characterized by the projection numbers  $m_J = -J, -J+1, \dots, +J$  of the orbital angular momentum along an axis (typically a magnetic field). In the presence of a magnetic field, such states will have their energies shifted relative to the depicted levels by the Zeeman shift. For weak fields it is given by [20, p. 91]:

$$\Delta E_{\text{Zee}} = g_J \mu_B B m_J, \quad g_J \approx \frac{3}{2} + \frac{S(S+1) - L(L+1)}{2J(J+1)}, \quad (1.1)$$

where  $g_J$  is the Landé g-factor,  $\mu_B$  the Bohr magneton and  $B$  the field strength, so here  $\Delta E_{\text{Zee}} = 0$  for  $m_J = 0$ .

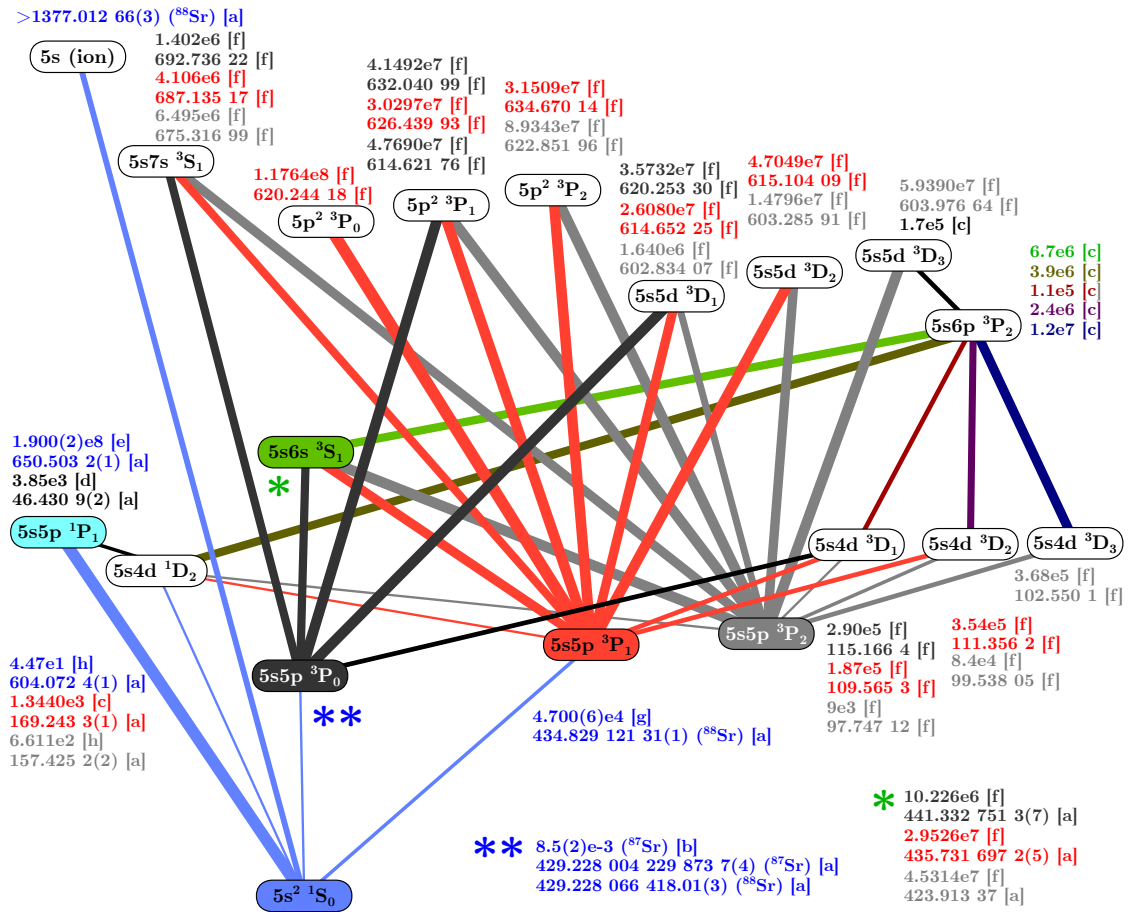


Figure 1.1: Some of the many levels and transitions of strontium. Transition linewidths in angular units,  $s^{-1}$ , are specified in E notation, and frequencies in THz are specified in regular notation near the upper state of transitions. In this thesis we will work with the transitions between the colored levels and their Zeeman states. References: [a]: [19], [b]: [21], [c]: [22], [d]: [23], [e]: [24], [f]: [25], [g]: [15], [h]: [26].

The first useful property from the level structure of strontium is that it can easily be laser-cooled to very low temperatures using transitions connected to the ground state  ${}^1S_0$ . We will consider laser-cooling techniques in Chapter 3, but for these we note that the 30 MHz wide  ${}^1S_0-{}^1P_1$  transition at 461 nm enables rapid cooling to mK temperatures, and the 7.5 kHz wide  ${}^1S_0-{}^3P_1$  transition can be used for further cooling to  $\mu\text{K}$  temperatures. Secondly, it also has narrow spin-flip transitions accessible from the ground state. The doubly-forbidden  ${}^1S_0-{}^3P_0$  "mHz transition" is the one of most interest for metrology due to its linewidth of just 1.35 mHz in  ${}^{87}\text{Sr}$ . This occurs due to the nonzero nuclear spin of  ${}^{87}\text{Sr}$ . In  ${}^{88}\text{Sr}$  the corresponding linewidth is practically zero unless a strong magnetic field is applied, which makes it possible to engineer a linewidth in the  $\mu\text{Hz}$  range. As an alternative the singly-forbidden  ${}^1S_0-{}^3P_1$  "kHz transition" is in an intermediate region between the narrow clock transitions and the MHz-wide allowed transitions. This allows for avoiding the much larger technical demands associated with transitions in the mHz range, making it useful for exploring the physics of metrological systems and developing systems where simplicity is also important. This is the "pendulum" transition we will be working with throughout the thesis.

### 1.3 Atomic clocks, optical cavities and lasers

The second is currently defined by the transition frequency between two hyperfine states in caesium-133. And since the atoms behave identically, anyone can shine microwaves on caesium-133 atoms at different locations - if they absorb the photons and are not disturbed

by their environment, then we know the frequency of the photon's oscillations is 9.2 GHz, and can keep track of the oscillations to make a clock. As we saw magnetic field can disturb the frequency of some transitions by the Zeeman effect, but other effects also include different electric fields, gravitational acceleration or Doppler shifts from relative motion, so it is still important to understand the influence of the environment. The prospects of nuclear clocks are interesting because they can be even less sensitive to some environmental effects compared to clocks based on electronic transitions [27].

In addition to atoms being identical, another big advantage of atoms is the large transition frequency which enables a much finer division of time than mechanical clocks can achieve. If the arm of a clock swings once per second, you cannot divide time much finer than that and use it to distinguish time intervals of  $\mu\text{s}$ . But using the microwave transition of caesium at 9.2 GHz corresponds to having an arm that swings back and forth during just 110 picoseconds, so much smaller time intervals can be distinguished. For this reason, the optical atomic clocks which have been developed over the past few decades have also rapidly progressed to outperform the older clocks based on microwave transitions, like caesium. The  $^1\text{S}_0$ - $^3\text{P}_1$  transition which we focus on in this thesis has a transition frequency of 434 THz, equivalent to a period of 2.3 femtoseconds (and wavelength 689 nm, visible as red light). With such a fine division of time, optical clocks can outperform the caesium standard by orders of magnitude, and there have been considerations [28] to use them in a redefinition of the second for over a decade now. The linewidth is also important as it determines how finely frequencies can be discriminated, so transitions can be characterized by a quality factor given by  $Q = \omega/\gamma$  which can be on the order of  $10^{17}$ , much larger than for other types of oscillators.

One challenge arising from the optical frequencies is that they are too high for direct electronic measurements. Instead optical frequencies can be measured relative to each other by using the interference of light waves, if they have the same polarization. This arises from the superposition principle, meaning the total electric field of the wave is the sum of the two separate waves. So if two laser beams are overlapped and one has a frequency that is 10 MHz higher than the other, a 10 MHz beat signal can be detected e.g. with a photodiode. In this way atomic frequency references can be compared to each other, or characterized with "reference lasers" which keep an approximately constant frequency on a short timescale, but may drift between random frequencies on longer timescales.

Because we can measure time so precisely, optical clocks are also used for some of the most precise measurements of other quantities. Since the frequency of atomic transitions can be disturbed by their environment, the clocks can be used to measure a select "disturbance" instead of avoiding it. For example the gravitational potential can be mapped out by comparing the frequency of an atomic clock at a fixed location with another one that is moved to different locations in the potential. This can reveal information about the composition or ongoing processes underground. Another application of atomic clocks is in geopositioning systems. For these, satellites in orbit with atomic clocks on board send out radio signals with time information from the clocks. These signals propagate at the speed of light, so the time at which they reach a receiver to be located will be delayed by  $d/c$ , where  $d$  is the distance to the satellite and  $c = 299792458$  m/s is the speed of light. In this way the delay time from three satellites pinpoints a location relative to the satellites. In practice four satellites are typically necessary, when the receiver does not have an accurate clock itself, which adds an additional unknown to the problem. With signals traveling at  $c$ , a 100 ns error in an atomic clock could result in 30 meters error in a calculated distance, highlighting how important the clock precision and accuracy is for these systems.

To get a better idea of the physics of atomic clocks and current challenges, we can consider an example of one of the best-performing atomic clocks today [29], illustrated in Fig. 1.2. Here on the order of 1000  $^{87}\text{Sr}$  atoms are first cooled and trapped using lasers, reaching a temperature of 3  $\mu\text{K}$ . Such low temperatures are important for the best atomic clocks because the typical (root mean square) velocity of an atom at a temperature  $T$  is  $v_{rms} = \sqrt{3k_B T/m}$ , where  $k_B$  is Boltzmann's constant and  $m$  is the mass of the atom [30, p. 242]. For  $^{87}\text{Sr}$  this gives  $v_{rms} = 3 \text{ cm/s}$  at this temperature. This causes a Doppler shift in the frequency which an atom will absorb or emit at. The Doppler shift in the resonance frequency of an atomic transition is  $\Delta\nu = \nu_0 \cdot v/c$ , where  $v$  is the relative velocity and  $\nu_0$  is the transition frequency. In this clock the  $^1\text{S}_0$ - $^3\text{P}_0$  transition in Fig. 1.1 at 430 THz is used. This means that at 3  $\mu\text{K}$  a typical Doppler shift is about 40 kHz, about  $10^{-10}$  of the clock transition frequency. This could be a problem if they disturb the frequency of the atomic clock. However there are equally many atoms with positive and negative shifts, so the frequency of the clock is disturbed far less than on the order of  $10^{-10}$ .

To use these cold atoms as a clock after cooling and trapping them, a laser beam with very stable frequency (resonant with the clock transition) is sent onto the atoms for 600 ms. This particular duration corresponds to a  $\pi$ -pulse and transfers the most atoms to the excited state,  $^3\text{P}_0$ . The  $\pi$ -pulse duration generally depends on the laser beam intensity, but also the linewidth of the atomic transition ( $1.35 \pm 0.03 \text{ mHz}$  in this case [21]). The narrow clock transitions imply that the  $\pi$ -pulse duration is relatively long and also that small changes in the laser frequency will significantly change how many atoms are transferred by the pulse. This means that if the laser used for the  $\pi$ -pulse has the wrong frequency, less atoms will be excited, and the frequency of the laser can be corrected back to the frequency of the atomic transition. Making such corrections continually is referred to as "locking" the laser to the atomic transition and yields a frequency reference, which is the core of an atomic clock (the remaining problem of using the very stable THz optical signal for actual timekeeping is mainly technical). To know how many atoms are excited by the  $\pi$ -pulse, a short pulse of light at a frequency matching a different (much broader) transition is sent onto the atoms before and after the  $\pi$ -pulse, which causes the non-excited atoms to fluoresce, emitting light that can be used to count them.

However this scheme is cyclic, because it takes time to first cool and trap the atoms, then send a  $\pi$  pulse, and then another pulse of light to read the state of the atoms to correct the laser, before starting over and repeating. You only get information about what the frequency of the laser was during the  $\pi$ -pulse - not during cooling or reading their state, which is "dead-time". This can reduce the frequency stability of atomic clocks [31]. During this dead-time, the system relies on an optical cavity with high finesse (implying it has highly reflecting mirrors) to stabilize its frequency. A photon can only enter through the mirrors if its frequency is within a very narrow range such that an integer number of photon wavelengths matches the cavity length, otherwise the photon will be reflected. This frequency range defines the cavity linewidth  $\kappa$  and the inverse of the power decay time within it, similarly to the atomic transition linewidth  $\gamma$ . This ability of cavities to discriminate frequencies like atoms can be exploited in the Pound-Drever-Hall locking scheme [32], to lock a laser

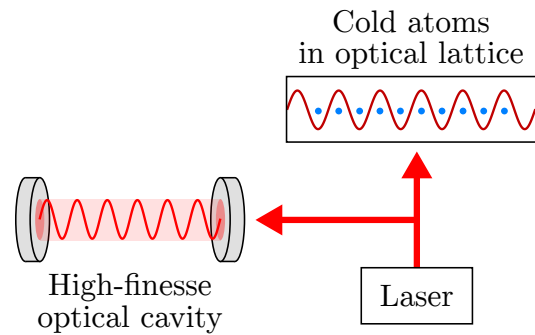


Figure 1.2: Example of a passive atomic clock. The laser corresponds to the "arm" of a mechanical clock, and its frequency is adjusted to be on resonance with a transition being interrogated in cold atoms. An optical cavity also helps to keep the laser frequency stable while the cold atoms are being prepared.

frequency to the cavity resonance frequency, which depends on the exact distance between its mirrors. But since the cavity is a mechanical construct, this distance can drift over time, and tiny thermal fluctuations in the mirrors can also cause noise on short timescales, which is a current limitation in the best frequency references [33, 34].

Therefore an ongoing goal in quantum metrology is to make continuous optical atomic clocks. This could be done for example by using an atomic beam so the preparation, interrogation and state readout can be separated in space instead of time. This would still be a passive reference, implying that the frequency of the clock laser is corrected using the transition of atoms which are not responsible for the laser emission itself. An alternative scheme is an active clock, using atoms with a narrow transition as a gain medium to directly generate light with a frequency determined by the atomic transition. This is the concept behind superradiant lasers, which are the focus of this thesis.

## 1.4 Superradiant lasers

Superradiant lasers are a promising type of active frequency reference - their principle is similar to the hydrogen maser [35], but with the benefit of operating at high optical frequencies. The differences between superradiant lasers and ordinary good-cavity lasers are illustrated in Fig. 1.3. For quantum metrology, the most important feature is that the phase and frequency of the emitted light in a superradiant laser are mainly determined by the resonance frequency of the gain medium (the atoms) rather than the optical cavity (which drifts over time, and as mentioned, limits the best frequency references). A superradiant laser requires operating in the bad-cavity regime, where the gain linewidth is significantly narrower than the cavity linewidth. The gain linewidth is fundamentally limited to the linewidth of the atomic transition, so narrow atomic transitions are used, just as for the passive frequency references. However even if the transition linewidth is very narrow, the gain linewidth can be broadened further both homogeneously and inhomogeneously, with different resulting effects. A broad cavity linewidth, as required by a superradiant laser, implies any photons within the cavity are quickly transmitted, and the intensity within the cavity itself is low compared to cavities with narrow linewidths and highly reflecting mirrors. In this way the phase-information in the atoms is long-lived in a superradiant laser, and any emission from the gain medium is quickly transmitted by the cavity, without the cavity significantly influencing the phase and frequency.

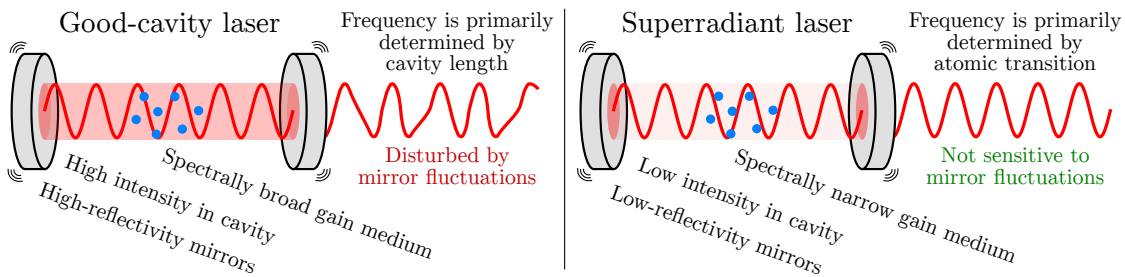


Figure 1.3: Comparison of superradiant lasers and ordinary good-cavity lasers.

Similarly to the passive references, superradiant lasers can be both pulsed and continuous. From an experimental point of view a pulsed superradiant laser is easier to realize. By trapping and cooling atoms (up to on the order of  $10^9$  on the order of a second) within an optical cavity and pumping them all to the excited state of the clock transition at once, the ensemble can emit a pulse into the cavity. A continuous superradiant laser requires either a constant flux of atoms or keeping the same atoms trapped while lasing. Because the superradiating atoms within the cavity can easily be disturbed by cooling light, it is hard to realize a high atom numbers with a continually operating superradiant laser, making it

harder to reach the threshold for operating. Therefore realizing fully continuous superradiant lasing on narrow optical transitions is an ongoing challenge.

### 1.4.1 Regimes of superradiant pulses

Superradiant lasers borrow the term superradiance from a range of phenomena where atomic dipoles phase-synchronize and radiate cooperatively into a common electromagnetic mode at a higher rate than independent spontaneous emission. This was originally considered mainly in a gas where particles were confined within a wavelength [36]. The particles are initially excited, and the cooperative emission rate scales with  $N^2$ . The result is a pulse characterized by a  $\text{sech}^2$  shape in the time domain, and a peak intensity which also scales with  $N^2$ .

Later studies focused on extended gases where one electromagnetic mode is favored due to the particle distribution, e.g. a pencil-shaped cloud. These systems share similarities with lasers, such as threshold density [37] or length [38], and exhibit additional regimes. A superradiating ensemble can be prepared with a finite initial coherence (determined by e.g. a pumping beam). This is a narrower definition of superradiance which has been used e.g. in the overview [39, p. 168]. Alternatively the ensemble can be prepared with no initial coherence, for example using a third level decaying to the excited state. The term superfluorescence has been introduced [40] to distinguish this case with no initial coherence, as the pulse requires a spontaneously emitted photon to be initiated. This affects the pulse buildup time and phase, as the rate of spontaneous emission scales with  $N$  rather than  $N^2$ , and decay events are random. The subsequent dynamics can still result in  $\text{sech}^2$ -shaped pulses with  $N^2$ -scaling peaks, which has been denoted "pure" superfluorescence [40, 41]. Other characteristics of the pure regime include a pulse duration scaling with  $1/N$  [42] and a delay between pumping and pulse peak which scales with  $\log(N)/N$  for a fully inverted ensemble [43, p. 309] [42, p. 334], and  $1/N^2$  for a half-inverted state Dicke-state (which has a macroscopic initial coherence) [43, p. 309].

A different regime is encountered when the gas length dimension becomes comparable to a "cooperation length" (so that the full ensemble no longer synchronizes), instead of being significantly smaller [38, 40, 44]. This results in afterpulses due to the effects of stimulated emission, and a transition to a regime where the intensity scales linearly with  $N$  [40], which has also been called "oscillatory superfluorescence" to distinguish it from the "pure" regime with  $\text{sech}^2$  pulses [40, 41]. In the oscillatory regime, delays scaling with  $1/\sqrt{N}$  have been reported [41].

Yet another term, amplified spontaneous emission (ASE), has been introduced for the case where a macroscopic dipole moment fails to build up, due to e.g. low density or large thermal dephasing rate [45, 46, 47]. In this regime the intensity becomes more chaotic over time compared to (oscillatory) superfluorescence, eventually with multiple peaks from different spontaneous emission events amplified by fractions of the ensemble, within an exponentially decaying trend on average [41, 46]. Note that the terminology within the field has been the subject of confusion and discussion [48, 49], and there are variations in the use of terms. In this thesis we will use the term superradiance relatively broadly, including superfluorescence and oscillatory regimes. Superradiance in gases in free space is still an active field of research [50, 51, 52], and is also progressing towards more continuous settings [53].

### 1.4.2 Pulsed superradiant lasers

The idea of treating superradiant emission within the framework of a cavity was introduced in [43]. Here a cavity loss rate  $\kappa = c/2L$  was used (where  $L$  is the cavity length), and since  $FSR = c/2L$ , the finesse is 1, mimicing the free-space gas setting. But simply introducing a higher cavity mirror reflectivity (lower  $\kappa$ ) serves to increase the effective length of the gas sample considered in previous settings. Photons emitted by the atoms then propagate for a longer time within the sample. The regimes of the extended gas are recovered, but can now depend on the cavity parameters instead of sample length. The pure superradiant regime is recovered when the photons escape the cavity fast enough to not act back on the atoms, which requires  $\kappa > \Omega_N = 2g\sqrt{N}$ , where  $g$  is the atom-cavity coupling (here assumed identical for all atoms), and  $\Omega_N$  is the collective coupling rate, with  $N$  atoms. If this is not fulfilled, photons piling up in the cavity may act back on the atoms (at the interaction rate  $2g\sqrt{n}$ , where  $n$  is the photon number), such that absorption and stimulated emission starts to play a significant role. This gives rise to the superradiant crossover regime, like the oscillatory regime considered for the extended gas, where the peak intensity scales linearly with  $N$  rather than with  $N^2$ .

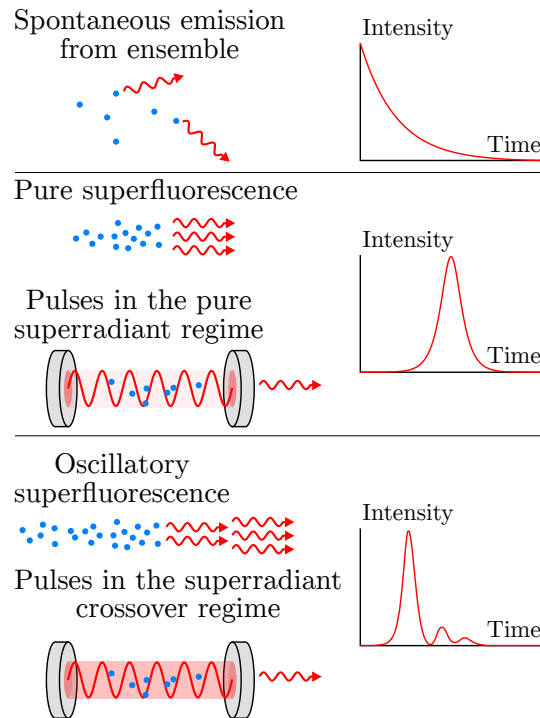


Figure 1.4: *Regimes for pulsed superradiance and independent spontaneous emission.*

In this way the different superradiant regimes are recovered in the bad-cavity regime of lasers mentioned earlier (see Fig. 1.4 and Fig. 1.5). Note that in the presence of e.g. thermal broadening, the simple distinction based on  $N$  no longer holds, as many of the fast-moving atoms in the ensemble may not be able to phase-synchronize with the slow ones, reducing the collective coupling rate. In this case an "effective" atom number may be considered, or alternatively whether  $\kappa \gg 2g\sqrt{n}$ , such that the cavity field population adiabatically follows the atomic dynamics as in the pure superradiant regime, versus  $\kappa \approx 2g\sqrt{n}$ , where oscillations can be expected.

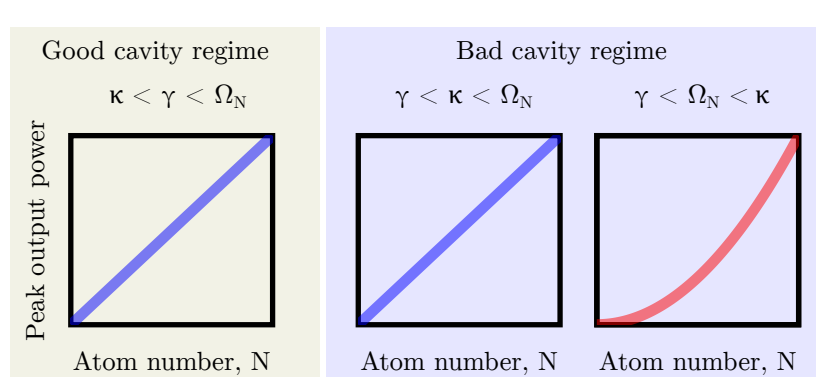


Figure 1.5: *Scaling of the peak output power with atom number depending on the relative magnitudes of  $\gamma$ ,  $\kappa$  and  $\Omega_N$ . Figure adapted from [54].*

Superradiant laser pulses in the pure regime have been studied experimentally on the 1.35 mHz wide  $^1S_0$ - $^3P_0$  transition in  $^{87}\text{Sr}$  [55, 56] and on the 375 Hz wide  $^1S_0$ - $^3P_1$  transition in  $^{40}\text{Ca}$ , where  $\log(N)/N$  delay scaling and pulse statistics from the pure regime are recovered [57]. It has also been investigated theoretically in [58], recovering  $N^2$ - and  $N$ -scaling of pulse heights in the pure and crossover regimes, respectively. Within this thesis we will also explore these regimes on the 7.5 kHz wide  $^1S_0$ - $^3P_1$  transition in  $^{88}\text{Sr}$  at mK temperatures (published in [54]), primarily the crossover regime. Spectral properties in this crossover regime have been reported in [59] and are also described in this thesis. The crossover regime has also been explored on this transition at  $\mu\text{K}$  temperatures in [60].

### 1.4.3 Continuous superradiant lasers

In [61] the idea of repumping superradiating atoms within a cavity via a three-level scheme was introduced - the continuous superradiant laser. Unlike the previously mentioned pulses, which will have linewidths larger than the transition linewidth  $\gamma$ , the linewidth of a continuous laser is not Fourier-limited in this way, making it of much greater metrological interest. Different regimes have also been distinguished for continuous superradiant lasers, as for the pulsed systems. In [62] a crossover between the good and bad cavity regimes has been defined based on the ratio of cavity photons to atoms being  $n/N \approx 1$ , assuming an optimal pumping rate in a three-level model. This yielded a crossover parameter given by  $Ng^2/2\kappa^2$  (for identical couplings  $g$ ), with  $Ng^2 \ll 2\kappa^2$  in the superradiant limit, and  $Ng^2 \approx 2\kappa^2$  in the crossover regime, similar to the considerations in the pulsed regime. The ratio  $n/N$  further quantifies to which degree the system's coherence is stored in the cavity photons relative to atoms, and the point at which cavity pulling grows to order unity. The crossover regime has also been described in more simple terms as the regime where gain and cavity linewidths are comparable [63]. In this context the criteria based on  $N$  or  $n$  can be related to the power broadening of the gain medium due to the cavity field. In [64] the pure and crossover regimes of a continuous superradiant laser have also been investigated, distinguishing between (pure) superradiance and a superradiant lasing regime where  $n > 1$ . For high photon numbers within the lasing regime, entanglement can lead to a narrowing of the laser linewidth [64, p. 3].

Another new aspect of continuous superradiant lasers is how to supply new excitations which are required for continuous operation. An overview of some different approaches have been presented in [65], and some examples are depicted in Fig. 1.6.

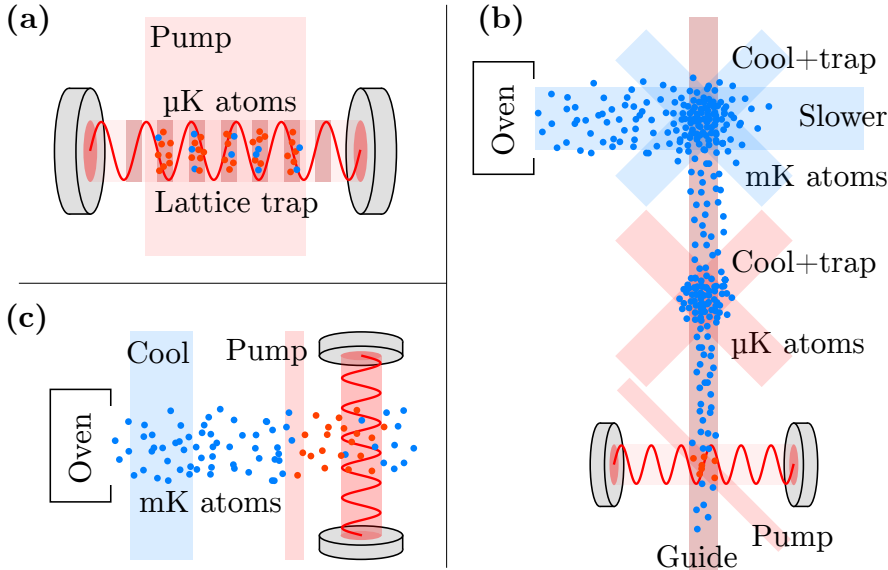


Figure 1.6: Examples of possible continuous superradiant laser architectures discussed in the main text. The functionality of different laser beams (shaded) are indicated, as well as atom temperatures at different locations. The red color of some atoms indicate excitation from optical pumping. The atom source is not depicted for the optical lattice laser (a), but may be trapped with a similar scheme to the guided beam (b) or a continuous 3D trap within the cavity mode (similar to the intermediate trapping stages in (b)).

If an atomic ensemble can be cooled and trapped within the cavity, the ensemble may be considered stationary and can be repumped incoherently as considered in [61, 62, 64, 66, 67, 68, 69]. The trapping can be done using a far-detuned high-power optical lattice within the cavity (Fig. 1.6(a)), giving rise to the term optical lattice laser [70]. This setting has also been investigated for  $^{40}\text{Ca}$  [71], and one proposal combines such a lattice with a cooling scheme for alkaline earth atoms [72]. Another approach for a lattice-like laser could be to exploit the superradiant lasing interaction itself for cooling and trapping atoms [73, 74, 75]. The mechanical effects of interaction with the superradiant field in a cavity have also been studied extensively in [76, 77], and the impact of dipole-dipole interactions between trapped atoms in [78]. In addition to these studies, more exotic lasing schemes have also been explored, such as lasing involving multiple Zeeman levels to achieve a narrow linewidth in  $^{88}\text{Sr}$  [79] and lasers based on virtual transitions [80].

For an optical lattice laser to work, it is crucial that the lattice has a wavelength which is magic for the superradiant transition, meaning that light shifts on the two lasing states cancel out so they will not disturb the laser. This issue was originally considered for passive optical lattice clocks [81, 82]. Similarly, light shifts from pumping or cooling lasers could also disturb the superradiant laser frequency if they do not cancel out. Another challenge is that the repumping laser introduces additional decoherence on the lasing transition - a higher repumping rate enables potentially more power, but increases the lasing threshold and can potentially ruin the narrow linewidth of the laser. Finally, light for cooling the atoms can easily introduce large decoherence rates that would destroy the lasing - this can be avoided by using transitions not directly connected to the states involved in superradiance (as in [72]), but can further complicate the pumping scheme.

Therefore some studies have considered settings where atoms are in continuous motion through the cavity (as in Fig. 1.6(b)). In the ultra-cold regime this has been investigated theoretically for atoms continually fed through optical lattices [83]. In this thesis we will also consider a system where atoms are transported along a dipole guide and are continually repumped within a cavity (also presented in [84]), without using a lattice. However most ultracold atom experiments ultimately rely on a hot beam of atoms from an oven as source, and complex intermediate stages are needed to produce a cold ( $\mu\text{K}$ ), slow (e.g. cm/s) and dense beam. Atom losses are inevitable throughout the many intermediate stages from the oven, so the atom flux and potential output power is reduced by orders of magnitude compared to what could be achieved if the total atom flux from the oven could be used for superradiance.

For this reason the simplest idea for continuous superradiance is to let such a hot beam of atoms pass directly through a pumping stage before the cavity [85] (Fig. 1.6(c)). The atoms can be transversely laser-cooled to the mK regime using broad transitions, which still implies Doppler dephasing on the order of MHz. This, combined with the high propagation speeds and limited interaction time with the cavity, makes such a hot beam approach most viable for relatively broad transitions on the order of kHz, and was originally considered using the 7.5 kHz transition in  $^{88}\text{Sr}$  and 375 Hz transition in  $^{40}\text{Ca}$  [85]. Laser linewidths of 10 mHz have been predicted as viable in a hot beam system using e.g. the 375 Hz transition in  $^{40}\text{Ca}$ , comparable to the best existing clock lasers [86]. The predicted output power, on the order of  $\mu\text{W}$ , is also decent for metrological purposes. However the significant thermal broadening leads to challenges and additional features, such as unstable regimes, which have been explored in [87, 88, 89, 87]. The impact of inhomogenous broadening on superradiant lasing has also been investigated more generally in [90, 91] and transit time broadening in [92]. We will also explore a continuous hot-beam system based on  $^{88}\text{Sr}$  in this thesis, for which some results are presented in [84].

#### 1.4.4 Experimental progress towards continuous superradiance

Continuous superradiant lasing has not been demonstrated on such narrow transitions as used in pulsed systems. One of the closest systems may be [93], where lasing on an 1470 nm hyperfine transition in a Cs gas cell was realized. Despite decay rates and Doppler widths in the MHz range, the much larger cavity decay rate of  $2\pi \cdot 244$  MHz places the system deep in the bad-cavity regime.

Some systems have also achieved quasi-continuous operation. These are based on repumping an ensemble of atoms just as in some proposals for continuous superradiance, but with technical limitations to the duration. Typically an ensemble of atoms is trapped, similar to the technique in Sec. 1.3 and in experiments with pulsed superradiance. Atom loss during lasing limits the duration to less than a second, while also causing changes in the dynamics over time which are not expected in a fully continuous regime, such as a gradual decrease in output power and change in spectral characteristics. Despite this, they demonstrate many of the properties and the over-all behavior expected in a fully continuous regime. Quasi-continuous superradiance has been demonstrated using a Raman transition in  $^{87}\text{Rb}$  up to 140 ms [94], where relaxation oscillations [95] and phase-synchronization dynamics [96] have also been studied in detail. The quasi-continuous regime has also been realized on the  $^1\text{S}_0 - ^3\text{P}_1$  transition in  $^{88}\text{Sr}$  for up to 1.5 ms [60].

The realization of continuous superradiant lasers also strongly depends on the development of atomic beams with high flux and density, and low temperature. Strontium beams in the ultra-cold  $\mu\text{K}$  regime have been used to realize the first continuous Bose-Einstein condensate [97] and characterized utilizing different isotopes [98], including  $^{88}\text{Sr}$ . A number of sources have also been developed [99, 100, 101, 102] yielding a higher atom flux closer to the mK regime, which are promising sources for realizing the hot beam proposals.

## 1.5 Thesis overview

In this thesis we will investigate superradiant lasing on the 7.5 kHz-wide  $^1S_0$ - $^3P_1$  transition of  $^{88}\text{Sr}$  in several different kinds of systems - both pulsed and continuous. The thesis contains both experimental work on realizing some of the systems, experimental characterization of superradiant lasing pulses, and a big part is also devoted to numerical simulations of lasing in the different systems. Therefore the numerical models have some variations, but share the same fundamental principles, which are described in Chapter 2.

The pulsed system, which is realized in the machinery at the University of Copenhagen, consists of a cold atomic cloud within an optical cavity. This cloud is trapped from a Zeeman-slowed atomic beam using a 3D magneto-optical trap (MOT). It is almost fundamentally a cyclic system because the superradiant lasing is heavily disturbed by the cooling and trapping process. However the cyclic nature enables the machine to accumulate many ( $\sim 10^7$ ) atoms within the cavity mode, making it relatively easy to reach lasing threshold. In this sense the machine is a stepping stone towards continuous superradiance and enables us to investigate the dynamics of superradiant lasing with simpler technical requirements.

Chapter 3 is devoted to the experimental details of this setup, and the upgrades that were made as part of this thesis to realize  $\mu\text{K}$  atom temperatures. Chapter 4 is devoted to simulations and experimental results from pulsed superradiance in the mK regime. Chapter 5 describes new regimes enabled by current and ongoing experimental upgrades, including pulses at  $\mu\text{K}$  temperatures and dynamics with continuous repumping. As such this chapter primarily presents simulations.

Another type of system which we will investigate is a continuous superradiant laser operating on the kHz-transition based on the hot-beam scheme. It is characterized by a large atom flux ( $\sim 10^{12} \text{ s}^{-1}$ ), high thermal velocities in the propagation direction, mK temperatures along the cavity axis, and its relative technical simplicity. This type of system is being developed at the University of Amsterdam, and work on the experimental setup during my secondment is described in Chapter 6, while simulations of the superradiant laser physics are described in Chapter 7.

A second variant of the continuous superradiant laser that we will investigate is a cold beam system. This is based on an atom source realized at the University of Amsterdam and was considered as an alternative candidate to the hot beam system before its development. The cold beam system is characterized by a lower atom flux ( $\sim 10^8 \text{ s}^{-1}$ ),  $\mu\text{K}$  atom temperatures, using magic dipole traps to transport and confine the atoms, and a repumping scheme to enhance emission, making it significantly more complex. Numerical simulations of this type of system are presented in Chapter 8.

## Theory for superradiant lasing and numerical treatment

The goal of the numerical models in this thesis is to predict observables, mainly the output power and spectrum of a superradiant laser, and how they depend on relevant physical parameters. In this chapter we will describe the general methods used for making these models. An example of a very general system that could be treated is illustrated in Fig. 2.1.

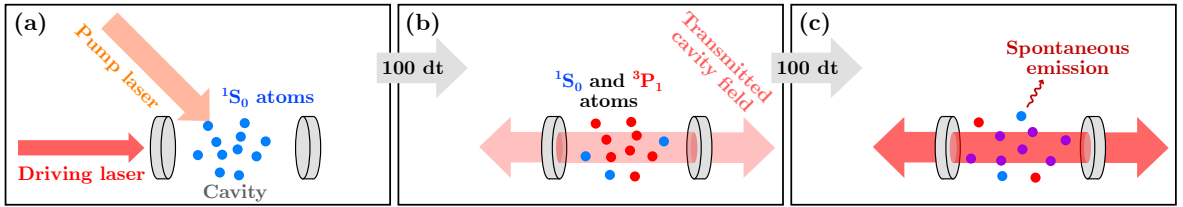


Figure 2.1: Example of the time evolution of a general superradiant laser system. The system changes significantly from panel (a) to (b) and then (c), but the dynamics may be solved numerically by dividing them into small time intervals of length  $dt$ , e.g. 100 timesteps between the situations in each panel. If the time intervals are short enough, the changes during each interval are small enough that they can be accurately solved.

In this example the system starts out in the state shown in panel (a). Here an ensemble of  $^1\text{S}_0$  atoms are located within the optical cavity of the superradiant laser. Right at this time a pumping laser is turned on to excite the atoms, and a driving laser is turned on to populate the cavity field with photons, but these dynamics have not yet changed the atom and cavity states. After a while, the system has changed to the state in panel (b). Here the lasers have been turned off again, but in the meantime, several atoms (red) have been excited by the pumping laser to  $^3\text{P}_1$ , and a cavity-field has built up due to the driving laser, which is now also leaking out of the cavity mirrors. The atoms start interacting with the cavity field, and a bit later, the system is as shown in panel (c). Here many of the atoms have emitted light into the cavity, or absorbed light from it, and are now in superpositions of  $^1\text{S}_0$  and  $^3\text{P}_1$  (purple), while some may spontaneously emit photons into the environment.

The aim of numerical treatment is to divide this time evolution into small timesteps (each with a length called  $dt$ ), because the dynamics cannot be solved analytically. The dynamics in between these three situations might be divided into e.g. 100 timesteps where the changes are small enough to get an accurate solution. Every timestep we consider the current state of the system and based on this we find the state one timestep later. For example if an atom has a velocity  $\mathbf{v}$ , the differential equation for its position  $\dot{\mathbf{r}}$  is simply  $d\mathbf{r}/dt = \mathbf{v}$ , giving the discrete variant  $d\mathbf{r} = \mathbf{v} \cdot dt$  (according to the Euler method) telling us the change in position  $d\mathbf{r}$  during the timestep. If gravity or optical forces are present,  $\mathbf{v}$  may also change during the timestep. In that case an accurate solution requires  $dt$  is small compared to the timescale of the relevant dynamics. For example if an atom is initially moving upwards at 1

m/s while being accelerated downwards at 10 m/s<sup>2</sup> by gravity, choosing dt=1 second while using a simple Euler integration would tell us the atom has moved 1 meter upwards after the timestep, and its new velocity is 9 m/s in the downwards direction. This velocity is correct as it changes at the same constant rate (10 m/s<sup>2</sup>) during the time interval dt. However the analytical solution tells us the atom would have fallen by 4 meters during this time interval. The predicted position is very inaccurate because the velocity changes significantly during the time interval, compared to the initial value that was used to calculate the position. This timestep is clearly too large to accurately treat an acceleration of this magnitude.

In similar fashion, using cavity quantum electrodynamics, we will derive differential equations to describe the cavity field and atomic states that can be treated by numeric integration. This allows us to describe systems with very complex dynamics that would need to be greatly simplified for analytical treatment. Lasers can be switched on and off or change intensity, random recoils from lasers may be treated for each atom individually, and so on. When modeling a superradiant laser numerically we encounter similar problems as for the falling atom. If atoms are Rabi oscillating at a rate  $\chi$  due to a pumping laser,  $dt \ll 1/\chi$  is required. If an atom is moving across a coherent light wave at a rate  $v/\lambda$ , interacting with a cavity field at a rate  $2g\sqrt{n}$ , decaying from some excited state at a rate  $\gamma$ , or light is leaking from the cavity at a rate  $\kappa$ , all these rates will similarly set requirements for how small dt must be. When treating the <sup>1</sup>S<sub>0</sub>-<sup>3</sup>P<sub>1</sub> transition in <sup>88</sup>Sr with Euler integration this can easily be on the order of 1 ns, however higher order numeric integration methods can allow for over an order of magnitude higher timestep at the cost of a few extra and more complex equations (which is often worth it). In this thesis a 2nd order Runge-Kutta method is generally used for the equations that require the shortest timesteps, in particular the variant of the method that minimizes the third order local truncation error (for more details see [103, p. 32] and [104, p. 1109]).

## 2.1 Cavity quantum electrodynamics

Here we will illustrate the general methods for deriving the time-evolution of the atomic and cavity field states in a system such as in Fig. 2.1. To make it relatively general we will assume the atoms have three levels,  $|g\rangle$ ,  $|e\rangle$  and  $|i\rangle$ , so the extension to any number of levels should be clear.  $|g\rangle$  represents the ground state and  $|e\rangle$  is the excited state of the superradiant laser transition, so  $|e\rangle$  can decay spontaneously to  $|g\rangle$ .  $|i\rangle$  represents a high energy that can decay to both  $|g\rangle$  and  $|e\rangle$ , and a laser is used to pump the atoms to  $|i\rangle$  so that they decay to  $|e\rangle$  and inversion on the lasing transition can be achieved.

### 2.1.1 Hamiltonians

A starting point for finding the time evolution of a quantum system is its Hamiltonian, representing the total energy. Considering the system in Fig. 2.1, a fairly general Hamiltonian of the physical system is given by:

$$H = H_{cav} + H_{at} + H_{int} + H_{pump} + H_{drive}. \quad (2.1)$$

$H_{cav}$ : We will start by defining the Hamiltonian in the Schrödinger picture, where the operators are time-independent. The energy of a cavity field,  $H_{cav}$ , is given by the number of photons  $n$  multiplied by the energy of each photon,  $\hbar\omega$ . In cavity QED this gives us the term  $\hbar\omega n$  in the Hamiltonian, where  $n$  is the photon number operator (we will omit hats on operators). We will write the number operator  $n = a^\dagger a$  in terms of the bosonic raising and lowering operators  $a^\dagger$  and  $a$ , which obey the commutation relation  $[a, a^\dagger] = aa^\dagger - a^\dagger a = 1$  [105, p. 12] [106, p. 11].

$H_{at}$ : For an atom we need to choose a zero point for the atomic energy levels. This choice does not affect the physics, as the dynamics depend on relative energy differences. Here we

choose the unperturbed ground state  $|g\rangle$  to have zero energy. In this case the Hamiltonian representing the atomic energy will have a term for each excited state of the excitation energy  $\hbar\omega$ . A superradiant laser requires many atoms, so the Hamiltonian of the atoms will be the sum of all the individual atomic Hamiltonians. For e.g. 10 atoms with the ground state  $|g\rangle$ , excited lasing state  $|e\rangle$  and one other excited state for pumping  $|i\rangle$ , we get  $\sum_{j=1}^{10} \hbar\omega_e^j \sigma_{ee}^j + \hbar\omega_i^j \sigma_{ii}^j$ . The transition frequencies  $\omega_e^j, \omega_i^j$  can vary from atom to atom if they are affected by frequency shifts such as light shifts. When referring to unperturbed atomic transitions we will generally use capital letters, as  $\omega_E, \omega_I$ , but include Zeeman shifts in these when they are uniform.  $\sigma_{ij}$  are the Pauli spin operators. The ones with identical indices  $i = j$  represent the populations of atomic states, while the ones with different indices act as transition operators. Sometimes  $\sigma_{eg}$  is written  $\sigma^\dagger$ , similar to the bosonic raising and lowering operators, in this case with  $\sigma_{ee} = \sigma^\dagger \sigma$ . However these are fermionic raising/lowering operators and obey the anticommutation relation  $\{\sigma, \sigma^\dagger\} = \sigma\sigma^\dagger + \sigma^\dagger\sigma = 1$  [106, p. 13].

$H_{int}$ : Just as for the atomic energies, the total atom-cavity interaction energy  $H_{int}$  will be a sum of the interaction energies of all the atoms. The interaction energy of one atom with the cavity mode is given by  $\hbar\omega g_j (\sigma_{ge} + \sigma_{eg}) (a + a^\dagger)$ .  $g_j$  is the atom-cavity coupling, and for a linear cavity with two equally reflecting mirrors it is given by (defining the  $z$  axis along the cavity axis):

$$g_j = c_g \sqrt{\frac{6c^3\gamma}{W^2 L \omega^2}} \sin\left(\frac{\omega}{c} z_j\right) e^{-(x_j^2 + y_j^2)/W^2}. \quad (2.2)$$

Here  $c_g$  is a Clebsch-Gordan coefficient, which is 1 for the  ${}^1S_0-{}^3P_1$   $m_J=0$  transition we consider for superradiance in this thesis. We see the coupling  $g_j$  depends on the atomic transition through both the transition frequency  $\omega$  and linewidth  $\gamma$  - narrow transitions lead to small values of  $g_j$ , leading to slowly evolving dynamics. We also see  $g_j$  depends on cavity parameters - the waist  $W$  and length between mirrors  $L$  - these must be chosen carefully to make a superradiant laser work. We see that a small mode volume (small  $L$  and  $W$ ) result in larger  $g_j$ . Finally we see that the atom-cavity coupling depends on the position of the atom - the coupling will be low, and the atom will interact very little, if it is located near a node in the standing wave in the cavity (sine term) or it is far away from the waist of the cavity (exponential). The sinusoidal change in  $g_j$  as an atom moves along the  $z$  axis gives rise to the Doppler effect in the atom-cavity interaction.

It is worth also considering the operators, e.g.  $\sigma_{ge}^j$  and  $a$ . In the most simple picture we can consider their expectation values. Here  $\langle \sigma_{ge}^j \rangle$  is a complex number with modulus between 0 and 1, and with additional constraints in combination with the populations  $\langle \sigma_{gg}^j \rangle, \langle \sigma_{ee}^j \rangle$  from the Bloch sphere. This contains the phase information of the atomic dipole, and equivalently  $\langle \sigma_{eg}^j \rangle = \langle \sigma_{ge}^j \rangle^*$ .  $\langle a \rangle$  is similarly a complex number with the phase information of the cavity field, but modulus of  $\sqrt{n}$ . So the atom-cavity interaction generally scales with  $g\sqrt{n}$ , and the cavity QED equivalent to the semiclassical Rabi frequency is  $\chi_{QED} = 2g\sqrt{n}$ . The mirror reflectivity does not directly enter into these equations, but a high mirror reflectivity/narrow cavity linewidth results in a higher intra-cavity photon number, as the photons escape more slowly, and leads to a stronger interaction (higher  $g\sqrt{n}$ ), but  $n$  often requires numerical simulations to determine.

$H_{pump}$ : To describe the pumping of the atoms, we will assume the pump lasers to be running waves with high enough intensity that they are not significantly attenuated by the interaction with the atoms. In this case we can describe the interaction semiclassically, giving for each atom:

$$H_{pump}^j = \hbar \frac{\chi_{gi}^j}{2} \left( \sigma_{gi}^j + \sigma_{ig}^j \right) \left( e^{i\mathbf{k}_{li} \cdot \mathbf{r}_j - i\omega_{li} t} + e^{-i\mathbf{k}_{li} \cdot \mathbf{r}_j + i\omega_{li} t} \right). \quad (2.3)$$

Note the similarity to Eq. 2.2, except that the laser phase terms (right) are running waves

(with  $\mathbf{k}_{li}$  being the wave vector of the laser and  $\mathbf{r}_j$  the position vector of the atom), and the Rabi frequency which for an atom is given by:

$$\chi_{li}^j = c_g \sqrt{\frac{6\pi c^2 \gamma I_{li}}{\hbar \omega^3}} e^{-(x_j^2 + y_j^2)/W_{li}^2}. \quad (2.4)$$

The Clebsch-Gordan coefficient  $c_g$  generally depends on the pumping transition, but is of order unity.  $I_{li}$  refers to the peak intensity of the laser beam (assuming its intensity profile is Gaussian) and is related to the laser power  $P_{li}$  by  $I_{li} = P_{li}/w_1 w_2$  for a beam with waist radii  $w_1$  and  $w_2$ . For a non-Gaussian laser beam, the exponential term should be omitted and the local intensity at a given atom should be used in place of  $I_{li}$ .

$H_{drive}$ : The final term,  $H_{drive}$ , can be used to describe an external laser beam coupling into the cavity:

$$H_{drive} = \frac{\eta}{2} (a + a^\dagger) (e^{-i\omega_d t} + e^{i\omega_d t}), \quad (2.5)$$

where  $\eta$  represents the driving strength. If no atoms were present, the cavity would be populated by  $\eta^2/(\kappa^2 + 4\delta_{cd}^2)$  photons in steady state, where  $\kappa$  is the cavity linewidth FWHM and  $\delta_{cd}$  is the laser detuning from the cavity resonance (for some examples see [103, p. 6]). Since the output power from a cavity with  $n$  photons is  $P_{out} = n\hbar\omega_c$ , which must be equal to the input power in steady state and with no atoms inside, this means  $\eta = \kappa\sqrt{k_{in}P_{in}/\hbar\omega_c}$ , where  $k_{in}$  is the coupling efficiency of the input beam to the cavity mode, and  $P_{in}$  is the input power.

The resulting Hamiltonian from these examples is then:

$$H = \hbar\omega_c a^\dagger a + \sum_{j=1}^N \hbar\omega_e^j \sigma_{ee}^j + \sum_{j=1}^N \hbar\omega_i^j \sigma_{ii}^j + \sum_{j=1}^N \hbar g_j (\sigma_{ge}^j + \sigma_{eg}^j) (a + a^\dagger) + \sum_{j=1}^N \hbar \frac{\chi_{li}^j}{2} (\sigma_{gi}^j + \sigma_{ig}^j) (e^{i\mathbf{k}_{li} \cdot \mathbf{r}_j - i\omega_{li} t} + e^{-i\mathbf{k}_{li} \cdot \mathbf{r}_j + i\omega_{li} t}) + \frac{\eta}{2} (a + a^\dagger) (e^{-i\omega_d t} + e^{i\omega_d t}). \quad (2.6)$$

The terms are illustrated in Fig. 2.2.

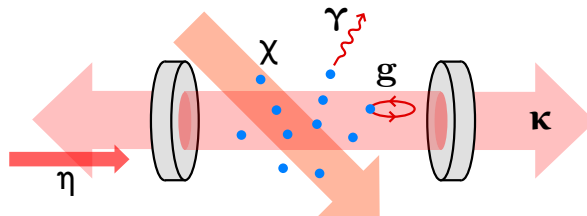


Figure 2.2: A superradiant laser consisting of an optical cavity with atoms inside. The atoms can be pumped by an external laser, causing each atom to oscillate with a Rabi frequency  $\chi_j$ . The atoms also couple to the cavity field with coupling rates  $g_j$  and emit spontaneously into the environment at a rate  $\gamma$ . Light leaks through the cavity mirrors at a rate  $\kappa$ . An external laser inputs light into the cavity, characterized by a driving strength  $\eta$ .

### 2.1.2 The interaction picture and rotating wave approximation

Once we have a Hamiltonian like Eq. 2.6, we start by noting that it contains many optical frequencies ( $\omega$ ) - these oscillate at hundreds of THz and it would be impossible to solve dynamics numerically on interesting  $\mu$ s or longer timescales if such rapidly oscillating terms were present. To deal with these we start by going to an interaction picture, choosing the non-interaction terms of the Hamiltonian (and so far keeping the frequencies  $\{\omega_1, \omega_2, \omega_3\}$  arbitrary):

$$H_U = \hbar\omega_1 a^\dagger a + \sum_{j=1}^N \hbar\omega_2 \sigma_{ee}^j + \sum_{j=1}^N \hbar\omega_3 \sigma_{ii}^j. \quad (2.7)$$

The interaction Hamiltonian, still in the Schrödinger picture, is then given by:

$$\begin{aligned} H_I^S = H - H_U &= \hbar\delta_{c1}a^\dagger a + \sum_{j=1}^N \hbar\delta_{e2}^j \sigma_{ee}^j + \sum_{j=1}^N \hbar\delta_{i3}^j \sigma_{ii}^j + \sum_{j=1}^N \hbar g_j (\sigma_{ge}^j + \sigma_{eg}^j) (a + a^\dagger) \\ &+ \sum_{j=1}^N \hbar \frac{\chi_{li}^j}{2} (\sigma_{gi}^j + \sigma_{ig}^j) (e^{i\mathbf{k}_{li}\cdot\mathbf{r}_j - i\omega_{li}t} + e^{-i\mathbf{k}_{li}\cdot\mathbf{r}_j + i\omega_{li}t}) + \frac{\eta}{2} (a + a^\dagger) (e^{-i\omega_dt} + e^{i\omega_dt}), \end{aligned} \quad (2.8)$$

where we define detunings as  $\delta_{ij} = \omega_i - \omega_j$ . The next step is to determine the time-dependence of the operators in this interaction picture - how they evolve due to  $H_U$ . For each of the operators  $o$  we can use the Heisenberg equation:

$$\dot{o} = \frac{i}{\hbar} [H_U, o]. \quad (2.9)$$

Then we get (with the  $I$  representing the operators being in the interaction picture):

$$\begin{aligned} \dot{a}_I &= i\omega_1 [a^\dagger a, a]_I = i\omega_1 (a^\dagger aa - aa^\dagger a)_I = i\omega_1 [a^\dagger, a]_I a_I = -i\omega_1 a_I \\ \dot{\sigma}_{ge,I}^j &= i\omega_2 [\sigma_{ee}^j, \sigma_{ge}^j]_I = -i\omega_2 \sigma_{ge,I}^j \\ \dot{\sigma}_{gi,I}^j &= -i\omega_3 \sigma_{gi,I}^j. \end{aligned} \quad (2.10)$$

This gives the following relations between the Schrödinger and interaction picture operators (the photon number operator  $n$  and atom populations  $\sigma_{ee}^j$  etc. are unaffected by these changes in picture):

$$a_I = a_S e^{-i\omega_1 t}, \quad \sigma_{ge,I}^j = \sigma_{ge,S}^j e^{-i\omega_2 t}, \quad \sigma_{gi,I}^j = \sigma_{gi,S}^j e^{-i\omega_3 t}. \quad (2.11)$$

Now we can replace the  $o_S$  operators in Eq. 2.8 with the new  $o_I$  operators and obtain the Hamiltonian in the interaction picture (dropping the picture subscripts again):

$$\begin{aligned} H_I &= \hbar\delta_{c1}a^\dagger a + \sum_{j=1}^N \hbar\delta_{e2}^j \sigma_{ee}^j + \sum_{j=1}^N \hbar\delta_{i3}^j \sigma_{ii}^j \\ &+ \sum_{j=1}^N \hbar g_j (\sigma_{ge}^j e^{i\omega_2 t} + \sigma_{eg}^j e^{-i\omega_2 t}) (ae^{i\omega_1 t} + a^\dagger e^{-i\omega_1 t}) \\ &+ \sum_{j=1}^N \hbar \frac{\chi_{li}^j}{2} (\sigma_{gi}^j e^{i\omega_3 t} + \sigma_{ig}^j e^{-i\omega_3 t}) (e^{i\mathbf{k}_{li}\cdot\mathbf{r}_j - i\omega_{li}t} + e^{-i\mathbf{k}_{li}\cdot\mathbf{r}_j + i\omega_{li}t}) \\ &+ \frac{\eta}{2} (ae^{i\omega_1 t} + a^\dagger e^{-i\omega_1 t}) (e^{-i\omega_dt} + e^{i\omega_dt}). \end{aligned} \quad (2.12)$$

If we then choose the arbitrary frequencies to be reasonably close (up to GHz, not THz) to the ones in the terms they add/subtract with, so  $\omega_1 \approx \omega_2, \omega_1 \approx \omega_d, \omega_3 \approx \omega_{li}$ , we can use the rotating wave approximation. Multiplying the brackets, terms with e.g.  $\exp(i(\omega_2 + \omega_1)t)$  would oscillate rapidly and average to zero, so that we can neglect them, while terms with frequency differences, e.g.  $\exp(i\delta_{21}t)$ , may oscillate on the physically relevant timescales. This gives us the interaction Hamiltonian in the rotating wave approximation:

$$\begin{aligned} H_I &= \hbar\delta_{c1}a^\dagger a + \sum_{j=1}^N \hbar\delta_{e2}^j \sigma_{ee}^j + \sum_{j=1}^N \hbar\delta_{i3}^j \sigma_{ii}^j + \sum_{j=1}^N \hbar g_j (\sigma_{ge}^j a^\dagger e^{i\delta_{21}t} + \sigma_{eg}^j a e^{-i\delta_{21}t}) \\ &+ \sum_{j=1}^N \hbar \frac{\chi_{li}^j}{2} (\sigma_{gi}^j e^{i\mathbf{k}_{li}\cdot\mathbf{r}_j - i\delta_{li3}t} + \sigma_{ig}^j e^{-i\mathbf{k}_{li}\cdot\mathbf{r}_j + i\delta_{li3}t}) + \frac{\eta}{2} (ae^{i\delta_{1d}t} + a^\dagger e^{-i\delta_{1d}t}). \end{aligned} \quad (2.13)$$

Now we can consider which frequencies to choose for  $\omega_1, \omega_2$  and  $\omega_3$ . Choosing them earlier can simplify the derivation, while choosing them later can make it easier to simplify the

final equations. In terms of computational performance it is often an advantage to get rid of exponential terms. For example choosing  $\omega_1 = \omega_d, \omega_2 = \omega_1, \omega_3 = \omega_I$  (with  $\omega_I$  being the unperturbed atomic transition frequency) would give:

$$\begin{aligned} H_I = & \hbar \delta_{cd} a^\dagger a + \sum_{j=1}^N \hbar \delta_{ed}^j \sigma_{ee}^j + \sum_{j=1}^N \hbar \delta_{il}^j \sigma_{ii}^j + \sum_{j=1}^N \hbar g_j (\sigma_{ge}^j a^\dagger + \sigma_{eg}^j a) \\ & + \sum_{j=1}^N \hbar \frac{\chi_{li}^j}{2} (\sigma_{gi}^j e^{i\mathbf{k}_{li} \cdot \mathbf{r}_j - i\delta_{li} t} + \sigma_{ig}^j e^{-i\mathbf{k}_{li} \cdot \mathbf{r}_j + i\delta_{li} t}) + \frac{\eta}{2} (a + a^\dagger). \end{aligned} \quad (2.14)$$

This would put the equations of the dynamics on the superradiant lasing transition in the reference frame at the driving laser frequency  $\omega_d$  (if  $\eta=0$  this could again just be arbitrarily chosen and further simplify the equations). An alternative that can be easier to interpret and keep track of is to fix all the frequencies to the relevant, unperturbed atomic transition frequencies, such that all detunings simply refer to the unperturbed transitions:  $\omega_1 = \omega_2 = \omega_E, \omega_3 = \omega_I$ . This gives us:

$$\begin{aligned} H_I = & \hbar \delta_{cE} a^\dagger a + \sum_{j=1}^N \hbar \delta_{eE}^j \sigma_{ee}^j + \sum_{j=1}^N \hbar \delta_{il}^j \sigma_{ii}^j + \sum_{j=1}^N \hbar g_j (\sigma_{ge}^j a^\dagger + \sigma_{eg}^j a) \\ & + \sum_{j=1}^N \hbar \frac{\chi_{li}^j}{2} (\sigma_{gi}^j e^{i\mathbf{k}_{li} \cdot \mathbf{r}_j - i\delta_{li} t} + \sigma_{ig}^j e^{-i\mathbf{k}_{li} \cdot \mathbf{r}_j + i\delta_{li} t}) + \frac{\eta}{2} (ae^{i\delta_{Ed} t} + a^\dagger e^{-i\delta_{Ed} t}). \end{aligned} \quad (2.15)$$

We will use this Hamiltonian to generate a set of equations for the system dynamics. We are interested in the light emitted by the superradiant laser - its power and spectrum. This requires that we know the time-evolution of the cavity field. In the simplest cavity QED model, first order mean field theory, we can neglect quantum fluctuations and describe the cavity field by the expectation value of  $a$ : here  $\langle a^\dagger \rangle = \langle a \rangle^*$  and the photon number expectation value is  $\langle n \rangle = \langle a \rangle^* \langle a \rangle$ . The time-evolution of expectation values can generally be determined using:

$$\langle \dot{o} \rangle = \frac{i}{\hbar} \langle [H, o] \rangle - \sum_k \frac{\gamma_k}{2} \left\langle o q_k^\dagger q_k + q_k^\dagger q_k o - 2 q_k^\dagger o q_k \right\rangle. \quad (2.16)$$

Here the first term represents the coherent dynamics from the Hamiltonian, and the second term describes dissipative dynamics due to interactions with the environment. The sum gives one term with a characteristic decay time  $\gamma_k$  for each decay channel. We will describe the coherent and dissipative terms in the following sections. Note that an open-source programming package called QuantumCumulants has been developed for Julia, which can be used to derive these kinds of equations from a Hamiltonian automatically [107, 108].

### 2.1.3 Coherent time-evolution

With Eq. 2.16 the coherent evolution can be determined using the commutation relations mentioned earlier. For the cavity field lowering operator we get:

$$\begin{aligned} \langle \dot{a} \rangle_{coh} = & i \delta_{cE} \left\langle [a^\dagger a, a] \right\rangle + i \sum_{j=1}^N g_j \left\langle \sigma_{ge}^j [a^\dagger, a] \right\rangle + i \frac{\eta}{2} \left\langle [a^\dagger, a] \right\rangle e^{-i\delta_{Ed} t} \\ = & -i \delta_{cE} \langle a \rangle - i \sum_{j=1}^N g_j \langle \sigma_{ge}^j \rangle - i \frac{\eta}{2} e^{-i\delta_{Ed} t}. \end{aligned} \quad (2.17)$$

We see this equation is coupled to  $\langle \sigma_{ge}^j \rangle$  (the coherences of all the atoms), so we determine this next. Treating the atomic operators, we can think of them as two ket-bras and use

orthogonality for the inner product in the middle:  $\sigma_{ab}\sigma_{cd} = |a\rangle\langle b| |c\rangle\langle d| = \sigma_{ad}\delta_{bc}$ , where  $\delta_{bc}$  is the Kronecker delta:

$$\begin{aligned}\langle \dot{\sigma}_{ge}^j \rangle_{coh} &= i\delta_{eE}^j \langle [\sigma_{ee}^j, \sigma_{ge}^j] \rangle + ig_j \langle [\sigma_{eg}^j a, \sigma_{ge}^j] \rangle \\ &\quad + i\frac{\chi_{li}^j}{2} \left\langle \left[ \left( \sigma_{gi}^j e^{i\mathbf{k}_{li} \cdot \mathbf{r}_j - i\delta_{liI}t} + \sigma_{ig}^j e^{-i\mathbf{k}_{li} \cdot \mathbf{r}_j + i\delta_{liI}t} \right), \sigma_{ge}^j \right] \right\rangle \\ &= -i\delta_{eE}^j \langle \sigma_{ge}^j \rangle + ig_j \langle (\sigma_{ee}^j - \sigma_{gg}^j) a \rangle - i\frac{\chi_{li}^j}{2} \langle \sigma_{ie}^j \rangle e^{-i\mathbf{k}_{li} \cdot \mathbf{r}_j + i\delta_{liI}t}.\end{aligned}\quad (2.18)$$

We find that the time evolution of the atomic coherence on the lasing transition depends on  $\langle (\sigma_{ee}^j - \sigma_{gg}^j) a \rangle$  and  $\langle \sigma_{ie}^j \rangle$ . The first of these is a second order correlation, which you could in principle also derive an equation of motion for. This procedure would often lead to third order correlations with three operators, and could quickly get out of hand. One approach to deal with third order correlations is to reduce them to lower orders with the approximation [107, p. 4] [109]:

$$\langle abc \rangle \approx \langle ab \rangle \langle c \rangle + \langle ac \rangle \langle b \rangle + \langle a \rangle \langle bc \rangle - 2 \langle a \rangle \langle b \rangle \langle c \rangle. \quad (2.19)$$

This assumes that at least one of the operators  $a$ ,  $b$  and  $c$  is statistically independent of the others. Numerical models have been used extensively for studying superradiant lasers using this approach [64, 79, 110] to obtain a closed set of equations in second order mean field theory (MFT), meaning expectation values with products of no more than two operators. However we proceed in first order MFT by making the approximation  $\langle ab \rangle \approx \langle a \rangle \langle b \rangle$ . As a result, quantum noise is neglected, unlike in second order MFT. However the number of equations in first order scales linearly with the number of atoms, rather than the square. As a result the model can be used to treat more atoms individually and include many other effects affecting each atom differently, which would be too computationally heavy to include in second order MFT, which often requires treating a small number of atom clusters where each atom in a cluster is assumed to be in identical states. With this factorization of expectation values we obtain:

$$\langle \dot{\sigma}_{ge}^j \rangle_{coh} = -i\delta_{eE}^j \langle \sigma_{ge}^j \rangle + ig_j \langle (\sigma_{ee}^j - \langle \sigma_{gg}^j \rangle) \langle a \rangle - i\frac{\chi_{li}^j}{2} \langle \sigma_{ie}^j \rangle e^{-i\mathbf{k}_{li} \cdot \mathbf{r}_j + i\delta_{liI}t}, \quad (2.20)$$

and we are left with the task of finding equations for  $\sigma_{ee}^j$ ,  $\sigma_{gg}^j$  and  $\sigma_{ie}^j$ :

$$\begin{aligned}\langle \dot{\sigma}_{ee}^j \rangle_{coh} &= ig_j \left\langle \left[ \sigma_{ge}^j a^\dagger + \sigma_{eg}^j a, \sigma_{ee}^j \right] \right\rangle = ig_j \left( \langle \sigma_{ge}^j \rangle \langle a^\dagger \rangle - \langle \sigma_{eg}^j \rangle \langle a \rangle \right) \\ &= 2ig_j [\text{Im} \langle \sigma_{ge}^j \rangle \text{Re} \langle a \rangle - \text{Re} \langle \sigma_{ge}^j \rangle \text{Im} \langle a \rangle] \\ \langle \dot{\sigma}_{gg}^j \rangle_{coh} &= -2ig_j [\text{Im} \langle \sigma_{ge}^j \rangle \text{Re} \langle a \rangle - \text{Re} \langle \sigma_{ge}^j \rangle \text{Im} \langle a \rangle] \\ &\quad + i\frac{\chi_{li}^j}{2} \left\langle \left[ \sigma_{gi}^j e^{i\mathbf{k}_{li} \cdot \mathbf{r}_j - i\delta_{liI}t} + \sigma_{ig}^j e^{-i\mathbf{k}_{li} \cdot \mathbf{r}_j + i\delta_{liI}t}, \sigma_{gg}^j \right] \right\rangle \\ &= -2ig_j [\text{Im} \langle \sigma_{ge}^j \rangle \text{Re} \langle a \rangle - \text{Re} \langle \sigma_{ge}^j \rangle \text{Im} \langle a \rangle] \\ &\quad - i\frac{\chi_{li}^j}{2} \left( \langle \sigma_{ig}^j \rangle^* e^{i\mathbf{k}_{li} \cdot \mathbf{r}_j - i\delta_{liI}t} - \langle \sigma_{ig}^j \rangle e^{-i\mathbf{k}_{li} \cdot \mathbf{r}_j + i\delta_{liI}t} \right) \\ \langle \dot{\sigma}_{ie}^j \rangle_{coh} &= i\delta_{eE}^j \left\langle \left[ \sigma_{ee}^j, \sigma_{ie}^j \right] \right\rangle + i\delta_{iI}^j \left\langle \left[ \sigma_{ii}^j, \sigma_{ie}^j \right] \right\rangle \\ &\quad + ig_j \left\langle \left[ \sigma_{ge}^j a^\dagger + \sigma_{eg}^j a, \sigma_{ie}^j \right] \right\rangle + i\frac{\chi_{li}^j}{2} \left\langle \left[ \sigma_{gi}^j e^{i\mathbf{k}_{li} \cdot \mathbf{r}_j - i\delta_{liI}t} + \sigma_{ig}^j e^{-i\mathbf{k}_{li} \cdot \mathbf{r}_j + i\delta_{liI}t}, \sigma_{ie}^j \right] \right\rangle \\ &= i(\delta_{iI}^j - \delta_{eE}^j) \langle \sigma_{ie}^j \rangle - ig_j \langle \sigma_{ig}^j \rangle \langle a \rangle + i\frac{\chi_{li}^j}{2} \langle \sigma_{ge}^j \rangle e^{i\mathbf{k}_{li} \cdot \mathbf{r}_j - i\delta_{liI}t}.\end{aligned}\quad (2.21)$$

Here we find that we also need to determine the equation for  $\langle \sigma_{ig}^j \rangle$ , which in turn depends on  $\langle \sigma_{ii}^j \rangle$ :

$$\begin{aligned}\langle \dot{\sigma}_{ig}^j \rangle_{coh} &= i\delta_{II}^j \langle [\sigma_{ii}^j, \sigma_{ig}^j] \rangle + ig_j \langle [\sigma_{ge}^j a^\dagger + \sigma_{eg}^j a, \sigma_{ig}^j] \rangle + i \frac{\chi_{li}^j}{2} \langle [\sigma_{gi}^j, \sigma_{ig}^j] \rangle e^{i\mathbf{k}_{li}\mathbf{r}_j - i\delta_{li}I t} \\ &= i\delta_{II}^j \langle \sigma_{ig}^j \rangle_{coh} - ig_j \langle \sigma_{ie}^j \rangle \langle a \rangle^* - i \frac{\chi_{li}^j}{2} (\langle \sigma_{ii}^j \rangle - \langle \sigma_{gg}^j \rangle) e^{i\mathbf{k}_{li}\mathbf{r}_j - i\delta_{li}I t} \\ \langle \dot{\sigma}_{ii}^j \rangle_{coh} &= i \frac{\chi_{li}^j}{2} \langle [\sigma_{gi}^j e^{i\mathbf{k}_{li}\mathbf{r}_j - i\delta_{li}I t} + \sigma_{ig}^j e^{-i\mathbf{k}_{li}\mathbf{r}_j + i\delta_{li}I t}, \sigma_{ii}^j] \rangle \\ &= i \frac{\chi_{li}^j}{2} (\langle \sigma_{ig}^j \rangle^* e^{i\mathbf{k}_{li}\mathbf{r}_j - i\delta_{li}I t} - \langle \sigma_{ig}^j \rangle e^{-i\mathbf{k}_{li}\mathbf{r}_j + i\delta_{li}I t}).\end{aligned}\tag{2.22}$$

Now the coherent set of equations is closed and can be solved by numerically integrating them over time. One of the populations could also be eliminated by using  $\langle \sigma_{gg}^j \rangle + \langle \sigma_{ee}^j \rangle + \langle \sigma_{ii}^j \rangle = 1$ .

### 2.1.4 Dissipation

To describe dissipation we need to evaluate the last term in Eq. 2.16 for relevant operators  $o$  and using the relevant dissipation rates in place of  $\gamma_k$  for each dissipation source. We have an equation for the coherent evolution of  $\langle a \rangle$ , representing the cavity field, so we can determine the dissipation term for  $o = a$  due to the coupling of the cavity mode to the environment with the rate  $\kappa$ . In this case the relevant raising and lowering operators to use are  $q^\dagger = a^\dagger$  and  $q = a$ :

$$\langle \dot{a} \rangle_{dis} = -\frac{\kappa}{2} \langle aa^\dagger a + a^\dagger aa - 2a^\dagger aa \rangle = -\frac{\kappa}{2} \langle [a, a^\dagger] a \rangle = -\frac{\kappa}{2} \langle a \rangle.\tag{2.23}$$

Next we can consider spontaneous emission into the environment, where state  $|e\rangle$  decays to  $|g\rangle$  with the decay rate  $\gamma_{eg}$ . The relevant raising and lowering operators here are  $q^\dagger = \sigma_{eg}^j$  and  $q = \sigma_{ge}^j$ . We will determine the effect on both the excited state population,  $\langle \sigma_{ee}^j \rangle$ , and the coherence,  $\langle \sigma_{ge}^j \rangle$ :

$$\begin{aligned}\langle \dot{\sigma}_{ee}^j \rangle_{dis} &= -\frac{\gamma_{eg}}{2} \langle \sigma_{ee}^j \sigma_{eg}^j \sigma_{ge}^j + \sigma_{eg}^j \sigma_{ge}^j \sigma_{ee}^j - 2\sigma_{eg}^j \sigma_{ee}^j \sigma_{ge}^j \rangle = -\gamma_{eg} \langle \sigma_{ee}^j \rangle \\ \langle \dot{\sigma}_{ge}^j \rangle_{dis} &= -\frac{\gamma_{eg}}{2} \langle \sigma_{ge}^j \rangle.\end{aligned}\tag{2.24}$$

The same procedure could be used to include spontaneous decays from  $|i\rangle$  to  $|g\rangle$  and  $|e\rangle$ , which would lead to similar equations for  $\langle \dot{\sigma}_{ii}^j \rangle$  and  $\langle \dot{\sigma}_{gi}^j \rangle$ . Lindblad terms can also be used to describe incoherent pumping as inverse spontaneous emission. In that case one just needs to switch the atomic operators for  $q$  and  $q^\dagger$ , and replace  $\gamma$  with the relevant pumping rate.

We can also consider how the coherence  $\sigma_{ie}$  is affected by the three decay channels:

$$\begin{aligned}\langle \dot{\sigma}_{ie}^j \rangle_{dis} &= -\frac{\gamma_{ie}}{2} \langle \sigma_{ie}^j \sigma_{ie}^j \sigma_{ei}^j + \sigma_{ie}^j \sigma_{ei}^j \sigma_{ie}^j - 2\sigma_{ie}^j \sigma_{ie}^j \sigma_{ei}^j \rangle \\ &\quad - \frac{\gamma_{ig}}{2} \langle \sigma_{ie}^j \sigma_{ig}^j \sigma_{gi}^j + \sigma_{ig}^j \sigma_{gi}^j \sigma_{ie}^j - 2\sigma_{ig}^j \sigma_{ie}^j \sigma_{gi}^j \rangle \\ &\quad - \frac{\gamma_{eg}}{2} \langle \sigma_{ie}^j \sigma_{eg}^j \sigma_{ge}^j + \sigma_{eg}^j \sigma_{ge}^j \sigma_{ie}^j - 2\sigma_{eg}^j \sigma_{ie}^j \sigma_{ge}^j \rangle = \frac{\gamma_{ie} + \gamma_{ig} + \gamma_{eg}}{2} \langle \sigma_{ie}^j \rangle.\end{aligned}\tag{2.25}$$

Here we see that the coherence is damped by all dissipation sources from either of the levels. Finally we could repeat the previous calculations for the ground state, or simply use conservation of population, which leads to

$$\langle \dot{\sigma}_{gg}^j \rangle_{dis} = \gamma_{eg} \langle \sigma_{ee}^j \rangle + \gamma_{ig} \langle \sigma_{ii}^j \rangle.\tag{2.26}$$

Compiling the completed set of equations derived from Eq. 2.15 using Eq. 2.16 while dropping the expectation value brackets, we get:

$$\begin{aligned}
 \dot{a} &= -i\delta_{cE}a - i \sum_{j=1}^N g_j \sigma_{ge}^j - i\frac{\eta}{2}e^{-i\delta_E t} - \frac{\kappa}{2}a \\
 \dot{\sigma}_{ii}^j &= i\frac{\chi_{li}^j}{2} \left( \sigma_{ig}^{j*} e^{i\mathbf{k}_{li}\mathbf{r}_j - i\delta_{li}t} - \sigma_{ig}^j e^{-i\mathbf{k}_{li}\mathbf{r}_j + i\delta_{li}t} \right) - \gamma_{ig} \sigma_{ii}^j \\
 \dot{\sigma}_{ee}^j &= 2ig_j [\text{Im}(\sigma_{ge}^j) \text{Re}(a) - \text{Re}(\sigma_{ge}^j) \text{Im}(a)] - \gamma_{eg} \sigma_{ee}^j + \gamma_{ie} \sigma_{ii}^j \\
 \dot{\sigma}_{gg}^j &= -\dot{\sigma}_{ii}^j - \dot{\sigma}_{ee}^j \\
 \dot{\sigma}_{ig}^j &= i\delta_{iI}^j \sigma_{ig}^j - ig_j \sigma_{ie}^j a^* - i\frac{\chi_{li}^j}{2} (\sigma_{ii}^j - \sigma_{gg}^j) e^{i\mathbf{k}_{li}\mathbf{r}_j - i\delta_{li}t} - \frac{\gamma_{ig} + \gamma_{ie}}{2} \sigma_{ig}^j \\
 \dot{\sigma}_{ge}^j &= -i\delta_{eE}^j \sigma_{ge}^j + ig_j (\sigma_{ee}^j - \sigma_{gg}^j) a - i\frac{\chi_{li}^j}{2} \sigma_{ie}^j e^{-i\mathbf{k}_{li}\mathbf{r}_j + i\delta_{li}t} - \frac{\gamma_{eg}}{2} \sigma_{eg}^j \\
 \dot{\sigma}_{ie}^j &= i (\delta_{iI}^j - \delta_{eE}^j) \sigma_{ie}^j - ig_j \sigma_{ig}^j a + i\frac{\chi_{li}^j}{2} \sigma_{ge}^j e^{i\mathbf{k}_{li}\mathbf{r}_j - i\delta_{li}t} - \frac{\gamma_{ig} + \gamma_{ie} + \gamma_{eg}}{2} \sigma_{ie}^j.
 \end{aligned} \tag{2.27}$$

## 2.2 The stochastic master equation

So far we have described how to determine the evolution of expectation values of operators. These expectation values represent the mean evolution, e.g.  $\langle \sigma_{ee}^j \rangle$  the mean evolution of the excited state of an atom, and  $\langle a^\dagger a \rangle$  the mean evolution of the cavity photon population. But in many cases there are fluctuations which can be important to consider. For example the linewidth of a laser depends on quantum fluctuations which vanish when considering the expectation values in first order MFT. Another example is the spontaneous decay of atoms. In the treatment in Sec. 2.1 the spontaneous decay occurs gradually over time, but if an atom moves in an optical potential that depends on the atomic state, discrete changes in the atom's state due to decays could have a large impact on its motion. Here we will present the stochastic master equation (SME) and density matrix framework, which is useful for describing stochastic dynamics. First we will link the density matrix to the previous approach of deriving expectation values. If we consider the Hamiltonian 2.15 and again assume we can treat the atomic states separately from the cavity field and each other, we can describe each atom fully by its internal state. We can choose a basis with bras:  $\langle e | = \begin{pmatrix} 0 & 0 & 1 \end{pmatrix}$ ,  $\langle g | = \begin{pmatrix} 0 & 1 & 0 \end{pmatrix}$ ,  $\langle i | = \begin{pmatrix} 1 & 0 & 0 \end{pmatrix}$ . In this basis we can write the density matrix of an atom's state as:

$$\rho_j = |\psi_j\rangle\langle\psi_j| = \begin{pmatrix} \rho_{ii}^j & \rho_{ig}^j & \rho_{ie}^j \\ \rho_{gi}^j & \rho_{gg}^j & \rho_{ge}^j \\ \rho_{ei}^j & \rho_{eg}^j & \rho_{ee}^j \end{pmatrix}, \tag{2.28}$$

the transition operators  $\sigma_{xy} = |x\rangle\langle y|$  then become matrices, such as:

$$\sigma_{ge}^j = |g\rangle\langle e| = \begin{pmatrix} 0 & 1 & 0 \end{pmatrix} \begin{pmatrix} 0 \\ 0 \\ 1 \end{pmatrix} = \begin{pmatrix} 0 & 0 & 0 \\ 0 & 0 & 1 \\ 0 & 0 & 0 \end{pmatrix}, \tag{2.29}$$

and the Hamiltonian 2.15 can be written as:

$$\begin{aligned}
 H_I = & \hbar \delta_{cE} a^\dagger a + \sum_{j=1}^N \hbar \delta_{eE}^j \begin{pmatrix} 0 & 0 & 0 \\ 0 & 1 & 0 \\ 0 & 0 & 0 \end{pmatrix}_j + \sum_{j=1}^N \hbar \delta_{lI}^j \begin{pmatrix} 1 & 0 & 0 \\ 0 & 0 & 0 \\ 0 & 0 & 0 \end{pmatrix}_j + \frac{\eta}{2} (ae^{i\delta_{Ed}t} + a^\dagger e^{-i\delta_{Ed}t}) \\
 & + \sum_{j=1}^N \hbar g_j \left[ \begin{pmatrix} 0 & 0 & 0 \\ 0 & 0 & 1 \\ 0 & 0 & 0 \end{pmatrix}_j a^\dagger + \begin{pmatrix} 0 & 0 & 0 \\ 0 & 0 & 0 \\ 0 & 1 & 0 \end{pmatrix}_j a \right] \\
 & + \sum_{j=1}^N \hbar \frac{\lambda_{li}^j}{2} \left[ \begin{pmatrix} 0 & 0 & 0 \\ 1 & 0 & 0 \\ 0 & 0 & 0 \end{pmatrix}_j e^{i\mathbf{k}_{li} \cdot \mathbf{r}_j - i\delta_{li} t} + \begin{pmatrix} 0 & 1 & 0 \\ 0 & 0 & 0 \\ 0 & 0 & 0 \end{pmatrix}_j e^{-i\mathbf{k}_{li} \cdot \mathbf{r}_j + i\delta_{li} t} \right]. \tag{2.30}
 \end{aligned}$$

The equations 2.27 can be derived again using Eq. 2.16 and the relation  $\langle o \rangle = \text{tr}(\rho o)$ . With this relation we see e.g. the populations are simply related by  $\langle \sigma_{ii}^j \rangle = \rho_{ii}^j$ ,  $\langle \sigma_{gg}^j \rangle = \rho_{gg}^j$  and  $\langle \sigma_{ee}^j \rangle = \rho_{ee}^j$ , and for the coherences the indices are flipped in the relations, e.g.  $\langle \sigma_{ge}^j \rangle = \rho_{eg}^j$ . Also note that above we assume the cavity field is still represented by the expectation value  $\langle a \rangle$ . Since the cavity can be populated by any number of photons, and these populations are linked to emission/absorption by the atoms, which ultimately become correlated, using a density matrix description of the cavity states becomes significantly more complicated. This may be described in a similar way to the dressed states of the Jaynes-Cummings model, and the correlations between atoms have been described by Dicke states [36, 111], which have also been used to illustrate the behavior of atoms in a superradiant laser in 2nd order MFT [64].

With the density matrix formalism we can now use the SME for the atomic states. Physically it is equivalent to continually measuring the atomic state by measuring the spontaneously emitted photons - once the photons are detected, the atomic state collapses. In practice you do not have to measure all the spontaneously emitted photons from the atoms, they could also simply be absorbed by some component in the vacuum chamber around a superradiant laser, breaking any entanglement and projecting the atomic state - then the evolution of the SME represents that we know of these events. The important part is the effect of these projections due to spontaneous emission and coupling to an environment. The SME can be written [104, p. 818]:

$$d\rho = -\frac{i}{\hbar} [H, \rho] dt - \sum_k \frac{\gamma_k}{2} \left( q_k^\dagger q_k \rho + \rho q_k^\dagger q_k - 2 \langle q_k^\dagger q_k \rangle \rho \right) dt + \left( \frac{q_k \rho q_k^\dagger}{\langle q_k^\dagger q_k \rangle} - \rho \right) dN_k. \tag{2.31}$$

Here the  $dt$  factor is not on the left side as usual, but is moved to the right because some of the right side terms do not scale with  $dt$  - instead they represent discrete quantum jumps that occur when  $dN_k = 1$  (for decay channel  $k$ ). Compared to the regular master equation, the first term is the same - the unitary evolution due to the Hamiltonian. The second term looks similar to the Lindblad superoperator, but it is a bit different - if you detect all the spontaneously emitted photons, you also gain information when no photons are detected. As a result the state evolves differently when no photons are detected, compared to the Lindbladian evolution. The final terms representing quantum jumps result in abrupt changes of the state - the left term in the parenthesis yields the final state, and we see the right term that contains  $\rho$  cancels out the initial value of  $\rho$  when  $dN = 1$ . It is the mathematical way of writing "if a decay happens from  $|x\rangle \rightarrow |y\rangle$  (so  $dN_{xy} = 1$ ), make population  $\rho_{yy}^j = 1$  and all other populations and coherences 0".  $dN_k$  must be chosen randomly (being either 0 or 1) each timestep based on the probability of the quantum jump occurring within the time interval  $dt$ . For one atom spontaneously decaying e.g. from state  $|e\rangle$  to  $|g\rangle$  this probability of  $dN_{eg}^j = 1$  is  $\rho_{ee}^j \gamma_{eg} dt$ .

The Hamiltonian part in Eq. 2.30 leads to the same coherent evolution as the atomic equations in Sec. 2.1.3 when looking at the resulting elements of  $d\rho$  according to Eq. 2.31. For the second and third terms of Eq. 2.31 we get the additional terms:

$$d\rho_{ii,SME}^j = \left[ -(\gamma_{ig} + \gamma_{ie}) (1 - \rho_{ii}^j) + \gamma_{eg}\rho_{ee}^j \right] \rho_{ii}^j dt - \rho_{ii}^j (dN_{ig}^j + dN_{ie}^j + dN_{eg}^j) \quad (2.32)$$

$$d\rho_{ee,SME}^j = \left[ (\gamma_{ig} + \gamma_{ie}) \rho_{ii}^j - \gamma_{eg} (1 - \rho_{ee}^j) \right] \rho_{ee}^j dt - \rho_{ee}^j (dN_{ig}^j + dN_{eg}^j) + (1 - \rho_{ee}^j) dN_{ie}^j \quad (2.33)$$

$$d\rho_{gg,SME}^j = \left[ (\gamma_{ig} + \gamma_{ie}) \rho_{ii}^j + \gamma_{eg}\rho_{ee}^j \right] \rho_{gg}^j dt + (1 - \rho_{gg}^j) (dN_{ig}^j + dN_{eg}^j) - \rho_{gg}^j dN_{ie}^j \quad (2.34)$$

$$d\rho_{ig,SME}^j = \left[ -\frac{\gamma_{ig} + \gamma_{ie}}{2} (1 - 2\rho_{ii}^j) + \gamma_{eg}\rho_{ee}^j \right] \rho_{ig}^j dt - \rho_{ig}^j (dN_{ig}^j + dN_{ie}^j + dN_{eg}^j) \quad (2.35)$$

$$d\rho_{ge,SME}^j = \left[ (\gamma_{ig} + \gamma_{ie}) \rho_{ii}^j - \frac{\gamma_{eg}}{2} (1 - 2\rho_{ee}^j) \right] \rho_{ge}^j dt - \rho_{ge}^j (dN_{ig}^j + dN_{ie}^j + dN_{eg}^j) \quad (2.36)$$

$$d\rho_{ie,SME}^j = \left[ -\frac{\gamma_{ig} + \gamma_{ie}}{2} (1 - 2\rho_{ii}^j) - \frac{\gamma_{eg}}{2} (1 - 2\rho_{ee}^j) \right] \rho_{ie}^j dt - \rho_{ie}^j (dN_{ig}^j + dN_{ie}^j + dN_{eg}^j). \quad (2.37)$$

In the square brackets we see the general forms that arise due to the second term in Eq. 2.31, depending on how the states and coherences are involved in the three decay routes from  $|i\rangle \rightarrow |e\rangle$ ,  $|i\rangle \rightarrow |g\rangle$  or  $|e\rangle \rightarrow |g\rangle$ . The rightmost term in Eq. 2.31 also gives rise to three terms for each density matrix element in Eq. 2.32.

In Fig. 2.3 the effect of the SME quantum jumps is illustrated in a slightly different three-level system. Here an intermediate state  $|i\rangle$  (orange) couples to the ground state  $|g\rangle$  (black) and higher excited state  $|x\rangle$  (green). The system starts in the ground state, but then begins Rabi flopping between the different states due to two semiclassical pumping lasers on resonance with the transitions, with Rabi frequencies  $\chi_{gi} = 5\gamma_{ig}$  and  $\chi_{ix} = 10\gamma_{xi} = 5\gamma_{ig}$ . The SME dynamics are highlighted and compared to the brightly-colored dynamics of optical Bloch equations. In panel (a) the dynamics for one atom is shown with two spontaneous decay events interrupting the Rabi flops. The usual decaying Rabi flops are distorted in shape due to the Lindblad-like term in the SME. In panel (b) we see the average of 1000 atom's states follow the OBE very closely with only small fluctuations due to the random, individual quantum jumps.

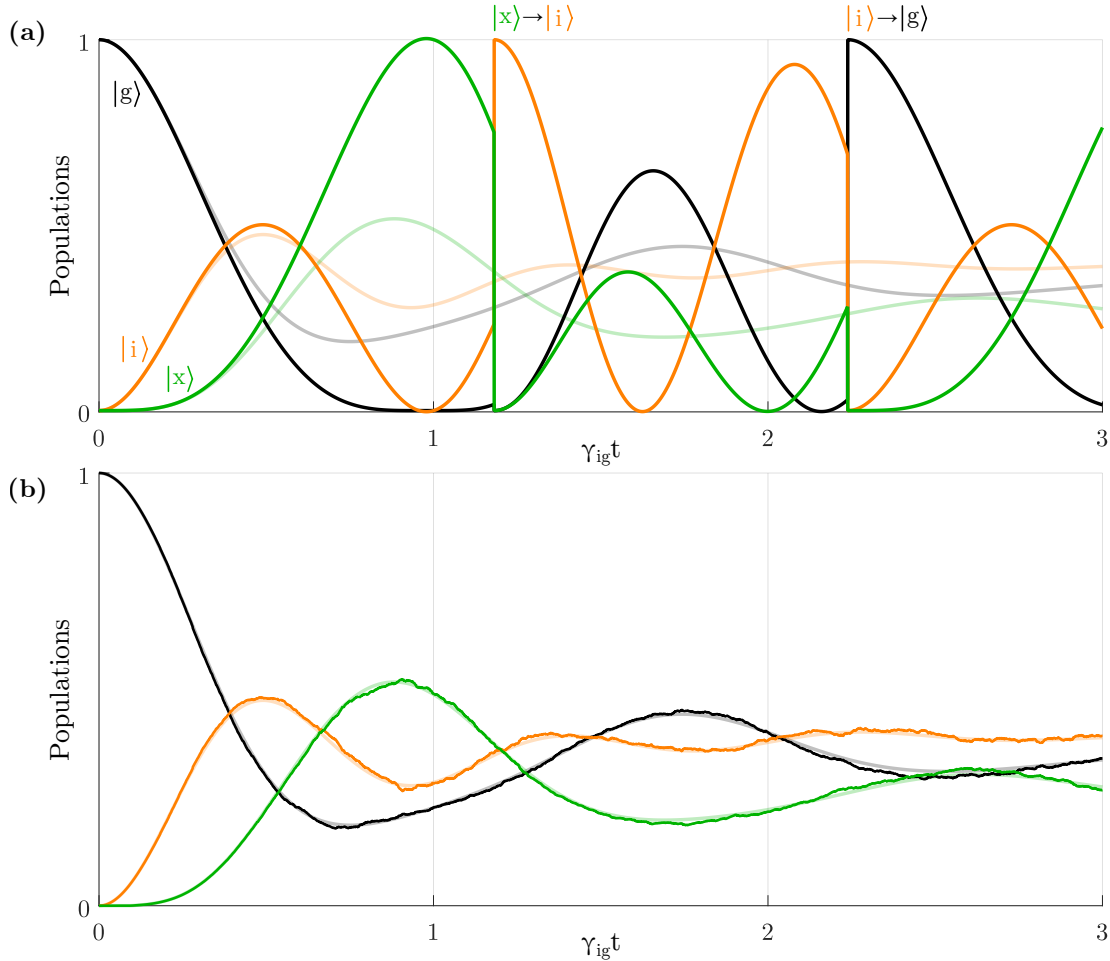


Figure 2.3: *Dynamics of a 3 level ladder system evolving under the optical Bloch equations/first order MFT (bright curves) vs the SME (dark curves), for (a) one atom and (b) averaging over 1000 atoms. In (a) we see how the individual atom's dynamics are changed by the SME and the effect of quantum jumps, and in (b) how these jumps, for many atoms, average out to the OBE dynamics.*

## 2.3 Coherent pumping vs rate equations

Modeling coherent interactions with even semiclassical laser beams can be computationally demanding, typically if the Rabi frequency is very high, such that a low timestep is required for numerical stability. These high Rabi frequencies can be encountered for pumping lasers driving broad transitions with MHz linewidths. An example could be a superradiant laser operating on the  $^1S_0$ - $^3P_1$   $m_J=0$  transition, where atoms are repumped incoherently from  $^1S_0$  to first  $^3P_1$   $m_J=-1$  and subsequently  $^3S_1$  (with laser wavelengths 689 and 688 nm). From  $^3S_1$  the atoms may decay to  $^3P_1$   $m_0=1$  as desired, but could also decay to several other Zeeman sublevels of  $^3P_2$  and  $^3P_0$ , which require additional lasers (with wavelengths 707 and 679 nm) to bring the atoms back to  $^3S_1$  so that they can end up in  $^3P_1$   $m_J=0$ . These 679 and 707 nm lasers operate on MHz wide transitions and their impact on the lasing transition coherence would be negligible due to the rapid decay rate of  $^3S_1$ , which links them to the lasing transition via the 688 and 689 nm lasers. In this case the details of atomic coherence are not relevant to keep track of for these levels, and it is an advantage to approximate the pumping between such levels using rate equations. In some cases when the details of pumping are not of interest, several pumping levels can even be bunched together or even eliminated to yield a two level model characterized by an effective incoherent pumping rate [68].

Here we will consider a simple two-level system with states  $|g\rangle$  and  $|e\rangle$ , and connect the rate equation approach to the coherent dynamics described by the optical Bloch equations (OBE), which can be written [104, p. 178]:

$$\begin{aligned}\dot{\rho}_{ee} &= \chi \operatorname{Im}(\rho_{ge}) - \gamma \rho_{ee} \\ \dot{\rho}_{gg} &= -\chi \operatorname{Im}(\rho_{ge}) + \gamma \rho_{ee} \\ \dot{\rho}_{ge} &= -(\gamma_T + i\delta) \rho_{ge} - i\frac{\chi}{2} (\rho_{ee} - \rho_{gg}).\end{aligned}\quad (2.38)$$

Here  $\chi$  is the Rabi-frequency,  $\delta$  is the laser detuning,  $\gamma$  is the decay rate from  $|e\rangle$  to  $|g\rangle$  and  $\gamma_T$  is the transverse decay rate.  $\gamma_T = \gamma/2$  when spontaneous emission is the only source of decoherence, but it can be larger, for example due to decoherence introduced by pumping lasers to other states. If  $\gamma_T \gg \gamma$  then  $\rho_{ge}$  decays much more quickly than the populations and can be adiabatically eliminated, giving [104, p. 191]:

$$\dot{\rho}_{ee} = -\frac{\chi^2}{2\gamma_T(1 + \delta^2/\gamma_T^2)} (\rho_{ee} - \rho_{gg}) - \gamma \rho_{ee}. \quad (2.39)$$

This is equivalent to the population rate equations from laser physics (e.g. [112, p. 150]), which are generally written in terms of a single parameter, the pumping rate  $w$ :

$$\dot{\rho}_{ee} = -w(\rho_{ee} - \rho_{gg}) - \gamma \rho_{ee}. \quad (2.40)$$

Comparing these, the pumping rate  $w$  can be connected to the Rabi frequency, transverse decay rate and laser detuning, and in turn to laser intensities in a setup. The magnitude of the Rabi frequency, in case of a linearly polarized field aligned with the atomic dipole along the z-axis, is given by [104, p. 154]:

$$\chi = \sqrt{\frac{2I}{\hbar^2 \epsilon_0 c}} \langle g | d_z | e \rangle. \quad (2.41)$$

In this situation the matrix element is related to the decay rate from  $|e\rangle$  to  $|g\rangle$  by  $\gamma = \omega^3 |\langle g | d_z | e \rangle|^2 / 3\pi\epsilon_0\hbar c^3$  [104, p. 154], giving:

$$\chi = \sqrt{\frac{6\pi c^2 \gamma I}{\hbar \omega^3}}. \quad (2.42)$$

This depends on  $\gamma$  (which can be looked up for a transition) and the laser intensity  $I$  at the atom. For a laser power  $P$  and Gaussian beam shape with waists  $W_x$  and  $W_y$  illuminating an atom, the Rabi frequency at the center of the beam profile is then:

$$\chi_0 = \sqrt{\frac{6c^2 \gamma P}{\hbar \omega^3 W_x W_y}}. \quad (2.43)$$

In Fig. 2.4 the dynamics according to the OBE (Eq. 2.38) and rate equations (Eq. 2.39 and  $\rho_{gg} = 1 - \rho_{ee}$ ) are shown for different combinations of  $\chi$ ,  $\delta$  and  $\gamma_T$ . The rate equations clearly deviate during coherent oscillations, but generally agree well in steady state as well as dynamically for  $\gamma_T \gg \gamma$ .

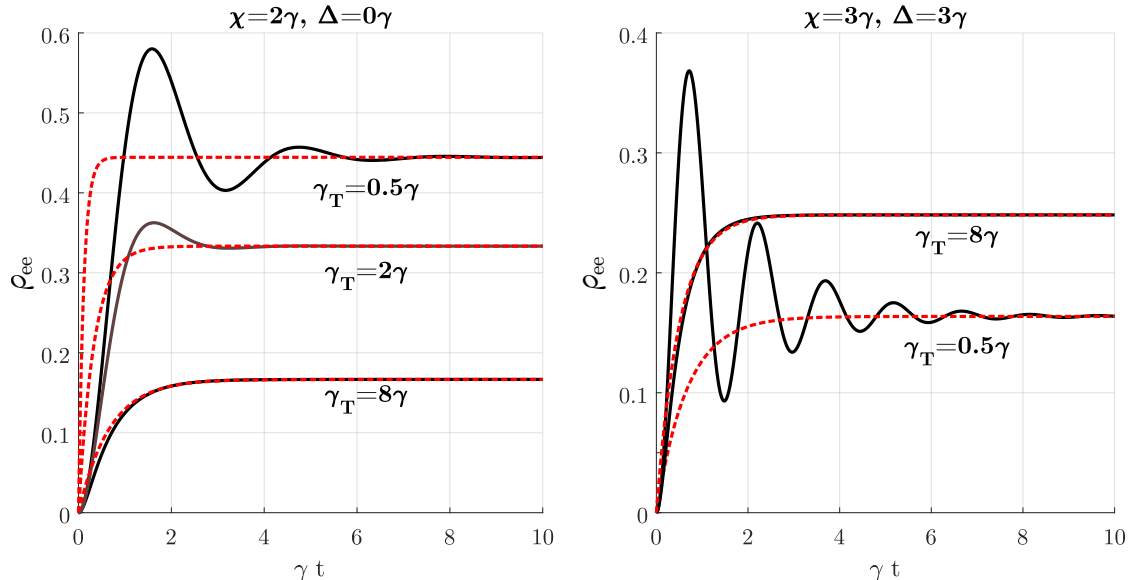


Figure 2.4: Dynamics of the excited population in a two level system according to optical Bloch equations (black curves) and rate equations (red dashed curves) for different combinations of parameters. The rate equations do not capture the coherent oscillations and only agree well for  $\gamma_T \gg \gamma$ , but in steady state the populations generally agree.

## 2.4 Transitions between Zeeman sublevels

A two-level model as in Sec. 2.3 can quickly become inadequate for a superradiant laser that relies on pumping between many different levels. The method in Sec. 2.1 can be used to derive equations for transitions between any number of Zeeman sublevels, so in this section we will only focus on how the coupling to electromagnetic fields are generally affected (impacting Rabi frequencies, cavity coupling, pumping and decay rates).

When an atom is in a state with total angular momentum  $J > 0$ , a magnetic field  $\mathbf{B}$  splits up the energies of the Zeeman sublevels depending on their angular momentum's projection along the  $\mathbf{B}$ -vector, giving the quantum number  $m_J \in \{-J, -J+1, \dots, +J\}$ . Photons are spin 1 particles, so their projected angular momentum along the axis may be  $p \in \{-1, 0, 1\}$ . These three values correspond to driving  $\sigma^-$ ,  $\pi$  or  $\sigma^+$  transitions of the atom, respectively, and depends on the photon polarization. For example a linear polarization parallel to  $\mathbf{B}$  would give  $p = 0$ , but a linear polarization orthogonal to  $B$  can be decomposed into two half-intensity interactions with  $p = -1$  and  $p = +1$ , equivalent to two components with circular polarizations of opposite helicities. The interaction between the atom and photon angular momenta can be treated using the formalism for coupling angular momenta in quantum mechanics, where we can write the lower atom state as  $|J_g, m_g\rangle$ , upper state  $|J_e, m_e\rangle$ , and photon as  $|1, p\rangle$ . These kets enter into the dipole matrix element in electromagnetic interactions as in Eq. 2.41 for the Rabi frequency, and similarly impact the atom-cavity coupling  $g$  and pumping rates  $w$ . The matrix element can be rewritten using the Wigner-Eckart theorem and solved as a separate problem. This yields a Clebsch-Gordan coefficient (see e.g. the online tool [113]), or equivalently, a 3j symbol (see e.g. [114, p. 9] [115] [104, p. 305]):

$$\begin{aligned} \chi &= \chi_0 \langle J_g, m_g | J_e, 1, m_e, p \rangle \\ &= \chi_0 (-1)^{J_g-1+m_e} \sqrt{2J_e+1} \begin{pmatrix} J_g & 1 & J_e \\ m_g & p & -m_e \end{pmatrix}. \end{aligned} \quad (2.44)$$

For the strontium transitions of interest, the Clebsch-Gordan coefficients  $c_g$  are shown in Fig. 2.5. Atom decays are affected via coupling to the vacuum field, so the branching ratios of decays are also given by  $c_g^2$ . For e.g.  ${}^3S_1$  we can look up the decay rate  $\gamma/2\pi = 7.2$  MHz

to the  ${}^3P_2$  manifold (as indicated in Fig. 1.1) and see in Fig. 2.5 that for the  ${}^3S_1$   $m_J = -1$  sublevel, the decay rates to  $m_J = -2, -1$  and 0 of  ${}^3P_2$  are  $6\gamma/10$ ,  $3\gamma/10$  and  $\gamma/10$ , respectively.

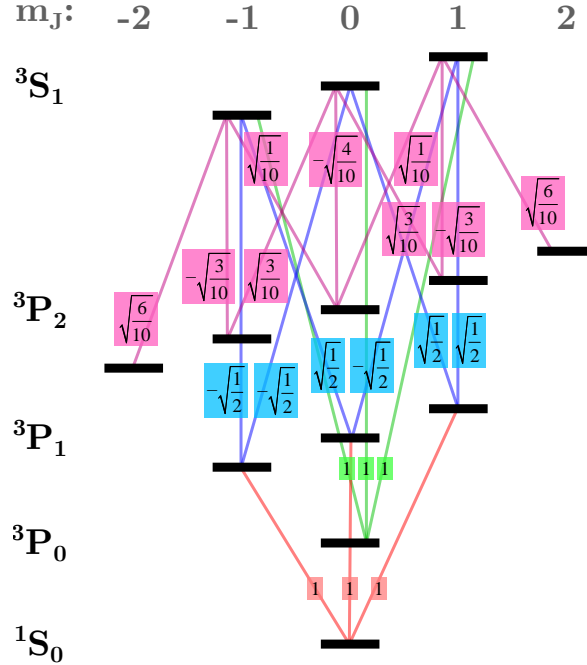


Figure 2.5: Clebsch-Gordan coefficients,  $\langle J_g, m_g | J_e, 1, m_e, p \rangle$ , of transitions between Zeeman levels.  $|J_g, m_g\rangle$  refers to the lower level.

If the laser  $\mathbf{k}$ -vector is not orthogonal to the  $\mathbf{B}$ -field, for example near the center of the anti-Helmholtz field used in a magneto-optical trap, the strengths of  $\sigma$  and  $\pi$  transitions will also change. This can generally be determined in a spherical basis as done in [116]. A more specific example for the effect on a linearly polarized pump laser is given in [103, p. 27] and in Sec. 3.2.1 the effect on beam interactions in a magneto-optical trap is considered.

## 2.5 Heating

Heating of atoms in a superradiant laser can arise from interactions with the cavity field, pumping lasers and spontaneous emission. This can happen due to photon recoils, but in the presence of an optical potential (for example a dipole guide/optical lattice used to confine atoms), changes in state can also change the potential energy and cause additional heating.

The motion of atoms due to the interaction with e.g. the cavity field can be treated quantum mechanically by including a kinetic energy term in the system Hamiltonian, Eq. 2.1. Both the quantum mechanical and semiclassical treatment of light forces on atoms is described extensively in e.g. [117]. The semiclassical approach is generally accurate when the de Broglie wavelength of atoms is significantly less than the light field wavelength [117, p. 6], which we can also write as a temperature requirement:

$$\lambda_{dB} = \frac{h}{p} \ll \lambda \implies v \gg \frac{h}{m\lambda}, \quad T = \frac{mv_{rms}^2}{3k_B} \gg \frac{h^2}{3k_B m \lambda^2}. \quad (2.45)$$

For  ${}^{88}\text{Sr}$   $h/m = 4.55 \cdot 10^{-9} \text{ m}^2/\text{s}$ , so for  $\lambda = 689 \text{ nm}$ , the condition is  $v \gg 6.6 \cdot 10^{-3} \text{ m/s}$ . In terms of the temperature, the requirement is  $T \gg 150 \text{ nK}$ , with a "stronger"  $\gg$  due to the  $v^2$ -dependency. In this thesis we will generally consider atoms from the  $\mu\text{K}$  to the  $\text{mK}$  regime, and the recoils we will treat are so numerous that the semiclassical condition will generally be fulfilled. However we will still consider the effect of discrete recoils, which cause momentum diffusion.

Discrete recoils are easy to treat in the SME framework in Sec. 2.2, since the changes in state are already discrete, and a momentum kick can simply be associated with the quantum jumps, along the laser wavevector for laser recoils or in a random direction for spontaneous emission. However the treatment in Sec. 2.1 describes the mean evolution of operators such as the atomic states. Forces would be proportional to the changes in these states associated with an interaction, but in a superradiant laser we would also try to balance the forces of e.g. repumping lasers, such that a net force will not push atoms out of the cavity. Here fluctuations due to individual recoils will play an important role.

We know that if  $\langle \sigma_{ee}^j \rangle$  changes from 0 to 1, an atom has changed state to  $|e\rangle$ , and if this occurs gradually,  $\int_0^T \langle \dot{\sigma}_{ee}^j \rangle dt = 1$  implies the state change occurred from time 0 to  $T$ . However, if we consider  $\dot{\sigma}_{ee}^j$  in Eq. 2.27 (again dropping the angle brackets):

$$\dot{\sigma}_{ee}^j = 2ig_j [\text{Im}(\sigma_{ge}^j) \text{Re}(a) - \text{Re}(\sigma_{ge}^j) \text{Im}(a)] - \gamma_{eg}\sigma_{ee}^j + \gamma_{ie}\sigma_{ii}^j. \quad (2.46)$$

In 1st order MFT, the atom may gradually emit light into the cavity and environment, implying  $2ig_j [\text{Im}(\sigma_{ge}^j) \text{Re}(a) - \text{Re}(\sigma_{ge}^j) \text{Im}(a)] < 0$  and  $-\gamma_{eg}\sigma_{ee}^j < 0$ , and simultaneously it may be gradually repumped,  $\gamma_{ie}\sigma_{ii}^j > 0$ . These interactions may sum up to zero such that the atomic state, on average, is in steady state. Therefore to track the change in state due to an interaction, it must be integrated separately:  $\int_0^T 2ig_j [\text{Im}(\sigma_{ge}^j) \text{Re}(a) - \text{Re}(\sigma_{ge}^j) \text{Im}(a)] dt$  gives the total change in state  $|e\rangle$  due to interaction with the cavity field for the  $j^{th}$  atom, and equivalently for the other terms. Keeping track of integrals like these enables us to set conditions for recoils in a numerical simulation: if  $\int_0^T \gamma_{ie}\sigma_{ii}^j dt$  crosses an integer value at time  $T$ , we can apply a recoil corresponding to a spontaneous decay from  $|i\rangle$  to  $|e\rangle$  (numerically: a kick with momentum  $\hbar k_{\text{photon}}$  in a random direction). This can be done separately for all the interactions, but also allows for some approximations. For example if an atom is pumped from  $|g\rangle$  to  $|i\rangle$  in a repumping scheme that involves 10 different intermediate levels, all those recoils can be treated simultaneously when  $\int_0^T \gamma_{ie}\sigma_{ii}^j dt$  crosses an integer value, assuming that the individual recoils do not significantly affect the dynamics ( $\lambda_{dB} \ll \sum_{k=1}^{10} \lambda_k$ ).

When an optical potential is present and an atom is pumped between different levels, treating the atomic states with the average values from mean field theory can be inaccurate: if the atomic states are in steady state due to different interactions canceling out on average, the potential energy of an atom that is evaluated based on its state would also remain constant at a given position. In reality, the atom would be transferred between different states and may pick up kinetic energy while it is cycled between the states with different potential energy. This effect can be accounted for by treating the transitions with quantum jumps as in the SME approach.

## 2.6 Cavity field phase and spectral information

The main advantage of superradiant lasers lies in their reduced sensitivity to cavity mirror fluctuations. This results both in a potentially narrow laser linewidth, but also in a low amount of cavity pulling - the lasing frequency that can stay close to the atomic transition even if the cavity is detuned. Quantifying these parameters requires spectral information from the system, so here we will describe how to extract this information from simulations.

In first order MFT the phase of the electric field of the cavity mode is represented by the phase of  $\langle a \rangle$ , and the amplitude spectrum of the cavity field can be calculated by Fourier transforming  $\langle a(t) \rangle$  over the relevant time interval, and subsequently squared to obtain the power spectrum. In a numerical simulation this can be done using the fast Fourier transform (FFT) algorithm which requires just a single command in some programming languages. It

requires a list of the values of  $\langle a \rangle$  saved on a time interval characterized by the total duration  $T$  and sampling frequency  $1/\delta t_a$  at which  $\langle a(t) \rangle$  is saved. The highest frequency that one can hope to gain information about (without aliasing) is then the Nyquist frequency  $\nu_{Ny} = \delta t_a/2$ , and the spectral resolution will be Fourier-limited to  $1/T$ .

The advantages of the Fourier transform method is that the data from a simulation can be post-processed in different ways. Storing  $\langle a \rangle$  in an array once every 10 or 100 timesteps and saving the array to a file typically takes an insignificant fraction of the time of a simulation, but could result in large data files. The data files can then be used to obtain a spectrum from any part of the time interval, or generate spectrograms. A spectrogram can be generated by applying a window function to the data (typically a Gaussian characterized by a standard deviation  $\sigma_W$ ), where the window weighs the data around a certain time  $\tau$  which is varied:

$$a(\omega, \tau) = \frac{1}{\sqrt{2\pi}} \int_0^T a(t) e^{-(\tau-t)^2/2\sigma_W^2} e^{-i\omega t} dt. \quad (2.47)$$

The spectral intensity  $I(\omega, \tau) \propto |a(\omega, \tau)|^2$  can then be plotted on a heatmap as function of the frequency  $\omega$  and time  $\tau$  to reveal how the spectrum changes over time. A small window  $\sigma_W$  gives better time-resolution but poorer frequency resolution due to the Fourier limit. In the opposite regime as  $\sigma_W \rightarrow \infty$  one trivially obtains the spectrum over the entire time interval no matter the value of  $\tau$ .

### 2.6.1 Importance of the reference frame

The phase evolution of  $\langle a \rangle$  is also interesting in itself in terms of physical information, and can be compared to an experimentally observed phase of a beat signal between a superradiant laser and a reference laser. Such a beat signal will have oscillations at the frequency difference between the superradiant laser and reference laser. In many cases the reference laser may also have an offset from the atomic transition. If the reference laser frequency is different from the rotating frame frequency ( $\omega_1$ ) chosen in Eq. 2.7, the phase of  $\langle a \rangle$  must first be transformed to a frame rotating at the same frequency as the reference laser to make a direct comparison. This can be done by adding  $\delta \cdot t$  to the unwrapped phase, shifting the reference frame by an angular frequency  $\delta$ . "Unwrapped" here means the phase is defined beyond  $[0; 2\pi[$  such that there are no discontinuities in the phase when it "wraps" from  $2\pi$  back to 0 or the other way around. The procedure of wrapping/unwrapping can be done e.g. with a command in programming languages such as Matlab, or modulo operations.

Shifting the reference frame can also be an advantage before using the Fourier transform method, as the Fourier transformation will give a symmetric two-sided spectrum around zero, which corresponds to the reference frame frequency. If there are spectral features both 1 MHz above and below the frame frequency, the frame can be shifted by 2 MHz such that these can be distinguished in the spectrum after Fourier transforming.

### 2.6.2 Filter cavities

For simulations of long timescales where one is interested e.g. in a narrow spectrum of a continuous superradiant laser, a method based on "filter cavities" can be used which does not require saving values of  $\langle a \rangle$ . This method also works in second order MFT [64, 79, 110], where Fourier-transforming  $\langle a(t) \rangle$  is not a reliable method to extract the spectrum of the cavity field. In the filter cavity approach, a spectral range of interest must be chosen initially, e.g. a range of frequencies with span  $\Delta\omega$  around a center frequency  $\omega_0$  and desired spectral resolution  $\delta\omega$ , which could be set e.g. near the Fourier limit based on the simulation time. Then a term  $H_{fil}$  with  $N_f = \Delta\omega/\delta\omega$  filter cavities are added to the Hamiltonian (e.g. Eq.

2.1):

$$H_{fil} = \sum_{k=1}^{N_f} h g_f (a + a^\dagger) (f_k + f_k^\dagger). \quad (2.48)$$

This Hamiltonian and the connection of filter cavities to the intensity spectrum is illustrated in Fig. 2.6.

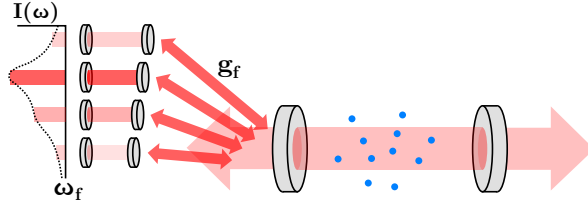


Figure 2.6: Illustration of filter cavities for calculating the spectrum of a superradiant laser. The filter cavities couple to the science cavity at rates  $g_f$  and their relative photon populations yield the intensity spectrum as illustrated in the top left. Figure adapted from [84].

The filter cavities can be thought of as a spectrum analyzer: light from the science cavity couples to the filter cavities, each with their own resonance frequency  $\omega_f^k$ . But since the filter cavities are only used for calculating the spectrum, we let the coupling between the science and filter cavities  $g_f \rightarrow 0$ , so that back-action on the science cavity field can be neglected. This also means that the photon populations within the filter cavities will be tiny. The spectral power distribution is given by the relative photon population as function of the filter cavity resonance frequency. In this thesis the loss rate of the filter cavities is taken to be 0, meaning that there is no memory loss and the resulting spectrum will include the full simulated timespan. By saving the relative photon populations at different time intervals, the filter cavity method can also be used to generate a particular form of spectrogram where the window includes all the dynamics up to time  $\tau$ . In terms of the Heaviside step function, the window function is then  $H(\tau - 0)H(t - \tau)$ . However the amount of data that must be saved then scales with  $N_f$  times the desired time resolution, a disadvantage compared to the Fourier transform method, which is also not limited in the type of window function. The simulation will also take longer to run when including filter cavities in the model, but typically  $N_f \ll N_{atoms}$  and the performance impact is not very significant. On the other hand no post-processing is required, such as the FFT algorithm for different window sizes, which can be very time-consuming.

### 2.6.3 Superradiant laser linewidth

Here we will consider the limitations of 1st order MFT in predicting the the linewidth of superradiant lasers, and the alternatives. One limitation is the neglect of spontaneous emission into the cavity mode, which occurs at the Purcell rate  $4g^2/\kappa$ . Since these photons are emitted with random phases they will lead to broadening of the laser linewidth. We can consider the prospects of modeling this by looking for the cavity photon number in 2nd order MFT, based on the Hamiltonian 2.15:

$$\langle a^\dagger a \rangle_{coh} = i \sum_{j=1}^N g_j (\langle \sigma_{eg}^j a \rangle - \langle \sigma_{ge}^j a^\dagger \rangle) + i \frac{\eta}{2} (\langle a \rangle e^{i\delta_E dt} - \langle a^\dagger \rangle e^{-i\delta_E dt}). \quad (2.49)$$

If we then look for the equation for e.g.  $\langle \sigma_{eg} a \rangle$ , we get:

$$\begin{aligned} \langle \sigma_{eg}^j a \rangle_{coh} &= i(\delta_{eE} - \delta_{cE}) \langle \sigma_{eg}^j a \rangle - ig_j [\langle \sigma_{ee}^j (a^\dagger a + 1) \rangle - \langle \sigma_{gg}^j \langle a^\dagger a \rangle \rangle] \\ &\quad - i \frac{\chi_{li}^j}{2} \langle \sigma_{ei}^j a \rangle e^{i\mathbf{k}_{li} \cdot \mathbf{r}_j - i\delta_{liI} t} - i \frac{\eta}{2} \langle \sigma_{eg}^j \rangle e^{-i\delta_E dt}. \end{aligned} \quad (2.50)$$

Here we see the atom-cavity interaction term (with  $g_j$ ) includes a term with the excited population,  $\sigma_{ee}^j$ , that contains  $a^\dagger a + 1$ , corresponding to an excited atom emitting into the cavity via stimulated emission (scaling with  $\langle a^\dagger a \rangle$ ) or spontaneous emission (the extra  $+1$ ). The impact of spontaneous emission can be found in the filter cavity framework looking for e.g. the filter cavity populations  $\langle f_k^\dagger f_k \rangle$  which eventually couples to  $\langle \sigma_{eg}^j a \rangle$  via equations involving the cavity field. The equations here also do not yet involve atom-atom correlations (like  $\langle \sigma_{ge}^i \sigma_{eg}^j \rangle$ ) so the number of equations does not necessarily scale with  $N^2$  if they can be closed without atom-atom correlations (these can of course also have an impact on the spectrum). However including this in the model has been considered outside the scope of the thesis.

The linewidth from pulsed and quasi-continuous lasing will ultimately be Fourier-limited by the pulse duration, if nothing else broadens the linewidth further. Fully continuous superradiant lasers are not limited in this way, making them of greater metrological interest. Using 2nd order theory in [72],  $\Delta\omega = C\gamma$  was found as an estimate for the minimum linewidth of a continuous superradiant laser characterized by incoherent repumping at a rate  $w$ . Here  $C = 4g_0^2/\kappa\gamma$  is the cooperativity parameter, and this  $\Delta\omega$  is exactly the Purcell rate of the system. It was found to be a good estimate for pumping rates within  $1/T_2 < w < NC\gamma$ .  $1/T_2$  is an effective relaxation rate due to all inhomogenous processes, such as finite temperature, and the pumping rate must overcome this for atoms to become phase-locked. Near  $w = NC\gamma$  the pumping rate becomes too high and begins to destroy the coherence, leading to a sharp increase in linewidth.

An analytical expression for the linewidth in such a system was derived in [62], given by:

$$\Delta\omega = \frac{C_N + 1}{2(C_N d_0 - 1)} \frac{\Gamma}{w + \gamma} \frac{4g_0^2 \kappa}{(\kappa + \Gamma)^2}, \quad (2.51)$$

where  $\Gamma = \gamma + w + 1/T_2$  represents the decoherence rate,  $C_N = 4Ng_0^2/\kappa\Gamma$  is a generalized cooperativity parameter, and  $d_0 = (w - \gamma)/(w + \gamma)$  characterizes the inversion due to pumping in absence of the cavity. This expression was compared to simulations based on 2nd order theory in [64], showing good agreement for a broad range of pumping rates down to near lasing threshold for a system using the  ${}^1S_0$ - ${}^3P_1$  transition, all the way up until the limit where the coherence is destroyed by pumping. It was also illustrated that further narrowing could occur deep within the superradiant lasing regime for sufficiently high atom numbers and appropriate pumping rates, giving linewidths potentially orders of magnitude below the Purcell rate. This regime is also described by Eq. 2.51.

In some proposals for continuous superradiance the atoms are pumped prior to entering the cavity instead of being continuously pumped within the cavity. Such a pumping scheme does e.g. not introduce decoherence on the lasing transition of atoms within the cavity, so Eq. 2.51 is not directly applicable to these systems. The Purcell rate still offers an estimate of the linewidth in this regime.

In addition to estimates of the linewidth, lower limits on the linewidth have also been derived, such as a generalized version of the Schawlow-Townes limit that applies outside the good-cavity regime. This approach has been applied to a thermal atomic beam that is pumped to the excited lasing state prior to entering the cavity [85]:

$$\Delta\omega_{ST} = \frac{\kappa}{4\pi n} \frac{\rho_{ee}}{\rho_{ee} - \rho_{gg}} \left( \frac{1}{1 + (\kappa/\Gamma_G)} \right)^2. \quad (2.52)$$

Here  $n$  is the cavity photon number, which can be found by numerical simulations or analytical expressions in sufficiently simple systems (as also given in [85]). Similarly the populations  $\rho_{ee}$

and  $\rho_{gg}$  can be found using simulations, but for efficient pumping giving a significant inversion, the fraction is of order unity.  $\Gamma_G$  is the gain bandwidth, and the equation was originally derived in a regime without inhomogenous broadening. The impact of inhomogenous effects was investigated in [118], showing that the total gain bandwidth, including both homogenous and inhomogenous mechanisms, is a good approximation for  $\Gamma_G$ . The equation is often expressed in terms of the cavity output power,  $P_{out} = \hbar\omega\kappa n$ .

#### 2.6.4 Instantaneous frequency and transfer functions

Cavity pulling is often defined in a stationary regime, where a pulling coefficient can be defined simply as  $c_{pull} = \delta_L/\delta_{cE}$ , with  $\delta_L$  being the shift in lasing frequency from the atomic transition, and  $\delta_{cE}$  being the cavity detuning relative to the transition. However one of the main motivations for building superradiant lasers is that cavity mirrors tend to not be stationary, so it is also important to quantify how superradiant lasers respond to fluctuations such as changes in cavity detuning. This can be described with a transfer function for the frequency response, using linear response theory. The cavity pulling coefficient is associated with the response at the lowest frequencies. Linear response theory has been applied to superradiant lasers in [63].

In 1st order MFT we can define the instantaneous frequency as  $\nu(t) = d\langle\phi(t)\rangle / 2\pi dt$  from the unwrapped phase  $\langle\phi(t)\rangle$  of  $\langle a(t)\rangle$ . To extract the frequency response transfer function, one method in simulations is to subject the superradiant laser (once it has reached steady-state behavior) to a sudden step in cavity detuning (at  $t = t_J$ ). This gives us the step response of the instantaneous frequency,  $\nu(t)$  for  $t > t_J$ . From this we can obtain the impulse response,  $d\nu(t)/dt$ , and the frequency response transfer function as the Fourier transform of  $d\nu(t)/dt$ . The transfer function can be normalized by the jump size in cavity detuning, in which case the transfer function of a system will typically be identical for different jump sizes, if the jumps are not too big. The same procedure can also be used to extract the phase and power transfer functions, with  $\langle\phi(t)\rangle$  or  $P_{out}(t)$  in place of  $\nu(t)$ .

### 2.7 Atom group approximation and performance considerations

If the number of atoms is very large and takes too long to simulate even in 1st order MFT, an atom group/clustering approximation can be used. This works by representing many atoms (e.g.  $N_{pg}=100$ ) as a single unit, sharing position, velocity and state, and the  $\sigma_{xy}^j$  operators then represent atom group  $j$  instead of the  $j$ 'th atom in e.g. Eq. 2.6. This reduces the number of terms in the sum, while giving a factor  $N_{pg}$  at each atom operator, if their normalization is to be preserved. The atom group approximation generally leads to a quicker buildup of a macroscopic dipole from a random configuration because all the coherences  $\langle\sigma_{ge}^j\rangle$  within a group are identical and add up, while they would (under randomizing conditions) tend to cancel each other out to a degree. As a result atom groups can result in biases leading to quicker buildup of superradiant pulses, which was investigated in [103, p. 34]. Since fluctuations in atom number scale with  $1/\sqrt{N}$  relative to the total atom number, phase fluctuations etc. originating from the atoms will also be larger when using the approximation. However mean values of e.g. emitted power can still be accurately predicted while using the approximation, especially in steady state where a macroscopic coherence has already been established.

Optimizing the performance of simulations is crucial to limit the need for such approximations. In high-level programming languages the most important factor is to vectorize the operations involving atoms, as loops tend to be very slow. Running simulations where atomic variables are stored in large vectors that are multiplied can be sped up further using a GPU

instead of CPU when the vectors are sufficiently large. A CPU typically has a few cores (on the order of 10), meaning it can do 10 simultaneous operations at the clock frequency (on the order of a few GHz) under optimal conditions, and reads and stores the vectors in RAM. On the other hand a GPU has many more cores (e.g. thousands) and a clock frequency typically lower, but similar, to a CPU. It also has its own memory, but reading to/from the GPU is typically slower than RAM, which makes the CPU faster for small vector sizes. The GPU architecture with many cores was made to process pixel values in parallel but is equally useful for parallel calculations of the elements in large vectors. In Fig. 2.7 the benefit of using a GPU for numerical simulations is illustrated, and how it depends on the number of particles (atoms or atom groups). The GPU used here is an nVidia GTX 1080 Ti, while the CPU is an AMD Ryzen 2700X. The example is based on the model of pulsed superradiance in a mK atom cloud presented in Chapter 4, but the over-all scaling is similar for other models (with their regimes in atom number highlighted). The atom group approximation will only be used generally for the hot atomic beam system (typically with 100 atoms/group) and in a few other cases where it is stated. Using the GPU is an advantage for  $> 10^5$  particles.

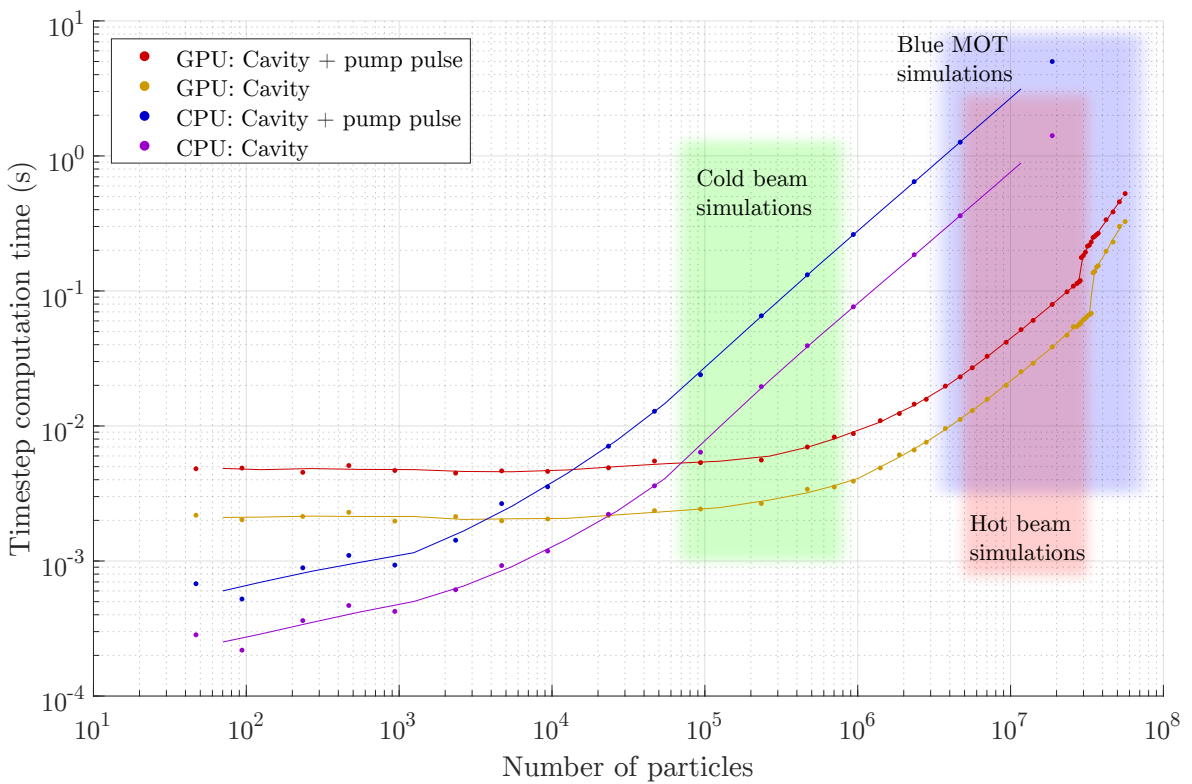


Figure 2.7: Comparison of performance when storing and calculating the atomic states on GPU vs CPU and RAM. The data is from simulations of superradiant pulses in a mK atom cloud, showing the calculation time of a timestep when the atoms interact only with the cavity mode, as well as when the pump pulse is also on, which requires more calculations. Curves show a moving mean. The regimes of different types of simulations in the thesis are highlighted in terms of the number of particles if no atomic grouping is used.

Finally, we can consider one approach to a concrete numerical implementation, beyond the trivial task of storing data at appropriate time intervals with the desired physical quantities to be saved in files. Fig. 2.8 shows an approach to keeping track of a simulation (the cold beam model in Chapter 8) by live-plotting different relevant quantities and overviews. In the upper left, different parameters from the simulation are listed for reference, and in the lower left, atoms are color-coded by their state. The panels on the right show the cavity field dynamics (upper center), intensity spectrum from filter cavity calculations (upper right), spatial distribution of populations (lower center) and temperature (lower right). Periodically plotting and saving these enables monitoring how the system evolves over time. It is not viable to do every timestep, as it takes a lot of performance, but skipping every e.g. 1000 timesteps allows the monitoring to have an insignificant impact on performance. Generally, the more parameters that are monitored, the easier it is to understand the dynamics intuitively, spot problems or unphysical behavior and to debug the code.

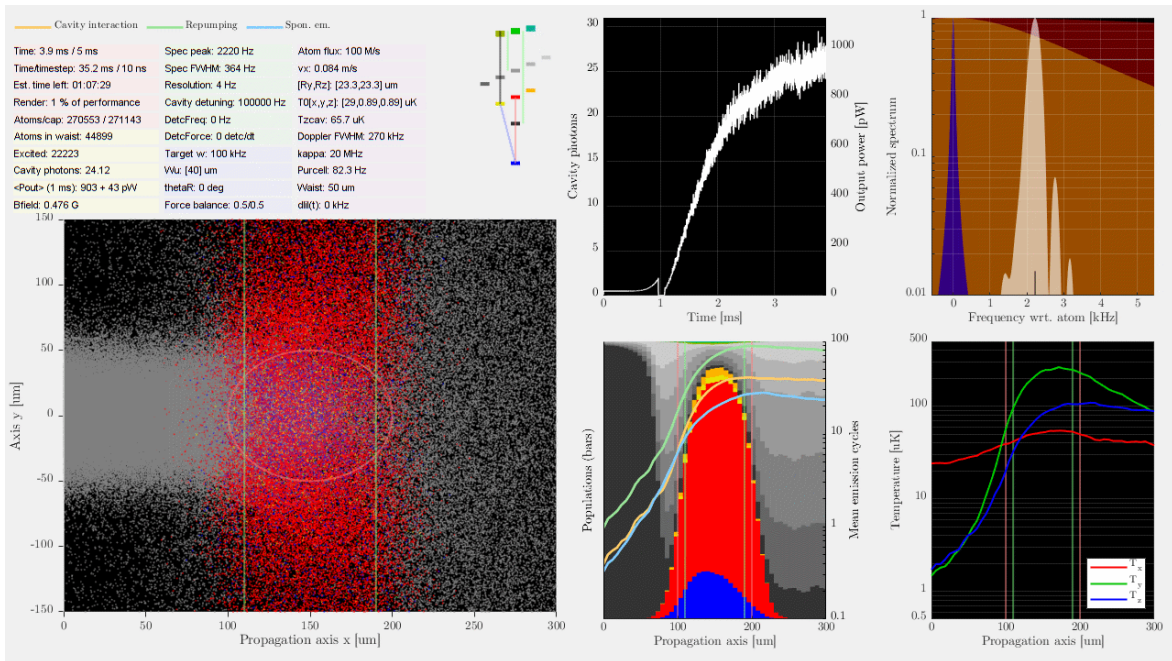


Figure 2.8: Example of live plotting for the cold beam simulations in Chap. 8. The different aspects of the dynamics are monitored in the different panels.

## Atom cloud machine for superradiant laser pulses

This chapter describes the atom cloud machine at UCPH which is used for investigating superradiant laser pulses. Investigations of the pulses are presented in later chapters. Here we focus on the components of the machine and related physics, and the parts that were upgraded during the work of this thesis. This was done in collaboration with several people (see [Acknowledgements](#)). The core part of the machine is illustrated in Fig. 3.1.

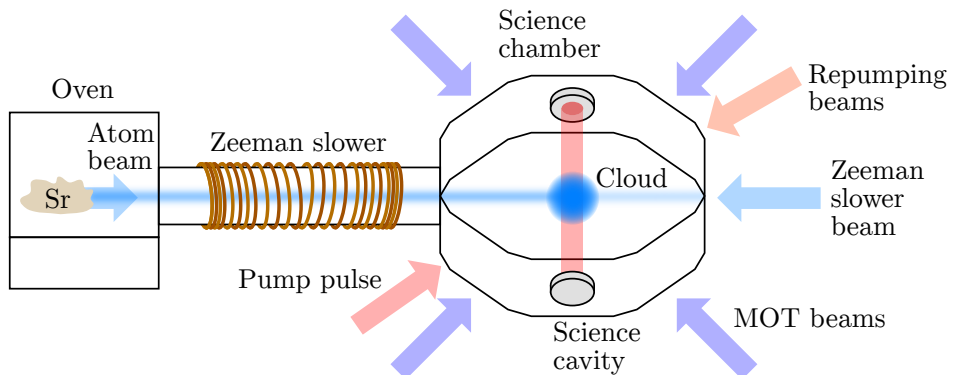


Figure 3.1: *The core part of the strontium cloud machine. The inside is under vacuum. When the oven is heated up, an atomic beam forms, providing a source for trapping an atom cloud within the science chamber. Additional laser beams can be used to pump the atoms and enable us to investigate superradiant emission into the mode of the science cavity.*

The first part of the machine is an oven containing strontium. The strontium is heated to typically 530 °C, yielding a beam of atoms from the oven nozzle. The atoms of the beam then pass through a Zeeman slower, which relies on a laser beam and the magnetic field of a solenoid. The magnetic field of the coil splits up  $^1\text{P}_1$  into  $m_J = \{-1, 0, 1\}$ , and the laser beam is circularly polarized and red-detuned 440 MHz from the unshifted resonance. The particular variation in the solenoid windings causes the Zeeman shift to change gradually as the atoms move through it, such that the fastest velocity-class is continually slowed by the laser beam. The atoms entering the Zeeman slower from the oven move at several hundreds of m/s and are slowed down to the order of 10 m/s as they enter the science chamber.

Here atoms from the slowed beam are trapped in a magneto-optical trap (MOT). The slow velocities are required to be within the capture range of the MOT - without the Zeeman slower, only a tiny fraction of the thermal atoms from the oven would be slow enough to be captured by the MOT alone (see e.g. examples of the velocity distributions in a thermal beam in Fig. 7.1).

The MOT utilizes the same principle as the Zeeman-slower, but in three dimensions to trap atoms in a cloud. The MOT initially uses 461 nm beams, operating on the  $^1S_0$ - $^1P_1$  transition (the "blue MOT"). As part of the work of this thesis, the machine was upgraded to enable 2nd stage cooling - using 689 nm beams after the blue MOT stage to trap and further cool atoms in a red MOT cloud. Once a blue or red MOT cloud has formed, a pump pulse can be used to excite the atoms from  $^1S_0$  to  $^3P_1$ , and the excited atoms may subsequently emit a superradiant pulse into the cavity mode. Since the science cavity mirrors are not perfectly reflecting, light from the pulse will eventually couple out of the cavity, where the pulses can be investigated. The parameters of the science cavity are given in Table 3.1.

Atom-cavity coupling	$g_0/2\pi$	813.5 Hz
Finesse	$F$	1260
Free spectral range	$FSR$	781 MHz
Length	$L$	192 mm [119, p. 118]
Linewidth (FWHM)	$\kappa/2\pi$	$620.3 \pm 0.4$ kHz [103, p. 63] *
Mirror radius of curvature		9 m [119, p. 118]
Mirror reflectivity		99.751%
Purcell rate	$(4g_0^2/\kappa)/2\pi$	4.27 Hz
Single-atom cooperativity	$C$	$5.72 \cdot 10^{-4}$
Waist radius	$W$	450 $\mu$ m [119, p. 118]

Table 3.1: *Parameters of the science cavity within the atom cloud machine, for laser light resonant with the 689 nm  $^1S_0$ - $^3P_1$  transition.* \*Note the linewidth (and related parameters) can change over time - it may increase if materials accumulate on the mirrors, reducing the reflectivity. At the time of writing, there are indications that it has increased to  $\sim 800$  kHz.

The repumping laser beams at 679 and 707 nm are crucial for efficient MOT operation, as the  $^1P_1$  state has tiny decay routes into the long-lived states  $^3P_2$  and  $^3P_0$  (see Fig. 1.1). The repumpers pump these atoms to  $^3S_1$  so that they can decay to  $^3P_1$  and subsequently  $^1S_0$ , such that they can interact with the MOT beams again. As a result they increase the atom number within the blue MOT cloud on the order of a factor 13 (see e.g. [120, p. 15]), depending on the pressure within the science chamber.

### 3.1 Laser systems for the atom cloud machine

A highly simplified overview of the laser systems on the "Sr1" optical table, used for the atom cloud machine, is shown in Fig. 3.2.

#### 689 nm Master Laser

The 689 nm Master Laser system is located on a separate optical table, but this has not changed significantly since the overview given in [121, p. 32-34], [122, p. 101-104] and [119, p. 85-87]. Here the 689 nm Master Laser is locked to a high-finesse cavity ( $F=7500$ ) in vacuum, using the Pound-Drever-Hall (PDH) technique. The main recent changes were adding more fiber couplings for beat measurements and replacing the original flat-cut optical fiber to the Sr1 table with an angle-cut one, which reduced etalon effects and enabled us to eliminate one of the two optical isolators. This fiber transmits the light for injecting the 689 nm Slave 1 laser.

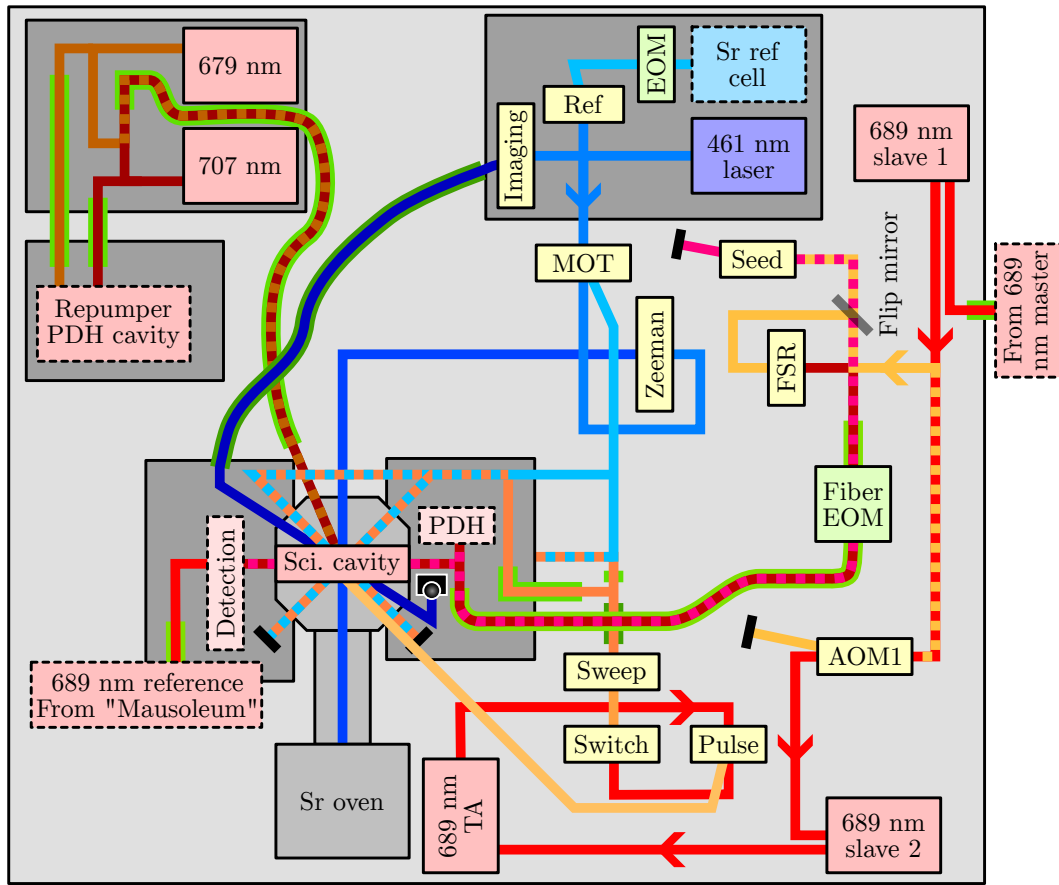


Figure 3.2: Simplified overview of laser systems for the Sr cloud machine. Changes in beam colors (arbitrary) indicate changes in frequency by AOMs (yellow boxes). Dashed lines indicate overlapping beam paths. Fibers are indicated by green lines.

### 689 nm slave lasers and tapered amplifier

The "Slave 1" laser diode derives its name from the fact that it ideally inherits its frequency from the 689 nm Master Laser. This is done by the injection-locking technique, which only works within a narrow range of laser diode current and temperature, and relies on sending a small amount of light from the Master Laser into Slave 1. In terms of power, at least about 1.1 mW must be sent into the diode, out of the isolator protecting it, with the current mode-matching. This isolator also sends the light component with unwanted polarization from the slave diode towards the fiber to the Master Laser table. As a result the power transmitted from Slave 1 through the fiber is a good proxy for optimizing the mode-matching of the injecting beam with the laser diode. In terms of laser diode current, a stable injection is typically characterized by a plateau in the power emitted by the diode as function of the diode current. This is usually observed on an oscilloscope, displaying the detected power from a photodiode as function of a triangle wave reference voltage. This reference voltage is simultaneously used as a modulation input for the laser diode current. A typical plateau for Slave 1 can be seen in [119, p. 94]. This qualitative behavior has persisted, though the exact diode current and temperature have been adjusted slightly over time.

The beam from Slave 1 is sent to AOM 1. The 0th order from AOM 1 is used for injecting Slave 2, and these injection characteristics were described in [103, p. 55]. All the power from Slave 2 is subsequently used as input for a tapered amplifier (BOOSTA) with fiber-coupled ports. The BOOSTA is a replacement for the original TA described in [103, p. 56-57], as the power from it degraded over time (see Appendix A.1). This commonly occurs in tapered amplifiers, and is also observed in the BOOSTA. From the output fiber of the BOOSTA we obtain on the order of 200 mW, which is used for the pump pulse and red MOT beams. The

pump pulse is switched via the pulse AOM, using the -1 order and a frequency close to 40 MHz. The beam is focused within the AOM to minimize the rise/fall time of the intensity when switching to the order of tens of ns. This transient behavior is described in more detail in [103, p. 57-58], but the quantitative characteristics have changed slightly since then due to the changes in the optics.

### Red MOT optics

Since the pump pulse is not needed while capturing atoms into the red MOT cloud, the 0th order of the pulse AOM is used for the red MOT, so that the full TA power can be used for either. The subsequent red MOT optics are shown in Fig. 3.3. Here one single-pass AOM ("Switch") enables quickly switching the red MOT beams on/off, and a second ("Sweep") is double-passed so that it can be continually scanned to frequency-broaden the red MOT beams with minimal misalignment. The beam is subsequently fiber-coupled and divided between the vertical and horizontal axes of the MOT. Then it is expanded with telescopes and finally overlapped with the blue MOT beams using dichroic mirrors. Since the dichroic mirrors do not preserve circular polarization well, achromatic  $\lambda/4$ -plates were mounted right before the chamber windows for the MOT beams.

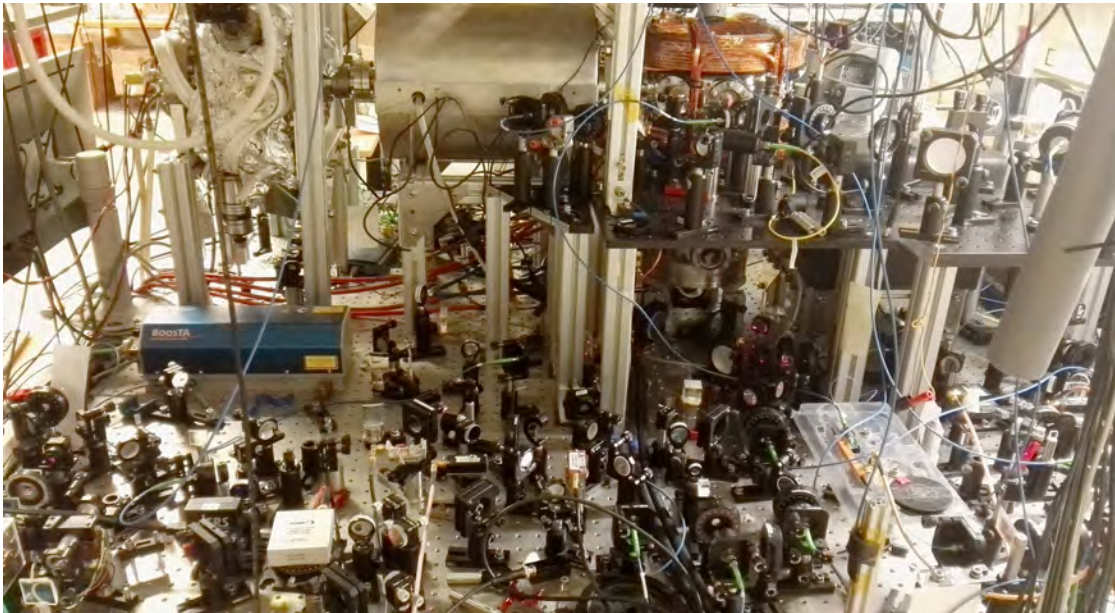


Figure 3.3: *The Sr1 table seen from the lower right side in Fig. 3.2, including the pump pulse and red MOT optics, and the atom cloud machine in the background.*

### Science cavity input beam

A laser beam is sent to the science cavity to lock it via the PDH technique. The beam from 689 nm Slave 1 is first double-passed in AOM1 and then sent to either the "Seed" or "FSR" AOM, depending on the configuration of a flip mirror. If the mirror is flipped up, the beam single-passes the FSR AOM and is then detuned 781 MHz from the atom resonance, but is on resonance with the next FSR of the science cavity. If the mirror is flipped down, the beam instead double-passes the Seed AOM and is shifted close to the atomic resonance. This enables populating the cavity mode with light that affects the atomic dynamics (defining the  $\eta$  and  $\omega_d$  parameters in Chapter 2). In either case the beam from one of the AOMs is eventually coupled into a fiber EOM which adds sidebands at 10 MHz used for the PDH lock. The optics layout is described in more detail in [121, p. 29-31]. The only significant change was replacing the fiber EOM to one with angle-cut fibers, which reduced disturbances from etalon effects. The power of the 10 MHz RF signal for the EOM is typically on the order of 15 dBm.

### Blue laser system

The 461 nm laser system for laser cooling on the  $^1S_0$ - $^1P_1$  transition is mounted on a breadboard, which also includes a hollow-cathode cell for locking the laser frequency to the atomic transition using saturated absorption spectroscopy. The beam for the Sr1 machine is subsequently divided via the MOT AOM and Zeeman slower AOM. The optical path from this laser system to the atom cloud was shortened compared to an older system based on frequency-doubling, which makes the blue MOT less sensitive to minor changes in alignment e.g. from random temperature changes from day to day. Some light from the blue laser system is also used for an absorption imaging system.

### 679 and 707 nm repumpers

The 679 and 707 nm repumpers are Littman-Metcalf type external cavity diode lasers (ECDLs) housed in temperature-stabilized boxes. The lasers themselves are described in more detail in [119, p. 106-108]. For space management and portability they were mounted onto a breadboard, with a new optics layout shown in Fig. 3.4. A setup for locking both of the repumper lasers to a cavity is described in [123].

### 689 nm reference laser system

The reference laser system was set up in a separate well-isolated room (the "Mausoleum") - the initial system used for beat signal data presented in this thesis is described in [121, p. 33-38]. Here, the laser was locked to a high-finesse cavity temporarily borrowed from SYRTE (described in [124]), using the PDH-technique. Fibers link the reference laser system to the main lab. At the atom cloud machine, optics enabled for overlapping a reference laser beam with the output of the cavity mode, for beat note detection of superradiant pulses from the blue MOT cloud. Fiber-noise cancellation was also employed for this link.

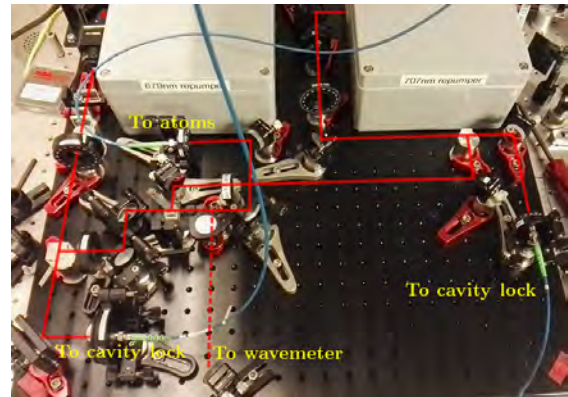


Figure 3.4: The repumper breadboard with beam paths highlighted.

## 3.2 Magneto-optical trap

The MOT is a central component in the atom cloud machine. Here we will first consider how a MOT works qualitatively. It relies on two coils in the anti-Helmholtz configuration, which generate a magnetic field with the shape shown in 3.5a. The field is symmetric around the z axis, has a zero-point near the center, and the magnitude of the field increases linearly as one moves away from the center. From Gauss' law for magnetism  $\nabla \cdot \mathbf{B} = 0$  we know the gradient along the z axis is twice, and opposite, of the x and y axes:  $\frac{\partial B}{\partial z} = -\frac{\partial B}{\partial x} - \frac{\partial B}{\partial y}$ .

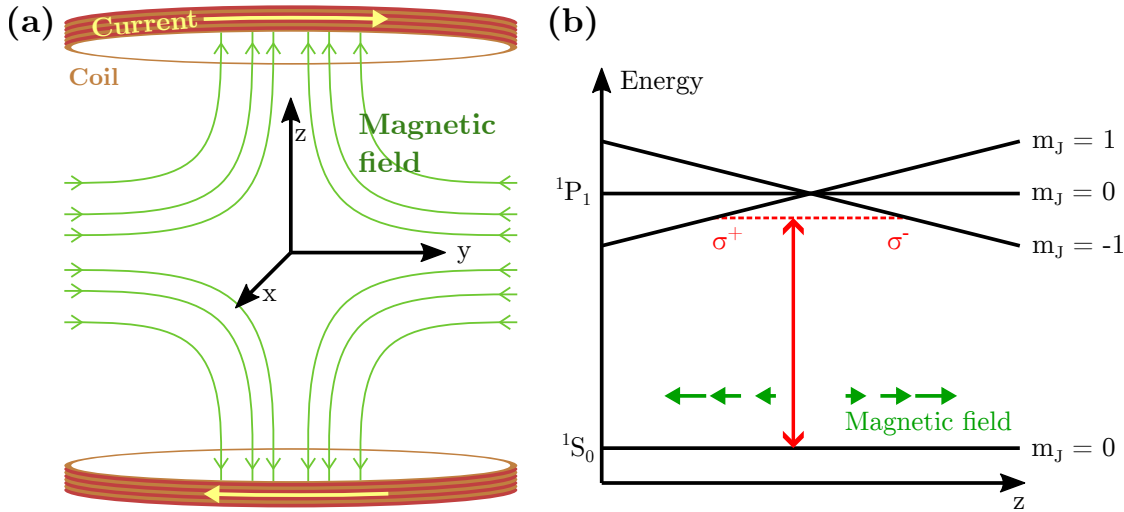


Figure 3.5: (a) The magnetic field of coils in the anti-Helmholtz configuration. Both current can also be reversed, reversing the field lines. (b) The dependency of Zeeman-shifted energies of different levels on the atom's position along the  $z$  axis in a MOT. The red arrow indicates the energy of MOT photons, which are red-detuned from the  $m_J=0$  transition.

A second ingredient in the MOT is the level structure of  $^{88}\text{Sr}$ , which we encountered in Fig. 1.1. A magnetic field will split up any levels with angular momentum. The ground state of Sr,  $^1\text{S}_0$ , has zero angular momentum and is unaffected, but the blue/red MOT excited states,  $^1\text{P}_1$  and  $^3\text{P}_1$ , have total angular momentum of  $J = 1$ , and are therefore split into three levels with different energies, depending on the projection of the angular momentum along the  $z$  axis:  $m_J = +1$  if the angular momentum vector points along  $z$ , 0 if it is zero, and -1 if it points towards  $-z$ . As a result the energies of the three levels vary along the  $z$  axis as shown in Fig. 3.5(b). For  $x$  and  $y$ , the scaling with  $m_J$  is lower by a factor two and flips sign.

The third ingredient is the laser light. If we consider a circularly polarized laser beam coming from below (so  $\mathbf{k} \parallel \hat{\mathbf{z}}$ ), we can classify it as right-handed if its E-field rotates counter-clockwise around  $\mathbf{k}$  as it propagates. In this case a photon from the laser beam has angular momentum +1 around the  $z$  axis, and can drive  $\sigma^+$  transitions from  $^1\text{S}_0$  to  $^1\text{P}_1$   $m_J=1$ , pushing any atoms upwards that are on resonance with it.

If this beam is simply reflected back by a mirror,  $\mathbf{k}$  will flip, but its angular momentum along the  $z$  axis will stay the same. As a result it would be "left-handed". But for the atoms it is the angular momentum relative to  $\hat{\mathbf{z}}$  that matters, not the handedness (defined relative to  $\mathbf{k}$ ). So if the beam is simply reflected back, it would again drive the  $\sigma^+$  transition, and the atoms on resonance would be pushed equally up and down by the laser beam. However if a quarter-wave plate is placed before the mirror, the angular momentum of the photons can be flipped after the two passes, such that the reflected beam drives the  $\sigma^-$  transition.

Now the Zeeman shifts shown in Fig. 3.5(b) become useful. If the laser is red-detuned from the unperturbed atom resonance (from  $^1\text{S}_0$  to  $^1\text{P}_1$   $m_J=0$ ) by  $\delta_l$ , it will preferentially drive transitions where the combined Zeeman and Doppler shifts obey  $\delta_l = \delta_Z + \delta_D$ . So if an atom is standing still a bit below the magnetic field center,  $\delta_D = 0$  but  $\delta_Z$  is positive for  $m_J=-1$  and negative for  $m_J=1$ . Then the laser would be closest to the  $\sigma^+$  resonance and as a result the atom would tend to be accelerated upwards. For an atom a bit above the center, the laser frequency matches the  $\sigma^-$  transition better, which can only be driven by the back-reflected beam, so this atom will be accelerated downwards. The effect of Doppler shifts is similar. For an atom standing still in the center both laser beams are red-detuned from the transitions, but if it is moving upwards, the photons from above will appear blue-shifted closer to resonance, while the ones from below will be red-shifted further away. Thus the

two laser beams slow down atoms and trap them near the magnetic field center. The center can be moved by changing the relative coil currents, and if the light intensities are not equal, atoms may also be trapped a bit off-center. For the x and y axes, the same considerations can be used - the light polarization just needs to be changed so that it drives the opposite transitions, since the magnetic field lines run in the opposite direction, as indicated in Fig. 3.6.

A Zeeman slower uses the same principles as a MOT to slow a beam of atoms, rather than to trap them. Here a solenoid is built around the atomic beam path with a variation in the density of loops such that one laser beam antiparallel to the atomic beam is continually kept on resonance with a Zeeman-shifted transition of the fastest atoms as they travel along the path. The MOT principles can also be used in 2 dimensions to transversely cool and confine a beam of atoms, and the similar optical molasses technique (without the coils and magnetic field of the MOT) can also be used to cool atoms without confining them.

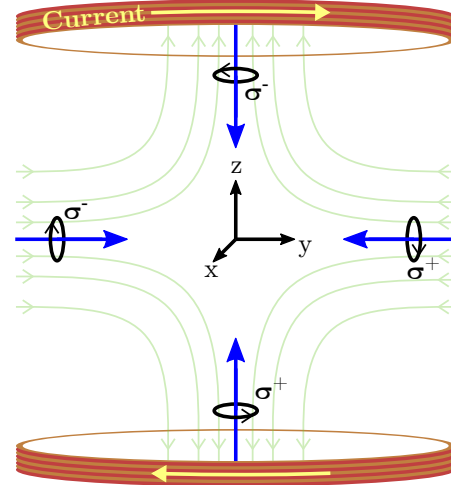


Figure 3.6: The light polarization and  $\sigma$  transitions driven in a MOT.

### 3.2.1 Model of a MOT

Here we will consider a model of a MOT to illustrate the qualitative behavior of atom trapping and cooling in the Sr cloud machine, and the challenges involved with 2nd stage cooling. Each MOT beam will be treated independently (which is accurate for low saturation), and for one MOT beam we can consider three different force contributions [20, p. 188]:

$$F = F_{sca} + \delta F_{abs} + \delta F_{spont}. \quad (3.1)$$

Here  $F_{sca}$  is the average scattering force, which stems from absorbing MOT beam photons,  $\delta F_{abs}$  are the fluctuations due to the randomness of individual laser recoils, and  $\delta F_{spont}$  are the fluctuations due to spontaneous emission into all directions.  $F_{sca}$  and the scattering rate  $R_{sca}$  from a MOT beam is [20, p. 180] [116]:

$$F_{sca} = \hbar k R_{sca} = \hbar k \frac{\gamma}{2} \sum_j \frac{W_j I / I_{sat}}{1 + W_j I / I_{sat} + 4\delta_j^2 / \gamma^2}. \quad (3.2)$$

Here we will use  $R_{sca}$  to calculate the probability of a scattering event from a MOT beam,  $R_{sca} dt$ , for atoms during each timestep in a simulation. Each time a scattering event occurs, a quantized recoil from the MOT laser is imparted, along with a random recoil from subsequent spontaneous emission. In this way both the mean force and fluctuations are included.  $R_{sca}$  depends on the saturation intensity of the MOT transitions (with Lorentzian linewidths  $\gamma$ ), which are given by [20, p. 142] [104, p. 193]:

$$I_{sat} = \frac{\hbar \omega^3 \gamma}{12\pi c^2}. \quad (3.3)$$

Note this is specifically the resonant value of  $I_{sat}$  (which is most commonly used, laser detunings are usually accounted for separately, as also done here) and definitions in other sources can differ by a factor 2. For the blue MOT transition where  $\gamma = 2\pi \cdot 30.24(3)$  MHz this gives  $I_{sat}^B = 403.8(4)$  W/m<sup>2</sup>, while for the red MOT transition  $\gamma = 2\pi \cdot 7.480(1)$  kHz gives  $I_{sat}^R = 29.87(4)$  mW/m<sup>2</sup>. We will model the intensity profiles with simple Gaussian functions.

The parameter  $W_j$  accounts for the fact that the quantization axis of each atom generally points along the B-field vector  $\mathbf{B} = B_{grad}(-x, -y, 2z)$ . This is used in [116] where the circularly polarized light of each laser beam is considered in a spherical basis and a rotation matrix is used to map it onto  $\mathbf{B}$  at each atom to determine how strongly the  $\sigma^\pm$  and  $\pi$  transitions of each atom are driven by the MOT beams. By assuming that each laser beam has exactly the desired circular polarization, and defining the angle  $\theta$  between  $\mathbf{k}_{laser}$  and  $\mathbf{B}$ , we obtain the following results for the x axis (y and z are equivalent):

$$\begin{aligned} W_+ &= \left( \frac{1}{2} + \frac{1}{2} \cos \theta_x \right)^2 = \left( \frac{1}{2} + \frac{1}{2} \frac{B_x}{|\mathbf{B}|} \right)^2 \\ W_0 &= \frac{1}{2} \sin^2 \theta_x = \frac{1}{2} - \frac{1}{2} \left( \frac{B_x}{|\mathbf{B}|} \right)^2 \\ W_- &= \left( \frac{1}{2} - \frac{1}{2} \cos \theta_x \right)^2 = \left( \frac{1}{2} - \frac{1}{2} \frac{B_x}{|\mathbf{B}|} \right)^2. \end{aligned} \quad (3.4)$$

For example, if an atom is located along the z-axis at  $(0, 0, z)$ ,  $\mathbf{B} = 2B_{grad}(0, 0, z)$  and for the downwards-pointing MOT beam with  $\hat{\mathbf{k}} = (0, 0, -1)$  we get  $W_+ = 0$ ,  $W_0 = W_- = 1$ , while for the upwards-pointing MOT beam we get  $W_+ = 1$ ,  $W_0 = W_- = 0$ . And as illustrated in Fig. 3.5(b), neglecting Doppler shifts, the red-detuning of the MOT beams will then result in the  $\sigma^-$  transition being driven the strongest, which only the downwards-pointing beam (with  $W_- > 0$ ) can do, so the atom will most likely be pushed towards  $(0, 0, 0)$ . But we see that in general, all the MOT beams can drive  $\sigma^\pm$  and  $\pi$  transitions for the off-axis atoms. The dependency on the projection angle is illustrated in Fig. 3.7.

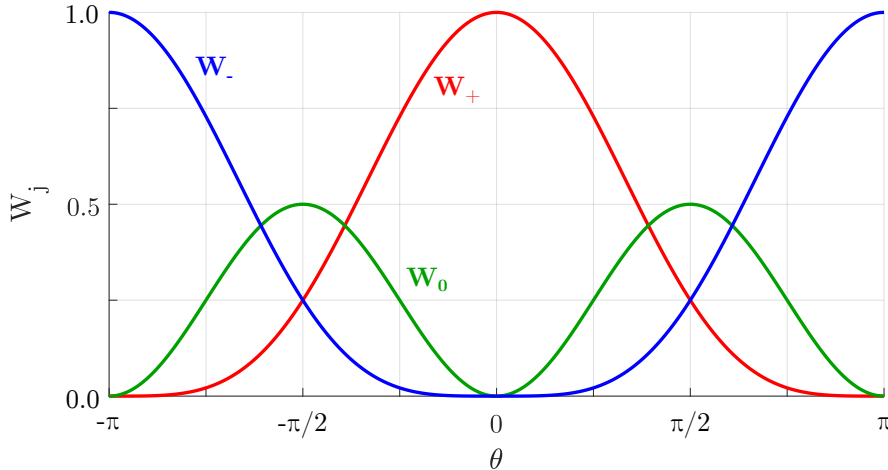


Figure 3.7: The dependency of the  $\sigma^\pm$  and  $\pi$  transition strengths,  $W_j$ , on the angle between the laser  $\mathbf{k}$ -vector and local  $\mathbf{B}$ -vector.

In addition to the intensity and polarization of the laser beams, the detuning  $\delta_j$  is important, as the atoms in a MOT experience both Zeeman and Doppler shifts in addition to the laser detuning. We can write the laser detuning experienced by the  $m_j = +1$  state of an atom from a laser beam propagating towards  $+x$  as:

$$\delta = \delta_l - kv + \frac{g_J \mu_B}{\hbar} x \frac{dB}{dx}. \quad (3.5)$$

The equations for  $y$  and  $z$  are equivalent, while for the opposing beams the Doppler shift  $kv$  flips sign. For the  $m_J = -1$  level the Zeeman shift flips sign, while  $m_J = 0$  has no Zeeman shift.  $g_J = 1$  for  ${}^1\text{P}_1$  of the blue MOT and  $3/2$  for  ${}^3\text{P}_1$  of the red MOT. Typical values for the field gradients along the coil axis are 370 mT/m for a blue MOT and 31 mT/m for the red MOT. The blue MOT beams are detuned by 40 MHz, while the red MOT beams are typically detuned on the order of hundreds of kHz to a few MHz, initially with frequency modulation.

### 3.2.2 Simulations of 2nd stage cooling

With the method and parameters in Sec. 3.2.1 we can start by considering the behavior of the blue MOT. In experiments, common parameters for a blue MOT are  $10^8$  atoms,  $R = 1$  mm (standard deviation of density profile) and  $T = 5$  mK. Assuming a power of 7 mW in each horizontal beam, 4.9 mW in the vertical beams and a waist radius of 10 mm, we get a peak intensity of  $70 \text{ W/m}^2$  and  $I_{max}/I_{sat} = 0.173$  from a horizontal beam. We will also use a typical vertical gradient of 370 mT/m. The simulated evolution of blue MOT with these parameters is shown in Fig 3.8. First of all we see that the temperature decreases to about 1 mK. This temperature is primarily determined by the detuning in the model. At 15 MHz ( $\gamma/2$ ) the temperature reaches the Doppler cooling limit (726  $\mu\text{K}$ ), but at 40 MHz the forces on slow atoms are weaker. This value is chosen experimentally to capture a larger range of velocities the Zeeman-slowed beam. We also see that the cloud in the simulation compresses significantly.

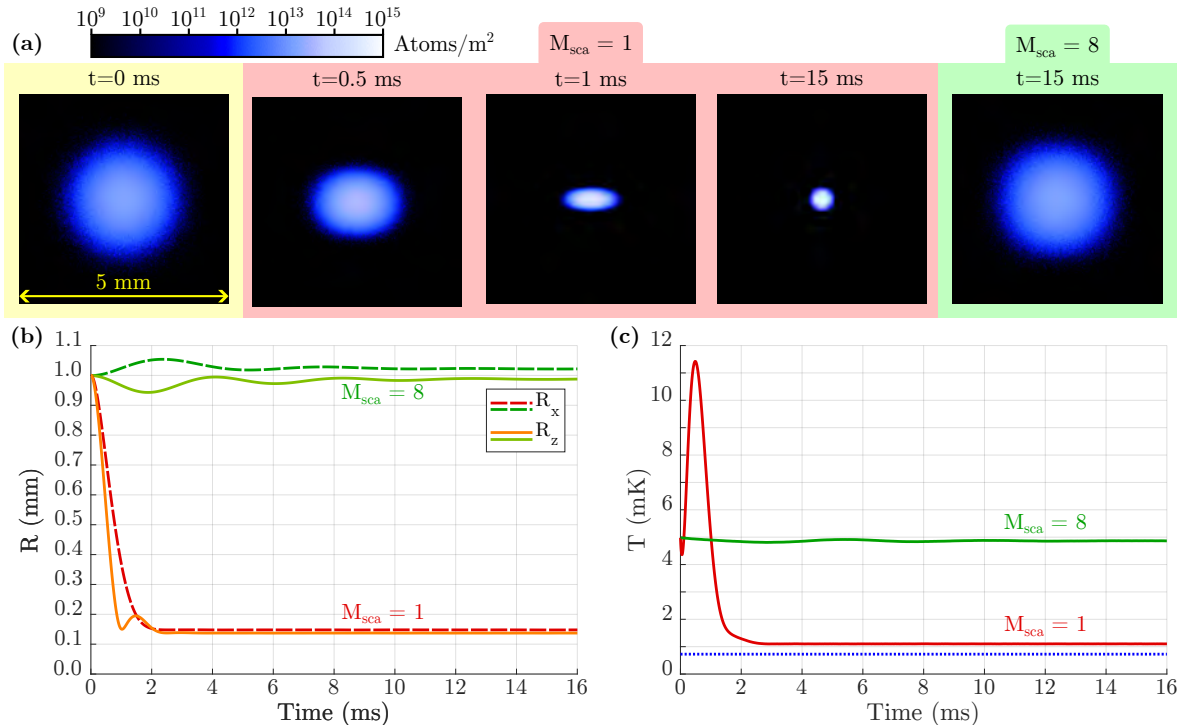


Figure 3.8: *Simulation of blue MOT, (a)* Time evolution of the cloud with  $I = 0.173I_{sat}$  and  $M_{sca} = 1$  random photon recoil per MOT beam interaction (red panel) vs  $I = 0.015I_{sat}$  and  $M_{sca} = 8$  (green panel), which replicates the experimental cloud parameters. *(b)* Evolution of the cloud radius along two dimensions for the two cases. *(c)* Time evolution of the temperature.

This discrepancy can largely be attributed to the fact that the atoms in the model can only scatter one photon from the MOT beams, while in experiments, photons from the MOT beams will be re-emitted by the atoms and be reabsorbed by other atoms, creating a repulsive force (see e.g. [125]) and heating them. To account for this we assume each absorption event is accompanied by  $M_{sca} = 8$  spontaneous emission events, which primarily affects the cloud temperature, but also increases the cloud radius. In reality this scattering will also have a density-dependence, and the absorbed photons will tend to kick atoms away from the center of the cloud, but we will neglect these effects. Shadow effects within the cloud, saturation effects from multiple beams as well as experimental imperfections such as imperfect polarizations, power imbalances etc. can also cause an additional expansion of the cloud in experiments. To account for these we simply assume a lower effective intensity of  $0.015 I_{sat}$ . With these assumptions the cloud temperature and radius obtained in simulations agree with experiments. Effects such as shadowing and saturation from multiple beams have been con-

sidered in more detail in e.g. [126, 127]. The temperature discrepancy between experiments and Doppler cooling theory for a  $^{88}\text{Sr}$  blue MOT has been investigated quantitatively in [128].

With these initial conditions we can investigate the dynamics when loading atoms into a red MOT. For the red MOT beams we assume 3 mW in the horizontal beams, 6 mm in vertical beams, and 5 mm waists, giving  $I_{max} = 120 \text{ W/m}^2$  and  $I_{max}/I_{sat} = 4020$  (horizontally). The target red MOT gradient is 31 mT/m vertically, and we will investigate the influence of the time it takes to shift from the blue to red MOT gradient. The model will use a logistic function with a characteristic timescale  $\tau$ :

$$B_{grad}(t) = B_{grad}^R + \frac{1}{2}(B_{grad}^B - B_{grad}^R) \left[ 1 + \tanh\left(-\frac{t - t_L}{\tau}\right) \right]. \quad (3.6)$$

Furthermore, the red MOT cooling will be divided into two phases to recreate typical experimental procedures and parameters. The first phase (broadband) lasts 70 ms, and here the laser detuning is varied sinusoidally between 0 and -3 MHz with a modulation frequency of 25 kHz. The second phase (single-frequency) lasts 50 ms. Here the laser detuning is fixed at -150 kHz, and we assume the intensity is reduced by a factor 10 and constant. The dynamics of the atoms are shown for  $\tau = 1 \text{ m/s}$  in Fig. 3.9. One dilemma is when to turn off the blue laser light while ramping the B-field. In the example shown here it was done halfway through the ramp ( $t = t_L$  in Eq. 3.6). The blue light will cause the atom cloud to start expanding as the B-field is ramped down, but we see it was not very significant in this case, due to the short ramping time.

Switching to the broadband red MOT phase, the atom cloud initially expands quickly, as the red MOT forces are orders of magnitude lower than the blue MOT forces. With a scan range of 3 MHz, the red MOT detuning can in principle address most of the atoms in the 5 mK cloud (the comparable Doppler broadening is 2.3 MHz). However the magnetic field gradient similarly imposes a spatial region that the red MOT beams can address. This region has the shape of an oblate spheroid, with a radius that scales with the gradient and scan range. This is another reason why ramping the B-field quickly is critical - otherwise the lasers can only trap the atoms within a tiny volume at the center of the blue MOT. In Fig. 3.9(a) we can see a "fingerprint" of the oblate region from about 5-20 ms. The atoms that were outside this region tend to simply escape, but within the region, they tend to become trapped.

From  $t = 10$ -70 ms the remaining atoms start to cool and accumulate within the red MOT. The timescale of this is determined by the MOT beam intensities and scan range. A higher intensity enables quicker trapping, but a broader scan range slows the trapping dynamics as the laser power is distributed over a larger region in position and velocity space. The final broadband red MOT has the shape of a droplet and sags because the red MOT forces are of the same order of magnitude as gravity. A larger scan range also increases the final size and temperature of the broadband MOT - in this case 20  $\mu\text{K}$  within the high-density region according to the simulation.

At  $t = 70$  ms the single-frequency cooling phase begins. With a detuning of 150 kHz, the region in position and velocity space that can be addressed becomes much smaller, however forces on atoms in this region will generally be larger, even with the factor 10 reduction in intensity. As a result the atoms start to accumulate within in a tiny region, and we especially see the high-density region starting to change. Some atoms that were outside the velocity capture range get accelerated away by the single-frequency MOT beams and form small jets of escaping atoms at  $t = 80$ -90 ms - such losses can be avoided by using a more gradual reduction of the scan range. Many of the low-density parts of the broadband MOT are similarly outside the spatial capture range and start falling due to gravity - however they can then reach velocities that bring them back into resonance with the upwards-propagating laser beam, preventing them from falling freely.

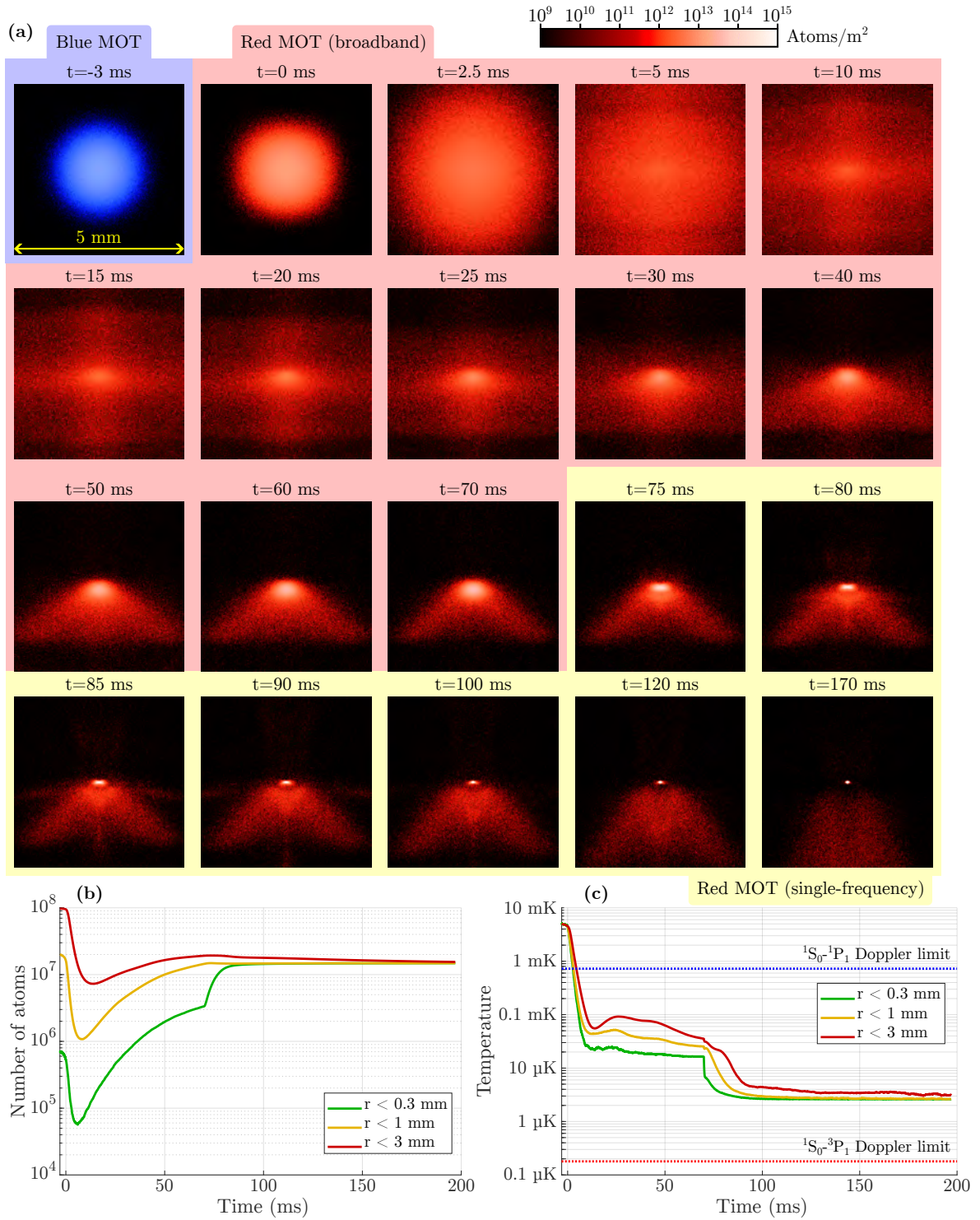


Figure 3.9: Simulation of red MOT, (a) Time evolution of the cloud spatially for the parameters given in text and  $\tau = 1$  ms. (b) Evolution of the atom number within a given spherical radius from the magnetic field center. (c) Time evolution of the temperature within the radii.

The result product of the MOT stages is a 3  $\mu\text{K}$  cloud with radius on the order of just 50  $\mu\text{m}$  containing 15% of the original  $10^8$  atoms. About 80% of the original atoms were lost in the transition from the blue MOT to the broadband MOT, while the transition to single-frequency MOT was much more efficient.

We can compare this example to what happens for a slower switching time of  $\tau = 10$  ms (see Fig. 3.10). In this example we again switch from blue to red MOT light at  $t = t_L = 0$ . Since the magnetic field already changes on the ms timescale before  $t_L$ , the blue MOT expands somewhat even before  $t = 0$ , compared to the case for  $\tau = 1$  ms. This presents a new range of optimization parameters - the optimal time to switch off the blue lasers relative to the gradual change in B-field, and possibly power and detuning ramping, to minimize the atom loss.

After  $t = 0$  the slower change in gradient significantly reduces the spatial region from which the red MOT beams can initially trap the atoms. This region expands as the B-field gradient approaches the target value, but the loss during the transfer from blue to red MOT increases significantly. In Fig. 3.10(b) the evolution of the atom numbers are compared for the two switching times. Here we see that the transfer efficiency from blue to broadband red MOT is decreased from 20% to 8%.

The schemes shown here for dividing the red MOT trapping process into two stages, with sine modulation of the laser frequency and the particular scan ranges, are just a few out of many options. Other groups have achieved good trapping efficiencies by using a SWAP (sawtooth-wave adiabatic passage) technique [129, C. 10] [130, 131, 132]. The main ingredient is an upwards sawtooth function when scanning the laser frequency. This implies that in the dressed state picture, the ground state  ${}^1S_0$  is initially equivalent to one of the dressed states, but this dressed state gradually transforms into  ${}^3P_1$  as the laser frequency sweeps above the atom resonance. These dressed states are the eigenstates of the Hamiltonian including the laser interaction, so the atoms follow them from  ${}^1S_0$  to  ${}^3P_1$  for modulation frequencies that are not too high. However such coherent effects require a quantum treatment of the atomic state as in Chap. 2 and are out of the scope of the model presented here.

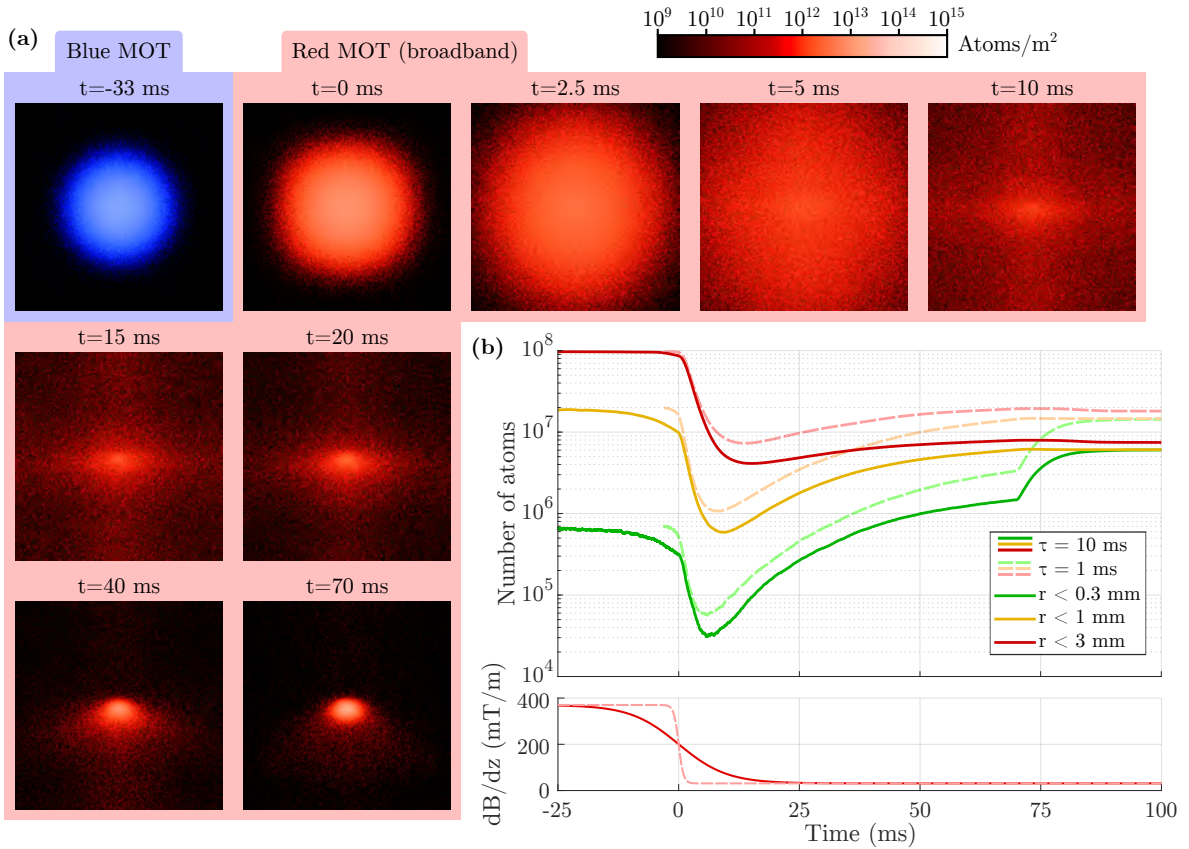


Figure 3.10: *Simulation of red MOT,* (a) *Time evolution of the cloud spatially for the same parameters as in Fig. 3.9, but  $\tau = 10$  ms.* (b) *Evolution of the atom number within a given spherical radius from the magnetic field center, compared to the  $\tau = 1$  ms case (light dashed curves).* (c) *Comparison of the magnetic field gradient along the z axis for  $\tau = 1$  ms (light dashed) and 10 ms (dark line)*

### 3.3 Implementation of second stage MOT cooling

As discussed in Sec. 3.2.2, ramping the magnetic field within a few ms is crucial. A system of electronics was developed for this purpose. This was integrated with a computer control system developed for controlling TTL signals to the AOMs. In addition a new set of MOT coils were also made which were capable of ramping on the ms timescale. These developments are presented in this section.

#### 3.3.1 Electronics for controlling the coil currents

An overview of the circuit for controlling the current in one MOT coil is shown in Fig. 3.11. The MOSFET part of the circuit (marked in yellow) was heavily inspired by [129, p. 38] - we similarly use APTM50UM09FAG MOSFETs, UFL230FA60 diodes, and a TAP800K1R0 resistor ( $1\ \Omega$ ). We added another  $10\ \Omega$  resistor in series, which allowed us to reduce the coil switching time further. Varistors were added in parallel with the MOSFET to protect it from voltage spikes which can occur when switching too fast. Significant power is dissipated in the MOSFETs when ramping, so they can heat up significantly. Therefore these parts are mounted onto aluminium plates with copper water-cooling parts mounted onto them, to keep the temperature acceptable.

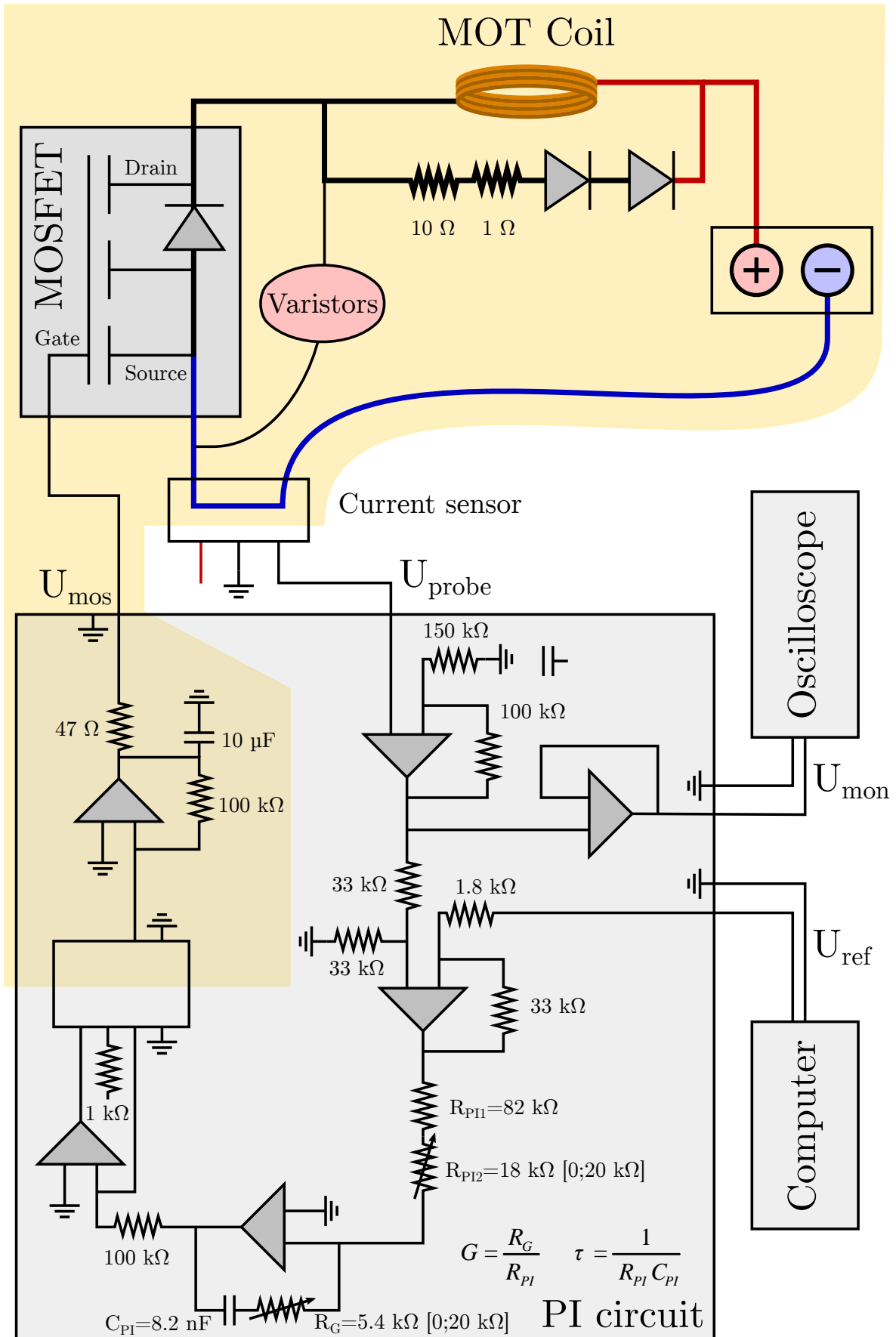


Figure 3.11: Circuit for controlling the current in one of the MOT coils. In the PI circuit several additional capacitors are placed between nodes and ground, which are not shown here.  $G$  and  $\tau$  indicate the gain and angular corner frequency of the PI circuit, respectively.

The PI-circuit in Fig. 3.11 was made to control the gate-source voltage  $U_{MOS}$  of the MOSFET, which determines how much current it allows to run from source to drain and thus through the coil. One PI circuit was built for each coil, and there is similarly one MOSFET circuit and a separate power supply for each coil. A Hall probe (ACS758LCB-100B-PFF-T) is connected in series with each coil, giving a signal  $U_{probe}$  which is proportional to the coil current. This is then compared to an analog control signal  $U_{ref}$  which is output from a computer, where it can be customized. The resulting signal from the comparison goes through the main PI part of the circuit, where the gain and corner frequency can be adjusted using the variable resistors. "PI" refers to the fact that it gives proportional and integral (over time) responses to the deviation in the current from the desired value according to  $U_{ref}$ . For more details about PI circuits, see e.g. [133, Chap. 7-8], in particular Sec. 7.12.1.1. Finally, the output from this stage goes through an optocoupler before being sent to the MOSFET, in order to electrically isolate the coils and their ground from the rest of the circuit. The rest of the circuit shares ground with the computer, laser diode current sources and many other parts of the setup where voltage spikes (which could occur while ramping) could cause damage. Thus it is very important that no connection is made between the "MOT coil power group" (marked yellow in Fig. 3.11) and the rest of the experiment.

The realization of these circuits in the lab is shown in Fig. 3.12. Due to the small resistance of the coils, any poor connection in the rest of the circuit with a significant resistance will reduce the available voltage drop over the coils and dissipate a significant amount of power. In the worst case, with soldering connections, the solderings can melt and possibly cause fires. Therefore the coil circuits use clamped connections.

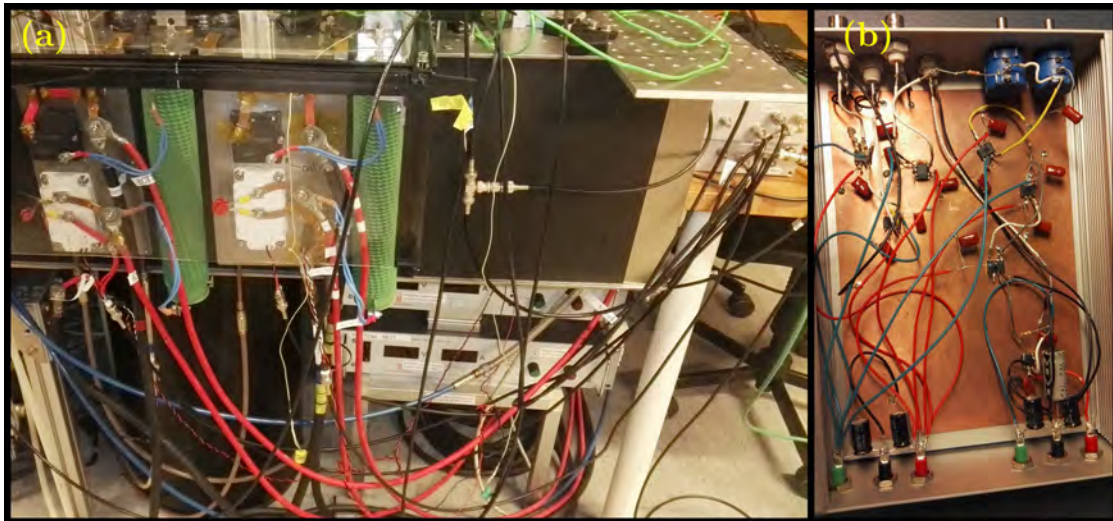


Figure 3.12: (a) Photo of the two circuits for switching the MOT coils (left), power supplies (below table) and PI circuit boxes (right, on table). (b) The inside of one PI box.

A calibration of the coil current one obtains for a given reference voltage is shown in Fig. 3.13. The slight difference between the coils is attributed to slightly different resistances in the connections to the current sensors in each circuit, which affects how much they heat up for a given current, altering their characteristics.

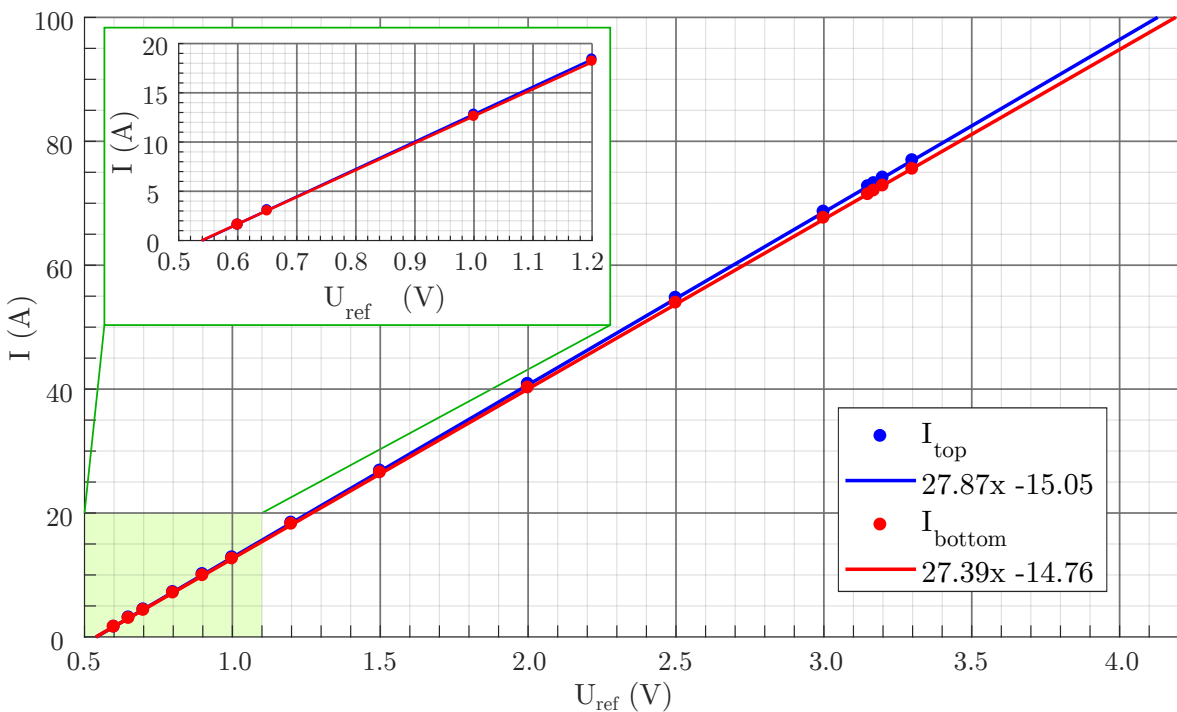


Figure 3.13: *MOT coil current dependencies on the analog reference signals.*

### 3.3.2 System for controlling the experimental sequence and imaging

The reference voltage function for the MOT coil control circuits is controlled via a GUI. This was developed to be part of the QWeather system for controlling many parts of the setups in the lab. The QWeather system is written in Python and consists of server and clients scripts and a broker which facilitates communication between them. A few scripts have been developed specifically for controlling the experimental cycle of the strontium cloud experiment.

The NI6259 script starts the StrontiumBrain server which is responsible for communicating with a NI6259 card, using the PyDAQmx library. This card is connected to a BNC2110 interface, such that BNC connections can be made to a number of digital and analog input and output channels. The digital output channels are used for the TTL signals to control e.g. switching AOMs during the experimental cycle, and the analog output channels are used for the MOT coil reference voltages  $U_{\text{ref}}$ .

The StrontiumBrainGUI client is the primary GUI for controlling the experimental cycle. For digital output channels the on/off switch times of the signals can be set. It also includes a section for adjusting the analog output signals. There are simple options such a square, triangle and a constant level, the option to load a custom waveform from a file, and finally the MOT control signal waveform which was made for the experiment. This waveform is characterized by the parameters illustrated in Fig. 3.14. It was chosen based on testing, where a logistic function for ramping the coil current (characterized by tauSafetyRed) proved to be most suitable for quickly ramping the current. Alternatives such as a simple exponential function with an initial kink tended to require more gentle parameters, resulting in slower ramping.

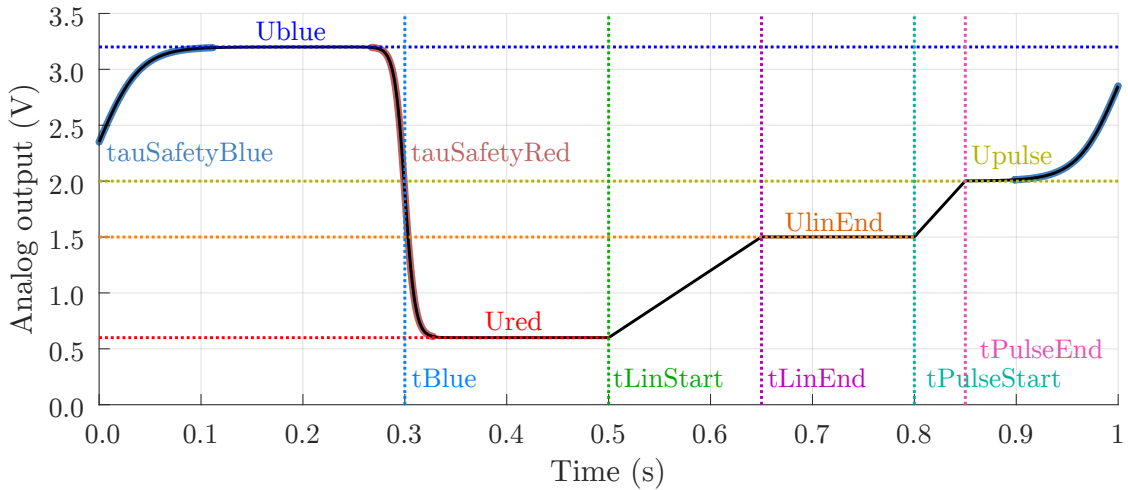


Figure 3.14: Variables determining the shape of the analog reference signal for controlling the MOT coil currents. The variable values are chosen for illustrative purposes.

Four of the parameters are voltage levels.  $U_{blue}$  is used for the initial blue MOT current levels to get a high field gradient, and  $U_{red}$  for the red MOT gradient.  $U_{linEnd}$  can be set to make a linear ramp to a higher gradient level that can be used to compress the red MOT. Finally  $U_{pulse}$  can be used to control the Zeeman splitting during pumping and lasing, by quickly shifting the current levels of the coils (e.g. in opposite directions). The  $\tau_{SafetyBlue}$  and  $\tau_{SafetyRed}$  variables represent the characteristic timescale  $\tau$  of the ramping functions, as in Eq. 3.6. Making very fast changes, such as an instant ramp between two significantly different current levels, can result in voltage spikes and risk of avalanche within the MOSFET, which can cause it to degrade over time. This is most relevant for  $\tau_{SafetyRed}$ , which is often pushed to near its limit and can be set to about 2 ms when ramping from e.g. 72 A to 6 A. When pushing into a new regime, such as ramping from a higher blue MOT current level, or lowering  $\tau_{SafetyRed}$ , the current sensor signals from the coils should be monitored while changing the parameters in small steps. Noise appearing in the signal during the steepest part of the ramp is usually a first sign that the parameters may be too rough. Safety is also very important to consider while making changes to ramping and the circuits. Energy dissipated in the wrong components can heat them up, cause failures and in the worst case fires, and voltage spikes that are not contained can cause damage to equipment or injury.

After defining analog channel parameters and switching times of digital channels, the cycle pattern is "armed" by the arm button in the GUI, which prepares the cycle within the NI6259 card. If any parameters are changed, the cycle must be armed again to update it in the card. After arming, the pattern can then be started and stopped.

While the StrontiumBrainGUI can in principle be run by itself, it is also imported into a tab in the CameraGUI script. This is more typically used for experimental sessions because it also has GUI elements for imaging the atom cloud and showing the atom number over time, which are useful for optimization. The CameraGUI communicates with a Blackfly camera (BFS-U3-31S4M-C) via another server script, "BlackFlyCameraServer". The CameraGUI is shown in Fig. 3.15, with the StrontiumBrainGUI embedded in the lower part.

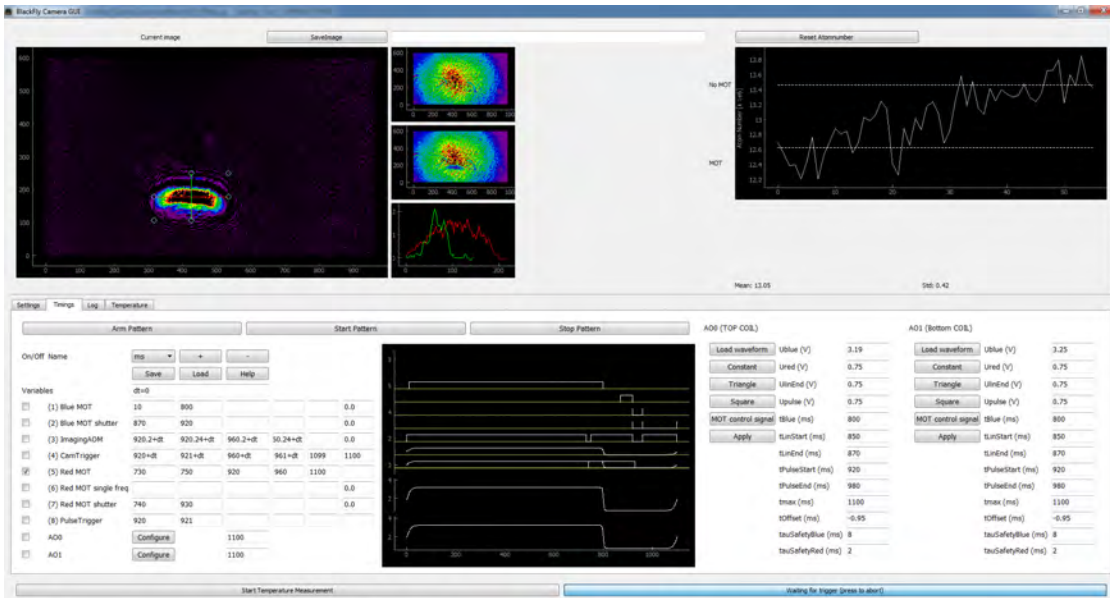


Figure 3.15: The CameraGUI which is used for monitoring the atom cloud and atom number, and controlling analog and digital signals defining an experimental cycle. The Strontium-BrainGUI is loaded within the Timings tab in the bottom, where parameters for an experimental cycle can be controlled.

Imaging is done using the absorption imaging technique. The main tool in this technique is an AOM-regulated laser beam resonant with the  $^1S_0$ - $^3P_1$  transition. This beam, when switched on, has a path that intersects the atom cloud before reaching a the Blackfly camera (indicated in Fig. 3.2). The CameraGUI enables choosing a cycle with suitable switching times for the imaging AOM while gathering images from the camera. Constructing the atom column density distribution from the absorption imaging technique relies on Beer's law for the exponential attenuation of light (the laser beam) as it propagates through a medium (the cloud),  $I = I_0 e^{-OD}$  [134, p. 348]. The optical density is related to the column density  $n$  according to  $OD = \sigma n$  [135, p. 3], where the absorption cross section is:

$$\sigma = \frac{\sigma_0}{1 + 4(\delta/\gamma)^2 + I_0/I_{sat}}, \quad (3.7)$$

and  $\sigma_0 = \hbar\omega\gamma/2I_{sat} = 3\lambda^2/2\pi$ , which is a good approximation for  $\sigma$  when the imaging beam is on resonance and the intensity is low compared to the saturation intensity. The optical density can be determined using the following equation [134, p. 353]:

$$OD_{meas} = \ln \left( \frac{I_{light} - I_{dark}}{I_{atoms} - I_{dark}} \right). \quad (3.8)$$

Here the quantity  $OD_{meas}$  offers an approximate value of the optical density  $OD$ , without taking into account optical density saturation as done in [134, p. 353]. We see that  $OD_{meas}$  depends on three different intensities (images):  $I_{atom}$  is the intensity distribution obtained after the imaging beam has been attenuated by the atom cloud.  $I_{light}$  is the intensity distribution from the imaging beam, but with no atom cloud, used for normalization. Finally,  $I_{dark}$  is the background to be subtracted; the intensity distribution with no laser beam and no cloud. These calculations are performed within the CameraGUI script based on images taken at different times during each cycle. By integrating the column densities obtained from the images, the estimated number of atoms in the MOT can also be monitored. Finally, the temperature of a MOT can be determined via the time of flight method. Over time the radius of an atom cloud along a given axis will expand depending on its temperature (along the axis) according to [135, p. 5]:

$$r(t) = \sqrt{r_0^2 + \frac{k_B T}{m} t^2}. \quad (3.9)$$

By gathering absorption images from experimental cycles with a delay  $t$  introduced between turning off the MOT lasers and imaging the atom cloud,  $r(t)$  can be assigned to the standard deviation of Gaussian fits to the absorption images. Eq. 3.9 can then be fitted to the values of  $\{t, r(t)\}$  to determine the temperature (the fit parameter  $T$ ).

### 3.3.3 Performance and challenges of original MOT coils

Here we will consider the challenges with the original MOT coils in the setup and motivation for replacing them. The original MOT coils consisted of solid wires and separate water tubes for cooling (see Fig. 3.16), and contain full copper rings along the top and bottom. When switching the current to another level, these rings act as large wire loops and a current starts to flow in them that counteracts the change in magnetic field. Since they are located almost on top of the wires, they also have a good inductive coupling  $M$ . We can model this as two circuits coupled by mutual inductance as shown in Fig. 3.17.

The mutual inductance results in an emf in each circuit,  $\mathcal{E}_{coil} = -M\dot{I}_H$  and  $\mathcal{E}_H = -M\dot{I}_{coil}$ . Kirchoff's loop rule [136, p. 855] gives:

$$\begin{aligned} 0 &= U_{coil} + \mathcal{E}_{coil} + U_R + U_L = U_{coil} - M\dot{I}_H - R_{coil}I_{coil} - L_{coil}\dot{I}_{coil} \\ 0 &= \mathcal{E}_H + U_{RE} + U_{LH} = -M\dot{I}_{coil} - R_H I_H - L_H \dot{I}_H. \end{aligned} \quad (3.10)$$

From Eqs. 3.10 we get these coupled equations for the currents in the coil and holder:

$$\dot{I}_{coil} = \frac{U_{coil} - R_{coil}I_{coil} - M\dot{I}_H}{L_{coil}}, \quad I_H = -\frac{M\dot{I}_{coil} + R_H I_H}{L_H}. \quad (3.11)$$

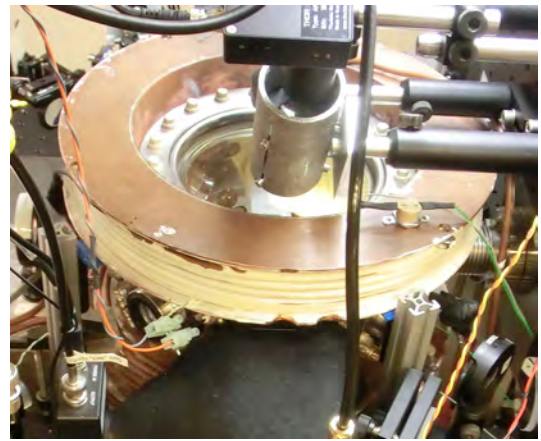


Figure 3.16: Original MOT coils in the atom cloud machine. Wire loops are hidden by separate cooling pipes with thermal paste (white) and copper plates forming separate closed loops.

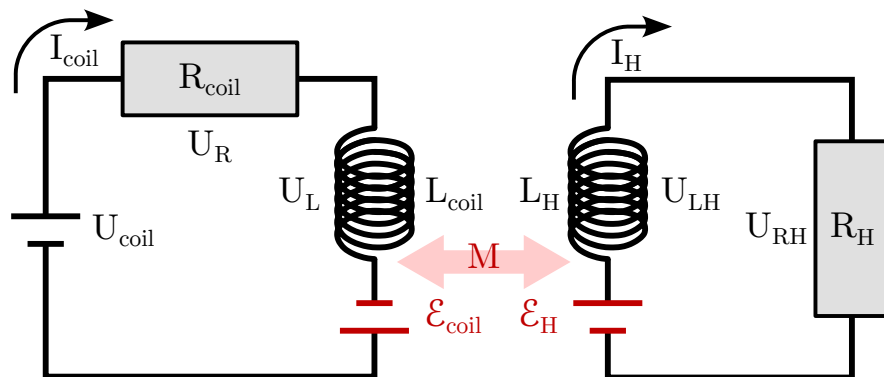


Figure 3.17: Model circuit of one of the original MOT coil in the atom cloud machine. The coil itself (left) has a resistance within the wire,  $R_{coil}$  and inductance  $L_{coil}$ , and the voltage over the coil  $U_{coil}$  can be controlled to regulate the current  $I_{coil}$ . This circuit is inductively coupled to a copper holder with its own resistance and inductance. Any change in current within one of the circuit induces a current in the other.

We see that for  $M = 0$  and  $U_{coil} = 0$ , the current decays on the timescale  $\tau_{coil}^0 = L_{coil}/R_{coil}$  within the coil, and a current within the holder would decay with  $\tau_H^0 = L_H/R_H$ . Using a Laplace transform [137, p. 243], the decay time of the coil current when the circuits are coupled can be determined as  $\tau_{coil} = \tau_{coil}^0 + \tau_H^0$  for constant  $U_{coil}$ . However since the coupling is not perfect ( $M < \sqrt{L_{coil} \cdot L_H}$ ), one idea was to overshoot the down ramp in coil current, possibly even reversing it - this has been demonstrated as an effective way to lower the switching time in presence of eddy currents in [138]. By overshooting, the new current level in combination with the induced current in the holders could yield the desired magnetic field when added together. This behavior was simulated in Matlab (see Fig. 3.18). Here we assume  $M = 0.999\sqrt{L_{coil} \cdot L_H}$  and use the estimates  $L_{coil} = 1 \text{ mH}$ ,  $L_H = 0.5 \mu\text{H}$ ,  $R_{coil} = 250 \text{ m}\Omega$  and  $R_H = 23.9 \mu\Omega$ . Especially the mutual inductance is uncertain and the simulations should primarily be considered as qualitative examples of the behavior and potential solution options.

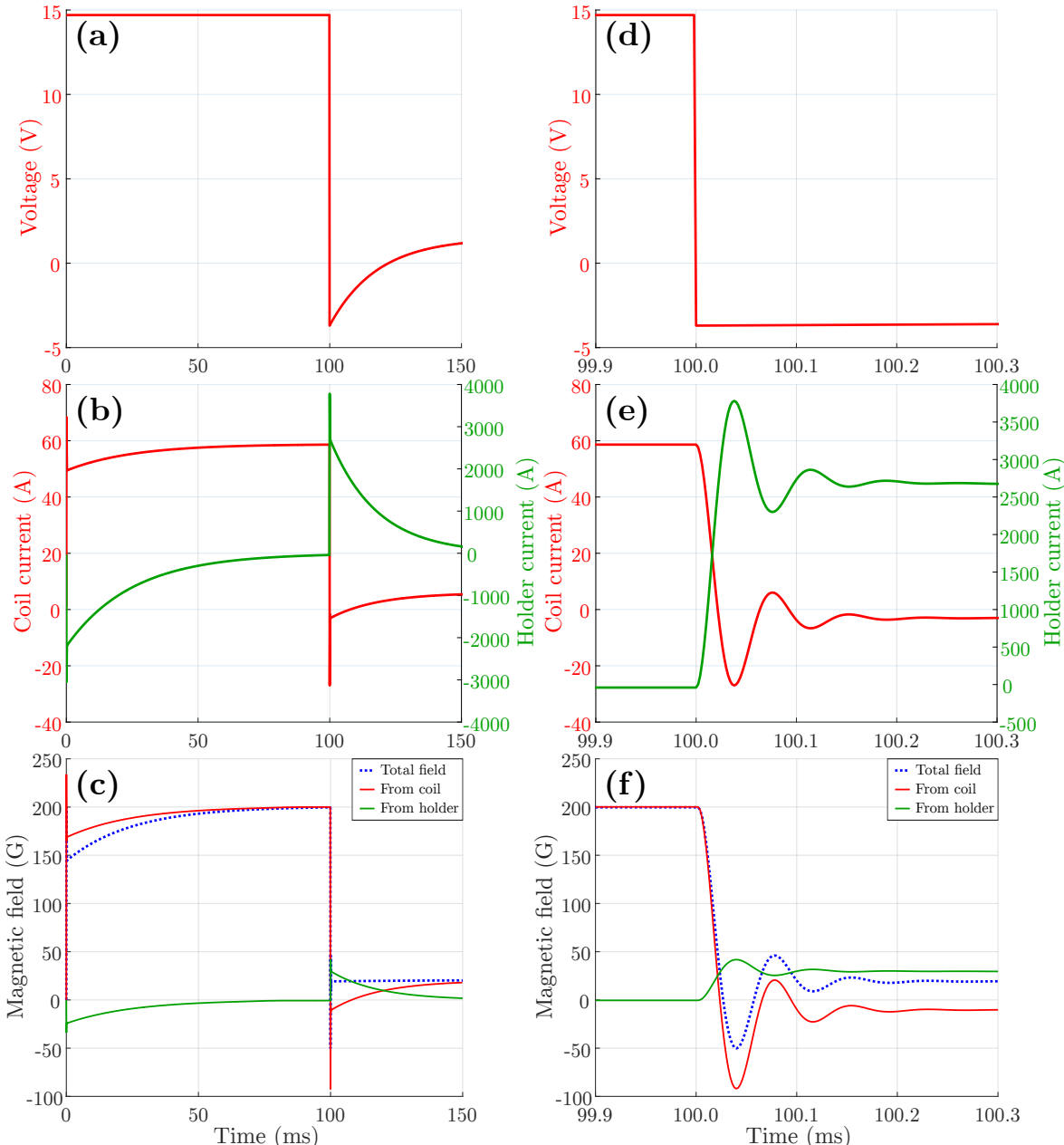


Figure 3.18: Simulation of the behavior of one of our original coils if the voltage is reversed when we desire to go to a lower magnetic field value at  $t = 100 \mu\text{s}$ . By overshooting the naive target value when ignoring the copper holder, an even larger current is induced in the copper holder, but due to the finite inductive coupling, the total magnetic field at the center of the coil reaches the desired value after  $200 \mu\text{s}$ .

At  $t = 0$  the voltage across the coil is abruptly switched to 14.7 V, but due to interaction with the copper holder, the magnetic field gradually builds up to the target value over the course of 100 ms. A similar behavior could be expected when abruptly switching the voltage to a lower value targeting the desired current level in the coil for operating the red MOT, assumed 1.5 V in this simulation. But instead we overshoot this value by 5.2 V (thus reversing the voltage to -3.7 V) and then ramp exponentially towards the desired level of 1.5 V. The timescale of the ramp is set to 18 ms and is chosen based on the timescale of energy dissipation due to the resistance of the copper holder. The resulting behavior in the simulation is that the current in the coil and holder interact with each other, resulting in damped oscillations in the total magnetic field on a timescale of 100  $\mu$ s. This timescale is related to the mutual inductance - if  $M$  were simply  $1 \cdot \sqrt{R_{coil} \cdot R_H}$ , the oscillations would continue forever, while if it were 0 there would be no current induced in the holder from switching the coil. After just 200  $\mu$ s the magnetic field settles at the target value for the red MOT in this example (an arbitrary value can be chosen by simply changing the overshooting value), and the remaining current in the copper holder after the interaction now decays exponentially due to the resistance. By matching this exponential decay in the voltage across the coil, going from -3.7 V to the naive target value of 1.5 V, the magnetic field is kept constant as the contribution from the coil gradually replaces the contribution from the holder.

A drawback of this method is the need to reverse the voltage (if the mutual inductance is high), which complicates the electronics, as well as the need to spend time optimizing extra parameters to counteract the copper holder. This could become a complex procedure if we would desire to not just switch the magnetic field gradient between two values, but also ramp it over time to optimise the cooling stages further. However making new coils and opening vacuum to replace the old ones is also a lengthy procedure so we investigated the behavior of our original coils while overcompensating without reversing the voltage.

The optimized reference signal for the original coils was based on a hyperbolic tangent with a soft overshooting part. The behavior of the top coil during a test is shown in Fig. 3.19. Here the reference signal causes the current to approach 0, where it stays clamped for 25 ms while the measured B-field is decaying, presumably due to induced currents in the holders. A hyperbolic tangent fit yields a timescale of 10 ms for the B-field, which can significantly reduce the transfer efficiency to a red MOT, as we saw in Fig. 3.10. So to obtain a good transfer efficiency we would need to upgrade the coil switching circuit to reverse the current, adding more optimization parameters, complexity and potential issues, or replace the MOT coils, which we chose as the solution.

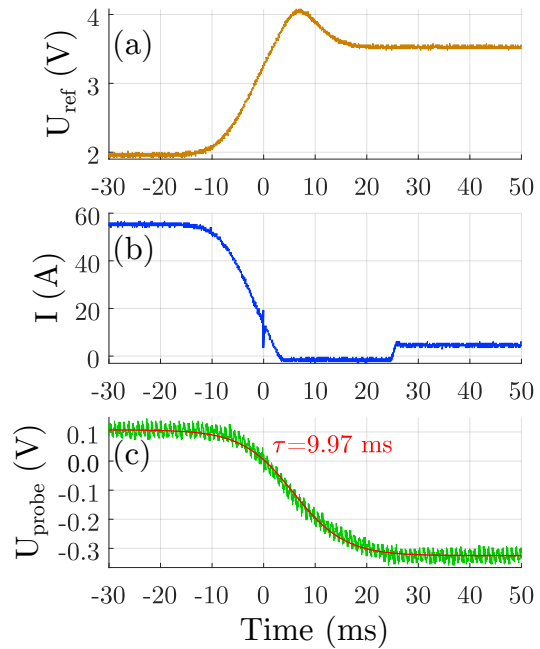


Figure 3.19: A test of switching the current in our original top coil from 56 A to 5 A using the control signal in panel (a) (here the coil PI circuit was different, resulting in a different current scaling than in Fig. 3.14). The current in panel (b) cannot be reversed and clamps at 0 A for a while. The measured B-field above the coil is shown in panel (c) with a characteristic decay time of 10 ms.



Figure 3.20: Hollow wire MOT coils. (a) Winding the top coil on a lathe. (b) The completed bottom coil before mounting. (c) One of the electrical connections for the coil. (d) Mounting the vacuum chamber after installing the bottom coil. (e) Coil testing setup. (f) The setup after installing the new MOT coils.

### 3.3.4 Hollow wire MOT coils

Inspired by the setup in [129, p. 36] we designed new MOT coils based on hollow copper wire. We used cylindrical wire with inner and outer diameters of 3 and 5 mm respectively. Each coil consists of three sections that are water-cooled in parallel but electrically connected in series, with each section having three layers and approximately nine windings per layer, yielding a total of about 81 windings for each coil. Kapton tape was added as insulation to the bare copper wire as we wound the coil, and several layers were also added all around the final coil to protect it and hold it together. We considered enameled wire as an alternative insulation, but kapton tape seemed more scratch-resistant, and we wanted to minimise the risk of short-circuits appearing in the new coils. The coils are shown in Fig. 3.20, and prior to mounting them we tested their resistance. These are shown in Table 3.2 in thermal equilibrium at the given temperatures.

Segment	$R_{top}$ (mΩ)	$R_{bottom}$ (mΩ)
Inner	30.9	32.5
Middle	37.6	35.3
Outer	40.5	36.7
All	109.0	104.6

Table 3.2: Resistances of the hollow wire MOT coils according to four terminal measurements. The top coil temperature was 20.6 °C during the measurements, and the bottom coil was 22.6 °C.

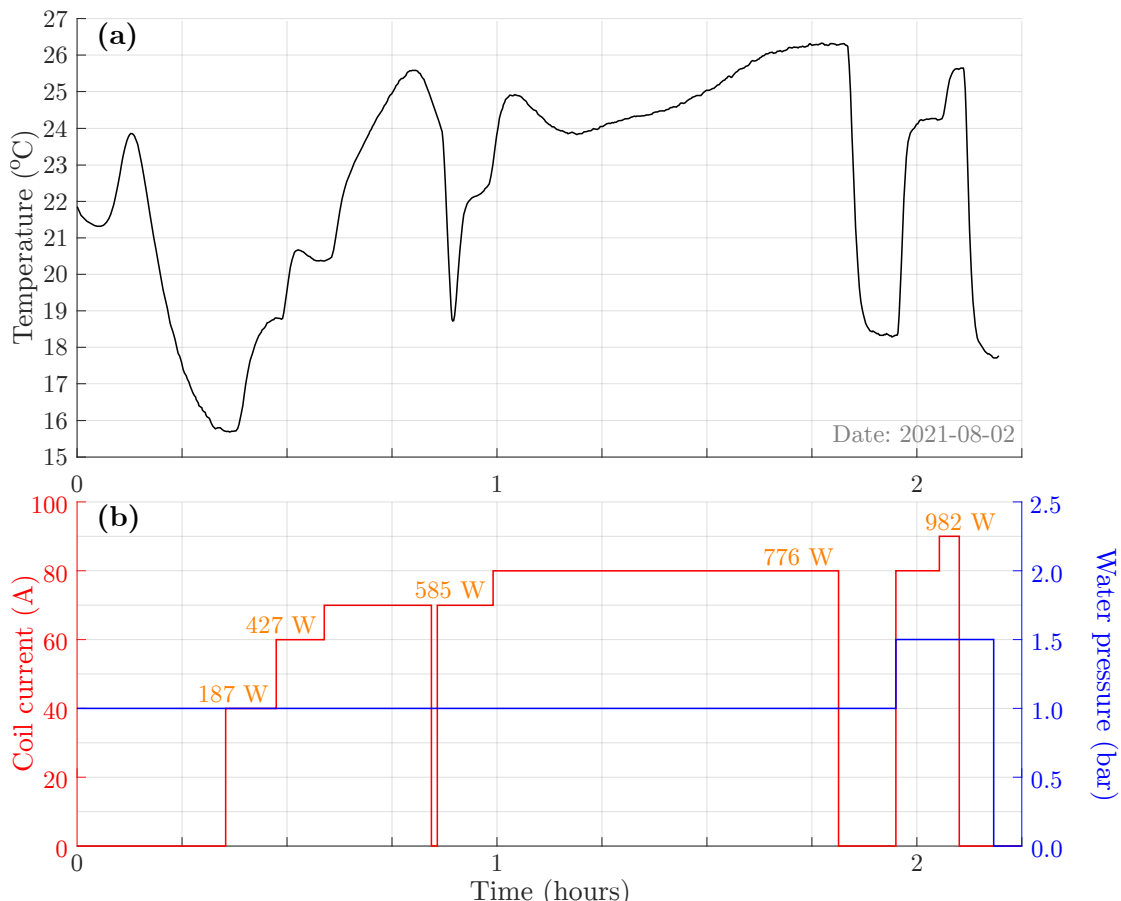


Figure 3.21: Temperature test of the top coil before mounting it onto the chamber. (a) Temperature from thermistor mounted on the coil during the test, near the water exit of the outermost wire loop. (b) Coil current and water pressure during the test. The total dissipated power (including wires and connections) is also indicated.

We also tested how the coil temperature responded to different coil currents and water pressures, shown in Fig. 3.21. The test demonstrated that 1.5 bar is enough to cool the coil efficiently for up to about 90 A. In addition it is also important to make sure all connections are clamped with a good contact surface. At 80 A, the contacts to the power supply rose to 50 °C, and 65 °C for 90 A. After using some sandpaper on the wire contact surface, we achieved 35 °C at 75 A.

Finally, we tested the ramping behavior of the coils. When the coils are mounted on the vacuum chamber, they can induce eddy currents within the chamber, similarly to the copper disk on the original MOT coils (but much less pronounced). They will also interact when they are ramped simultaneously. Therefore some differences in behavior are expected when they are tested individually or together while mounted on the setup. An example of the behavior under optimized conditions in the setup is shown in Fig. 3.22. Here both the coils are switching simultaneously, from approximately 74 A to 6 A, yielding a characteristic time of 3.37 ms for the magnetic field.

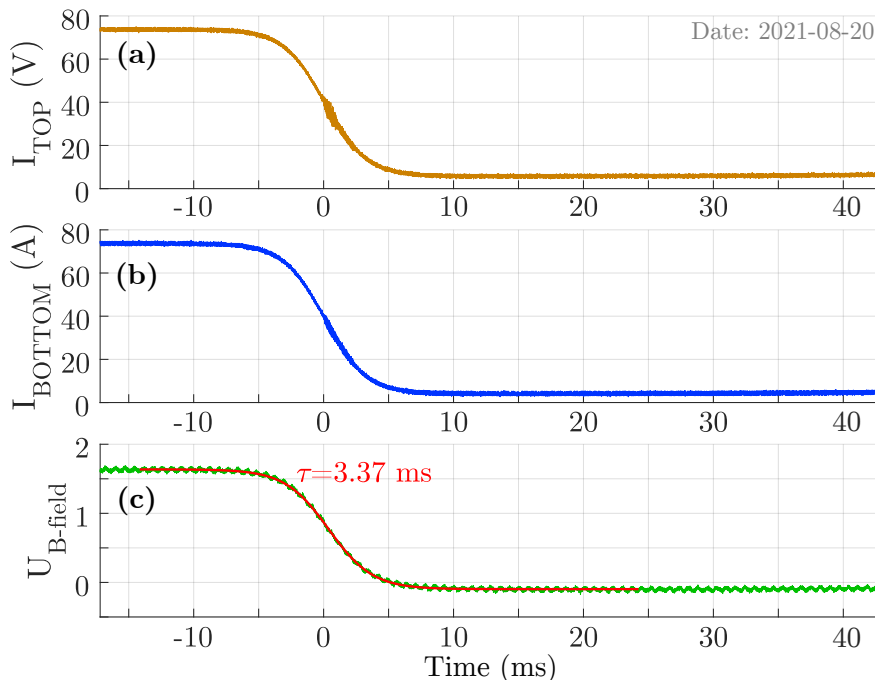


Figure 3.22: *Switching the hollow wire MOT coils mounted on the chamber, here with a total resistance of 11 Ω in the MOSFET circuit. (a) The reference signal for controlling the bottom coil current. A similar one is used for the top coil. (b) The current measured by a Hall probe in series with the bottom coil. (c) The signal of a Hall probe close to the top coil, showing the behavior of the magnetic field near the chamber while ramping.*

### 3.3.5 Compensation coils

We added compensation coils along both the horizontal axes to gain additional degrees of freedom for optimizing the MOT (a vertical bias can already be created by separately changing the MOT coil currents). This is especially important for the red MOT which is very sensitive to offsets in the magnetic field, which could cause it to be trapped with an offset relative to the cavity.

The compensation coils were made simply by winding lacquered copper wire around the existing coils until we got around 20 turns (for the coils along the atomic beam axis: 20 turns with  $222\text{ m}\Omega$  resistance near the Zeeman laser beam entry and 18 with  $202\text{ m}\Omega$  near the Zeeman coil). Running these in the Helmholtz configuration can offset the magnetic field zero point about 18 mm in either direction with 5 A (assuming a central gradient of 15.5 mT/m with 6 A in the MOT coils). The field is illustrated in Fig. 3.23 in relation to the horizontal gradient of the MOT coils near the center.

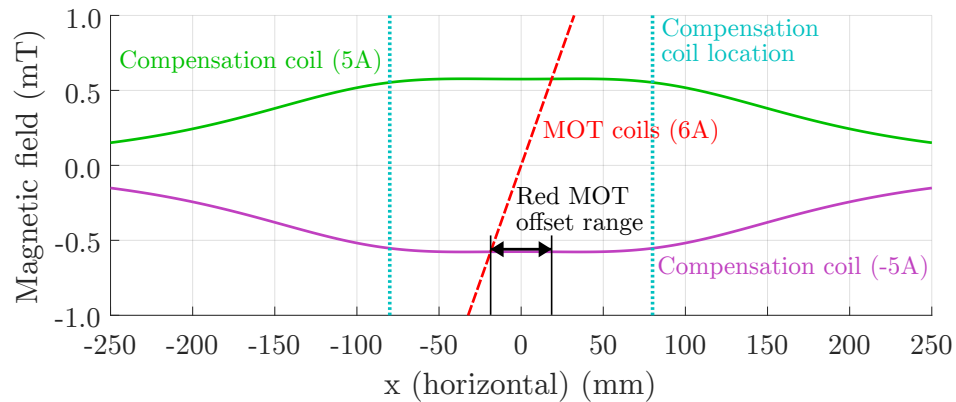


Figure 3.23: The magnetic field from MOT coils at 6 A (red, dashed) along a horizontal axis, compared to the magnetic field from a pair of compensation coils at  $\pm 5$  A. The combined zero-point can be shifted within  $\pm 18$  mm depending on the compensation coil currents.

## 3.4 Experimental routines

Here we will describe the steps towards trapping and optimizing the blue and red MOT clouds for realizing superradiant laser pulses, given the setup and improvements described earlier in this chapter. To obtain pulses, the atom cloud must have a sufficiently high atom number and density, a low temperature, and a good overlap with the mode of the science cavity.

### 3.4.1 Optimizing the science cavity incoupling

Aligning the input beam for the science cavity is necessary for locking the cavity during superradiant pulses (such that  $\omega_c$  in Chapter 2 is a known parameter), and also makes it possible to excite atoms within the cavity using a resonant input beam, which can help during alignment of MOT beams. The finesse of 1260 makes it non-trivial, but not too hard, to couple light into the cavity. Mode-matching is simple as the radius of curvature of the cavity mirrors is 9 m, and the output beam divergence is small, keeping a waist radius near 450  $\mu\text{m}$  for tens of cm. To couple into the cavity, a basic tool is the photodiode signal of the light reflected by the cavity, which is also required for the PDH lock. An additional tool which can be useful is a beam-profiler camera monitoring the profile of the cavity transmission. While aligning the beam into the cavity one can then look for dips in the cavity reflection signal, or look for high order Gaussian modes appearing in the transmission (as in Fig. 3.24), while scanning the cavity piezo voltage across any resonances. With a high amount of input power (limited by the fiber EOM tolerance to the  $\mu\text{W}$  magnitude) spotting high order Gaussian modes in the beam profiler is relatively easy with a bit of alignment and piezo voltage adjustments. Then the symmetry of the high order Gaussian modes can be used to reduce the number of "blobs" along each dimension by walking the input mirrors, while regularly checking different scan ranges until the TEM00 mode is found. Finally, the scan range can be adjusted to correlate the TEM00 mode on the beam profiler with the corresponding reflection dip, which is often easier to optimize.

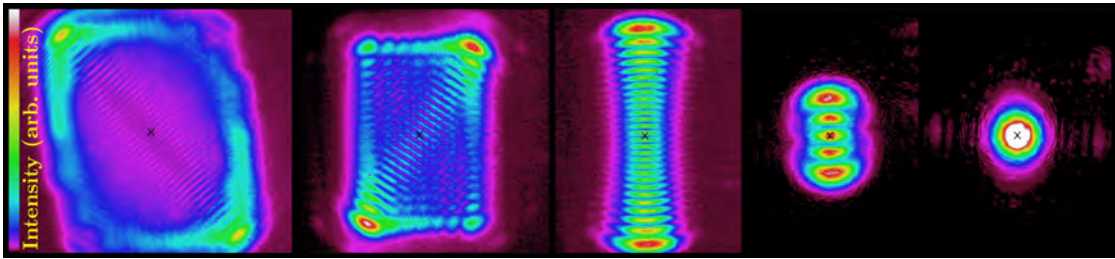


Figure 3.24: Examples of cavity transmission beam profiles encountered while optimizing the incoupling to the science cavity, from high order Gaussian modes (left) to the TEM00 mode (right).

### 3.4.2 Pound-Drever-Hall locking

The PDH technique is used for locking the science cavity resonance to the input beam frequency, but is also used in other systems in the lab. In the PDH technique a laser beam is frequency-modulated using an EOM, placing sidebands often tens of MHz next to the carrier frequency. This beam is then coupled into a cavity, and the reflected beam from the cavity is detected. The reflection signal is mixed with a phase-shifted signal oscillating at the modulation frequency to obtain the PDH signal. For an overview of the science cavity PDH lock electronics, see [119, p. 120, p. 68-70]. As a function of the laser frequency relative to the cavity resonance, the PDH signal has a shape that can have some similarities to bat wings - the function is given by [139, p. 273]:

$$D(\delta) = -4 \frac{\omega_m^2 (\kappa/2) \delta \left[ (\kappa/2)^2 - \delta^2 + \omega_m^2 \right]}{\left[ \delta^2 + (\kappa/2)^2 \right] \left[ (\delta + \omega_m)^2 + (\kappa/2)^2 \right] \left[ (\delta - \omega_m)^2 + (\kappa/2)^2 \right]}. \quad (3.12)$$

This depends on the cavity linewidth  $\kappa$ , modulation frequency  $\omega_m$  and the laser detuning with respect to the cavity resonance,  $\delta = \omega_l - \omega_c$ . The steep variation of the signal near the cavity resonance is used to provide feedback via e.g. a PI or PID circuit, like the role  $U_{probe}$  in Sec. 3.3.1. If the feedback acts on the laser diode current, fast (MHz) adjustments can be made to the laser frequency, while acting on the piezo of a macroscopic cavity mirror or ECDL cavity typically allows responses below the MHz range. The slope of the central part of the PDH signal is the metric for how well the laser or cavity can be locked - a bigger slope implies sensitivity to smaller changes in the cavity resonance frequency and requires a narrow cavity linewidth. This can be seen in Fig. 3.25(a) where two examples of calculated PDH signals are shown - one for the master laser system, and one for the science cavity system.

The slope of the PDH signal also changes depending on the power of the reflected signal, affecting the characteristics of the lock. As a result, especially the science cavity PDH lock can require frequent optimization, when a different input power is desired. This can be done by adjusting the PI parameters and gain based on the spectrum of the PDH signal during locking. An example of such a spectrum is shown in Fig. 3.25(b) for the master laser PDH lock for three different gain values. It shows the typical "servo bumps" separated some hundreds of kHz from the carrier/modulation frequency difference (10 MHz). The goal is to "push" the servo bumps far away, implying the corrections from feedback effectively remove low-frequency noise. A balance must be struck where the servo bumps do not add a lot of high frequency noise instead, as in the regime approached in the high gain example.

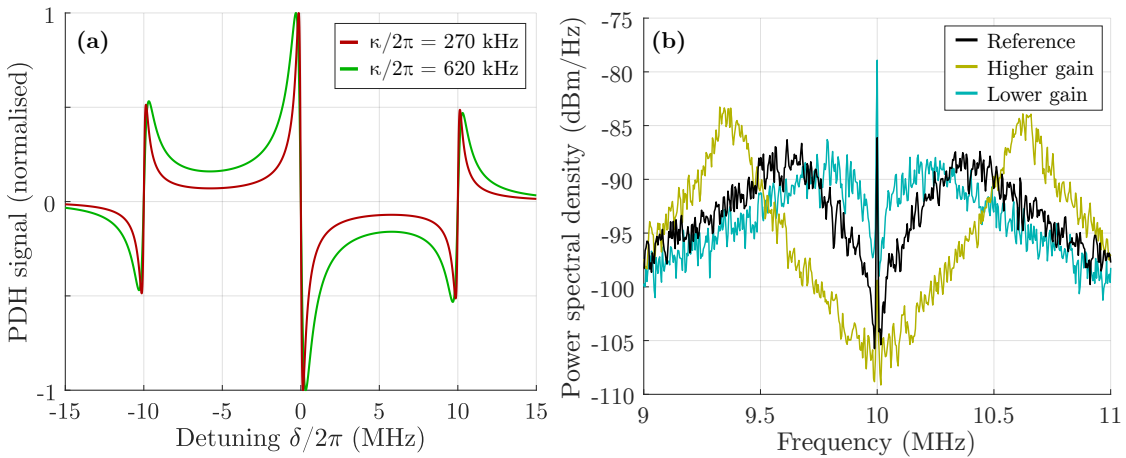


Figure 3.25: (a) Examples of calculated PDH signals for the master laser and science cavity systems, with  $\kappa/2\pi = 270$  kHz and 620 kHz, respectively, and  $\omega_m/2\pi = 10$  MHz. (b) Power spectral density of the PDH detector signal in the master laser system during locking, for three different PID lock gain levels.

### 3.4.3 Maintaining the repumper ECDLs

The 679 and 707 nm repumping lasers tend to increase the number of captured atoms in a MOT cloud by over an order of magnitude, so their condition is important. They should be giving a single-mode (frequency) beam, which can be verified with a wavemeter (which tend to show interference signatures) or the reflection/transmission from a monitoring cavity. These should be dominated by a single (or periodic) feature which is stable, and not different, fluctuating features which indicate "multimode" oscillation of the laser with many spectral components. Often an effect on the MOT cloud can be seen for repumper detunings of tens of MHz from the transition frequencies, and sometimes even in multimode condition, giving a starting point for adjusting the piezo-voltage to bring them to the right frequency. As homebuilt ECDLs, the 679 and 707 nm repumpers may often prefer to start "multimoding" at a piezo-voltage on the way towards the desired frequency. One can look for another FSR of the ECDL at a different piezo voltage, and if that does not work, small adjustments to the laser diode current can often enable single-mode oscillation within a range of tens to hundreds of MHz around the desired frequency in terms of piezo voltage. Over the course of several months to years, such a regime may become continually harder to obtain, in which case the grating within the laser boxes and/or the laser diode temperature may need to be adjusted.

### 3.4.4 Making and optimizing a blue MOT cloud

Starting with only a Zeeman-slowed beam, the first step is trapping a blue MOT cloud, which is relatively easy due to the very broad linewidth of the  $^1S_0$ - $^1P_1$  transition, but a few parameters must be within "reasonable" ranges. Verifying that the MOT beam polarizations are correct in combination with the coil current directions (as in Fig. 3.6) is important, as well as the MOT beam detuning. A detuning near 40 MHz from the transition frequency tends to be most effective. Aligning the MOT beams can also be a lengthy procedure - without a cloud to judge from, a good starting point is to ensure the back-reflected MOT beams overlap well far back along the beam path, verifying the horizontal beams keep the same height and all beams intersect with approximately right angles, which must usually be deduced from their locations on vacuum chamber windows. With larger MOT beam waists the initial beam alignment is less critical, making it easier to obtain a cloud. Simply looking for the cloud by eye can be preferable to setting up fluorescence-collecting photodiodes or absorption imaging systems for the first time. These tools can easily overlook a cloud forming outside their field of view, but are useful tools for optimizing a cloud.

Once a small cloud has been obtained, the number of trapped atoms can be improved by going through all the different parameters affecting it and optimizing them several times based on the cloud appearance or absorption image. A MOT fluorescence signal can be very sensitive to the cloud location, depending on the optics, making it risky to optimize for. It is usually optimal to have the MOT beams reflected close to directly back, so a "beam-walking" technique is usually used where either the vertical or horizontal axis of two mirrors on opposite sides of the chamber are aligned simultaneously. The current values of top and bottom MOT coils should also be checked regularly, as small changes in alignment can make different ratios optimal, if the beams are shifted relative to the magnetic field zero point. They can also be "walked" to change the gradient while preserving the field center. The power ratios of the MOT beams (controlled via  $\lambda/2$  plates) is another parameter to be optimized periodically. The first step of optimization based purely on appearance should mainly aim to get a blue MOT cloud of reasonable size (10-100 million atoms). At this point the overlap with the cavity mode should be accounted for in the optimization if the goal is superradiant pulses. The location of the cavity mode along two dimensions in an absorption image can be determined by coupling on the order of 100 nW light into the cavity while a blue MOT cloud is at least partially overlapping with it. When the cavity is on resonance with the  $^1S_0$ - $^3P_1$  transition, this will keep a significant fraction of the atoms in  $^3P_1$  in steady state, giving a stripe in the absorption image as in Fig. 3.26. In some cases this can be visible in the cloud as a less bright stripe even to the eye. This stripe determines the optimal location of the cloud in the plane of the image, but still leaves one dimension uncertain.

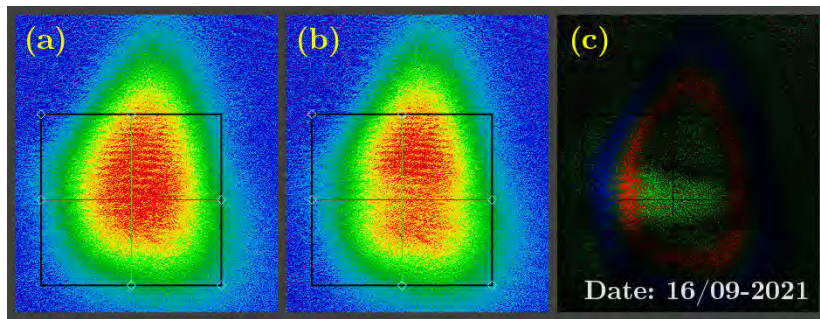


Figure 3.26: *Absorption image of a blue MOT (blue: low density, red: high density).* (a) No light coupled into the cavity, (b) light is coupled into the cavity, resulting in fewer atoms within the cavity responding to the imaging light, visible horizontally near the crosshair. (c) The pixel values of the two images are subtracted, illustrating the location of the cavity mode.

A more quantitative method for optimizing the MOT is to directly measure how efficiently it absorbs the light in the cavity mode. Since the blue MOT can load atoms in a steady-state condition with no experimental cycle needed, one option is to simply scan the piezo voltage of the science cavity across the atom-cavity resonance over time, with light sent into the cavity that is resonant with the atoms. One can then compare the peak amplitude of the cavity transmission signal when there is no atom cloud (blocking the blue laser beams) to the situation with the atom cloud present, to find how much it is reduced - the absorption. Using an input power below the order of 1-10 nW is preferable at this point to reduce possible saturation effects, but in any case the MOT alignment and other parameters can be optimized to minimize the cavity transmission peaks. Superradiant pulses have been observed for approximately >70% absorption in a blue MOT cloud with an optimized pump pulse. However continuing to optimize the absorption can often be more efficient than optimizing the pulses because the pulses have larger random variations. Up to approximately 95% absorption has been achieved for the blue MOT. In addition to providing a good starting point for superradiance, a highly absorbing blue MOT also gives a good starting point for trapping a red MOT, as it should presumably be trapped in the same location. Some examples of blue MOT clouds within the setup can be seen in Fig. 3.27.

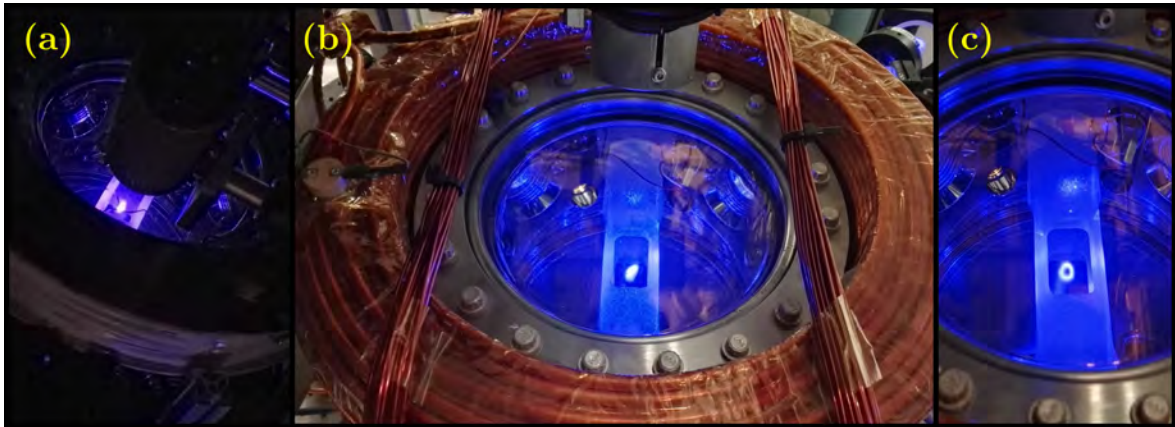


Figure 3.27: *Photos of some blue MOT clouds, (a) in the system with old MOT coils, (b) in the system with hollow wire MOT coils, (c) a ring-shaped "race track" cloud obtained due to misalignment of the mirrors.*

### 3.4.5 Red MOT cloud discovery

As for the blue MOT, trapping a red MOT for the first time requires many parameters to be in order - the red MOT beam frequency, intensity profile, polarization, power balances and alignment, as well as the magnetic field. It is significantly harder to realize than the blue MOT due to the many additional parameters, required experimental cycle, and the narrower linewidth of the  $^1S_0$ - $^3P_1$  transition which results in much weaker forces. When we first saw a red MOT cloud, we ran a cycle with the blue MOT light on for 800 ms and off for 81 ms. We ramped the coil currents while switching off the blue MOT light and turning on the red MOT light. The most clear method for us to get the first red MOT was to look at a photodetector signal of the blue MOT fluorescence. If we do not trap or slow any atoms with the red light, then the blue MOT fluorescence increases slowly once the blue light is turned on again as new atoms accumulate. But as soon as the red light starts to slow or trap the atoms, the fluorescence signal increases faster in the beginning. This enabled us to optimize all the different parameters - compensation coil currents, MOT coil currents, red MOT laser carrier and modulation frequency, and so on, to increase the slope after turning on the blue MOT light as seen in Fig. 3.28. After a bit of optimization the red MOT was visible in the imaging system (Fig. 3.29).

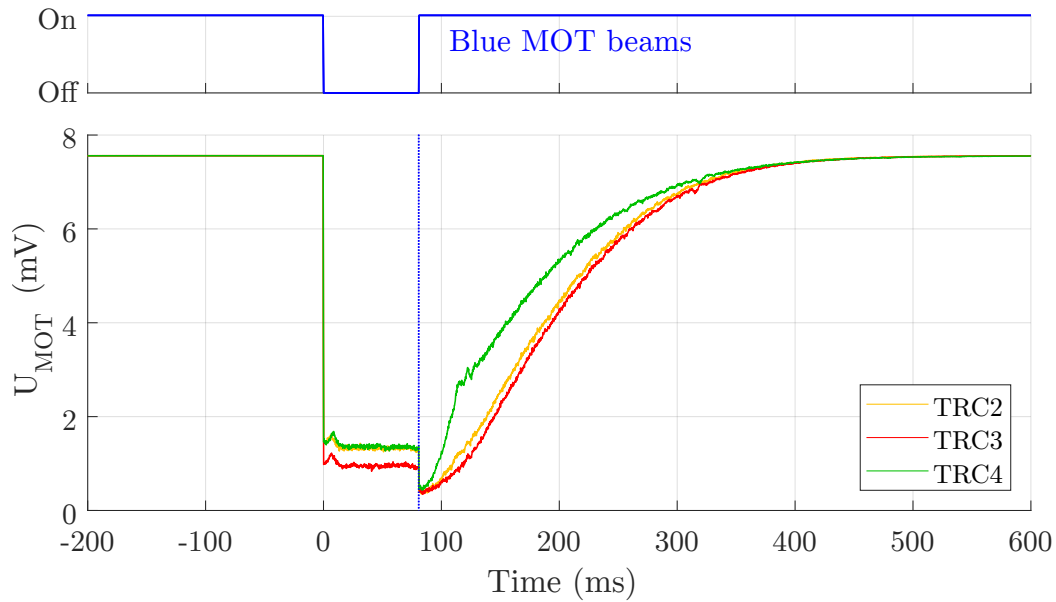


Figure 3.28: Three different traces of the blue MOT fluorescence detected before and after attempting to catch a red MOT cloud. TRC3: Injection beam blocked for the red MOT laser, thus we do not trap any atoms in the red MOT. TRC2 and 4: The red MOT laser is injected and the center frequency of the red MOT beams are set to different values.

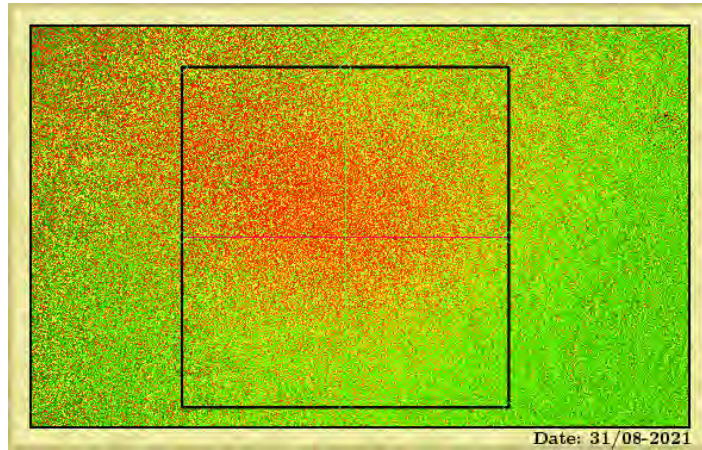


Figure 3.29: Initial imaging of the red MOT 10 ms after the red MOT light is turned off (red: atoms, green: no atoms).

### 3.4.6 Optimizing the red MOT

The red MOT cloud is not visible to the eye and requires several steps in an experimental cycle to make, which makes it more tricky to optimize than the blue MOT cloud, though the same general procedure can still be used - going through all the different parameters affecting it several times based on e.g. absorption images. The red MOT is very sensitive to any near-resonant light in the cavity, so optimizing it while continually coupling light into the cavity is likely to disturb it. The overlap with the cavity can still be inspected by comparing absorption images with and without light in the cavity. An example of this is shown in Fig. 3.30 where the cloud shape is also disturbed by the cavity photons.

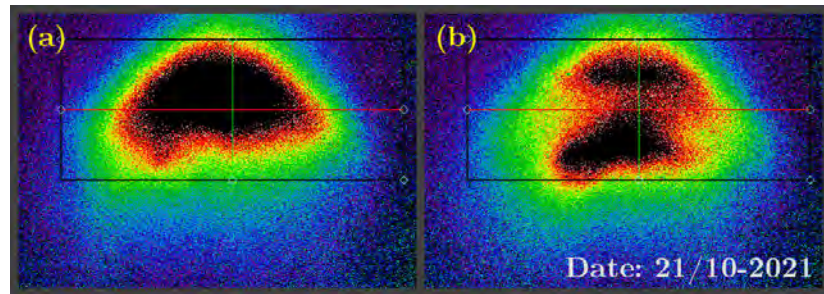


Figure 3.30: *Absorption image of a red MOT (blue: low density, red/black: high density). (a) No light injected into the cavity, (b) light is injected into the cavity, disturbing the cloud shape and causing atoms within the cavity mode to be less responsive to imaging light.*

As for the blue MOT, a more quantitative method for optimizing the red MOT is to measure the absorption of light in the cavity mode. Scanning the cavity piezo with a period adapted to the experimental cycle duration can provide a good measure without disturbing the cloud significantly. In Fig. 3.31 two traces of the cavity transmission signal are shown (with the background value subtracted) when scanning the cavity with and without a red MOT cloud overlapping with the cavity mode, after turning off the red MOT beams at  $t = 0$ . In the center of the transmission profile with a red MOT cloud, the dip is approximately 20% of the peak value without the cloud. This dip within the profile forms due to the low temperature of the atoms, indicating that their Doppler width is significantly lower than the cavity linewidth of 620 kHz, while the wings of the transmission feature can be distorted by the dispersive interaction with the atoms. The blue MOT, on the other hand, has a Doppler width of about 2 MHz and simply reduces the height of the entire transmission feature when scanning the cavity. The dip formed by the red MOT cloud changes shape on the scale of hundreds of kHz, and depending on the magnetic field, three separate dips may be found when shifting the cavity input laser frequency a few 100 kHz, attributed to the three Zeeman levels of  ${}^3P_1$ .

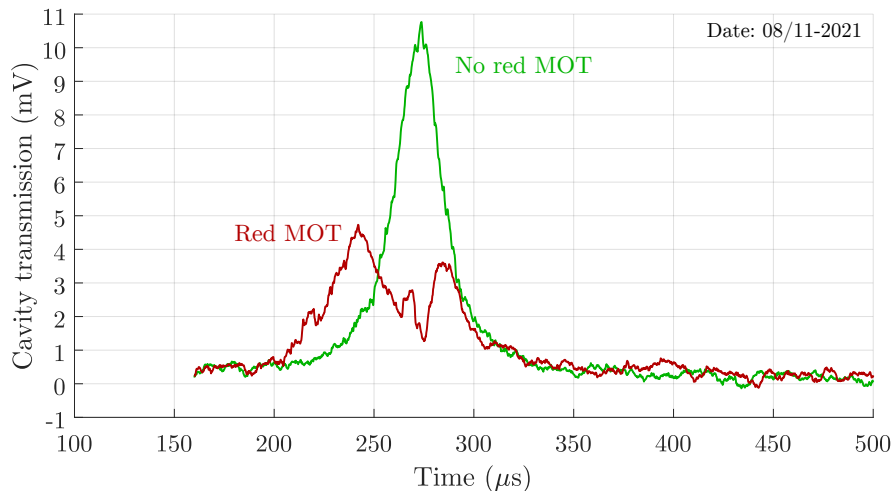


Figure 3.31: *Cavity transmission signal while scanning across the resonance with the input beam frequency and  ${}^1S_0$ - ${}^3P_1$  transition with and without a red MOT cloud present. The red MOT cloud absorbs and distorts the Lorentzian feature.*

A high absorption translates directly into the potential amplitude of superradiant pulses, assuming the atoms are pumped efficiently to  ${}^3\text{P}_1$ . A "seed laser" - resonant light coupled into the cavity - can be used to obtain superradiant pulses in a less optimal setting, both for a blue and red MOT cloud. Atoms excited by a pumping pulse will immediately couple to the finite cavity field and build up a lasing pulse. An example of a small, seeded pulse is shown in Fig. 3.32. As the seeded lasing pulse grows bigger, the seed power can be reduced, eventually reaching the regime where superradiant pulses are emitted without any seeding.

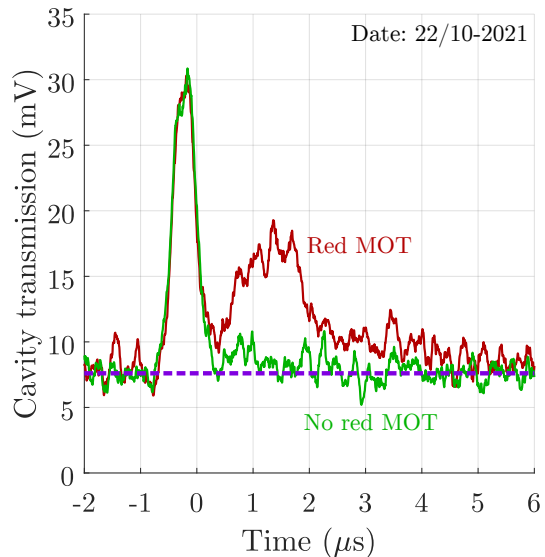


Figure 3.32: *A seeded superradiant pulse from a red MOT, compared to the cavity transmission without a red MOT. The initial peak are detected photons from the pump pulse, while the second pulse, visible only with a red MOT, is emitted by the ensemble into the cavity. The background level is highlighted with dashed lines.*

## Superradiant crossover pulses from a mK atom cloud

Here we will explore pulsed lasing primarily in the superradiant crossover regime within the strontium cloud setup presented in Chapter 3, specifically in the regime where the atom cloud is cooled only on the  $^1S_0$ - $^1P_1$  transition to about 5 mK. As a result the lasing transition linewidth of a single atom is  $\gamma_{eg} = 2\pi \cdot 7.5$  kHz ( $^1S_0$ - $^3P_1$ ), which is much narrower than the cavity linewidth ( $\kappa = 2\pi \cdot 620$  kHz), however the Doppler width of the ensemble ( $\Gamma_D = 2\pi \cdot 2.3$  MHz for  $T = 5$  mK) is in turn even broader. In addition to these linewidths, we will primarily look at the case where the effective collective coupling rate  $2g_{eff}\sqrt{N_{eff}}$  is also larger than  $\kappa$ , but also the transition where it becomes comparable to and smaller than  $\kappa$ . It is in the regime with large collective coupling where we observe the superradiant crossover dynamics, and the combination with significant Doppler broadening leads to partial synchronization among atoms with different velocities. Many of the results presented in this chapter have been published in [54, 59], and some are also described in Stefan's thesis [121].

### 4.1 Setup and numerical model

The system we investigate here is illustrated in Fig. 4.1. It consists of a blue MOT cloud overlapping with the science cavity. The cloud consists of  $\sim 10^8$  atoms, of which  $\sim 10^7$  are within the cavity waist. A Gaussian density profile is assumed, characterized by a standard deviation  $\sigma_R \sim 1$  mm. The atoms are initially pumped to  $^3P_1$  using a  $\pi$  pulse from an off-axis pump laser, with an efficiency on the order of 80% for atoms within the cavity mode. A few  $\mu$ s after pumping, the atoms emit a superradiant pulse into the cavity mode, which also lasts on the order of a few  $\mu$ s. These pulses are detected outside the vacuum chamber. In some cases they are detected directly, giving a signal proportional to the cavity output power. In other cases the pulses are overlapped with a reference laser beam on the detector to record a beat signal with phase-information of the pulses. We will generally look at the single-side output power,  $P_{out}^S$ , which is half the total output power in absence of a driving laser, for easier comparison to experiments.

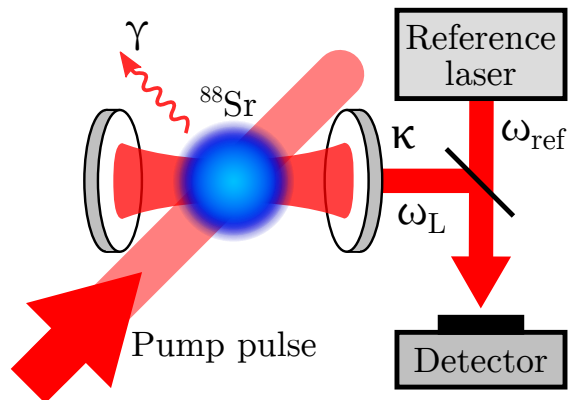


Figure 4.1: *Setup for experiments with superradiant pulses in a blue MOT cloud. The atoms can be coherently pumped with a pump pulse, and subsequently emit light into the cavity. A detector outside the vacuum chamber is used to detect the output power from the cavity, or a beat signal with a reference laser beam. Figure adapted from [59].*

A numerical model of the system based on a Tavis-Cummings Hamiltonian was developed in Matlab during my master's thesis. There the dynamics of atom populations and cavity output power were explored when coherently pumping the atoms [103]. Since then, filter cavities were included in the model to simulate the spectrum of the laser pulses. Using the notation in Sec. 2.1, the Hamiltonian describing the full system is given by:

$$H = \hbar\omega_c a^\dagger a + \sum_{j=1}^N \hbar\omega_e \sigma_{ee}^j + \sum_{k=1}^{N_f} \hbar\omega_f^k f_k^\dagger f_k + \sum_{j=1}^N \hbar g^j (\sigma_{ge}^j + \sigma_{eg}^j) (a + a^\dagger) \\ + \sum_{j=1}^N \hbar \frac{\chi_p^j}{2} (\sigma_{ge}^j + \sigma_{eg}^j) (e^{i\mathbf{k}_p \cdot \mathbf{r}_j - i\omega_p t} + e^{-i\mathbf{k}_p \cdot \mathbf{r}_j + i\omega_p t}) + \sum_{k=1}^{N_f} \hbar g_f (a + a^\dagger) (f_k + f_k^\dagger). \quad (4.1)$$

This can be used to derive the equations for time evolution of the expectation values of the operators, using the method in Chapter 2, here in the reference frame of the pumping laser (with frequency  $\omega_p$ ):

$$\langle \dot{\sigma}_{ge}^j \rangle = - \left( i\delta_{Ep} + \frac{\gamma_{eg}}{2} \right) \langle \sigma_{ge}^j \rangle + i \left( g^j \langle a \rangle + \frac{\chi_p^j}{2} e^{-i\mathbf{k}_p \cdot \mathbf{r}_j} \right) (\langle \sigma_{ee}^j \rangle - \langle \sigma_{gg}^j \rangle) \quad (4.2)$$

$$\langle \dot{\sigma}_{ee}^j \rangle = -\gamma_{eg} \langle \sigma_{ee}^j \rangle + i \left( g^j \langle a^\dagger \rangle + \frac{\chi_p^j}{2} e^{i\mathbf{k}_p \cdot \mathbf{r}_j} \right) \langle \sigma_{ge}^j \rangle - i \left( g^j \langle a \rangle + \frac{\chi_p^j}{2} e^{-i\mathbf{k}_p \cdot \mathbf{r}_j} \right) \langle \sigma_{eg}^j \rangle \quad (4.3)$$

$$\langle \dot{a} \rangle = - \left( i\delta_{cp} + \frac{\kappa}{2} \right) \langle a \rangle - \sum_{j=1}^N i g^j \langle \sigma_{ge}^j \rangle \quad (4.4)$$

$$\langle \dot{f}_k \rangle = - \left( i\delta_{fp}^k + \frac{\kappa_f^k}{2} \right) \langle f_k \rangle - i g_f \langle a \rangle. \quad (4.5)$$

In addition to including filter cavities, a few changes were also made compared to the model presented in the master's thesis. Rather than using a Gaussian approximation of the pump pulse beam profile, the imaging data from a beam profiler is used to calculate the Rabi frequencies of atoms depending on their position. An uneven beam profile leads to a spatial spread in Rabi frequencies that can reduce the obtainable inversion. The impact is small, but enables a slightly more direct comparison between simulations and experiments.

Motion in the model is treated classically, with fixed velocities based on an initial thermal distribution. The code was also changed to use a GPU for calculations, such that the atomic group approximation used in the master's thesis can be omitted and each atom can be treated individually. This eliminates some systematic biases from the approximation. Compared to using the CPU and RAM, the calculations are sped up when above  $\sim 10^5$  atoms are involved (as was shown in Fig. 2.7).

## 4.2 Lasing pulse dynamics and phase behavior

Here we will consider the intensity- and phase-dynamics of individual superradiant lasing pulses within the atom cloud, and the random variations from pulse to pulse. We will base the parameters on experiments with an estimated atom number  $N = 7.5 \cdot 10^7$ ,  $T = 5$  mK,  $\sigma_R = 0.8$  mm, and a pump pulse characterized by  $P_p = 98.4$  mW and a beam profile which, if a Gaussian is fitted to it, has waists of 1.51 and 2.69 mm (the beam profile used in simulations is shown in A.2). Three examples of simulated laser pulses are shown in Fig. 4.2, with the cavity output power presented in panel (a), and cavity field phases in panel (b), respectively. The phases we consider here are relative to the phase-evolution of a reference frame at the unperturbed atomic transition frequency,  $\omega_E$ .

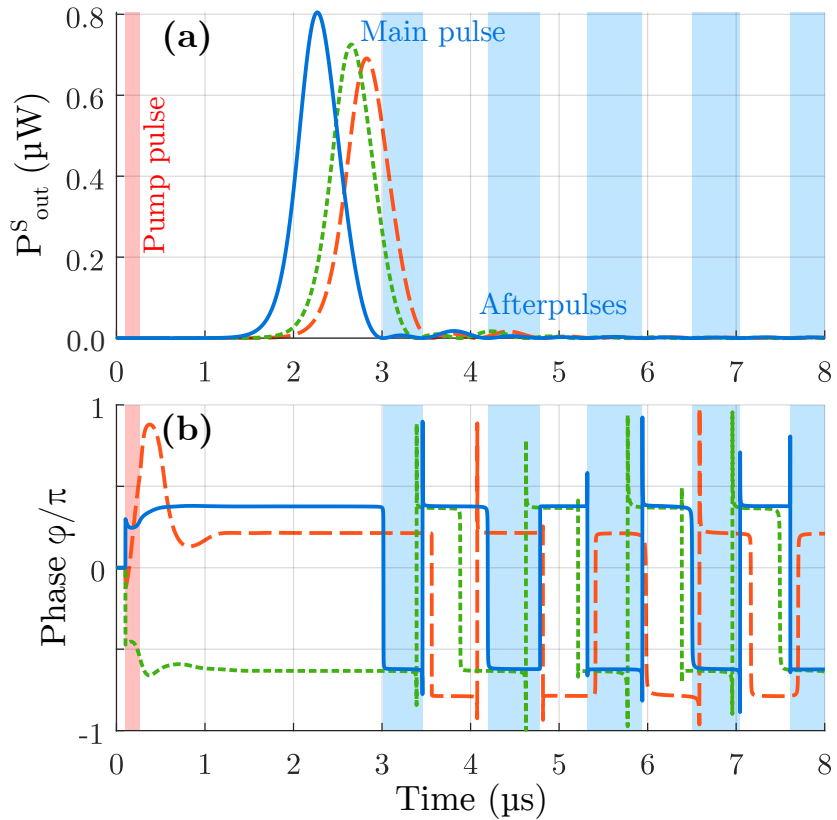


Figure 4.2: *Simulations of three laser pulses from the mK atom cloud after a pump pulse (initial red shading). (a) Time evolution of the single side cavity output power. (b) Time evolution of the cavity field phase. The cavity detuning is zero, and the phase flips sign during each afterpulse (highlighted by blue shading for the curve with the largest peak power).* Figure adapted from [59].

At the beginning of the simulation a 170 ns pump pulse is applied, which excites 85% of atoms within the cavity mode. The Bloch vector of the atoms cannot all be driven perfectly to the north pole, because of the finite ensemble temperature and non-uniform pump laser intensity profile. As a result, especially the slow atoms along the pump pulse  $\mathbf{k}$ -vector and atoms located near the cavity axis region are close to 100% excited, while fast atoms (on the order of 1 m/s) and atoms near the edge of the beam profile can even be less than 50% excited.

The pump pulse imprints a phase on each atom (the phases of  $\langle \sigma_{ge}^j \rangle$ ). In Eq. 4.2 we see that even if atoms were excited ( $\langle \sigma_{ee}^j \rangle \approx 1$ ), the cavity field amplitude will stay zero if  $\langle \sigma_{ge}^j \rangle = 0$  for all the atoms. However we also see that the change in  $\langle a \rangle$  depends on the sum of  $g^j \langle \sigma_{ge}^j \rangle$ . For example, if all atoms had the same value of  $\langle \sigma_{ge}^j \rangle$ , the sum could still be zero if they were distributed equally on the positive and negative antinodes of  $g^j$  (this configuration is considered in e.g. [140]). Such a configuration could be called sub-radiant, because coherent emission by the atoms into the cavity mode would destructively interfere, suppressing emission. In a thermal atom cloud that we consider here, the sign and value of  $g^j$  indeed varies randomly from atom to atom, so the sum  $\sum_j g^j$  will be small but nonzero.

Next we can consider the impact of  $\langle \sigma_{ge}^j \rangle$ . As the pump pulse is angled 45° with respect to the cavity axis, the phases projected onto  $g^j$  in  $\sum_j g^j \langle \sigma_{ge}^j \rangle$  will still tend to cancel out on average, and the sum will be small, but nonzero. This results in a random, macroscopically

preferred cavity field phase by the ensemble. As the atoms are moving up to a few m/s,  $g^j$  also changes over time for each atom, so this preferred phase can similarly change on the order of  $\mu\text{s}$ . However, as the cavity field builds up, the atoms will partially phase-synchronize due to their interaction with the cavity field and reinforce the macroscopically preferred phase against fluctuations. As a result of this we see the phases become fixed within a  $\mu\text{s}$  in Fig. 4.2(b).

In addition to the atomic phases, a small cavity field amplitude also builds up during the pump pulse itself, corresponding to a population of 0.1 photons in the semiclassical model. In Fig. 4.2(b) we see how the initial phase of the cavity field is pulled towards the macroscopically preferred phase by the atoms over the course of about a  $\mu\text{s}$ . If the atomic coherence were destroyed after the pump pulse (this could be done experimentally by applying a pulse of 461 nm light, projecting the atoms into  ${}^1\text{S}_0$  and  ${}^3\text{P}_1$ ), a lasing pulse would build up, but with whatever phase the cavity field had at the end of the pump pulse, since the atoms no longer have any macroscopically preferred phase.

A third effect which plays a role in experiments, but is not included in the simulations, is spontaneous emission into the cavity mode. Given the Purcell rate of the system, on the order of 60 photons will be spontaneously emitted into the cavity within 1  $\mu\text{s}$  after the pump pulse. These will have a random phase and cause additional fluctuations in the phase of the cavity field, compared to the smooth behavior seen in Fig. 4.2(b), and also cause the field amplitude to initially grow more quickly.

Once the cavity field phase has settled, a lasing pulse builds up over the course of a few  $\mu\text{s}$  before peaking, and is followed by small afterpulses. These dynamics are consistent with the superradiant crossover regime described in Sec. 1.4.2. We see that the pulses have some random properties - the exact peak output power and lasing delay (defined as the time from the end of the pump pulse to the peak output power) vary from pulse to pulse, though they are also correlated - pulses that build up more slowly also tend to be smaller, such as the dashed orange in Fig. 4.2. We see that for the orange pulse, the cavity field phase takes a longer time to settle after the pump pulse. Random variations in the initial atom configuration can cause these differences, and in experiments, the randomness of spontaneously emitted photons can also disturb the cavity field phase and contribute to variations in lasing delays. Another contribution to the correlation is the  ${}^3\text{P}_1$  decay time of 21  $\mu\text{s}$ , which means there is slightly less gain for the pulses that build up more slowly.

Considering the afterpulses, we see that the initial (primary) pulse is generally followed by a small, short afterpulse, then a slightly larger, longer afterpulse. This is a general pattern for this particular parameter regime (atom number, temperature, zero cavity detuning from the atom transition frequency). At zero cavity-detuning the intensity goes to zero between the afterpulses, so the phase of the cavity field flips sign between them. This is highlighted by the blue shading of every other afterpulse for the blue full-line simulation.

The phase  $\phi$  of the cavity field can be compared to an experimental beat signal by using the transformation  $\sin(\phi) \cdot \sqrt{P_{\text{out}}}$ . This is shown in panel (a) in Fig. 4.3, using the phases from Fig. 4.2(b). Three experimental beat signals are shown in Fig. 4.3(b) for comparison. Because the phase varies randomly from pulse to pulse, only the qualitative behavior can be compared.

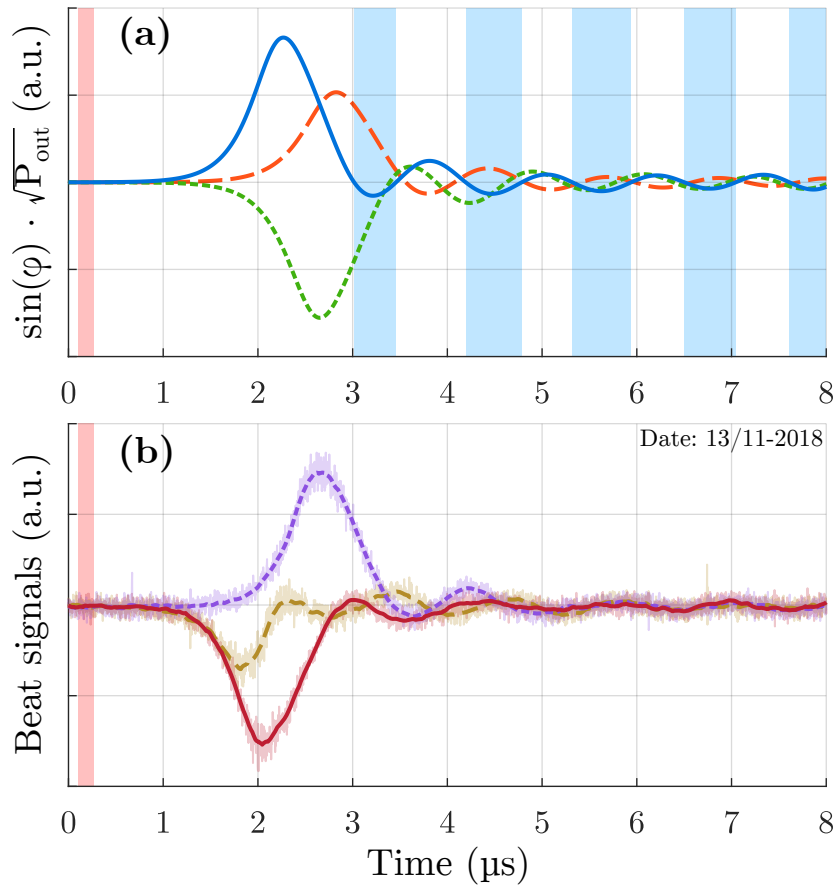


Figure 4.3: *Examples of signals from simulations and experiments. (a) Calculated beat signals based on the pulses in Fig. 4.2. (b) Beat signals detected from lasing pulses in an experiment. Figure adapted from [59].*

### 4.3 Lasing regimes and scaling with atom number

In this section we will consider the different regimes realized in our system when varying the number of atoms, considering the variation in lasing dynamics, output power and lasing delay. In Fig. 4.4 we show how pulses, such as those presented in Fig. 4.2(a), vary with the atom number in simulations (panel (a)) and experiments (panel (b)). The data is aligned by the peak output power for easier comparison of pulse shapes due to the large variations in pulse delays. The lasing delays are indicated by green points, binning the individual end time of pumping pulses for a range of atom numbers. Error bars show the standard deviation within the samples. The bin size is 30 samples of neighboring atom numbers for the simulations and 40 for experiments. For the experiments, the atom number has significant random variations for each MOT cloud realization, giving a non-uniform distribution of  $N$ . These atom numbers were determined from the fluorescence during the cooling stage before pumping. The calibration of atom number from fluorescence was based on correlating its variation with the number of photons emitted in lasing pulses (this method is described in more detail in [103, p. 59-61]).

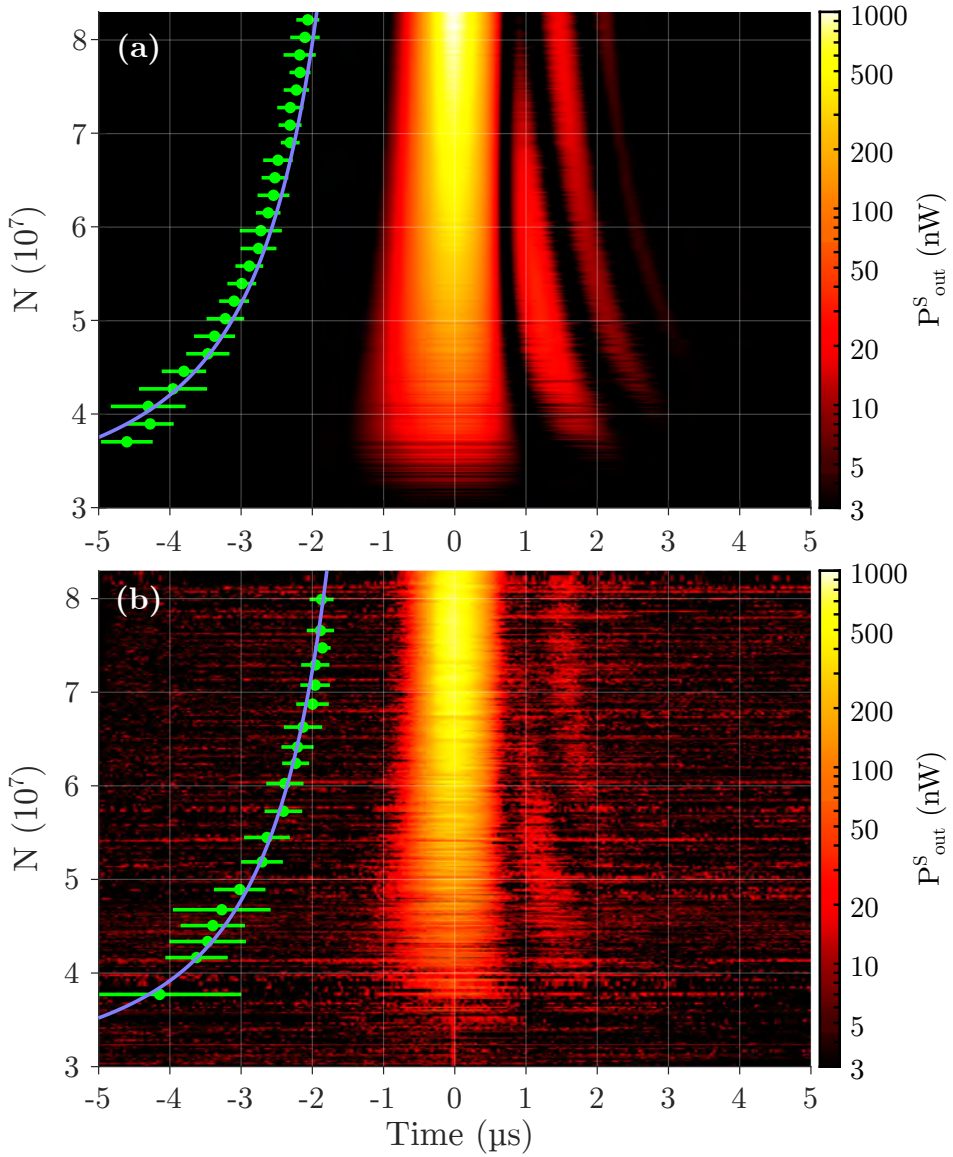


Figure 4.4: *Time evolution of the cavity output power of superradiant lasing pulses for varying number of atoms, (a) simulations and (b) experiments (date: 13/11/2018). The peak output power is aligned at  $t = 0$ , and the time of the end of pump pulses are binned, shown as green points with standard deviations indicated. The lasing delay  $\tau = \tau_0 / \sqrt{N - N_{th}}$  is fitted (blue curves) prior to binning. Figure adapted from [54].*

We find a good agreement between the dynamics of simulations and experiments in terms of lasing threshold, pulse and afterpulse shape variations within the regime. The first afterpulse is emitted by atoms which reabsorb some light at the end of the main pulse and has the opposite phase of the main pulse (as we saw in Fig. 4.2(b)). For the highest atom numbers this becomes less prominent as more atoms synchronize with the main pulse. On the other hand, for the very lowest atom numbers above threshold, the cavity photon number becomes too low for atoms to absorb significantly from the field, and the pulse resembles the pure superradiant dynamics more closely, emitted by a fraction of the ensemble. Of the functions discussed in Sec. 1.4.1, an  $1/\sqrt{N}$ -scaling shows best agreement with the data (in agreement with findings in the oscillatory superfluorescent regime [41]), consequently fits with  $\tau = \tau_0 / \sqrt{N - N_{th}}$  to the lasing delay are shown. Only  $N$  is a fit parameter, while the threshold atom number  $N_{th}$  is determined separately from fits to the peak output power. The scaling of the peak output power with atom number is shown in Fig. 4.5 in panel (a), and in panel (b) the lasing delays from simulations and experiments are compared.

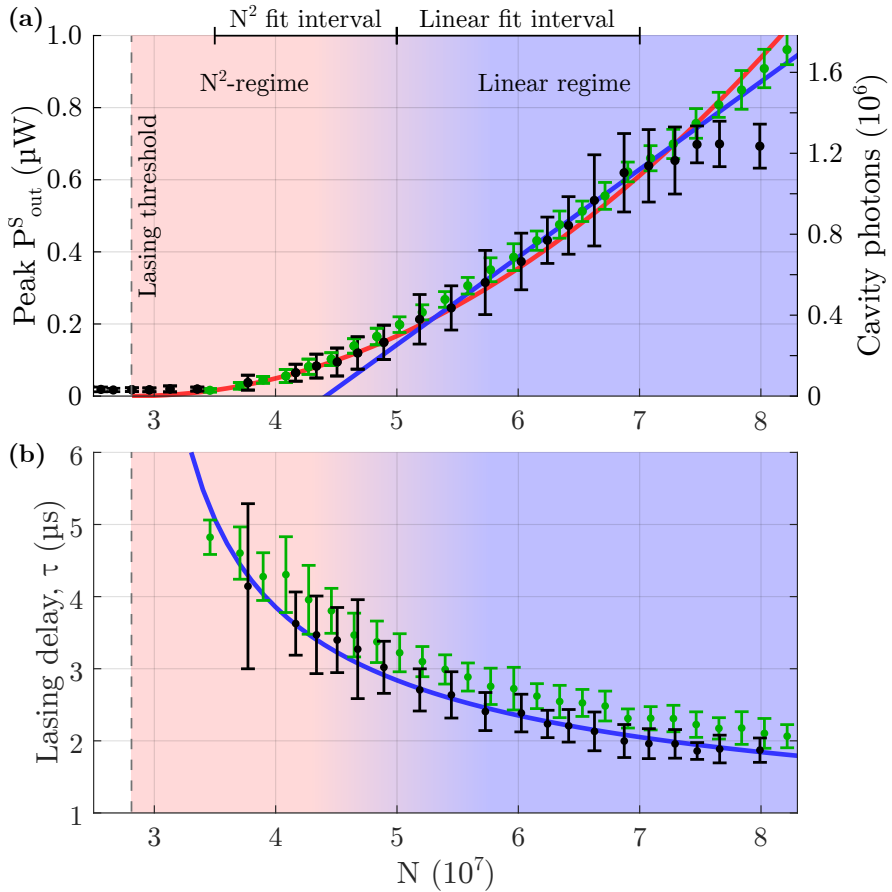


Figure 4.5: Scaling of (a) the peak cavity output power and (b) the lasing delay with number of atoms in the cloud. Points show binned data from experiments (black) and simulations (green). For the output power,  $P = a(N - N_{\text{th}})^2$  is fitted to experimental data near the lasing threshold, and  $P = b(N - N_0)$  is fitted for higher atom numbers. For the lasing delay,  $\tau = \tau_0 / \sqrt{N - N_{\text{th}}}$  is fitted to all the experimental data. Functions are fitted prior to binning. Figure adapted from [54].

Three regimes are visible, highlighted by the background color. In the white region, there are no observable pulses as the number of atoms is below the threshold number for lasing. In the red region ( $3 \cdot 10^7 < N < 5 \cdot 10^7$ ), the peak output power scales with  $N^2$ . A fit to experimental data within this regime (prior to binning) is shown as a red dashed line, and the experimental lasing threshold is determined by extrapolating this fit. For higher atom numbers a linear scaling with  $N$  is found. The blue line shows a fit to experimental data within this region. Data for the very highest atom numbers is excluded from the fit as the scaling breaks down in this regime according to the experimental data. This may be due to systematic bias in determining the atom number in this regime, or varying density or temperature with atom number, as the simulations indicate that the linear trend continues (see also Appendix A.3 for simulations and comparison of scalings for these up to  $N = 1.33 \cdot 10^8$ ). As such simulations help us to distinguish the  $N^2$ - and  $N$ -scaling regimes with a transition around  $N \sim 5 \cdot 10^7$ . As delay times in our data only span a factor 3, with large variations especially in the experimental data for low atom numbers, a different regime for low atom numbers cannot be clearly distinguished.

To consider the transition between the pure regime and crossover regime, as they were described in Sec. 1.4.2,  $\kappa \approx 2g\sqrt{N}$  is ambiguous because the coupling varies vastly between atoms in the ensemble, where many are far outside the cavity waist. We can consider the sinusoidal variation in  $g$  to define  $g_{\text{eff}}^2 = g_0^2/2$  and account separately for the atom-cloud overlap by introducing an effective atom number,  $N_{\text{eff}}$ , from the overlap with the non-sinusoidal

terms of  $g^2$ :

$$N_{eff} = N \iiint_{-\infty}^{\infty} e^{-\frac{2x^2+2y^2}{W^2}} \cdot \frac{e^{-\frac{x^2+y^2+z^2}{\sigma_R^2}}}{(2\pi)^{3/2} \sigma_R^3} dx dy dz = \frac{N}{1 + 4\sigma_R^2/W^2}. \quad (4.6)$$

In this case for  $N = 75 \cdot 10^6$ ,  $\sigma_R = 800 \mu\text{m}$  and  $W = 450 \mu\text{m}$  we get  $N_{eff} = 5.5 \cdot 10^6$ . We fulfill  $N_{eff} = \kappa^2/4g_{eff}^2 = 2.9 \cdot 10^5$  at only  $N = 4.0 \cdot 10^6$ , which is far below the threshold number of atoms. The reason for the threshold and  $N^2$  scaling at much higher atom numbers is the 5 mK temperature, which means that only a small fraction of the ensemble consisting of the slowest atoms within the cavity waist participates in emitting the pulses near the threshold. The Doppler broadening could be interpreted as lowering the effective atom number further.

Alternatively we can consider when the power broadened transition linewidth  $\Gamma_P$  becomes comparable to the cavity linewidth  $\kappa$ . The maximum power broadening experienced by an atom due to the cavity field scales with the Rabi frequency of the cavity field interaction for high intensities, and can be related to an observed (single side) cavity output power using [20, p. 143] [112, p. 162] and a few relations:

$$\Gamma_P^0 = \gamma_{eg} \sqrt{1 + \frac{8g_0^2 n}{\gamma_{eg}^2}} = \gamma_{eg} \sqrt{1 + \frac{48c^3 n}{W^2 L \omega_E^2 \gamma_{eg}}} = \gamma_{eg} \sqrt{1 + \frac{96c^3 P_{out}^S}{\hbar \kappa W^2 L \omega_E^3 \gamma_{eg}}}. \quad (4.7)$$

Observed lasing pulses from the system range in the order of nW and  $\mu\text{W}$ . An atom located at a field node in the center of the waist then experiences a power broadening from the natural linewidth 7.5 kHz to e.g. 97 kHz (1 nW) or 3.1 MHz (1  $\mu\text{W}$ ). Neglecting the unity term in the square root and considering  $g_{eff}$  rather than  $g_0$ , we may expect the crossover regime when  $\kappa \sim \Gamma_P^{eff}$ . In terms of observables this gives the characteristic output power (from one side of the cavity):

$$\kappa = \Gamma_P^{eff} \approx \sqrt{\frac{48\gamma_{eg} c^3 P_{out}^S}{\hbar \kappa W^2 L \omega_E^3}} \implies P_{out}^S = \frac{\kappa^3 W^2 L \hbar \omega_E^3}{48c^3 \gamma_{eg}}. \quad (4.8)$$

This corresponds to  $P_{out}^S = 81 \text{ nW}$  in our system, but should be considered approximate as  $g$  is lower for most atoms, and  $P_{out}^S$  also varies over time. For comparison the transition in Fig. 4.5 occurs for pulses where the peak  $P_{out}^S \sim 200 \text{ nW}$ .

## 4.4 Lasing pulses in a detuned cavity

By detuning the science cavity away from resonance with the atomic transition frequency we can investigate to which degree cavity fluctuations can be suppressed in the mK cloud system - one of the key parameters of a superradiant laser. We will again start by considering the dynamics of individual pulses, which is the focus of this section. In Fig. 4.6 the lasing pulse and phase dynamics are shown for a cavity detuning of 1 MHz. The cavity output power is shown in panel (a), while the unwrapped phase evolution in a reference frame rotating at the atomic transition frequency is shown in panel (b).

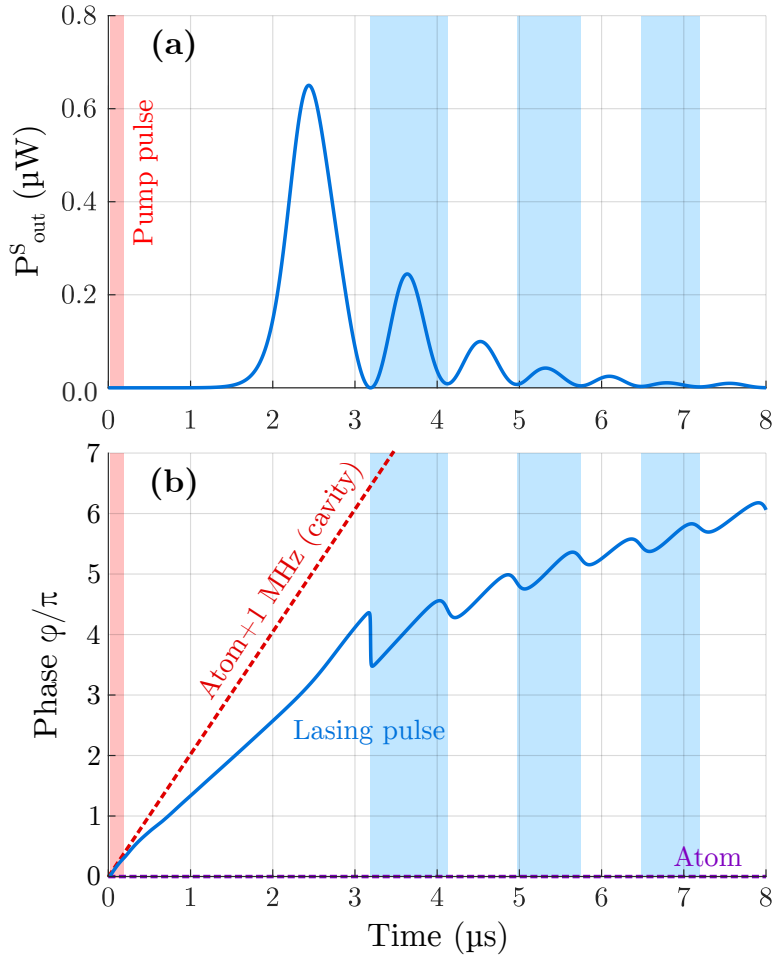


Figure 4.6: Dynamics of (a) cavity output power and (b) cavity field phase (unwrapped) in a simulation with cavity detuning  $\delta_{cE}/2\pi = 1$  MHz. Unlike for  $\delta_{cE} = 0$ , there are large afterpulses. The power only goes to zero before the first afterpulse, so the phase evolution is generally more smooth. The general phase slope tells us the lasing frequency is between the atomic and cavity resonances (dashed lines), with a notable chirp during the afterpulses.

We see very pronounced afterpulses in panel (a), which is a general feature when the cavity is detuned by hundreds of kHz in this system, also seen in other atom-cavity systems [141]. Regarding the phase evolution, as in Fig. 4.2, every other afterpulse of the full-line blue simulation is highlighted by shading. In this example the unwrapped phase is shown to highlight the sloped behavior, which is generally in-between what would be obtained for emission at the atomic transition frequency (purple dashed line) and the cavity resonance frequency (orange dashed line). We can see the frequency of the lasing pulse is partially pulled towards the cavity resonance. The intensity drops to zero between the primary pulse and first afterpulse, associated with a  $\pi$  phase shift familiar in Fig. 4.2. This does not happen in the following afterpulses, and there is a more gradual jump in phase between them. The slopes tell us the instantaneous frequency during the lasing pulse relative to the atom transition frequency,  $\nu_E$ , initially being  $\nu_E + 600$  kHz before the peak of the primary pulse and then shifting to  $\nu_E + 850$  kHz during the peaks, and lower when approaching the phase jumps.

As for the case at zero cavity detuning, we can calculate a theoretical beat signal from the simulated phase and compare it to experimental beat signals. This is shown in Fig. 4.7, where the simulated phase was first transformed to a rotating frame at the cavity resonance frequency for comparison with the experimental signals. For the experimental data, the Slave 2 Laser (injected by the 689 nm Master Laser) was used as reference laser for the beat signals here, but locked 1 FSR (781 MHz) from the cavity resonance with which the atoms interact.

The beat signals were demodulated by 1 FSR electronically to produce the recorded data, such that the reference frame is the same as in panel (a).

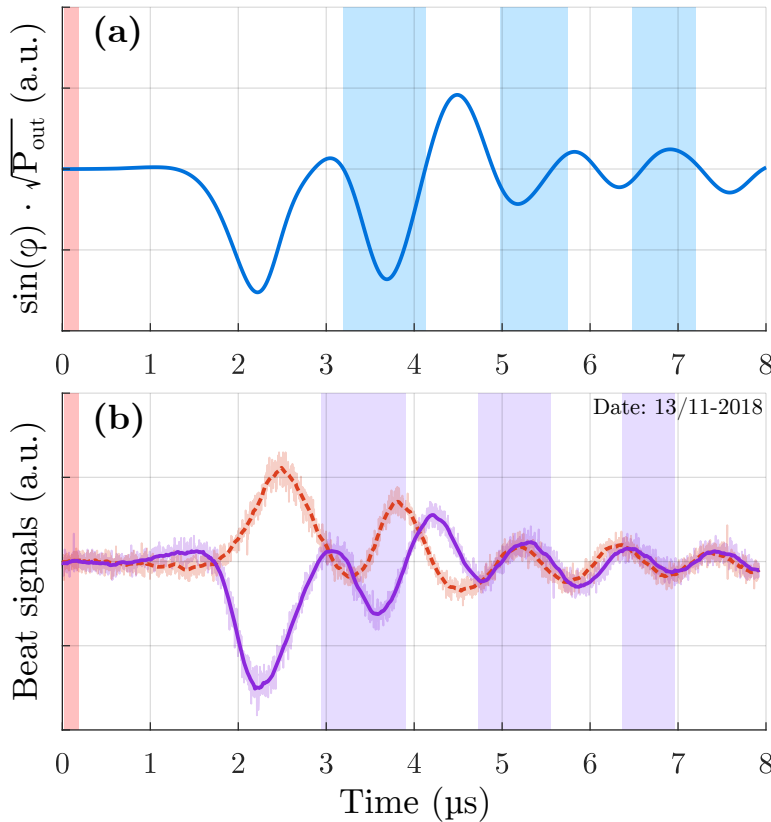


Figure 4.7: Examples of (a) calculated beat signal from the phase evolution in Fig. 4.6(b), and (b) two demodulated beat signals recorded between superradiant laser pulses and a reference laser beam originating from the 689 nm Master Laser. Curves highlight the moving mean of raw data.

The phase behavior has given an indication that the lasing pulse frequency does not simply follow the cavity resonance as in the good-cavity regime, but lies somewhere in-between the atom and cavity resonance frequencies. We can consider the spectral properties of lasing pulses at a detuning of 1 MHz using the beat signal shown in Fig. 4.8(a), and associated spectrograms in panel (b) and (c). For these experiments an independent reference laser was used for obtaining the beat signal. The reference laser was locked to a cavity 171 MHz from the atom transition frequency, and the detected signal was mixed at 120 MHz prior to recording, resulting in the rapid oscillation frequency of the signal near 51 MHz in Fig. 4.8(a). The evolution of the power spectrum is shown with different window functions in panel (b) (Gaussian window spectrogram with  $\sigma_W = 400$  ns) and c (Heaviside function with increasing window size, as mentioned in Sec. 2.6.2). Here the frequency axes are shifted to show the lasing frequency shift relative to the atomic transition. Estimated parameters for this experiment are  $N = 1.05 \cdot 10^8$ ,  $T = 5$  mK,  $\sigma_R = 0.9$  mm, and a pump pulse characterized by  $P_p = 90$  mW and approximately the same beam profile as in Appendix A.2.

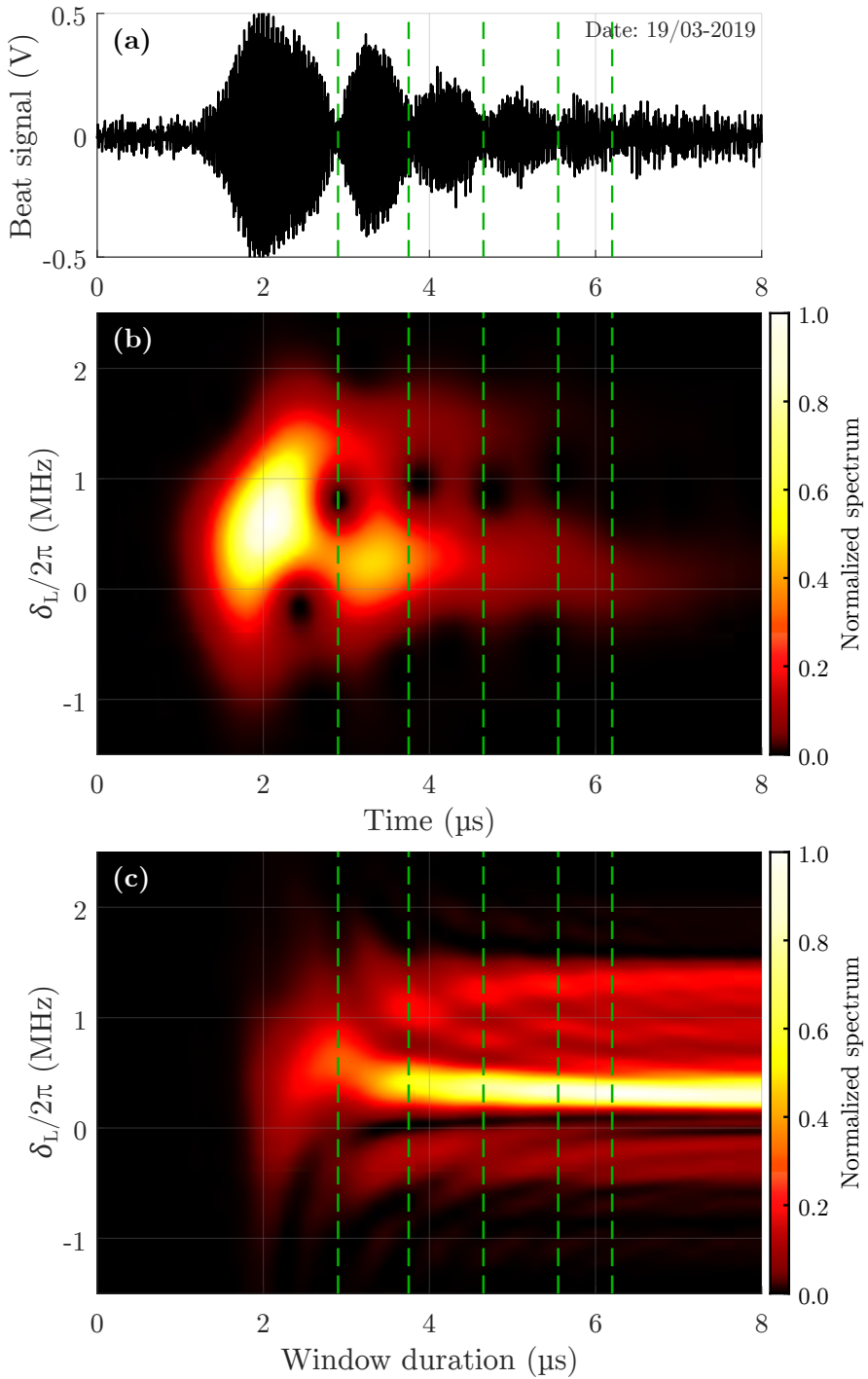


Figure 4.8: (a) Beat signal between a superradiant laser pulse for  $\delta_{cE}/2\pi = 1$  MHz and an independent reference laser beam. (b) Intensity spectrogram with a Gaussian window ( $\sigma_W = 400$  ns) showing the lasing frequency shift  $\delta_L$  relative to the transition frequency  $\omega_E$ . (c) Power spectrum for increasing window durations, starting from  $t = 0$ . Green lines indicate minima in the output power. Figure adapted from [59].

The spectrogram in panel (b) shows an intense component peaking around  $\nu_E + 600$  kHz and two tones during the afterpulses - the most intense one near  $\nu_E + 250$  kHz and a faint component near  $\nu_E + 1.5$  MHz which fades more quickly. As panel (c) uses an expanding window it shows how the simpler components in panel (b) interfere when recording a spectrum of the full pulse, giving bifurcations during each afterpulse. The spectrum of the full beat signal corresponds to the vertical slice at  $t=8$  μs in panel (c) and has a peak just 250 kHz from the atom transition frequency, but also a broader structure with smaller peaks up to about  $\nu_E + 1.4$  MHz.

The spectral evolution of a comparable simulated lasing pulse is shown in Fig. 4.9, using the Heaviside window in panel (a). In panel (b) the final spectrum is shown, compared to relevant lineshapes in the system - the lineshape of a single atom, of the Doppler-broadened ensemble, and the resonance of the cavity.

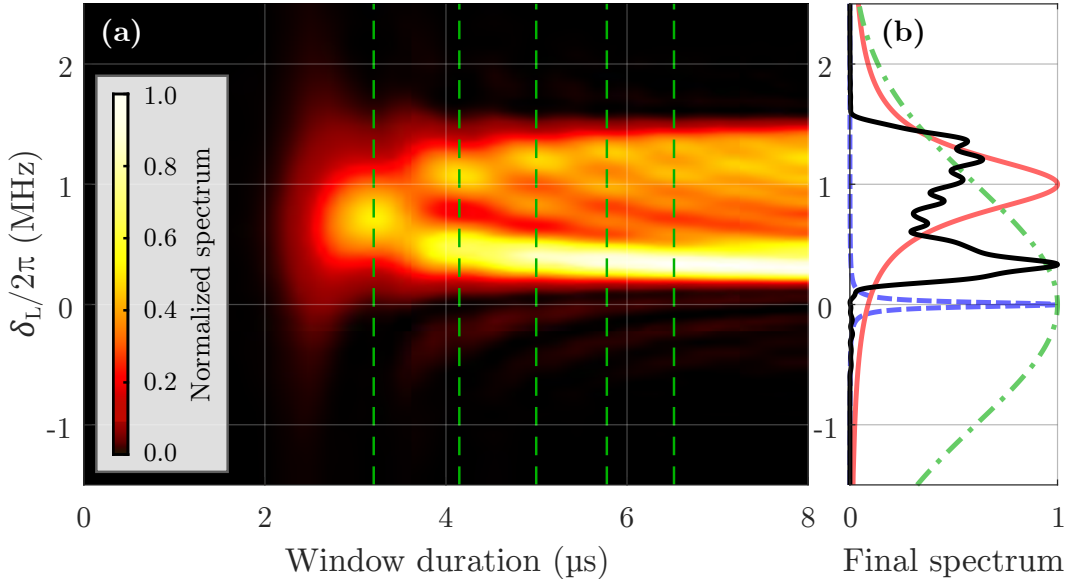


Figure 4.9: (a) Power spectrum of a simulated lasing pulse for increasing window durations, starting from  $t = 0$ . Green lines indicate minima in the output power. The cavity detuning is  $\delta_{cE}/2\pi = 1$  MHz. (b) The final spectrum of the lasing pulse (black full line), compared to the atomic lineshape (blue dashed), ensemble Doppler lineshape (green dot-dashed) and cavity resonance (red full line). Figure adapted from [59].

The simulation replicates the bifurcating patterns seen in the experiment, giving a spectrum with a prominent peak closer to the atom transition frequency than cavity resonance, and also a broad, multi-peaked background within the cavity and Doppler lineshape curves. The background peaks are a bit more prominent in the simulation, and could suggest the temperature is lower than the 5 mK estimate. An example of how the relative prominence of the structures vary with temperature is shown in Appendix A.4.

#### 4.4.1 Impact of a thermal distribution

The properties of the lasing pulses we have seen examples of so far are a result of the three linewidths in the system in combination with the high atom number which places the system in the crossover regime. The thermal distribution of atoms with narrow linewidth means that each individual atom interacts differently with the cavity mode, depending on their velocity along the cavity axis,  $v_z$ . Detuning the cavity with respect to the center of the Doppler distribution changes the response of the atoms, but only the absolute value  $|v_z|$  matters due to symmetry. In Fig. 4.10 the mean rate of absorption and emission due to interactions with the cavity is shown for different velocity classes, based on  $|v_z|$ . Panel (a) shows the variations in emission and absorption for zero cavity detuning, corresponding to the dynamics in Fig. 4.2. Panel (b) shows the response for  $\delta_{cE}/2\pi = 1$  MHz, corresponding to the dynamics in Fig. 4.6 and Fig. 4.9. The simulations use the parameters of the experiment with  $N = 7.5 \cdot 10^7$  atoms.

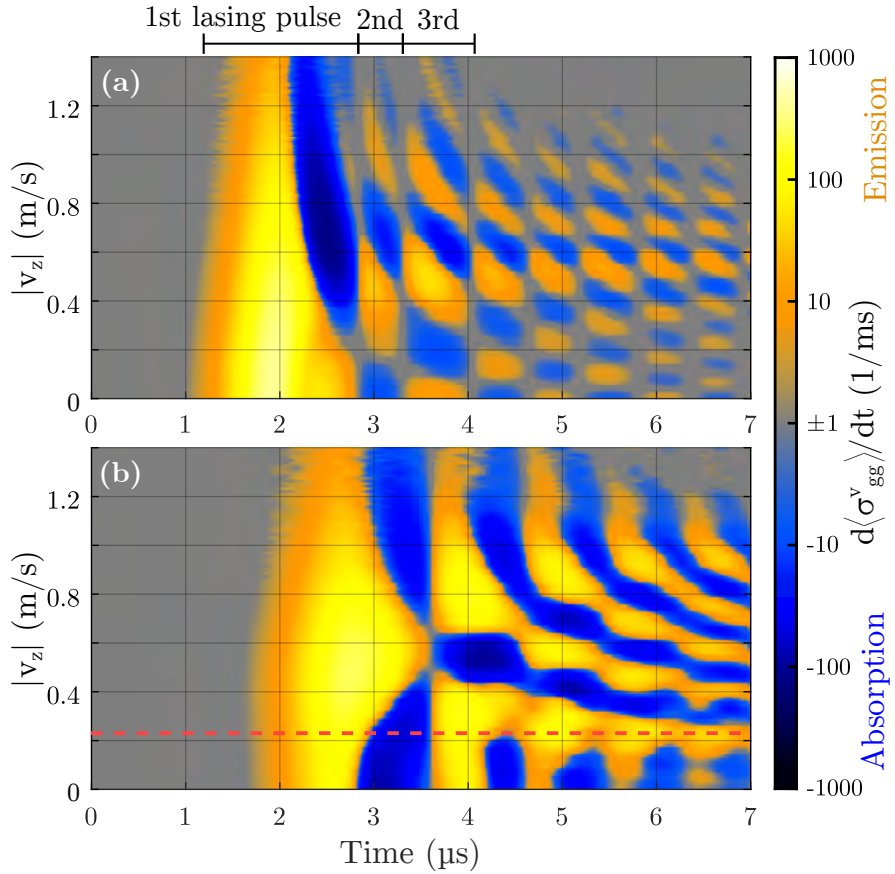


Figure 4.10: Mean rates of absorption and emission for an atom depending on its speed along the cavity axis,  $|v_z|$ , throughout superradiant lasing pulses for (a)  $\delta_{cE} = 0$  and (b)  $\delta_{cE}/2\pi = 1$  MHz. The red dashed line in (b) highlights  $k|v_z|/2\pi = 300$  kHz, the peak of the lasing spectrum. Note that slow atoms are more abundant due to the 5 mK distribution. Figure adapted from [54].

We see that for  $\delta_{cE} = 0$ , the main lasing pulse is emitted primarily by the slowest atoms, but the fast atoms start to absorb from it near the end, shifting some of the excitation from slow to fast atoms. As a result the afterpulses are mainly emitted by the faster atoms. We also see the abrupt changes from absorption to emission across different values of  $v_z$  between each pulse - different velocity classes alternate between absorbing and emitting during each pulse, giving rise to the alternating phases of the light in Fig. 4.2(b).

In panel (b) the main lasing pulse is built up primarily by atoms moving at a finite speed, and both the fastest and slowest atoms start to absorb from it as it ends. The roles of absorption and emission are clearly flipped across different velocities as the first afterpulse begins, but the emission and absorption changes much more gradually across the different velocities during the subsequent afterpulses, giving the gradual phase shifts in Fig. 4.6(b). The emission pattern resembles the spectrograms using the expanding Heaviside window in Fig. 4.8(c) and 4.9(a), and converting the velocity to Doppler shifts, we see that the spectral peak near 300 kHz stems from the atoms moving approximately 0.2 m/s along the cavity axis (red dashed line), which emit throughout all the afterpulses. Though these simulations were run with parameters from the experiment on 13/11-2018, the dynamics are very similar in the experiments with an independent reference laser, allowing for the comparison to Fig. 4.8 and 4.9.

## 4.5 Cavity-detuning dependency and pulling

Here we will look at how the dynamics and spectrum of the lasing pulses depend on the cavity detuning more generally. The dynamics of the cavity output power for different detunings are shown in Fig. 4.11, with simulations in panel (a) and experiments in (b). The power data is aligned by the peak values along the time axis to reduce variations from the random lasing delays. The lasing delays are instead indicated by the green points, which show the mean value and standard deviation within a given bin of cavity detunings. 801 simulations were run for continually varying detunings between  $\pm 2$  MHz. For the experiments, time traces were instead recorded in steps of 100 kHz, and 50 traces are distributed continuously for each 100 kHz along the detuning axis. Due to the high amount of information in the data, these experiments have served as one of the main benchmarks of the numerical model.

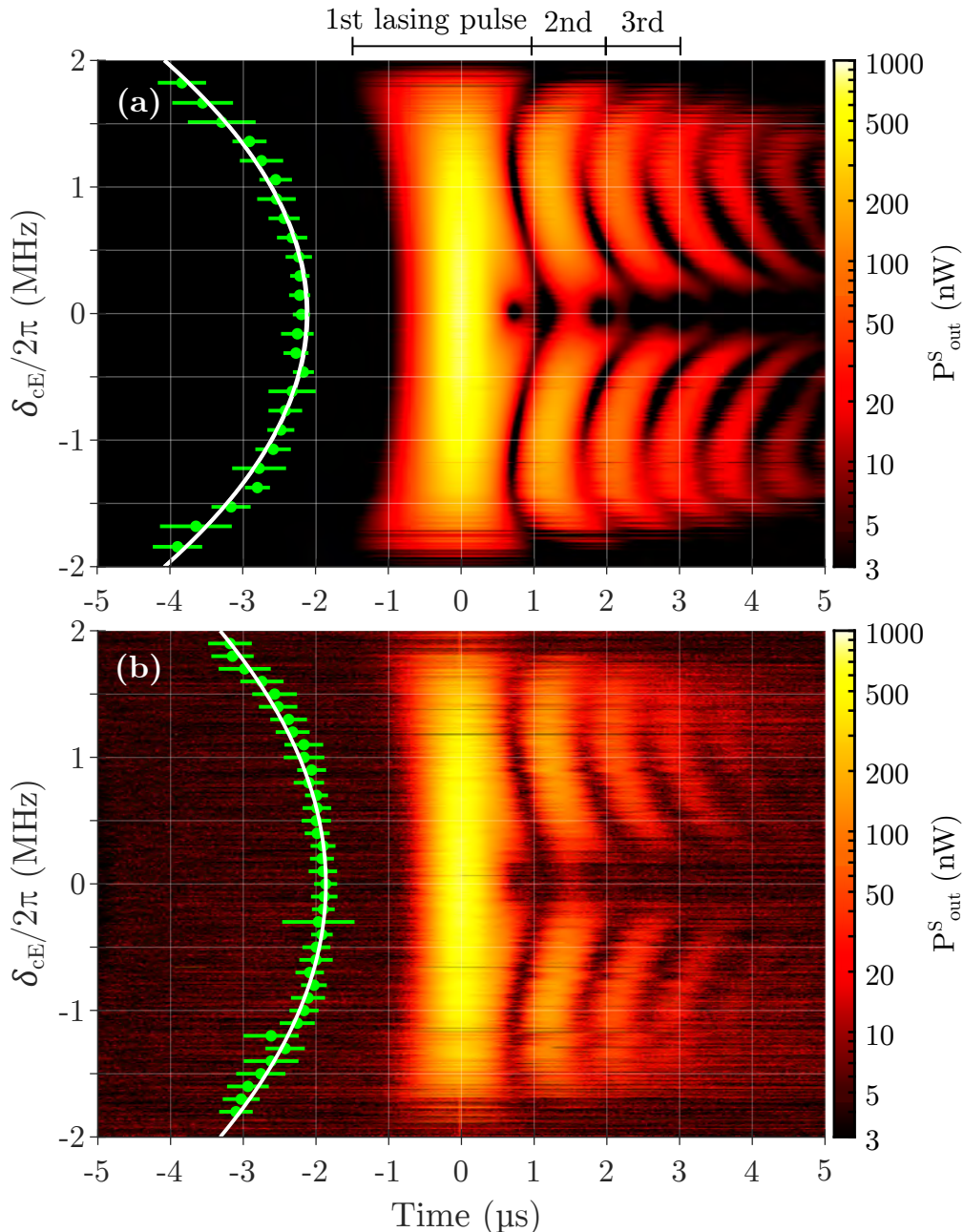


Figure 4.11: *Dynamics of the cavity output power for different cavity detunings, (a) simulations and (b) experiments (date: 13/11-2018).* The data is aligned by peak output power. Green points with error bars indicate mean values and standard deviation of the time at which the pump pulse ends for a bin of time traces. The white curves show fits given by  $t_0 + a \cdot \delta_{cE}^2$ . Figure adapted from [54].

Over-all we find a good agreement in the qualitative variations of pulse shapes across the different detunings. Afterpulses are prominent for detunings greater than a few hundred kHz. Near  $\delta_{cE} = 0$  and  $t = 0.8$  ns we see a zero-intensity "hole" in the output power, breaking up the pulse shape seen at larger detunings into two pieces. This is a signature of the finite temperature, which caused the fast velocity-groups to get out of sync with the slow groups as we saw in Fig. 4.10(a). When the cavity detuning is finite, the slowest atoms can synchronize with a larger range of atoms such that the tiny secondary pulse is avoided. This pattern is repeated in the later afterpulses near zero detuning. The frequency of the output power oscillations increase slightly with cavity detuning until near 1 MHz. At larger detunings the abundance of atoms with matching Doppler shifts becomes too low, resulting in lower gain, slower pulse buildup and increasingly smaller pulses. The range of detunings supporting lasing spans about 2 MHz in this regime, but this depends on the number of atoms and temperature, among other parameters.

The frequency of power oscillations is on the order of 1 MHz, but varies significantly over time and with detuning. Similar oscillations have been observed for a single atom interaction with a cavity [142], with oscillations in the emitted power at a rate corresponding to  $\sqrt{4g^2 + \delta_{cE}^2}$ . For an ensemble of  $N$  atoms the scaling extends with  $g_{eff}\sqrt{N}$  [141], where  $g_{eff}$  is an effective coupling accounting for the variations in  $g$ . Considering again the effective atom number from Eq. 4.6,  $N_{eff} = 5.5 \cdot 10^6$ , we get  $\sqrt{4N_{eff}g_{eff}^2}/2\pi = 1.9$  MHz for  $\delta_{cE} = 0$ . This is somewhat higher than the observed frequency of oscillations, but also does not account for the finite temperature and imperfect pumping, which reduces the pulse buildup and how many of the atoms participate in emitting the pulses, as also discussed in Sec. 4.3. Finally we saw how different velocity classes can emit asynchronously and break up pulses into multiple smaller components for some detunings, highlighting the limitations of such a simple expression when describing a thermal ensemble.

For the lasing delays, we see as in Sec. 4.3 that the delay is slightly lower for experiments than simulations ( $\sim 1.8$   $\mu$ s vs  $\sim 2.1$   $\mu$ s at  $\delta_{cE} = 0$ ), which could be due to the model neglecting spontaneous emission into the cavity mode.

#### 4.5.1 Cavity pulling

The beat signal presented in Fig. 4.8 is one example out of a data sample spanning cavity detunings within  $\pm 2$  MHz. In Fig. 4.12 the final power spectrum from simulations (panel (a)) and the full data sample from experiments (panel (b)) are shown. As in Fig. 4.11 the detuning in simulations is varied continuously, here in steps of 25 kHz, while for the experimental data, 100 data samples are distributed around the nominal detunings where they were taken, spaced by 100 kHz. The individual spectra are normalized by the peak value.

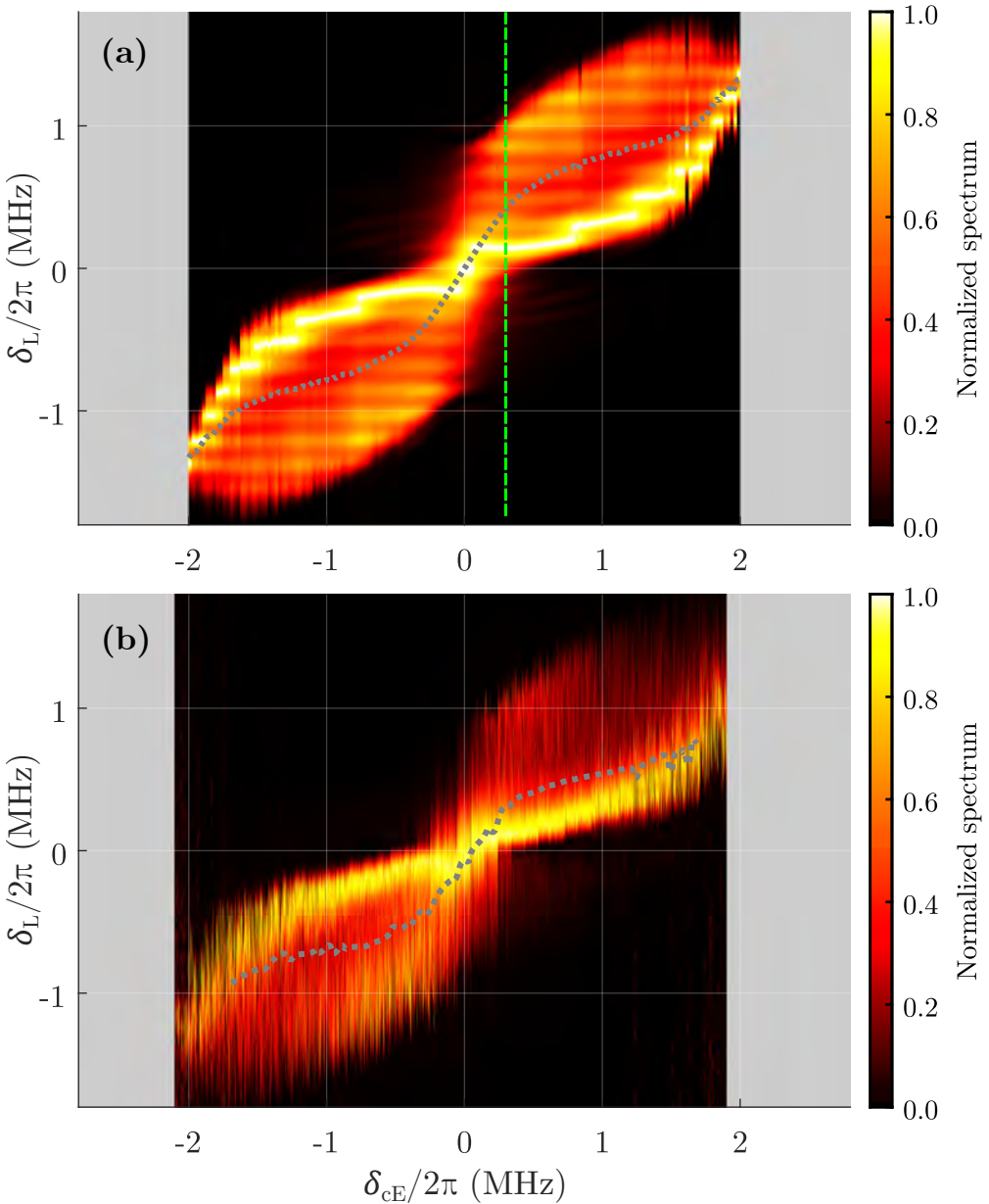


Figure 4.12: Power spectra of superradiant lasing pulses in the mK atom cloud at different cavity detunings  $\delta_{cE}$ , (a) simulations and (b) experiments. The spectra are normalized by the peak value. Gray dotted line indicates a moving mean of the center of mass peak. Green dashed line indicates a point in simulations where the peak frequency is locally insensitive to changes in cavity detuning. Figure adapted from [59].

These spectra enable us to characterize cavity pulling in the system. The local sensitivity of the lasing frequency to changes in cavity detuning is given by  $c_{\text{pull}} = d\delta_L/d\delta_{cE}$ . We can characterize the lasing spectrum both by its peak and "center of mass", where the frequencies are weighted by intensity.

Considering the center of mass (gray dotted curves in Fig. 4.12), we find a gradual variation with cavity detuning. Near  $\delta_{cE} = 0$  we find  $c_{\text{pull}}^{\text{CoM}} = 1.5$ , but as the detuning is increased,  $c_{\text{pull}}^{\text{CoM}}$  gradually becomes lower, reaching a minimum value of 0.25 at  $\pm 1.2$  MHz detuning. This is already a quite low value if simply comparing the 2.3 MHz Doppler width to the 620 kHz cavity linewidth. The dynamics in Fig. 4.10(b) (and other figures shown earlier for 1 MHz detuning) are representative of this regime. For larger detunings the gain is too low to build up an intracavity field that can interact significantly with the slowest atoms, such that the pulse is emitted by an increasingly narrow range of velocity classes with Doppler shifts

closer to the detuning. As a result cavity pulling increases again in this regime.

If we instead consider the peak, we find that cavity pulling varies significantly with the detuning. Around  $\delta_{cE} = 0$  the peak frequency jumps rapidly between  $\pm 150$  kHz, so the pulling coefficient  $c_{pull}^{peak}$  is even greater than 1. However for  $\delta_{cE}/2\pi = \pm 300$  kHz the simulations indicate that  $c_{pull}^{peak} = 0$  (marked by the green dashed line in Fig. 4.12(a)). This occurs due to the interplay between the different velocity groups in a thermal ensemble of narrow-linewidth atoms. Fig. 4.13 shows how the absorption and emission varies across velocity groups in this intermediate regime between the examples in Fig. 4.10.

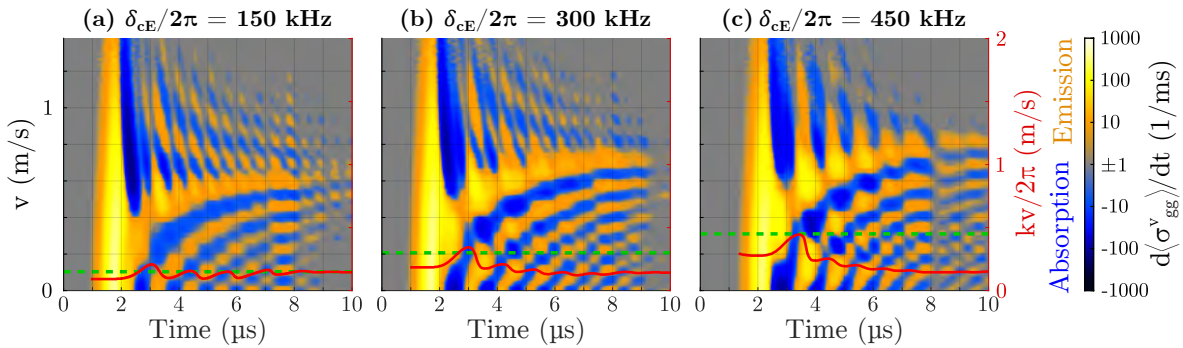


Figure 4.13: The mean absorption and emission rates of an atom during superradiant lasing pulses at three different cavity detunings in a regime where  $c_{pull}^{peak} = 0$ . The right axes show corresponding Doppler frequencies to the left velocity axes. The cavity detuning (green dashed line) and evolution of the peak lasing frequency (red curve) during emission is shown. Slow atoms pull the lasing peak closer to the atom transition during the afterpulses.

In this detuning range, the main lasing pulse is pulled towards the cavity resonance by a factor 0.6, but during the afterpulses, emission by slow atoms pulls the peak to  $\nu_E + 150$  kHz in all three cases. It highlights how atoms with narrow linewidths can be exploited in systems with complex dynamics, in ways that are not obvious e.g. from simply considering ratios between linewidths in the system. The lasing pulses here last only a few  $\mu$ s, so the linewidths are not metrologically interesting. However the considerations could be applied to systems with narrower transitions and possibly even continuous systems in the superradiant crossover regime.

The features in the experiments are not quite as clear as in the simulations, though the general structures persist. In particular the cavity lock PDH signal showed significant fluctuations, potentially due to frequency instabilities in the 689 nm Master Laser. This caused fluctuations in the pump pulse efficiency and in the cavity detuning from the nominal values, which are expected to be the main reasons for the reduction in the experimental data quality compared to the simulations. As a result individual laser pulses compare relatively well with simulations, but tend to vary more, and in many cases clearly correspond to the spectra seen at detunings shifted up to a few hundred kHz from the nominal value.

#### 4.5.2 Cavity noise suppression

As proof of principle we investigated the performance of the system as an active frequency reference based on the peak frequency of the experimental laser spectra in Fig. 4.12(b). The standard deviation of the peak frequencies are plotted in Fig. 4.14 for varying cavity detuning. Outliers are discarded based on a  $5\sigma$  criterium, which primarily filters away data where lasing pulses did not build up at all. The experimental results can be compared to variations expected from simulations (curves), assuming that random, Gaussian fluctuations in cavity detuning is the only source of variations in peak frequency. The curves are based on Monte-Carlo sampling of the lasing peak frequencies from a distribution of cavity detunings centered on the nominal values along the x axis. 1000 samples are included for each point in the curves, and the detunings are not fixed to the particular values of the simulations, but also include values in-between, for which the peak frequency is interpolated.

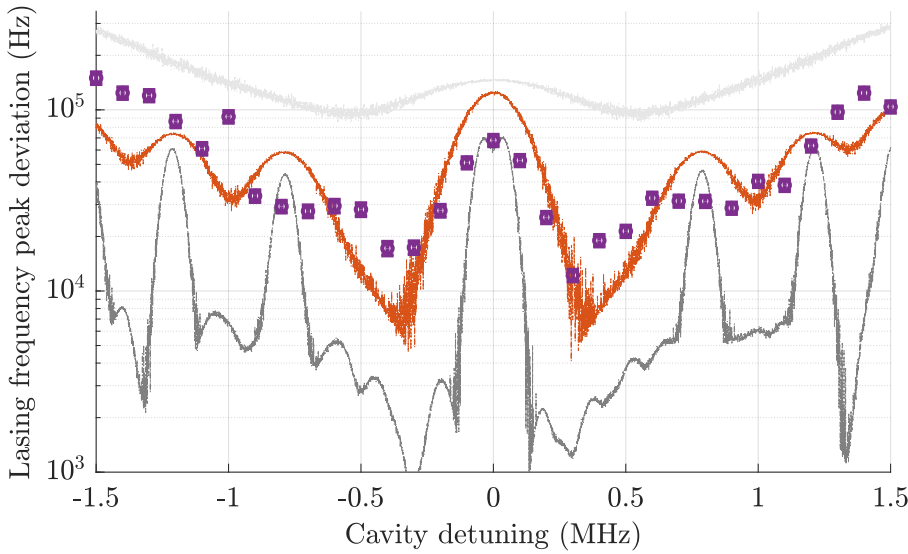


Figure 4.14: Standard deviation of the peak frequency of lasing spectra in experiments (purple points with error bars indicating the standard deviation within a sample) compared to simulations from Monte-Carlo sampling of cavity detunings within a Gaussian distribution (curves, dark gray:  $\sigma = 30$  kHz, orange: 100 kHz, light gray: 300 kHz). Figure adapted from [59].

We find that the variations in peak lasing frequency are reduced significantly at detunings on the order of 300 kHz, where cavity pulling is lowest, and increase significantly for large detunings and near zero, where cavity pulling is highest. However the variations also deviate from the curves based on simulations. This could be due to other sources of fluctuations present in the experiments, such as variations in excitation due to frequency fluctuations of the Master Laser, and of atom number due to drift of the repumping lasers and variations in the 461 nm laser power and frequency.

# Superradiant lasing in the upgraded atom cloud machine

In this chapter we will explore superradiant lasing in the atom cloud machine presented in Chapter 3 in new regimes which were enabled by implementing second-stage cooling. First we will look at superradiant lasing pulses in the crossover regime at  $\mu\text{K}$  temperatures, with the atoms coherently pumped, just as in Chapter 4. Then we will use simulations to explore a quasi-continuous regime, which is enabled by repumping the atoms incoherently and is being investigated in the lab at the time of writing. Finally, we will look at the requirements to realize fully continuous superradiance in the system.

## 5.1 Crossover pulses from atoms at $\mu\text{K}$ temperatures

Here we will consider pulsed lasing in the superradiant crossover regime which can be realized in the  $\mu\text{K}$  atom clouds trapped in the upgraded setup. Compared to the  $\text{mK}$  regime where a Doppler FWHM of 2.3 MHz was realized, this can be reduced to 63 kHz at 3.6  $\mu\text{K}$ , much less than the 620 kHz cavity linewidth. Therefore thermal dephasing will play a much smaller role compared to the behavior we saw in the  $\text{mK}$  regime. This applies both to lasing pulses and during pumping - the  $\text{mK}$  ensemble required a pump pulse duration of the order  $t_P < 1/\Gamma_D \approx 430$  ns to achieve inversion, which required a pump pulse power on the order of 100 mW. At 3.6  $\mu\text{K}$  the corresponding timescale is 2.5  $\mu\text{s}$ , making pumping significantly easier - close to 100% excitation can be achieved even for less than 10 mW, and a homogenous beam profile across the cloud becomes the primary limitation. The cavity coupling still varies greatly as atoms are distributed randomly on the wavelength scale. Similarly the variation due to the 450  $\mu\text{m}$  Gaussian waist is still significant, but smaller as the  $\mu\text{K}$  cloud radius can be reduced to  $\sim 300$   $\mu\text{m}$ , and even less along the vertical axis. Therefore perfect synchronization still cannot be expected for the pulses in the  $\mu\text{K}$  ensemble.

Fig. 5.1 shows simulations and experiments mapping out the cavity output power as function of cavity detuning deep within the crossover regime at  $\mu\text{K}$  temperatures. The setup and model for simulations is the same as in Sec. 4.1, only with parameters changed. For the atom cloud parameters, temperatures of  $\{T_{xz}, T_y\} = \{3.6, 2.6\}$   $\text{mK}$ , a cloud size of  $R_{xz} = 310 \pm 35$   $\mu\text{m}$ ,  $R_y = 135 \pm 35$   $\mu\text{m}$ , and atom number of  $11.5 \pm 1.0$  million were determined from absorption imaging. However the energy contained in the lasing pulses range up to  $15 \cdot 10^6 \hbar\omega$ , and considering the variations in cavity coupling, it is unrealistic that every atom emits a photon, suggesting an even higher atom number. This discrepancy is attributed to saturation effects at high densities, as the calculated atom number of a red MOT cloud can vary by a factor  $\sim 2$  for an expanded cloud compared to a compact one. Therefore  $N = 18 \cdot 10^6$  was assumed in the simulations, for which the peak output power agrees with the experiments.

The pump pulse power at the atoms was estimated at  $18 \pm 2$  mW. The beam profile is shown in Appendix A.5 and can be well approximated by a Gaussian with waists of 2.97 and 3.12 mm along two axes. However the resulting Rabi frequency for these pumping parameters implies a  $\pi$  pulse duration of 660 ns, significantly shorter than the 1030 ns used in experiments. This may be attributed to beam misalignment and polarization imperfections in the experiment. Based on this an effective pump pulse power of 7.6 mW was used in simulations, for which the  $\pi$  pulse duration is in agreement with the known pulse duration.

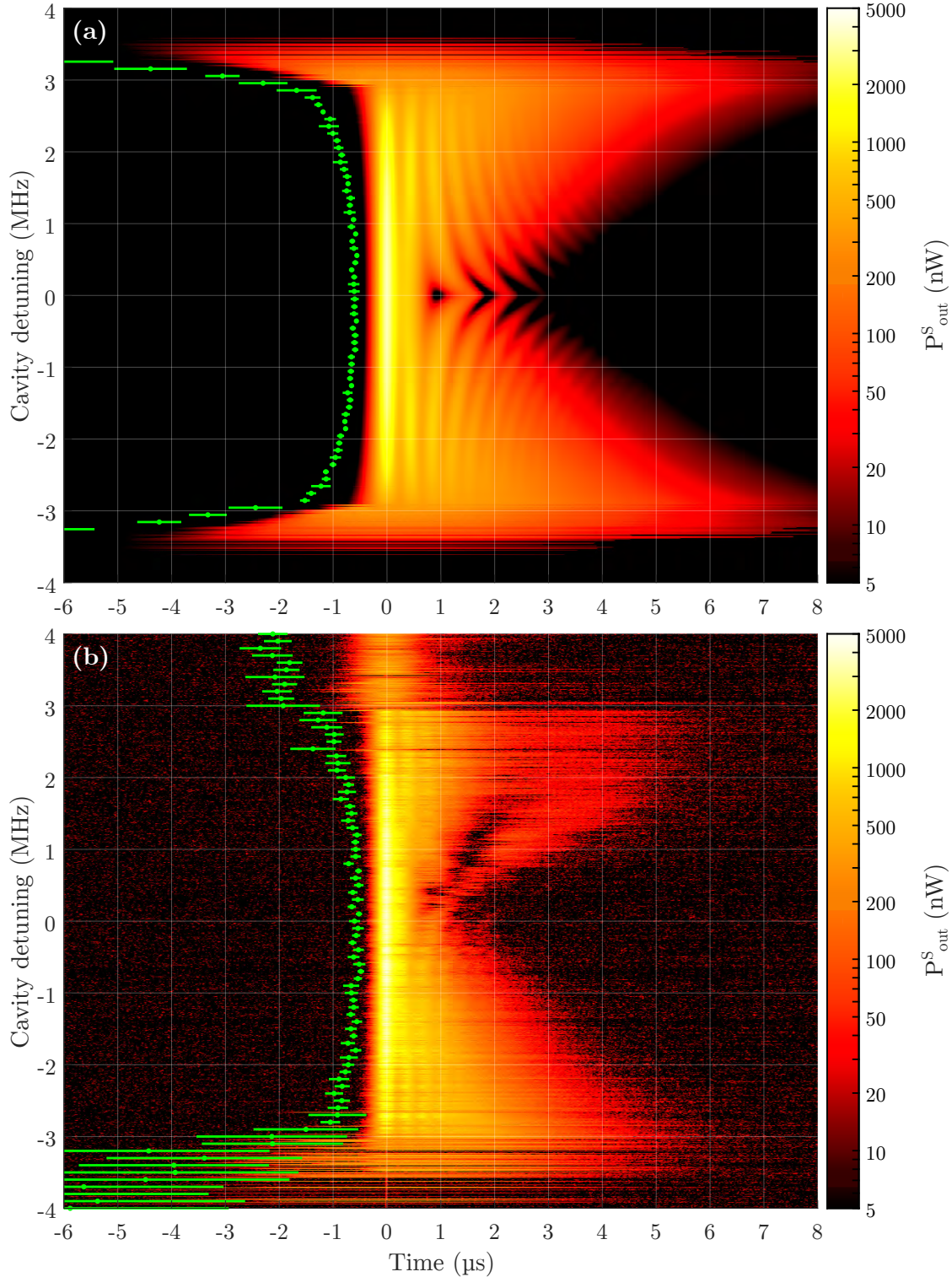


Figure 5.1: *Time-evolution of the cavity output power for different cavity detunings. The time traces are aligned with the peak output power at  $t=0$ . The mean value and standard deviation of the end time of the pump pulses relative to the peak power are indicated by the green data points and error bars. (a) Simulations, (b) Experiments (date: 04/05-2022)*

In this regime the single side output power reaches up to 5  $\mu\text{W}$ , and there are rapid oscillations ( $\sim 2$  MHz) compared to what we saw in Fig. 4.11 for the mK ensemble. This implies the effective  $g\sqrt{N}$  is much greater than  $\kappa$  and other linewidths in the system. Another difference from the pulses in the mK regime is the broader range of cavity detunings facilitating pulses, here up to 3.5 MHz. This range strongly depends on the atom number (see e.g. examples in Appendix A.6) - a larger collective coupling rate enables the ensemble to build up a pulse despite a larger mismatch between the gain and cavity resonances.

The lasing delay in simulations is about 600 ns at  $\delta_{cE} = 0$ , and the over-all variation with detuning is similar, except at large detunings, where the peak output power may be dominated by noise rather than lasing pulses. There are also some qualitative differences in the dynamics, especially at positive detunings. For detunings between 3 and 4 MHz there pulses which are much shorter and less sensitive to cavity detuning than in the simulations. These are most likely emitted by another Zeeman sublevel of  ${}^3\text{P}_1$ , which could be excited due to the imperfect pump pulse polarization. At smaller positive detunings interference effects between pulses from the different Zeeman levels might explain some of the qualitative differences between simulations and experiments in this range.

The power spectra of the simulated lasing pulses within this range of detunings are shown in Fig. 5.2.

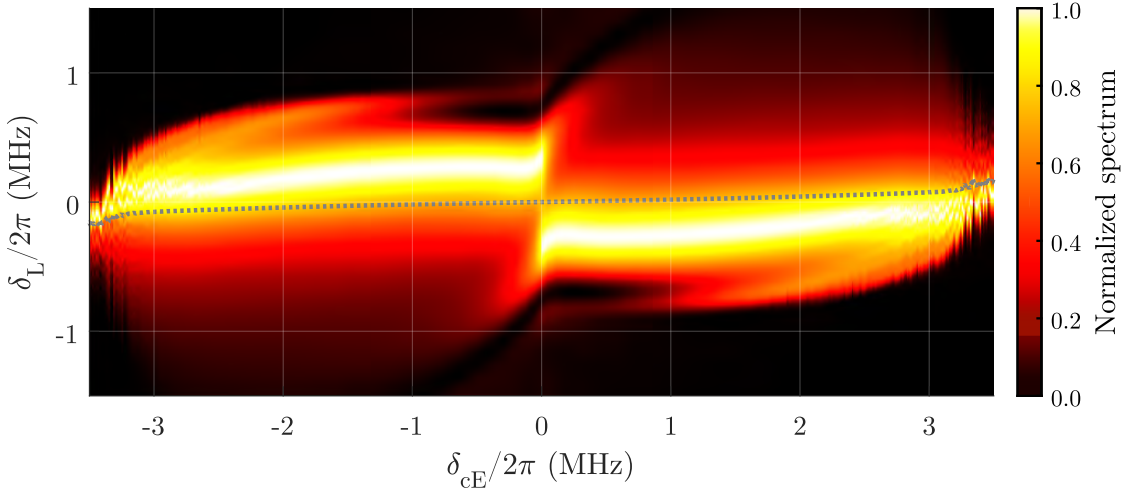


Figure 5.2: Variation of the normalized power spectrum with cavity detuning  $\delta_{cE}$  from simulated lasing pulses in the superradiant crossover regime at  $3.4 \mu\text{K}$ . The gray dotted line indicates the intensity-weighted center of mass of the spectrum.

Compared to the pulse spectra in the mK regime, the center of mass of the spectra (gray dotted line) varies far less with cavity detuning - the local pulling coefficient  $c_{\text{pull}}^{CoM}$  is approximately 0.018 within detunings of  $\pm 500$  kHz, then increases gradually to 0.035 at  $\pm 2.8$  MHz, beyond which it increases more rapidly as the oscillations die out and pulse amplitudes decrease. The peak of the lasing spectrum is consistently shifted with a sign opposite to the cavity detuning, with a jump from +340 to -340 kHz occurring at  $\delta_{cE}=0$ . This splitting corresponds to the period from the main pulse to the afterpulse at  $t=1.5 \mu\text{s}$  for  $\delta_{cE}=0$  in Fig. 5.1(a). Here the main pulse has a "shoulder" with the same phase, while the afterpulse at  $t=1.5 \mu\text{s}$  has the opposite phase. Changes in e.g. atom number or excited population can lead to regimes more similar to the dynamics in Fig. 5.1(a) where afterpulses are more heavily suppressed, if the initial lasing pulse and shoulder efficiently de-excites the ensemble. In these cases the spectral peaks join together around  $\delta_{cE}=0$  instead of splitting. Some examples of these variations in the dynamics within the crossover regime and the transition to the pure superradiant regime are also shown in Appendix A.6.

Besides from the jump, the lasing peak frequency varies in a more simple manner with detuning than what we saw in the mK pulses, as the atoms with different velocities synchronize to a higher degree. Similarly to the mK pulses, there is also a range of detunings where the peak frequency locally does not vary with cavity detuning to first order, here at  $\pm 600$  kHz.

## 5.2 Simulations of quasi-continuous superradiance

In this section we will consider quasi-continuous superradiant lasing which can be realized in the setup by continually repumping the atom cloud. To simulate this we model repumping as inverse spontaneous emission at a uniform rate  $w_{ge}$  from  ${}^1S_0$  to  ${}^3P_1$   $m_J=0$ :

$$\begin{aligned}\langle \dot{\sigma}_{ge}^j \rangle &= - \left( i\delta_{Ep} + \frac{\gamma_{eg} + w_{ge}}{2} \right) \langle \sigma_{ge}^j \rangle + ig^j \langle a \rangle (\langle \sigma_{ee}^j \rangle - \langle \sigma_{gg}^j \rangle) \\ \langle \dot{\sigma}_{ee}^j \rangle &= -\gamma_{eg} \langle \sigma_{ee}^j \rangle + w_{ge} \langle \sigma_{gg}^j \rangle + ig^j (\langle a^\dagger \rangle \langle \sigma_{ge}^j \rangle - \langle a \rangle \langle \sigma_{eg}^j \rangle) \\ \langle \dot{a} \rangle &= - \left( i\delta_{cp} + \frac{\kappa}{2} \right) \langle a \rangle - \sum_{j=1}^N ig^j \langle \sigma_{ge}^j \rangle \\ \langle \dot{f}_k \rangle &= - \left( i\delta_{fp}^k + \frac{\kappa_f^k}{2} \right) \langle f_k \rangle - ig_f \langle a \rangle.\end{aligned}\quad (5.1)$$

First it is worth considering the physics that the repumping term  $w_{ge}$  represents. To realize this requires a concrete scheme, where we here assume pumping to  ${}^3P_1$   $m_J=-1$ , then  ${}^3S_1$ , from which atoms decay into the  ${}^3P_0$ ,  ${}^3P_1$  and  ${}^3P_2$  manifolds. If they do not decay into  ${}^3P_1$   $m_J=0$  at first, 679 and 707 nm lasers pump them back to  ${}^3S_1$  until they eventually end up there. The laser-driven transitions between Zeeman levels are depicted in Fig. 5.3(a), for a choice of laser polarizations we will also consider in later chapters. Modeling all the transitions between these Zeeman levels as discrete jumps based on probabilities from rate equations, we can determine how atoms will be transferred between the different states during repumping. Defining pumping rates of  $2\pi \cdot 70$  kHz from  ${}^1S_0$  to  ${}^3P_1$   $m_J=-1$  and 5 MHz for the other transitions, the populations in a sample of  $10^6$  atoms evolve as shown in Fig. 5.3(b) when the decay of the target state  ${}^3P_1$   $m_J=0$  is set to zero. During such a repumping cycle the number of photon recoils are shown in the histograms in Fig. 5.3(c).

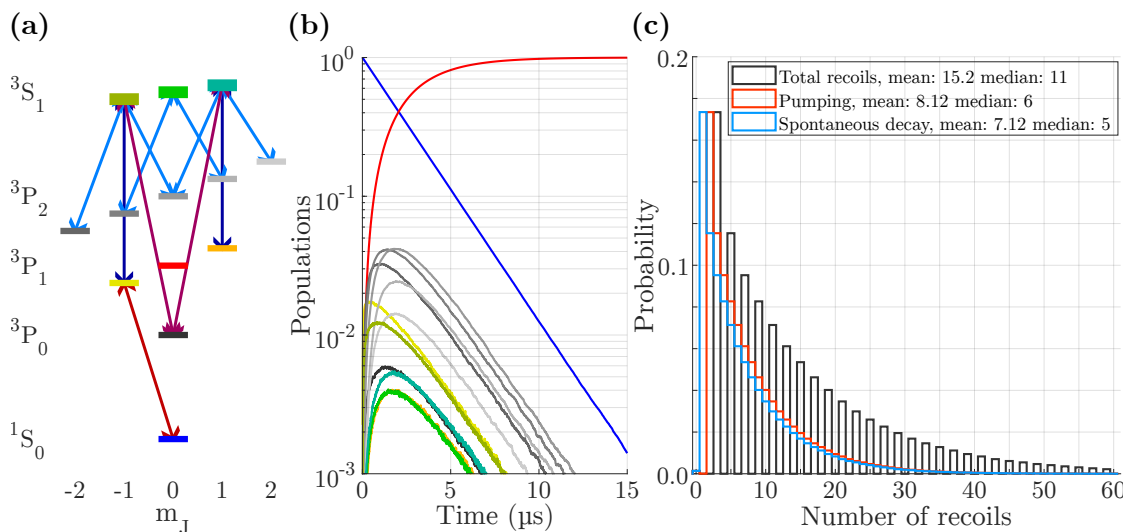


Figure 5.3: Quantum jump simulation of rate equations when pumping from  ${}^1S_0$  to  ${}^3P_1$   $m_J=0$ . (a) Zeeman-transitions driven by lasers, (b) populations in the simulation with decay from  ${}^3P_1$   $m_J=0$  set to zero (using the same colors as the states in (a)), (c) histogram of the number of recoils during the transfer to  ${}^3P_1$   $m_J=0$ .

Here we see that for this repumping scheme, a given atom is subjected to 8.1 photon recoils from the pumping lasers on average, and 7.1 subsequent recoils from spontaneous decays. For this choice of repumping transitions the recoil statistics are independent of the repumping rates except for the rate from  ${}^3\text{P}_1 m_J=-1$  to  ${}^3\text{S}_1 m_J=-1$ . Here atoms may fall back to  ${}^1\text{S}_0$  if the pump rate to  ${}^3\text{S}_1$  is lowered to the magnitude of  $\gamma_{eg}/2\pi = 7.5 \text{ kHz}$ .

One recoil kick at 689 nm corresponds to a velocity shift of  $\hbar\omega/mc = 6.6 \text{ mm/s}$ . Approximating all the recoils by 689 nm photons, we can find the mean momentum diffusion rate from spontaneous emission [104, p. 247] during repumping (assuming the rate  $w_{ge}$  represents the whole repumping cycle, neglecting any delays primarily from the  ${}^3\text{P}_1-{}^1\text{S}_0$  transition):

$$D = k_s w_{ge} \hbar^2 k^2, \quad (5.2)$$

Where  $k_s = 7.1$  is the number of spontaneous decay events per repumping cycle. We will consider blue and red MOT cloud parameters at 5 mK and 50  $\mu\text{K}$  respectively, for which  $v_{rms} = 1.2$  or  $0.12 \text{ m/s}$ , for comparison. The momentum diffusion grows as  $\sqrt{\langle p^2 \rangle} = \sqrt{Dt}$ , which we can use to find the timescale on which spontaneous emission changes the temperature comparably to the initial value, based on  $v_{rms}$ :

$$\tau_s = \frac{\langle p_0^2 \rangle}{\hbar^2 k^2} \frac{1}{k_s w_{ge}} = \frac{3mc^2 k_B T}{\hbar^2 \omega_E^2} \frac{1}{k_s w_{ge}}. \quad (5.3)$$

For a relatively high repumping rate of  $w_{ge} = 10\gamma_{eg} = 2\pi \cdot 75 \text{ kHz}$  this gives 50  $\mu\text{K}$  and 5 mK on the order of 100  $\mu\text{K}$  and 10 ms, respectively.

### 5.2.1 Quasi-continuous pulses in the $\mu\text{K}$ regime

Here we will consider a few examples of quasi-continuous lasing in a red MOT cloud with  $N = 10^7$  atoms, starting with  $T = 50 \mu\text{K}$  and  $\sigma_R = 300 \mu\text{m}$ . Photon recoils from repumping are included in these simulations, influencing the motion of atoms. This is done by applying photon kicks based on tracking the population change due to repumping, as described in Sec. 2.5. Gravity is neglected in the model, and recoils from the repumping laser beams are applied along the y-axis (vertical) with balancing forces. In an experiment the power balance from the two laser beam directions can simply be adjusted to counteract the force of gravity. We will consider a situation with a constant cavity detuning of 300 kHz to see how cavity fluctuations can influence the lasing spectrum.

In Fig. 5.4 the dynamics are shown for  $w_{ge}/2\pi = 75 \text{ kHz}$ . The evolution of the z-axis temperature of atoms within the cavity waist radius,  $T_z^W$ , is shown in panel (a), and the total cavity output power is shown in panel (b). As atoms move outside the cavity waist and the temperature increases, the power drops, which slows the rate of transitions ( $2g\sqrt{n}$ ) from  ${}^3\text{P}_1$  to  ${}^1\text{S}_0$ . This in turn slows the total repumping cycle time and the increase in temperature. In panel (c) snapshots of the spatial evolution of the atom cloud in the zy-plane are shown for  $t = \{0.1, 2.0, 3.0\} \mu\text{s}$ . The cavity waist is indicated by red dashed lines, and the atoms are color-coded by their state ( ${}^3\text{P}_1$ : red and  ${}^1\text{S}_0$ : blue). Here we see how the inversion increases spatially with time as  $g\sqrt{n}$  decreases.

A spectrogram is shown in panel (d), normalized by the peak PSD during the simulation. The window duration is chosen as 10  $\mu\text{s}$ . The lasing frequency is initially shifted by 80 kHz from the atomic transition, giving  $c_{pull}^0 = 0.27$ . However as the cloud expands and the temperature increases, cavity pulling also increases gradually, so the lasing frequency slowly chirps closer to the cavity resonance. This gives a 70 kHz-wide "pedestal" in the final spectrum (panel (e)) containing most of the energy. After 2.2 ms oscillations in the output power start here atoms no longer synchronize across velocity groups, and instead a subset of atoms begin lasing at a frequency 380 kHz from the atomic transition (this component is very faint in the

spectrogram). At this point the main frequency component stops pulling towards the cavity resonance, but remains more steady. This gives rise to the largest peaks in the spectrum - one at  $\delta_L/2\pi = 143$  kHz and another one at 153 kHz.

The faint sideband pulls towards the main peak and gives rise to a broad feature in the final spectrum, containing only 1% of the energy. Oscillatory regimes with multiple spectral components have been described in [87] in a continuous system based on a beam of hot atoms. A simple criterium arises when an atomic beam with uniform velocities is simply slanted with respect to the cavity axis, as in [89]. Here oscillations arise when the atoms move across more than half a wavelength along the cavity axis (such that the coupling changes sign) during the transit time. In our system the corresponding criterium is whether atoms in the ensemble tend to move more than  $\lambda/2$  along the z-axis during the emission timescale  $(2g\sqrt{n}/2\pi)^{-1}$ , as they are continually repumped. At  $t = 2.2$  ms the Doppler FWHM has reached 710 kHz, while the cavity photon population has decreased to  $n = 1.2 \cdot 10^5$ , giving a maximum  $2g_0\sqrt{n}/2\pi = 560$  kHz.

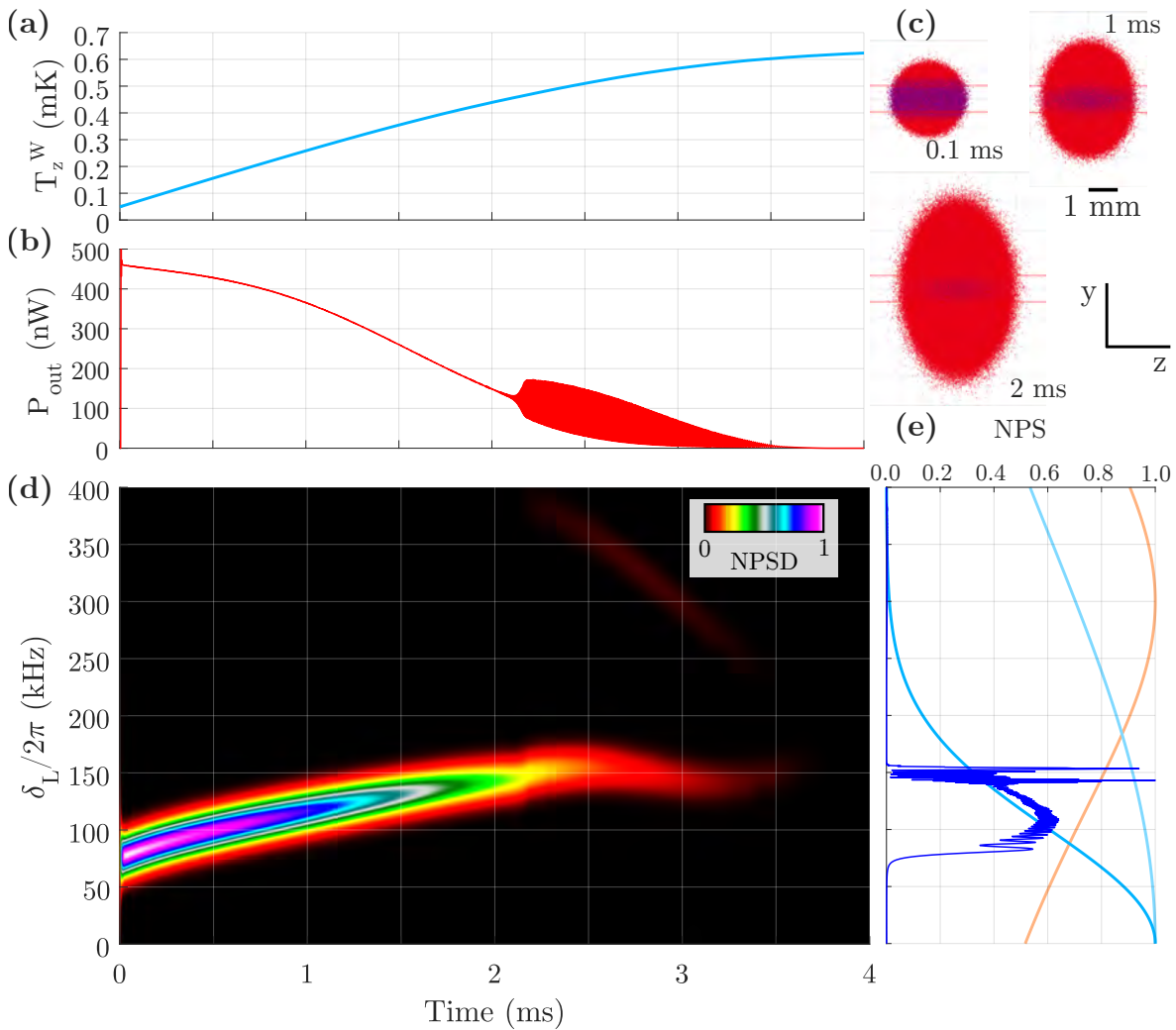


Figure 5.4: *Dynamics in quasi-continuous superradiant lasing in a red MOT cloud.* (a) Time evolution of the temperature along the cavity axis, for atoms within the cavity waist. (b) Cavity output power. (c) Expansion of the cloud during emission -  ${}^1S_0$  atoms are blue,  ${}^3P_1$  are red. (d) Normalized power spectrogram during emission. (e) Final power spectrum of the entire pulse (dark blue curve), compared to initial and final Doppler widths (medium and light blue) and the cavity resonance (orange).

We can compare the dynamics for a lower repumping rate  $w_{ge} = 2\pi \cdot 15$  kHz. The panels in Fig. 5.5 present the different dynamics in the same way as in Fig. 5.4. The lower repumping rate gives rise to a much smaller increase in temperature (panel (a)) and a lower output power (panel (b)). As a result the pulse duration is extended from 4 to 5 ms. In panel (c) the slower cloud expansion is illustrated, again for  $t = \{0.1, 2.0, 3.0\}$   $\mu$ s. The spectrogram in panel (d) shows several different components, appearing with the oscillations already after just 50  $\mu$ s. Here the Doppler FWHM is only 240 kHz, but with  $n = 3.6 \cdot 10^4$  the maximum Rabi frequency is also comparatively lower at  $2g_0\sqrt{n}/2\pi = 310$  kHz, so narrower ranges of velocity classes can synchronize, and the dynamics eventually become chaotic. The resulting spectrum in panel (e) is much more noisy, but at the same time lacks the very broad pedestal we saw in Fig. 5.4(e). The largest peak is at  $\delta_L = 2\pi \cdot 67$  kHz and has a FWHM of 540 Hz, but contains only  $\sim 15\%$  of the energy. 50% of the energy is contained within the major peaks between  $\delta_L = 55$  kHz and 70 kHz.

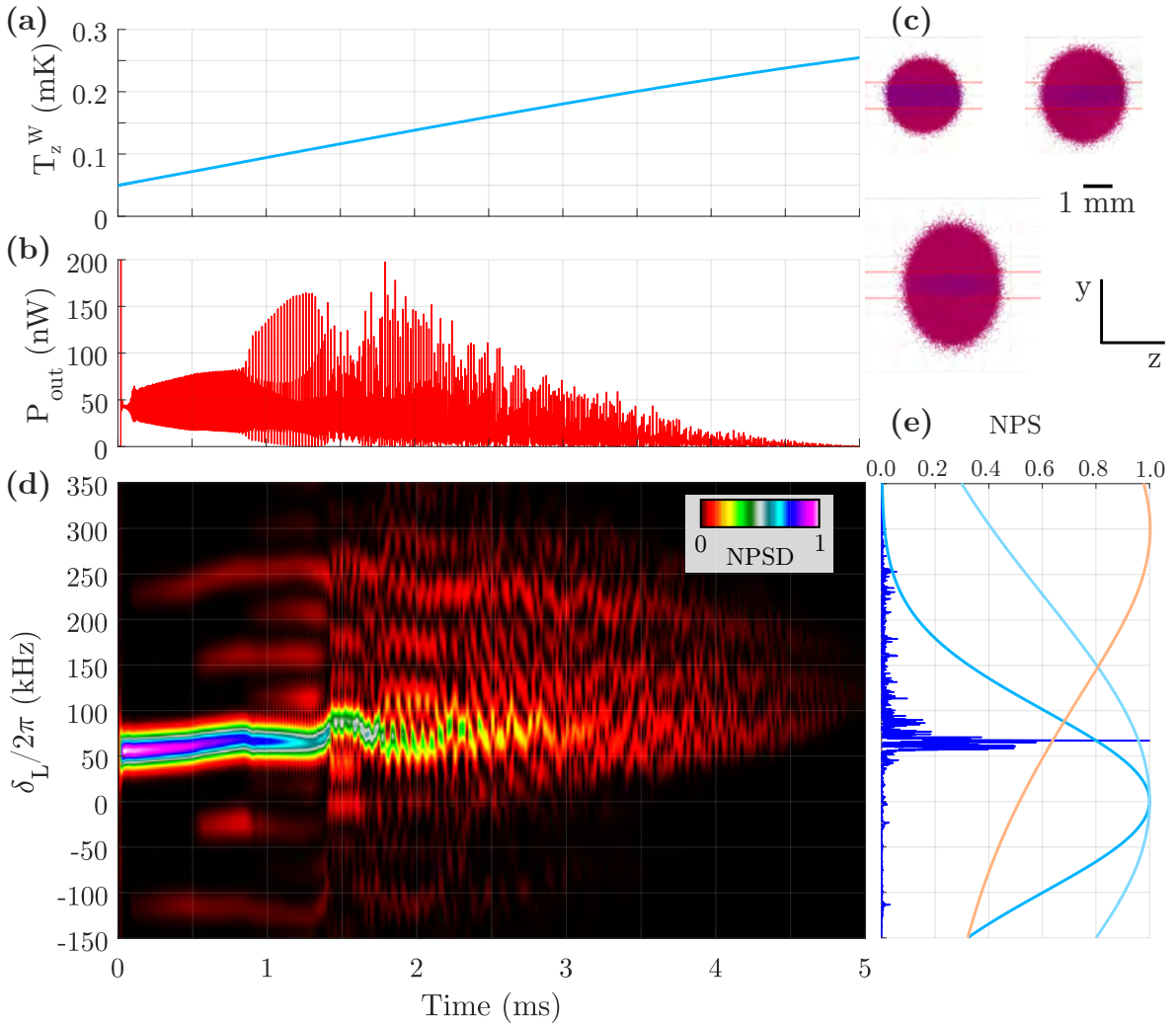


Figure 5.5: *Dynamics in quasi-continuous superradiant lasing in a red MOT cloud.* (a) Time evolution of the temperature along the cavity axis, for atoms within the cavity waist. (b) Cavity output power. (c) Expansion of the cloud during emission -  ${}^1S_0$  atoms are blue,  ${}^3P_1$  are red. (d) Normalized power spectrogram during emission. (e) Final power spectrum of the entire pulse (dark blue curve), compared to initial and final Doppler widths (medium and light blue) and the cavity resonance (orange).

These quasi-continuous pulses are dominated by features with widths significantly greater than the Fourier limit due to the changing conditions during the dynamics and the finite cavity detuning. If the detuning could be kept within a narrow range around zero, changes in  $c_{pull}$  would cause the frequency to wander less during the pulse, and narrower features could

be expected. Additionally the atoms might also be used in a "smarter" way that reduces changes in  $c_{pull}$ , by cancelling out some of the changes that are caused by the cloud expansion and heating. For example, trapping a cloud a bit off-center from the cavity and creating a slowly increasing atom density within the cavity might largely cancel out the changes in  $c_{pull}$  we saw here were caused by expansion and heating. This may also allow for linewidths closer to the Fourier limit.

### 5.2.2 Quasi-continuous pulses in the mK regime

As an alternative we can consider quasi-continuous pulses in a blue MOT cloud with  $N = 105 \cdot 10^6$  atoms,  $\sigma_R = 0.9$  mm and  $T = 5$  mK. The higher initial temperature implies a smaller relative change in the conditions due to heating from repumping. We consider a high repumping rate of 75 kHz again. The repump heating timescale of 10 ms (about four times the pulse duration) motivates recoils not being included in this model. Additionally the atom group approximation (Sec. 2.7) is used, with 28 atoms/group for these simulations.

In Fig. 5.6 the dynamics are shown for zero cavity detuning. The repumping rate puts the system in a regime with cavity output power of similar magnitude to the pulses in Sec. 4.5. From the emitted power during oscillations after the initial settling we can find  $\langle \sqrt{n} \rangle^2 = 3.9 \cdot 10^5$ , which gives  $2g_0 \langle \sqrt{n} \rangle^2 / 2\pi = 1.0$  MHz, significantly smaller than the Doppler FWHM of 2.3 MHz, so here we get multiple frequency components from different velocity classes from the very beginning, close to  $\delta_L = \pm 2g_{eff} \langle \sqrt{n} \rangle^2 = 2\pi \cdot 510$  kHz. Because the cavity detuning is zero, the central component is not influenced by cavity pulling. This gives a central peak which has a FWHM of 680 Hz and contains 65% of the spectral energy. Once the density becomes sufficiently low, the system transitions to a chaotic regime, and then to two symmetric components. These regimes were also found in [87, Fig. 8] occurring for increasing thermal widths in a continuous beam with constant density. They arise here as function of time because of the gradually decreasing emission timescale (due to decreasing density) relative to the thermal width.

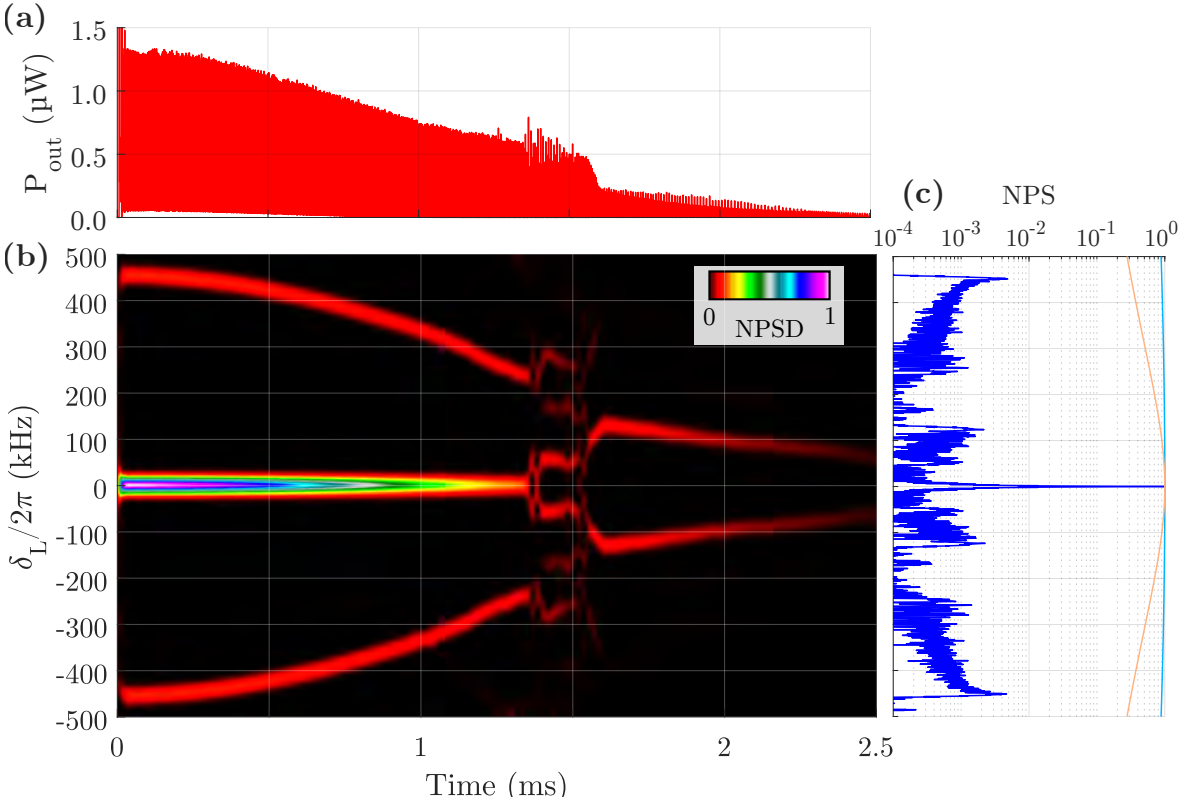


Figure 5.6: *Quasi-continuous lasing dynamics in a blue MOT cloud at zero cavity detuning.* (a) Cavity output power, (b) normalized power spectrogram, (c) final power spectrum.

In Fig. 5.7 three examples show the dynamics for cavity detunings of 200, 300 and 400 kHz - the "cavity-immune" regime in Sec. 4.5, according to the peak frequency of the pulse spectra. The finite detuning changes the relative size of the two sidebands, but also generally shifts the frequency of them. The change in density further shifts them over time. However there appears to be one exception - the central frequency component in panel (a) does not shift systematically before the chaotic regime beginning after 800  $\mu$ s. This gives a component at  $\delta_L/2\pi = 226$  kHz with a FWHM of 1.5 kHz and could be an interesting candidate for a component that is immune to small fluctuations in the cavity detuning.

Another interesting feature within this range of detunings is that the triple-peaked configuration is especially stable around  $\delta_{cE} = 2\pi \cdot 300$  kHz - at other detunings, chaotic or double-peaked lasing occurs at some point during the cloud expansion.

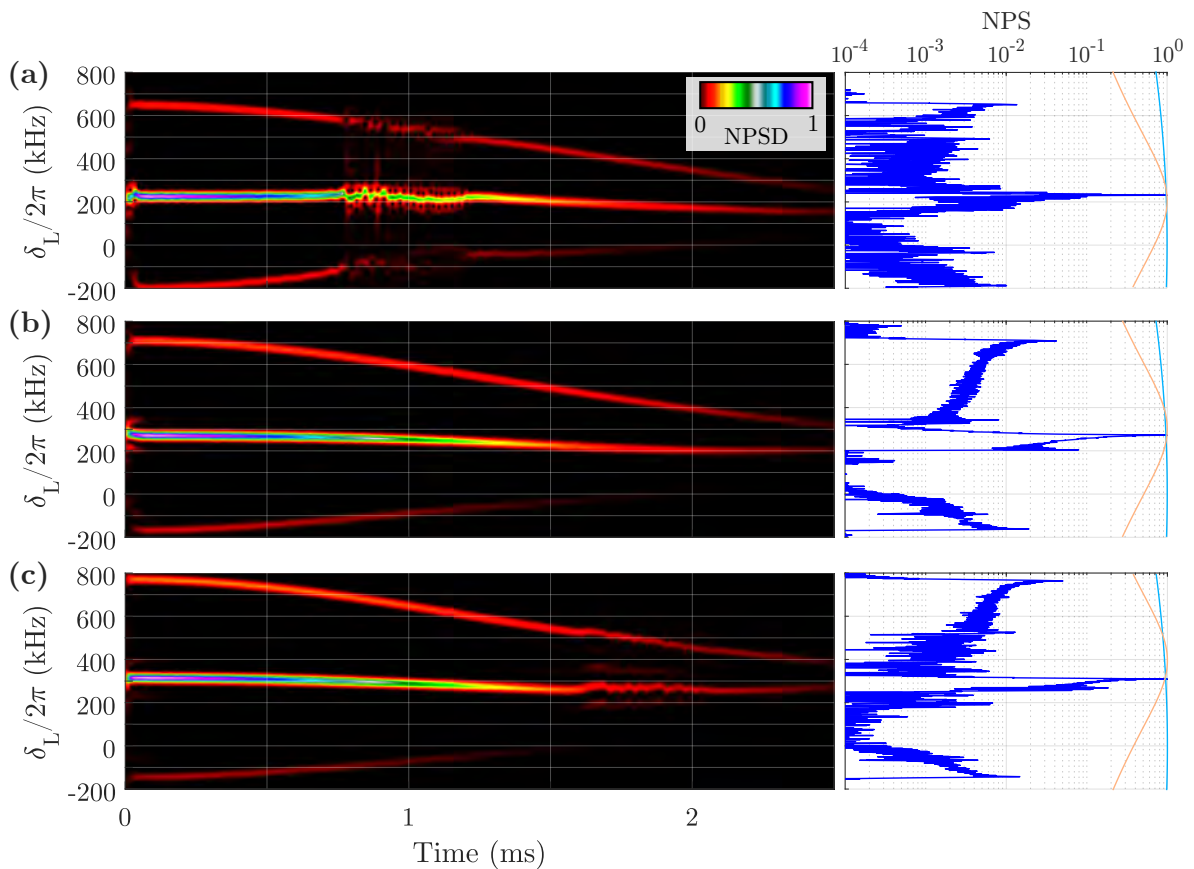


Figure 5.7: Spectrograms (left) and final normalized power spectra for cavity detunings of (a) 200 kHz, (b) 300 kHz and (c) 400 kHz. The frequencies of the peaks are influenced by different cavity pulling coefficients as the density decreases, broadening the spectral features. Around 300 kHz the triple-peaked configuration is especially stable - at other detunings, chaotic and double-component lasing occurs during the cloud expansion.

As for the red MOT cloud examples, a finite cavity detuning also appears to broaden any spectral features from a blue MOT cloud. Also here a strategy to reduce this effect would be to create as constant conditions (atom number and temperature) within the cavity waist as possible during the pulse. This would simultaneously prevent the jumps from triple-peaked lasing to chaotic or double-peaked lasing, which limited the laser linewidth for the zero-detuning case. If this can be realized, the laser pulse linewidth  $\Delta\nu$  could approach the Fourier limit set by the pulse duration for both the red and blue MOT cloud parameters - on the order of a few hundred Hz. This still requires the cavity detuning is kept within  $c_{pull} \cdot \Delta\nu$  for the duration.

### 5.3 Requirements for steady-state superradiance

By trapping a blue MOT cloud above the science cavity with a power imbalance that redirects the atoms through the cavity, continuous superradiance could potentially be realized in the machine. The atom temperature could be reduced further using a 9.8 MHz-wide transition from  ${}^3\text{P}_2$  to  ${}^3\text{S}_1$  at 604 THz (see Fig. 1.1) - this has been demonstrated in [22]. To investigate the requirements for this, we will assume the atoms are continuously repumped at a uniform rate while propagating through the cavity (as in Eqs. 5.1), and omit recoils from repumping. We assume the atoms can initially be described as a uniform beam, using the model for propagation which is presented in detail in Sec. 7.1, here with  $T_x = 5 \text{ mK}$  along the propagation axis, and a radial temperature in the range of 0-5 mK. The atom flux in the model is defined by the number of atoms starting within  $|y| < W$  at a distance of  $x = -1.5W$  from the center of the cavity, but the total number of atoms in the simulation is higher, as they are generated uniformly within  $|y| < 1.5W$ . The atom group approximation is used here, with 10 atoms/group for fluxes below  $10^9 \text{ s}^{-1}$  and 100 for higher fluxes.

In Fig. 5.8 the total cavity output power is plotted as function of the atom flux and repumping rate  $w_{ge}$  for different radial temperatures. For emission to occur,  $\sim 10^8$  atoms/s are required through the cavity mode at 0 K ( $\sim 6 \cdot 10^4$  within the mode in steady-state), increasing to  $3 \cdot 10^9 \text{ s}^{-1}$  at 5 mK. At higher temperatures, higher repumping rates are required for an optimal output power. The required atom flux is of the same order of magnitude as the peak loading rates for blue MOT clouds, so continuous operation is realistic if they can be funneled and cooled efficiently. Decoherence from stray light at 461 nm presents a risk, and an impact could be expected on the power in Fig. 5.8 if the decoherence rate grows to the order of the repumping rate (see e.g. more detailed considerations for the hot beam system in Sec. 7.2.3).

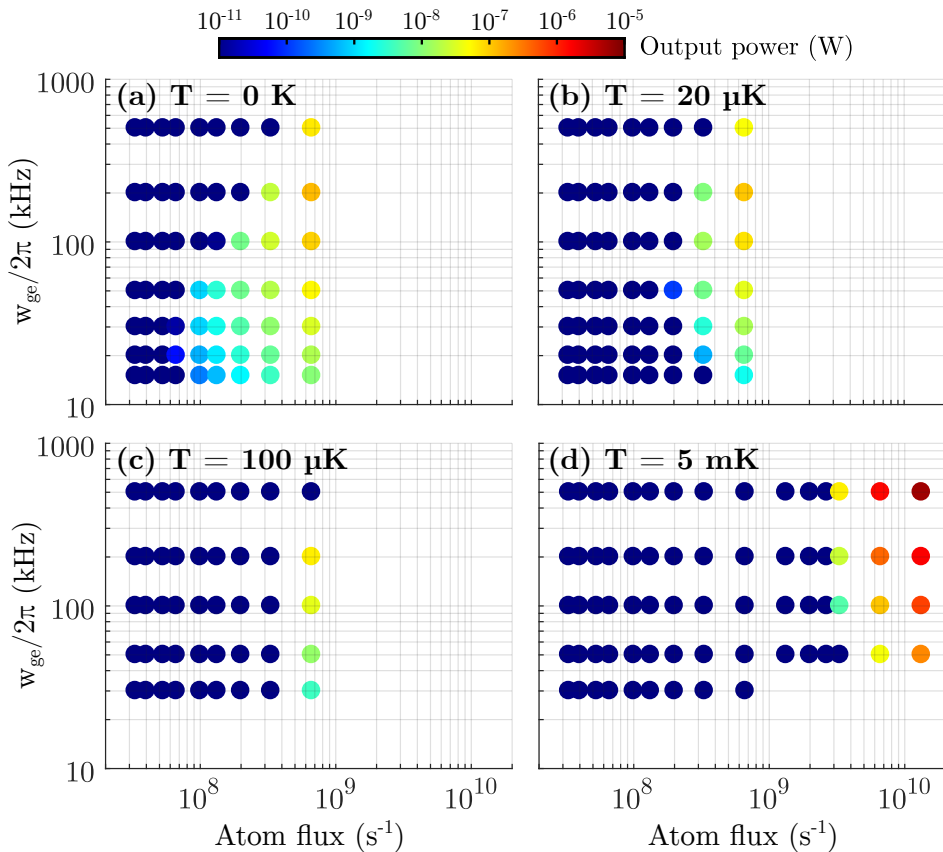


Figure 5.8: Total cavity output power in simulations for different repumping rates  $w_{ge}$ , temperatures (a-d) and varying atom flux, assuming a continuous atom source in the atom cloud machine.

# Machine for continuous superradiant lasing at UvA

In this chapter we will look at the progress of building a continuous superradiant lasing machine (SRLM) at the University of Amsterdam. Here I was on secondment for six months and joined the Strontium quantum gases group<sup>1</sup>, headed by Florian Schreck, shortly before the assembly of the SRLM began. In addition to Florian I also enjoyed working with Camila, Francesca, Sheng, Zeyuan, Stefan, Benjamin and Shayne on the project. The goal of the SRLM is to realize a proposal for continuous superradiance based on a hot atomic beam [86], in our case using the  $^1\text{S}_0$ - $^3\text{P}_1$  transition in  $^{88}\text{Sr}$ . The proposal is illustrated in Fig. 6.1. Here an atomic beam emitted from an oven is transversely laser-cooled, then pumped to the excited state before passing through an optical cavity. This is a simple system compared to other continuous schemes based on ultra-cold atoms transported through optical lattices. Since the scheme has no intermediate trapping and transfer stages, which tend to be lossy, it allows for a large atom flux through the cavity and a high output power. The full experimental system involved in realizing this proposal consists of extensive laser systems in addition to the machine itself, but here focus will be on the core machine and selected parts that I worked on. In addition we will also use numerical simulations to explore the pumping stages in the machine, where the atoms are prepared before they reach the cavity.

## 6.1 Monitor cavities

Six monitor cavities were assembled for monitoring the spectral components of laser beams in the lab. These cavities are peripheral systems, supporting but not directly involved in the SRLM. They consist of two mirrors separated by a spacer, with one mirror mounted on a piezo so that the cavity length can be scanned. They are designed to have a relatively small finesse ( $F \approx 240$  at 461 or 689 nm and  $L = 10$  cm). This means the piezo can be used to continually scan on the order of an FSR, and a single-frequency input beam will then give a Lorentzian peak in the cavity transmission. If the input beam instead has multiple frequency components, the cavity transmission will have peaks of varying size from each of these components. This makes the cavities a useful tool to monitor whether laser injections

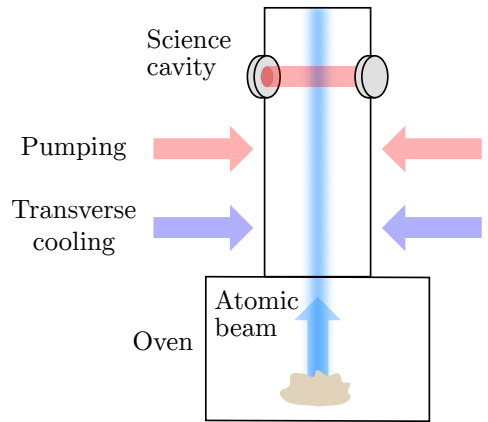


Figure 6.1: Illustration of the proposal for superradiant lasing based on a hot atomic beam. Atoms from an oven are transversely cooled and then pumped to the excited lasing state before entering the cavity for superradiant emission.

<sup>1</sup>Website: [strontiumbec.com](http://strontiumbec.com)

and locks are stable or have failed, which are common sources of problems in a setup.

The setup for assembly is shown in Fig. 6.2(a). A laser beam was sent through the cavity during assembly, while monitoring the transmission on a photodiode and beam profiler. The cavity mirrors were initially held in mounts fixed on translation and rotation stages. Cuts in the mounts give space for gluing the mirrors onto the cavity assembly. For gluing we used a two-component epoxy glue. First the piezo side mirror was glued (right side on the figure), after verifying that it was as centered as possible on the cavity. After the glue dried, the second mirror was moved into position (left side in the image, hidden by the holder) while scanning the piezo. The cavities are designed for a confocal arrangement, so when the second mirror is too far from its desired location, spatial modes show up with different resonance frequencies in the transmission while scanning. As the mirror is moved to the correct distance from the other, the modes in the transmission merge together (see e.g. similar behavior near the concentric configuration in [143, p. 10]). This configuration helps to ensure that different peaks encountered while scanning originate from different frequency components rather than simply transverse modes. After finding this position the mirror alignment was fine-tuned to achieve the narrowest possible linewidth, then the mirror was glued. The process of gluing can be tricky with a horizontal cavity, and depending on the viscosity of the glue, gravity can be a disturbance when placing it on a downwards-facing side.

In Fig. 6.2(b) a breadboard is shown with two monitor cavities mounted and intended beam paths highlighted. The optics are designed such that beams from three fibers can be coupled into each monitor cavity and monitored on the same photodiode.

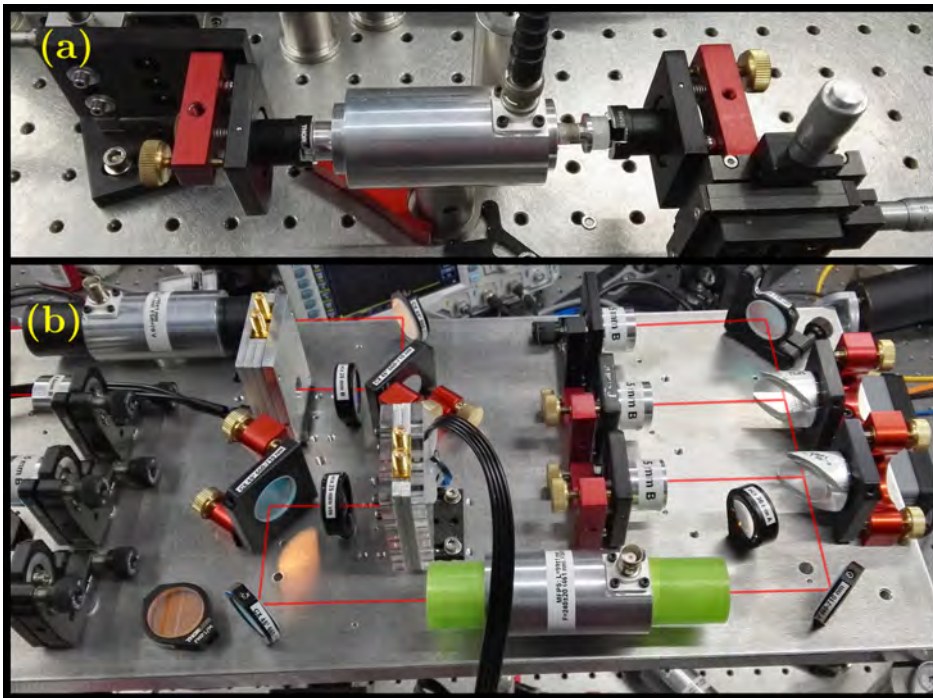


Figure 6.2: (a) A monitor cavity being assembled, with one mirror glued onto the piezo in the right end. (b) A breadboard for two monitor cavities with optics being assembled and beam paths highlighted. Each cavity is used to monitor up to three fiber-coupled laser beams.

## 6.2 The science cavity

The science cavity is a core component of the SRLM and its assembly and properties are described in this section. The cavity spacer is a custom design by Shayne Bennetts and is made of Macor glass-ceramic to keep the intra-mirror distance steady. One mirror is glued directly onto the spacer, and the other is glued onto an assembly of two piezo-electronic rings

and additional spacers. In this configuration the cavity becomes longer when the outer/inner piezo respectively expands/contracts, which helps to cancel out some of the nonlinear behaviors of the piezos. The glue used for the assembly is Epotek ND353, which must be cured at 80-150 °C for a certain duration depending on the temperature [144]. This glue initially becomes less viscous as it is heated up, but subsequently hardens and gains an amber color. In the assembly process the parts were first cleaned with acetone and ethanol. Then, over a couple of rounds, the pieces were glued together and heated up in an oven to cure the glue, except for the final mirror to be glued directly onto the spacer. This initial assembly process is shown in Fig. 6.3.

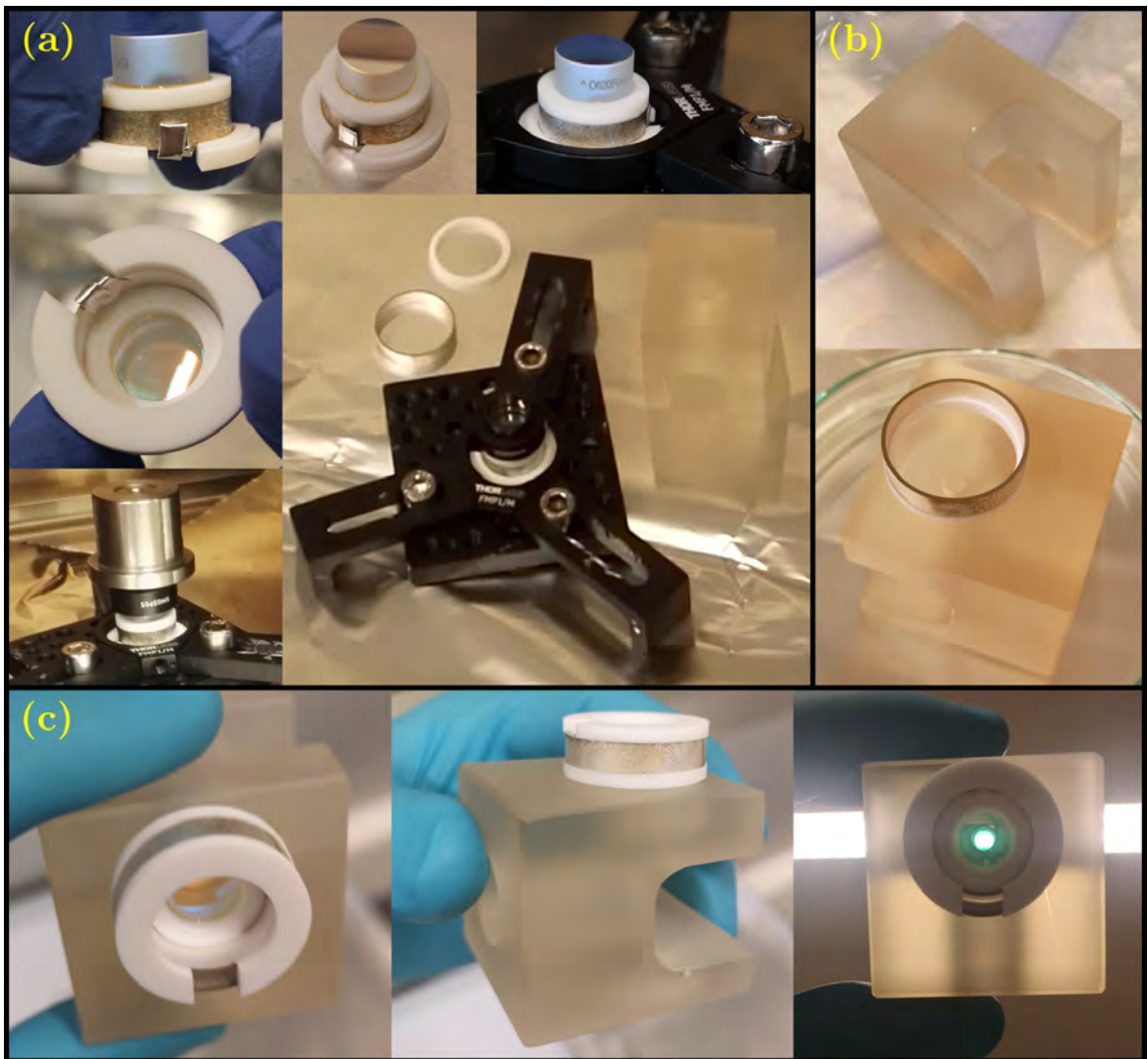


Figure 6.3: Assembly of the science cavity. (a) Gluing of the inner piezo ring and cavity mirror, and items added to apply force while heating the glue. (b) The cavity spacer and outer piezo ring. (c) Combination of spacer, piezo stack and mirror.

After the assembly, wires were soldered onto the piezos, and it was placed into a setup built for securing the second cavity mirror (Fig. 6.4). Based on the experience in Sec. 6.1, this setup was designed such that the mirror could be aligned and glued with the cavity oriented vertically. Due to the requirements of the glue a "curing oven" was designed, surrounding the assembly with aluminium plates which had resistors mounted onto them. The oven base was isolated with wooden spacers from the steel posts mounted onto the breadboard. This helped to reduce thermal conduction from the oven part to the optical elements and to minimize disturbing the laser beam path while curing the glue. Three thermistors were glued onto the oven to monitor the temperatures at the top, bottom and side.

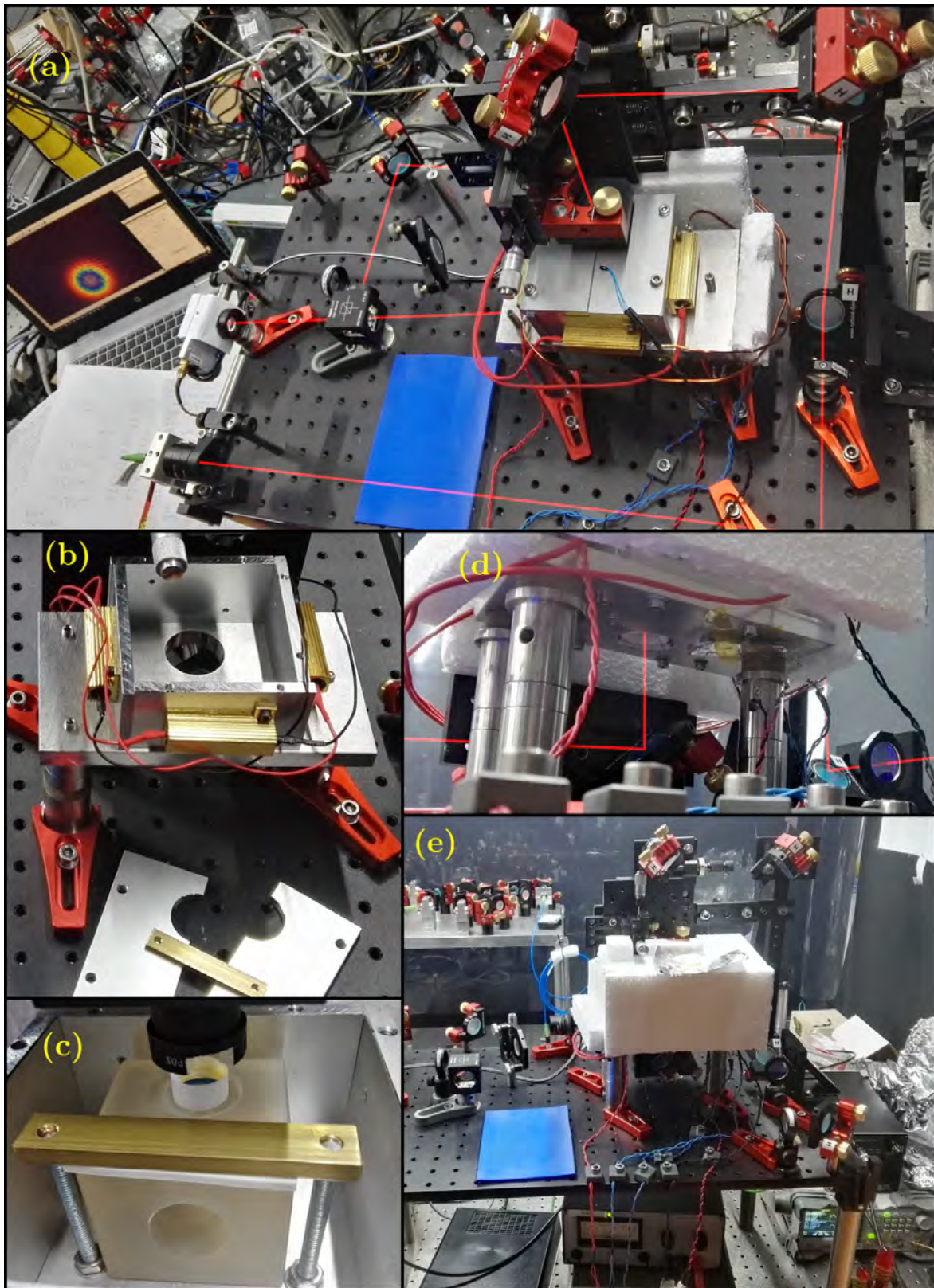


Figure 6.4: *Final assembly and glue curing of the science cavity.* (a) The glue curing oven assembled around the cavity and illustrated beam paths for alignment. (b) The inside of the empty curing oven. (c) The cavity assembly within the oven after completing the cure. (d) View of the assembly from below during curing. (e) The assembly covered with EPS pieces during curing.

The cavity mirror could be aligned using a holder with both translation and rotation degrees of freedom. However, during alignment, it proved to be enough to detach the mirror, letting it rest on the spacer and push it gently around with the horizontal translation degrees of freedom. This approach also reduced the risk of the holder exerting forces on the mirror after gluing, during heating or detachment. The cavity transmission was monitored both using a photodiode and a beam profiler, and the mirror was glued onto the spacer with three drops after ensuring a maximum TEM00 mode with the narrowest linewidth. Then the top of the oven and the resistors were fastened, and the assembly was isolated further using some pieces of EPS foam (seen in Fig. 6.4(d) and (e)). The resistor power dissipation was then controlled while monitoring the thermistor temperatures, shown in Fig. 6.5. The monitored beam profile changed slightly during heating, which was attributed to the thermal effects on the setup and beam path. This was indicated by the fact that the changes could be reversed by slightly adjusting the input mirror. They also consequently reversed again while the setup cooled down. Parameters of the completed science cavity are given in Table 6.1.

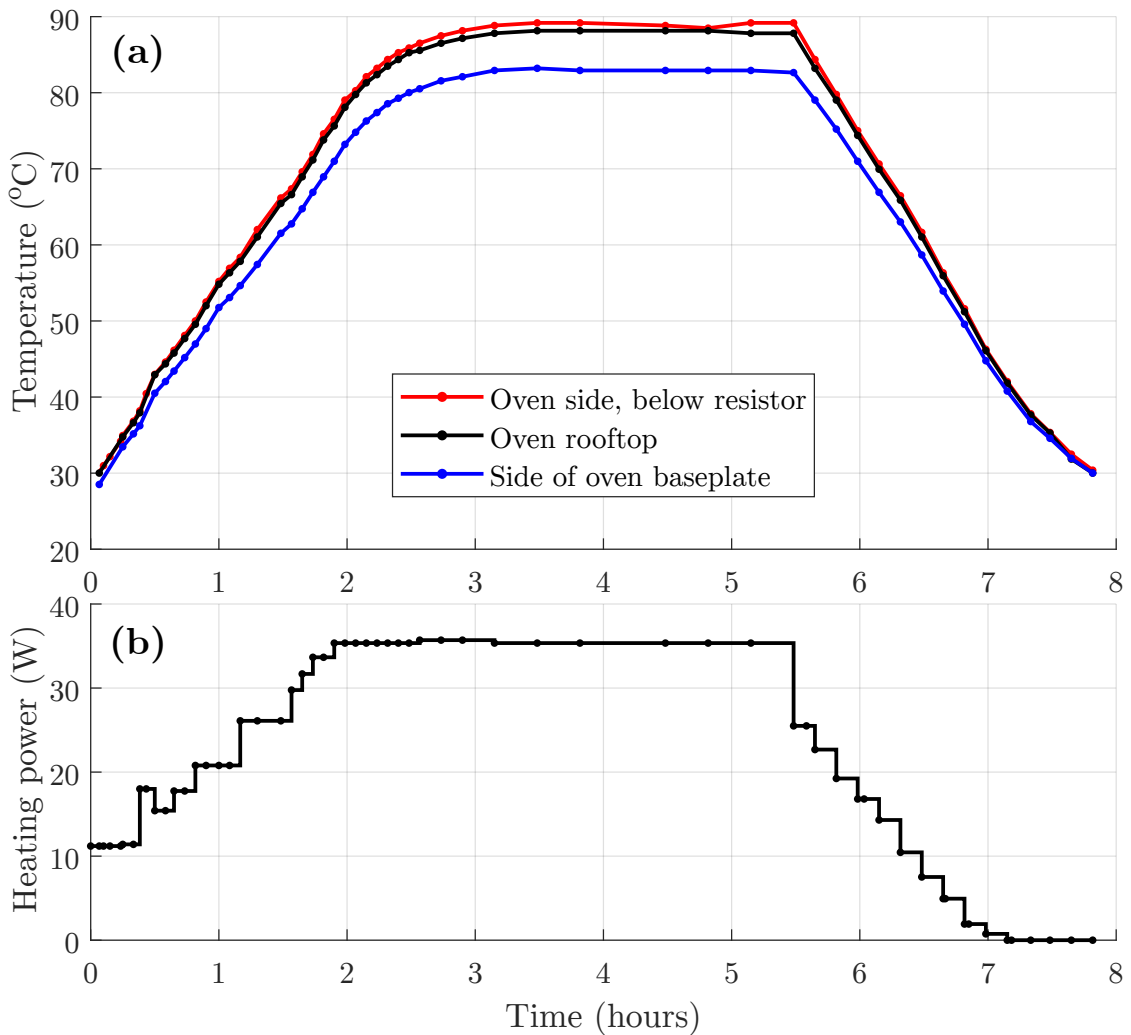


Figure 6.5: (a) Temperatures measured near the cavity while curing the glue, and (b) the power dissipated in the three resistors mounted onto the glue curing oven. The heating power was adjusted to avoid too large temperature gradients that might damage the cavity.

Atom-cavity coupling	$g_0/2\pi$	11.28 kHz
Finesse	F	$101.6 \pm 0.6$ [145]
Free spectral range	FSR	$5.479 \pm 0.001$ GHz [145]
Length	$L$	$27.358 \pm 0.005$ mm
Linewidth (FWHM)	$\kappa/2\pi$	$53.9 \pm 0.2$ MHz [145]
Mirror radius of curvature		$100.0 \pm 0.5$ mm (manufacturer)
Mirror reflectivity		96.96%
Purcell rate	$(4g_0^2/\kappa)/2\pi$	9.437 Hz
Single-atom cooperativity	$C$	$1.264 \cdot 10^{-3}$
Waist radius	$W$	86 $\mu$ m

Table 6.1: *Parameters of the SRLM science cavity.*

### 6.3 The superradiant lasing machine

After completing the science cavity, the piezo wires were soldered onto feedthrough wires, and the cavity was placed within a holder, resting on viton balls (we were forced to place these a bit differently than planned). The science cavity assembly was then lowered into the science chamber, shown in Fig. 6.6. Later an anti-laser part was also mounted at the top of the machine (seen in 6.6e), which is part of a separate project to investigate anti-lasing/super-absorption (see e.g. [146, 147]). The quality of the many vacuum sealings were then checked using helium and a mass spectrometer at the vacuum pump. By blowing helium gas at a vacuum seal, this will diffuse into the mass spectrometer (on the order of some seconds, depending on the pathway to the pump) and be detected if there is a leak. Small leaks can still be a bit tricky to detect with this method, especially around windows, because the helium can also diffuse through the windows.



Figure 6.6: *Mounting the science cavity inside the SRLM. (a) Placement of the cavity. (b) Soldering of piezo wire connections. (c) Lowering the cavity assembly into the vacuum chamber. (d) First observation of light transmitted through the science cavity within the SRLM. (e) Leak testing the vacuum with helium.*

The final step to complete the vacuum assembly was installing oven and heat shield parts and loading strontium into the oven. The loading process is shown in Fig. 6.7. For superradiance, atomic strontium is needed, but it oxidizes in contact with oxygen. Therefore the strontium must be stored in an inert gas until it is used, and the duration in contact with oxygen must be minimized, with our target being 15 minutes from breaking the jar until pumping vacuum. After this was completed, the machine was placed inside a large oven and baked in order to speed up gas release within the machine, which would otherwise be released on much longer timescales and degrade the vacuum quality. After baking, the machine was finally mounted onto breadboards for optics in the lab, while the electrical connections to the oven were completed.



Figure 6.7: *Final assembly of the SRLM.* (a) Strontium. (b) Loading strontium into the machine. (c) Preparing the machine for bake-out. (d) The SRLM within oven for baking. (e) The SRLM after assembly, lower part: heat shields and oven exit, center: Shayne, upper: science cavity. (f) Completion of oven connections and mounting onto breadboards.

### 6.3.1 Transverse cooling optics

A setup was built to transversely cool the atoms escaping from the oven down to the mK range. Optics plans (designed by Francesca Famà) were laid out for cooling along the parallel and perpendicular axes with respect to the cavity axis. These schematics are illustrated in Fig. 6.8, along with photos of the final breadboards in the setup (two breadboards of each type were made and placed on opposing sides of the chamber).

In panel (a) the optics for cooling along the cavity axis are shown. The beam coupling out of the fiber is first expanded and collimated, then downscaled horizontally and expanded vertically using cylinder telescopes. This gives a narrow beam profile that only addresses the part of the atomic beam that passes through the cavity. For the cooling beams perpendicular to the cavity axis, an equally tall but much broader beam is necessary, motivating the design in panel (b). This design recycles the power by making three passes before a final retroreflection and allows stacking the beam profiles next to each other. The polarization is shifted during each pass with waveplates. Panel (c), (d) and (e) show the transverse cooling system in operation.

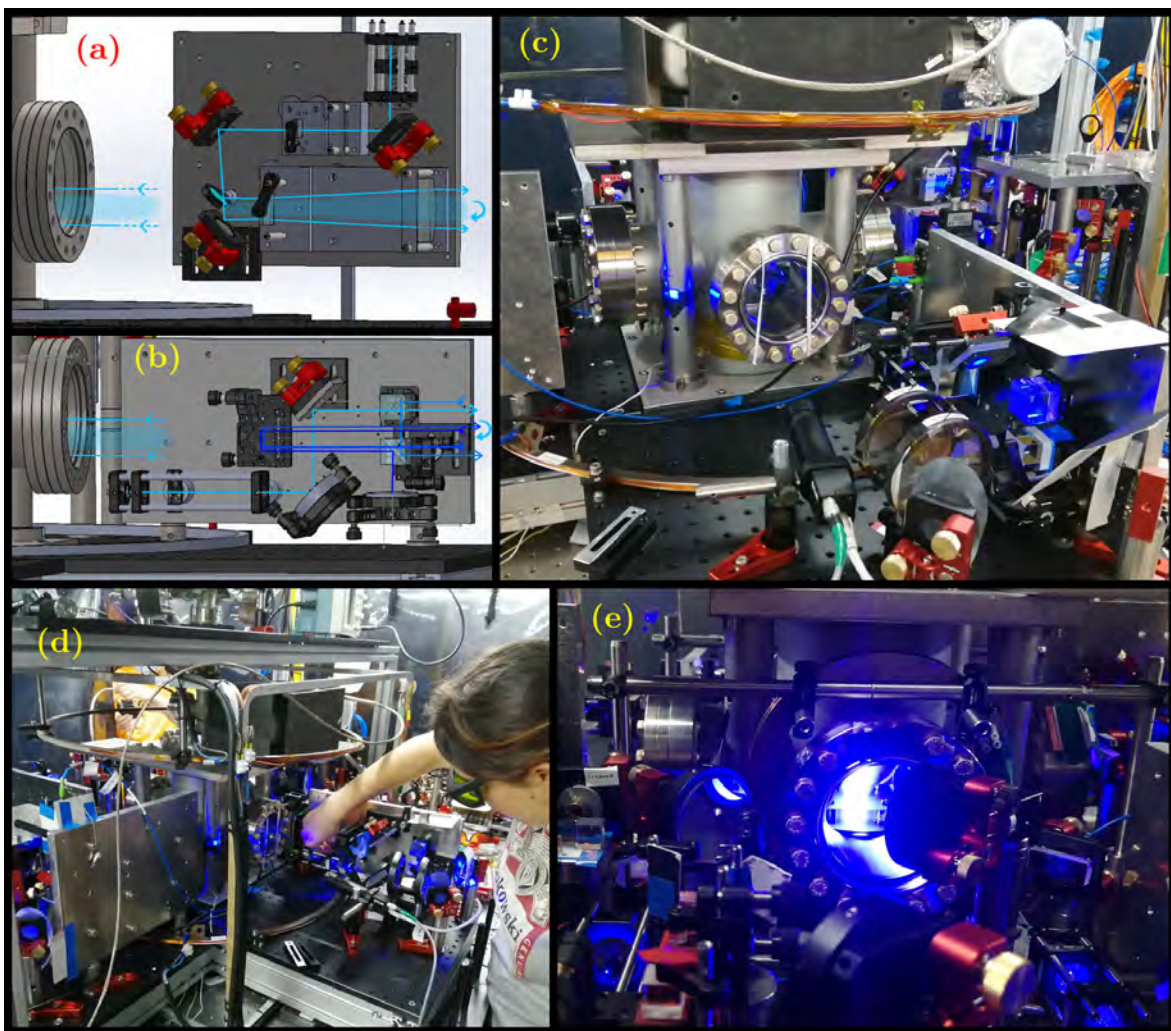


Figure 6.8: (a) *Schematic and approximate beam paths for cooling parallel to the cavity axis. Two alignment mirrors flip the final beam direction after the breadboard.* (b) *Schematic for cooling atoms in the perpendicular dimension to the cavity axis. The beam color is shifted to distinguish the passes.* (c-e) *The transverse cooling system in operation.*

### 6.3.2 Cavity-coupling optics

Two breadboards were also designed with optics for coupling to each side of the science cavity, which would enable PDH locking, probing the atoms, and detecting beat signals with a reference laser. The PDH technique was previously described in Sec. 3.4.2. The very broad linewidth  $\kappa = 2\pi \times 53.9$  MHz of the science cavity implies that the modulation frequency  $\omega_m$  also has to be quite high to obtain a reasonable PDH signal slope. In Fig. 6.9 the normalized PDH signal and maximum slope is shown for different values of  $\omega_m$ .

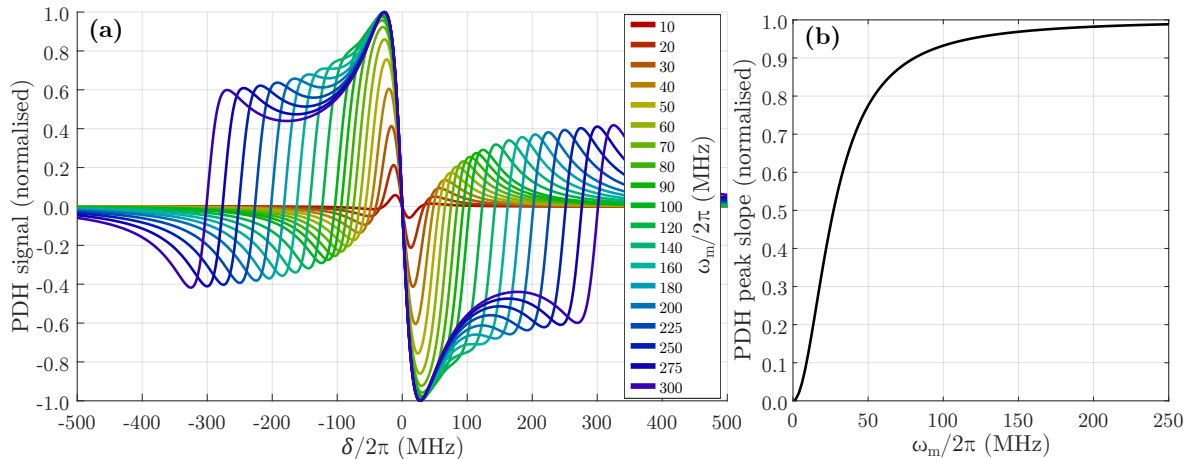


Figure 6.9: (a) Normalized PDH signal (Eq. 3.12) as function of the laser detuning  $\delta$  from the cavity resonance for different modulation frequencies  $\omega_m$ . (b) The maximum slope (at  $\delta = 0$ ) as function of  $\omega_m$  normalized to the value for  $\omega_m \rightarrow \infty$ .

Based on this we aimed for a modulation frequency of 40-50 MHz, as a balance between the frequency dependence of the slope, detector efficiencies and possible noise from other RF sources in the lab. An EOM was assembled (Fig. 6.10) for frequency modulating the laser beam to the cavity, and a resonance circuit (see e.g. [133, p. 65-68]) was built for driving it, optimized for a resonance at 40.5 MHz.

The optics plans for the breadboards are shown in Fig. 6.11). One, in panel (a), includes the EOM and PDH optics, and also has space for a detector for e.g. power monitoring. The other breadboard, in panel (b), is for overlapping the superradiant output with a reference laser beam for beat signal detection. With two detectors a balanced detection technique can be used. This enables canceling out common noise and measuring smaller signals than typically possible with a single detector. The beam paths are designed so that the cavity can be mode-matched with the collimated beams from the fibers by using a single f=400 mm lens positioned 215 mm from the chamber, neglecting disturbances by the window (see Fig. 6.12).

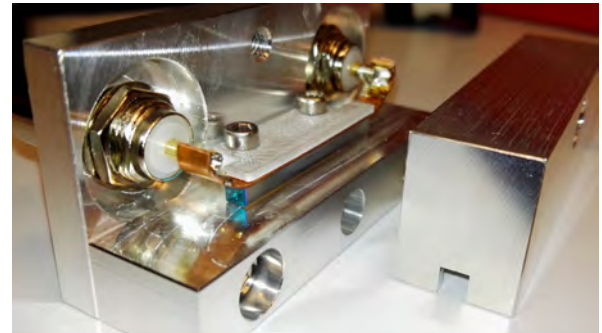


Figure 6.10: EOM for generating sidebands at  $\pm 40$  MHz used to lock the science cavity using the PDH technique. In the EOM the laser beam propagates through the elongated crystal with an apparent cyan surface.

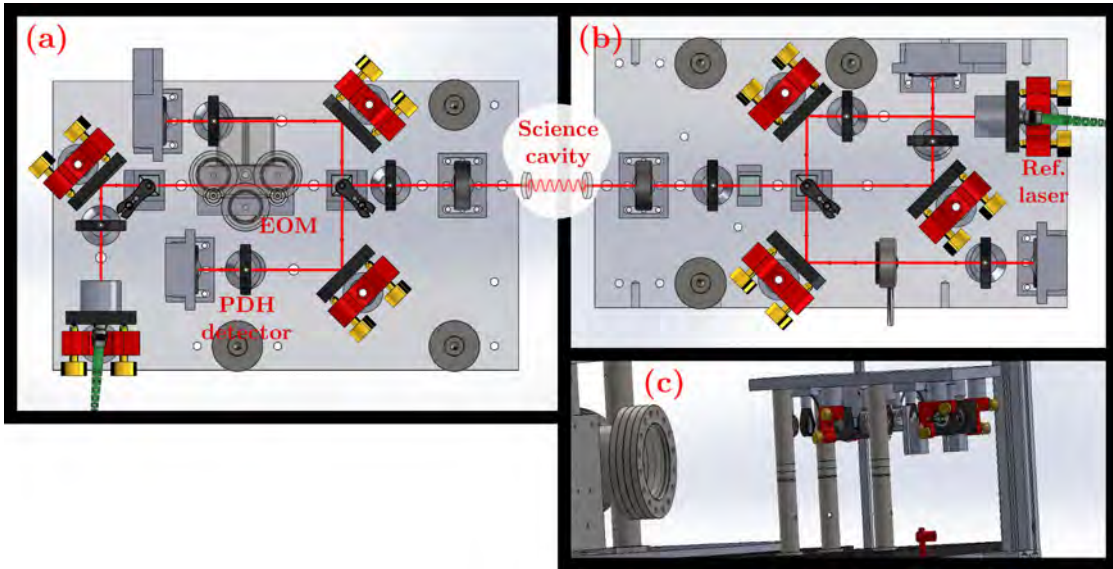


Figure 6.11: (a) Plan for cavity optics on the PDH lock side, including the 40 MHz EOM. (b) Cavity optics plan on the reference laser and detection side. (c) Illustration of the mounting plan relative to the vacuum chamber (other optics, e.g. the transverse cooling, are hidden).

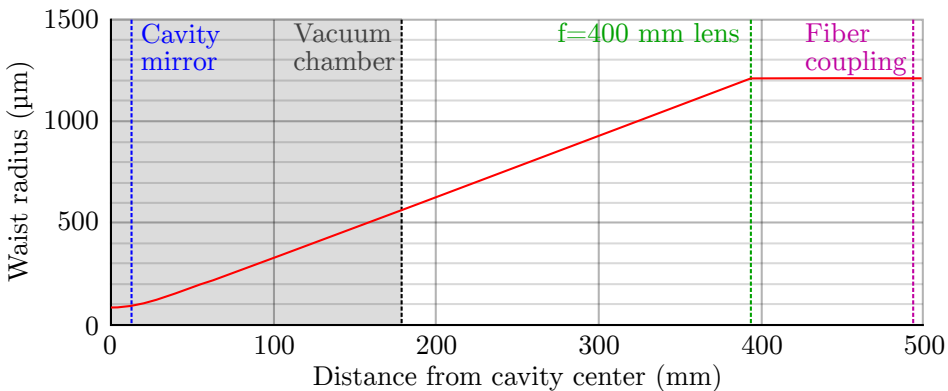


Figure 6.12: The beam waist radius (red) as function of position, and mode-matching to the fiber-coupled beams on breadboards using a 400 mm lens.

## 6.4 Simulations of pumping and velocity selection stages

In this section we present numerical simulations of the pumping stages within the SRLM, with the goal of illustrating the physics and describing the impact of laser parameters quantitatively. Before entering the pumping stages, the transverse cooling stage helps to collimate the atomic beam and cool the atoms to the mK regime transversely. Once the atoms are cooled, they must be pumped to  ${}^3\text{P}_1 \text{ } m_J=0$ . However the velocity distribution along the propagation axis is still characterized by the oven temperature of several hundreds Kelvin. The velocity distribution in the propagation direction ( $x$ ) of such a thermal beam is given by [148, p. 62]:

$$f(v_x) = \frac{v_x^3}{2 \cdot (k_B T_x / m)^2} \exp\left(-\frac{v_x^2}{2 k_B T_x / m}\right). \quad (6.1)$$

This distribution has a most probable velocity given by  $v_{px} = \sqrt{3k_B T_x / m}$ . The pumping to  ${}^3\text{P}_1$  can be done coherently or incoherently, but due to the velocity distribution it would be very hard to obtain a large inversion using coherent pumping in the form of a  $\pi$  pulse. This would rely on letting atoms pass through a laser beam, and very slow atoms might get a  $2\pi$  pulse while very fast atoms get a  $\pi/2$  pulse. Another coherent pumping scheme could be based on adiabatic passage, requiring spatial variations in the beam frequency which

introduces other complications, and was not investigated in detail. Coherent pumping also introduces a risk of the pumping laser influencing the phase and frequency of the superradiant laser, and ideally, this should be avoided. Therefore plans were made for incoherent pumping, using the 689 and 688 nm pumping scheme with 679 and 707 nm repumping demonstrated in e.g. [60].

About 30 mm is left between the edge of the transverse cooling stage and the cavity mode. This region was further divided into three regions to implement a velocity selection scheme in addition to pumping (see Fig. 6.13). In Stage 1 the atoms are pumped to the long-lived state  ${}^3P_0$  in a frequency-selective manner by modulating the 689 nm laser some hundreds of kHz. This modulation will cause atoms with a low velocity along the cavity axis,  $v_z$ , to be efficiently pumped to  ${}^3P_0$  via  ${}^3P_1$ , while atoms with high  $v_z$  will tend to stay in  ${}^1S_0$ . In the second stage a 461 nm beam accelerates the leftover atoms in  ${}^1S_0$  so they reach several m/s and do not interact significantly with the intracavity field. In the final stage the atoms in  ${}^3P_0$  are pumped to  ${}^3P_1 m_J=0$ .

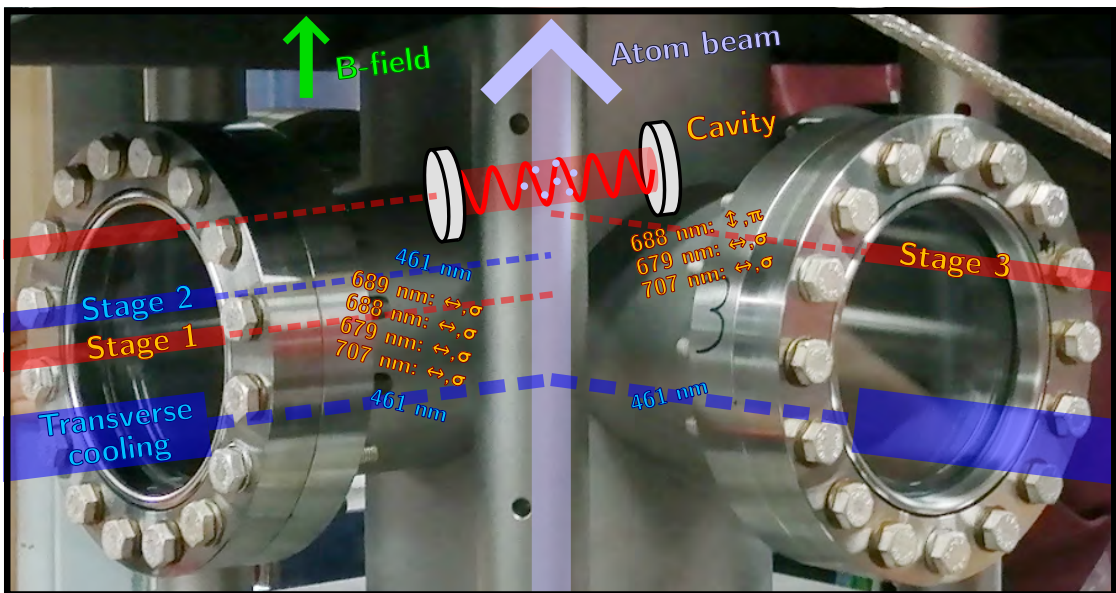


Figure 6.13: *Transverse cooling, state preparation and velocity selection stages for atoms propagating towards the cavity. Laser wavelengths and driven transitions are indicated.*

In terms of timescale, with atom velocities on the order of 400 m/s and 30 mm between the edge of the transverse cooling stage and the cavity, each atom will pass through the three stages on the order of 75  $\mu$ s. Using the method from Chapter 2, equations were derived for the 13 Zeeman sublevels of  ${}^1S_0$ ,  ${}^3P_0$ ,  ${}^3P_1$ ,  ${}^3P_2$  and  ${}^3S_1$  which are involved in the pumping scheme. The 689 nm laser is modeled coherently (with Rabi frequency  $\chi_{li}$ ), while the rest are modeled as incoherent interactions, giving rate equations (as in Sec. 2.3, with pump rates  $w$ ). We assume the magnetic field points in the propagation direction,  $\mathbf{B} \parallel \hat{x}$  (upwards in Fig. 6.13) with a magnitude of 1.5 G, and that all the lasers are linearly polarized. The 688 nm laser drives  $\sigma^\pm$  transitions in Stage 1 and  $\pi$  in Stage 2, while the rest drive  $\sigma^\pm$  transitions equally. In Stage 1, it is assumed that the laser beams are parallel to the cavity axis,  $\mathbf{k} \parallel \hat{z}$ , and in Stage 3, it is assumed  $\mathbf{k} \parallel \hat{y}$ . The direction of the 689 nm laser in Stage 1 is crucial to the velocity selection scheme. The polarization of the 707 nm laser is also crucial so that atoms not pile up in  ${}^3P_2 m_J=\pm 2$ , and similarly the 688 nm laser in Stage 1 should drive  $\sigma^\pm$  transitions as the  $m_J=0$  transition between  ${}^3P_1$  and  ${}^3S_1$  is forbidden. Besides from that the pumping scheme may work with smaller quantitative changes with different choice of orientations and polarizations.

Expectation value brackets are omitted in the following equations, and the following subscripts are used to refer to the different levels:

$$\begin{aligned} g &= {}^1\text{S}_0, n = {}^3\text{P}_0, \\ (i, e, u) &= {}^3\text{P}_1 \text{ m}_J = (-1, 0, 1), \\ (x, y, z) &= {}^3\text{S}_1 \text{ m}_J = (-1, 0, 1), \\ (p, q, r, s, t) &= {}^3\text{P}_2 \text{ m}_J = (-2, -1, 0, 1, 2). \end{aligned}$$

The atomic coherence involved in the 689 nm pump laser interaction evolves according to:

$$\dot{\sigma}_{gi}^j = i \frac{\chi_{li}^j}{2} \left( \sigma_{ii}^j - \sigma_{gg}^j \right) e^{-i\mathbf{k}_{li} \cdot \mathbf{r}_j + i\delta_{liI}t} - \frac{\gamma_{ig} + w_{ix}^j + w_{iy}^j}{2} \sigma_{gi}^j, \quad (6.2)$$

the equations for the  ${}^1\text{S}_0$  and  ${}^3\text{P}_1$  populations are given by:

$$\begin{aligned} \dot{\sigma}_{gg}^j &= -i \frac{\chi_{li}^j}{2} \left( \sigma_{gi}^j e^{i\mathbf{k}_{li} \cdot \mathbf{r}_j - i\delta_{liI}t} - \sigma_{ig}^j e^{-i\mathbf{k}_{li} \cdot \mathbf{r}_j + i\delta_{liI}t} \right) + \gamma_{eg} \left( \sigma_{ii}^j + \sigma_{ee}^j + \sigma_{uu}^j \right) \\ \dot{\sigma}_{ii}^j &= i \frac{\chi_{li}^j}{2} \left( \sigma_{gi}^j e^{i\mathbf{k}_{li} \cdot \mathbf{r}_j - i\delta_{liI}t} - \sigma_{ig}^j e^{-i\mathbf{k}_{li} \cdot \mathbf{r}_j + i\delta_{liI}t} \right) - \left( w_{ix}^j + w_{iy}^j + \gamma_{ig} \right) \sigma_{ii}^j + \frac{\gamma_{xi}}{2} \left( \sigma_{xx}^j + \sigma_{yy}^j \right) \\ \dot{\sigma}_{ee}^j &= -(\gamma_{eg} + w_{ex}^j + w_{ez}^j) \sigma_{ee}^j + \frac{\gamma_{xe}}{2} \left( \sigma_{xx}^j + \sigma_{zz}^j \right) \\ \dot{\sigma}_{uu}^j &= -(w_{uy}^j + w_{uz}^j + \gamma_{eg}) \sigma_{uu}^j + \frac{\gamma_{xu}}{2} \left( \sigma_{yy}^j + \sigma_{zz}^j \right), \end{aligned} \quad (6.3)$$

and for the long-lived states  ${}^3\text{P}_0$  and  ${}^3\text{P}_2$ :

$$\begin{aligned} \dot{\sigma}_{nn}^j &= -(w_{nx}^j + w_{nz}^j) \sigma_{nn}^j + \gamma_{xn} \left( \sigma_{xx}^j + \sigma_{yy}^j + \sigma_{zz}^j \right) \\ \dot{\sigma}_{pp}^j &= -w_{px}^j \sigma_{pp}^j + \frac{6}{10} \gamma_{xp} \sigma_{xx}^j \\ \dot{\sigma}_{qq}^j &= -w_{qy}^j \sigma_{qq}^j + \frac{3}{10} \gamma_{xp} \left( \sigma_{xx}^j + \sigma_{yy}^j \right) \\ \dot{\sigma}_{rr}^j &= -(w_{rx}^j + w_{rz}^j) \sigma_{rr}^j + \gamma_{xp} \left( \frac{1}{10} \sigma_{xx}^j + \frac{4}{10} \sigma_{yy}^j + \frac{1}{10} \sigma_{zz}^j \right) \\ \dot{\sigma}_{ss}^j &= -w_{sy}^j \sigma_{ss}^j + \frac{3}{10} \gamma_{xp} \left( \sigma_{yy}^j + \sigma_{zz}^j \right) \\ \dot{\sigma}_{tt}^j &= -w_{tz}^j \sigma_{tt}^j + \frac{6}{10} \gamma_{xp} \sigma_{zz}^j. \end{aligned} \quad (6.4)$$

For  ${}^3\text{S}_1$  we have:

$$\begin{aligned} \dot{\sigma}_{xx}^j &= w_{nx}^j \sigma_{nn}^j + w_{ix}^j \sigma_{ii}^j + w_{ex}^j \sigma_{ee}^j + w_{px}^j \sigma_{pp}^j + w_{rx}^j \sigma_{rr}^j - \gamma_x \sigma_{xx}^j \\ \dot{\sigma}_{yy}^j &= w_{iy}^j \sigma_{ii}^j + w_{uy}^j \sigma_{uu}^j + w_{qy}^j \sigma_{qq}^j + w_{sy}^j \sigma_{ss}^j - \gamma_y \sigma_{yy}^j \\ \dot{\sigma}_{zz}^j &= w_{nz}^j \sigma_{nn}^j + w_{ez}^j \sigma_{ee}^j + w_{uz}^j \sigma_{uu}^j + w_{rz}^j \sigma_{rr}^j + w_{tz}^j \sigma_{tt}^j - \gamma_z \sigma_{zz}^j, \end{aligned} \quad (6.5)$$

and due to the short decay time from  ${}^3\text{S}_1$  we assume these are in steady state and obtain:

$$\begin{aligned} \sigma_{xx}^j &= \frac{1}{\gamma_x} \left( w_{nx}^j \sigma_{nn}^j + w_{ix}^j \sigma_{ii}^j + w_{ex}^j \sigma_{ee}^j + w_{px}^j \sigma_{pp}^j + w_{rx}^j \sigma_{rr}^j \right) \\ \sigma_{yy}^j &= \frac{1}{\gamma_y} \left( w_{iy}^j \sigma_{ii}^j + w_{uy}^j \sigma_{uu}^j + w_{qy}^j \sigma_{qq}^j + w_{sy}^j \sigma_{ss}^j \right) \\ \sigma_{zz}^j &= \frac{1}{\gamma_z} \left( w_{nz}^j \sigma_{nn}^j + w_{ez}^j \sigma_{ee}^j + w_{uz}^j \sigma_{uu}^j + w_{rz}^j \sigma_{rr}^j + w_{tz}^j \sigma_{tt}^j \right). \end{aligned} \quad (6.6)$$

The assumed laser powers and waist sizes are given in Tab. 6.2, where  $W_2$  refers to  $W_x$  (Stage 1 and 2) or  $W_y$  (Stage 3). Identical waist sizes are chosen for x and y in Stage 1 and 2 as this requires the simplest optics. However a lower power can be used (preserving the intensity) if the beam waist along the y axis is reduced to a few times the cavity waist.

Laser	$W_x$ (mm)	$W_2$ (mm)	P (mW)	$\Phi_P$ ( $s^{-1}$ )	$\Phi_A$ ( $s^{-1}$ )
Stage 1, 689 nm	2.0	2.0	1.21	$2.6 \cdot 10^{16}$	$2.3 \cdot 10^{14}$
Stage 1, 688 nm	2.0	2.0	1.00	$2.2 \cdot 10^{16}$	$2.3 \cdot 10^{14}$
Stage 1, 707 nm	2.0	2.0	3.00	$6.7 \cdot 10^{17}$	$2.3 \cdot 10^{14}$
Stage 2, 461 nm	2.0	2.0	10.7	$1.6 \cdot 10^{17}$	$2.3 \cdot 10^{14}$
Stage 3, 688 nm	1.0	15	1.45	$3.2 \cdot 10^{16}$	$1.7 \cdot 10^{15}$
Stage 3, 707 nm	1.0	15	3.00	$6.7 \cdot 10^{16}$	$1.7 \cdot 10^{15}$
Stage 3, 679 nm	0.30	15	0.652	$1.4 \cdot 10^{16}$	$1.7 \cdot 10^{15}$

Table 6.2: *Laser waist radii and powers used in simulation of pumping and velocity selection.*  $\Phi_P$  is the corresponding photon flux of the laser beam.  $\Phi_A$  is an estimated atom flux through the laser beam during superradiant lasing.

Regarding Zeeman splittings,  $g_J=3/2$  for  $^3P_1$  and  $^3P_2$ , and  $g_J=2$  for  $^3S_1$ . Thus the  $^3P_J$  splitting is 3.2 MHz between neighboring sublevels, which is large enough that we can assume the 689 nm laser only affects the transition to the  $^3P_1 m_J=-1$  state (the primary motivation for this magnitude). We assume this laser frequency is swept as an upwards sawtooth centered on the Zeeman-shifted resonance. For the rest of the lasers, the frequencies will be chosen to be equal to the unshifted transition frequency for simplicity and symmetry. This gives the laser detunings illustrated in Fig. 6.14:  $\delta_{ix} = 2\pi \cdot 1.05$  MHz,  $\delta_{px} = 2\pi \cdot 2.10$  MHz,  $\delta_b = \delta_{iy} = \delta_{qy} = 2\pi \cdot 3.15$  MHz and  $\delta_a = \delta_{rz} = 2\pi \cdot 4.20$  MHz.

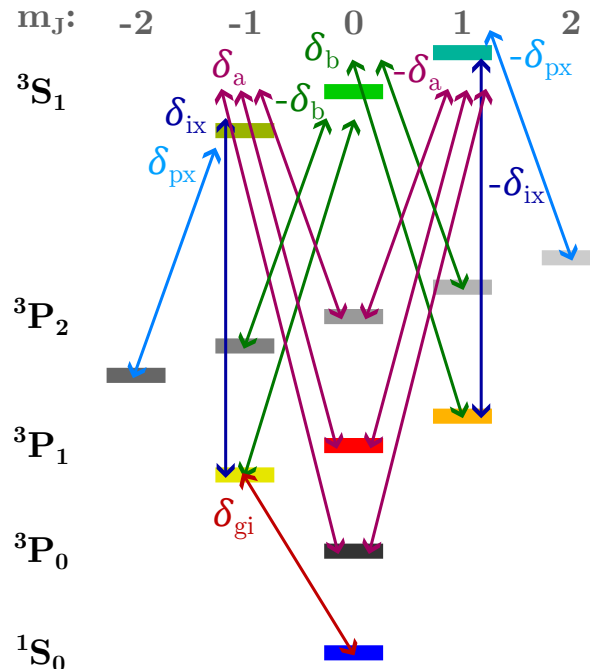


Figure 6.14: *Driven transitions and laser detunings due to Zeeman shifts in the model of pumping and velocity selection stages.*

A simulation of the stages can be seen in Fig. 6.15, assuming a most probable beam velocity of  $v_{px}=400$  m/s. In panel (a) and (b) the atoms are color-coded according to their state (using the colors of the levels in Fig. 6.14) as they propagate through the three stages and the cavity, assuming no atom-cavity interaction. The 689 nm laser is frequency modulated with a span of 400 kHz and modulation frequency of 20 kHz. This, in combination with power broadening on the order of  $\chi_{li}^{max}/2\pi = 300$  kHz, determines the range of Doppler shifts that are transferred to  ${}^3P_0$ . The waist size along the x axis is also crucial to velocity selection; a larger waist radius gives more interaction time, allowing for a lower intensity and thus  $\chi_{li}$ , such that the velocity range can be cut off more sharply. With a 2 mm waist the interaction time is approximately  $\tau=10$   $\mu$ s, and the required Rabi frequency for efficient transfer is on the order of  $1/\tau$ . The choice of parameters used here results in about 70% of the population being transferred to  ${}^3P_0$  (see the population bars in Fig. 6.15(c)), and the non- ${}^1S_0$  atoms have a temperature reduced from 3.6 to 2.0 mK. By increasing the laser powers (primarily the 689 nm laser) and scan range towards the 2 MHz Doppler width, the transfer rate can be increased towards 100% at the expense of the reduction in temperature.

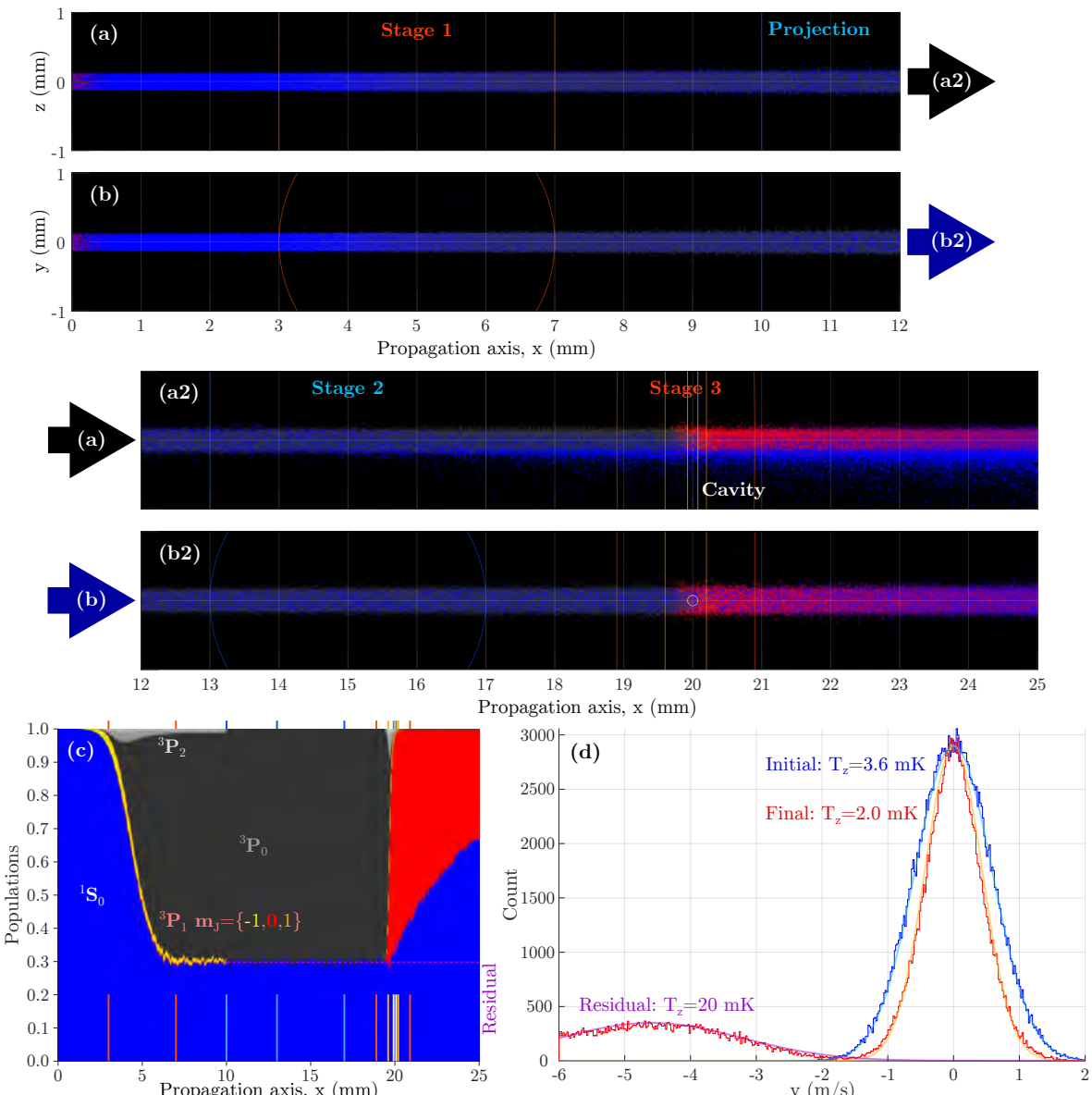


Figure 6.15: *Simulation of pumping and velocity selection in the SRLM. (a) and (b) show the atoms changing state (colors) while propagating through the stages described in the main text. (c) Quantitative evolution of the atom states as function of position while propagating. (d) Initial (blue) and final (red) velocity distributions along the z axis. The velocity selection scheme shifts 30% of the atoms by about 5 m/s and yields a flux of useful atoms at 2 mK.*

After Stage 1 the atoms are projected into either  ${}^1S_0$  or  ${}^3P_0$  at  $x=10$  mm, chosen randomly based on the respective populations. This is necessary for calculating an appropriate force in Stage 2 based on discrete populations we want to separate, as the populations escaping Stage 1 are mainly statistical mixtures, with a small component of coherent superpositions of  $|g\rangle$  and  $|i\rangle$ . Experimentally the 461 nm light in Stage 2 would also rapidly destroy any coherent superpositions of  $|g\rangle$  and  $|i\rangle$ . The tiny remnant populations of  ${}^3P_1$  and  ${}^3P_2$  are neglected in the projection.

Within Stage 2 the atoms in  ${}^1S_0$  are subjected to a semiclassical force (Eq. 3.2) from a 461 nm beam with an assumed detuning of 15 MHz, waist radius of 2 mm and  $I = 2I_{sat}$ , which accelerates the atoms on the order of 5 m/s along the cavity axis (the initial and final velocity distributions are compared in Fig. 6.15(d)). The amount that the atoms' velocity must be shifted can be determined based on the expected output power during superradiant emission. For an atom in  ${}^1S_0$  to not absorb significantly from the intracavity field, its Doppler shift must be approximately larger than the power-broadening of the transition due to the cavity field (Eq. 4.7):

$$\delta_D > \Gamma_P \implies v > \frac{c}{\omega_E} \gamma_{eg} \sqrt{1 + \frac{96c^3 P_{out}^S}{\hbar\kappa W^2 L \omega_E^3 \gamma_{eg}}} \approx \sqrt{\frac{P_{out}^S}{1\mu W}} \cdot 3.15 \frac{m}{s}. \quad (6.7)$$

Here we see that the velocity should be shifted on the order of 3 m/s to avoid disturbing superradiant lasing with a single-side output power of 1  $\mu$ W. The exact impact (including potential dispersive effects) will be determined with cavity QED simulations in Chapter 7, but experimentally the safest approach is to simply shift the velocities as much as possible. With an intensity of  $2I_{sat}$  there are no more orders of magnitude to gain just by increasing the laser power, but there is still space for expanding the beam waist if necessary.

In Stage 3, the atoms are finally transferred to  ${}^3P_1$   $m_J=0$  using three lasers at {688, 707, 679} nm. Since these laser beams are orthogonal to the cavity axis, the waist radii along the z axis must be wide enough to address the entire flux of atoms through the cavity (only the very central section of the atom flux is simulated here). The beams are centered on a point 100  $\mu$ m before the center of the cavity. The 688 and 707 nm laser waists are not very crucial along the x axis, as long as they are larger than the 679 nm waist and the transfer to  ${}^3P_0$  in Stage 1 is efficient, with few atoms remaining in  ${}^3P_2$ . However the narrow 300  $\mu$ m waist of the 679 nm laser is crucial for the transfer efficiency to  ${}^3P_1$  due to the decay time of 21  $\mu$ s. The fingerprint of this decay is clearly seen spatially in Fig. 6.15(c) from  $x=20$  to 25 mm; if the beams were misplaced just 1 mm with respect to the cavity, 10% of the  ${}^3P_1$  atoms would be lost to  ${}^1S_0$ . So ideally the 679 nm waist is very narrow, initiating the pumping right before the atoms enter the cavity, while all the lasers are also intense enough that the atoms are fully transferred upon entry.

### 6.4.1 Optical depth effects

The simulations presented here neglect optical depth effects, but for a high atom flux, the atoms closest to the incoming laser beams could create a shadow effect. The intensity of a laser beam propagating through a medium of ground-state atoms is attenuated exponentially according to Beer's law,  $I(r) = I_0 e^{-ar}$ , where  $a$  is an absorption coefficient [112, p. 115]. Of course the atoms subjected to high intensity will subsequently change state, such that the shadow effect becomes reduced further along the propagation axis within an extended laser beam waist. The simulations tell us the behavior that can be expected if the atoms experience the given laser intensities *after* accounting for any attenuation due to foreground atoms in relevant states for the wavelengths, and if internal shadowing within the simulated region of interest is negligible. For the Stage 1 and 2 lasers with  $\mathbf{k} \parallel \hat{z}$  there are no foreground atoms, but internal shadowing could be significant. On the other hand  $\mathbf{k} \parallel \hat{y}$  in Stage 3, so there may be many foreground atoms depending on the atom flux distribution, but internal shadowing should not be significant.

The photon flux in Table 6.2 can give an idea of the optical depth effects when compared to the expected atom flux. An atom flux on the order of  $10^{12}\text{-}10^{13} \text{ s}^{-1}$  intersecting the cavity mode is expected during superradiance - that is, a segment of the atom flux within  $|y| < W_{cav}$  but any possible  $z$  value. For shadow effects to be negligible, the photon flux should be a few orders of magnitude higher than the atom flux intersecting the laser beam, which will be larger than the atom flux through the cavity by a factor  $W_{laser}/W_{cav}$  if the atom distribution is uniform. These estimated values are given in the  $\Phi_A$  column for an atom flux of  $10^{13} \text{ s}^{-1}$  through the cavity, but will likely be lower for a non-uniform atomic beam. For the parameters chosen here there are about 1-3 orders of magnitude more laser photons than intersecting atoms, though it is worth noting that each atom may also require a couple of laser photons from each beam to be pumped to the correct state. For the Stage 2 laser about 500 photons are required per residual  $^1\text{S}_0$  atom to shift their velocities by 5 m/s. Finally, many atoms will not cause disturbances for some of the lasers if they are in states they do not drive transitions from, which is not considered in the table.

# Superradiant lasing from a hot atom beam

In Chapter 6 we presented the superradiant lasing machine (SRLM) constructed at the University of Amsterdam, and here we will explore the physics of continuous superradiant lasing within this machine using numerical simulations. The numerical model was originally developed to provide input for choosing the cavity parameters in Tab. 6.1 and determine the output power and cavity pulling we can expect from the SRLM. General theoretical scalings of output power, laser linewidth and pulling coefficients for a hot atomic beam system were already presented in [86]. As such the simulations are used to explore the concrete regime of the SRLM in detail, gaining independent estimates and investigating the impact of relevant physical effects. These effects include relativistic Doppler shifts, the impact of a finite temperature and the velocity selection scheme described in Sec. 6.4, the impact of stray light, and of dynamic changes in cavity detuning. Some of these results are also presented in [84]. Finally, some quantitative results are presented which characterize absorption and amplification in the system for a wide range of atom flux, including below the lasing threshold.

## 7.1 Numerical model

The numerical model of the superradiant laser is an adaptation of the model of pulsed superradiance in the mK atom cloud, which was presented in Chapter 4. The biggest difference is the atom source being a continuous beam rather than a cloud. The velocity of atoms is assumed to be constant, based on initial Gaussian distributions radially ( $T_R = 3.6$  mK) and the atomic beam velocity distribution along the propagation axis,  $x$  (Eq. 6.1 where we will consider  $v_{px} = 400$  m/s and 450 m/s). The atomic beam is modeled as a uniform flux through a square with a size of 4W along the  $y$  and  $z$  axes, centered on the cavity mode, with the cavity along  $z$ . The variation along  $y$  is important due to the Gaussian waist of the cavity, and in [103, p. 35] it was investigated how far away in a cavity waist that atoms must be before they could be neglected in a model of pulsed superradiance. This distance ultimately depends on the cavity and power parameters, as the value of  $2g(r(t))\sqrt{n(t)}$  along an atom's path determines if it can emit while it traverses the cavity mode. This means that in a regime with higher flux and power than investigated here, atoms with a larger range of  $y$  values may need to be considered. Quantitatively the atom flux,  $\Phi$ , used in this chapter will be defined as the flux only within the cavity waist radius along  $y$ , so that it is independent of the cutoff. Along the  $z$  axis the cavity mode waist radius expands from 86  $\mu\text{m}$  up to approximately 92  $\mu\text{m}$  at the mirrors, 13.7 mm from the center. This would also cause a slight reduction in coupling for atoms far along the  $z$  axis, but we neglect this variation as it is small and the density is expected to be highest near  $z=0$ . Thus the exact positions along  $z$  in the model are not important beyond the fact that the atoms are spread out across many wavelengths and can still move along this wave, giving rise to the Doppler effect when interacting with the cavity mode. Therefore the value of 4W along the  $z$  axis is arbitrary, but appropriate.

The simulations exclude the pumping and velocity selection stages presented in Sec. 6.4. To determine their impact, these stages are instead incorporated into the initial conditions of some of the simulations. This is done by assuming that a certain fraction of the atoms start in  ${}^3\text{P}_1 m_J=0$ , if their velocities along the cavity axis are sufficiently slow, and the remaining ones start in  ${}^1\text{S}_0$ . The velocity distribution of the fast atoms is then changed so that  $\langle v_z \rangle = 3$  m/s and  $T_z = 5$  mK to qualitatively mimic the impact of the push beam. The impact of the velocity shift magnitude will be investigated later, but these shifts are sufficient that the  ${}^1\text{S}_0$  atoms have a very small impact on the superradiant emission. The criterium distinguishing the slow and fast atoms is  $|v_z| < \lambda v_{px}/4W$ , which is based on the results in [89], where atoms moving further than half a wavelength along the cavity axis during transit in a superradiant laser can disturb single-mode emission.

With these assumptions we only treat the states  ${}^1\text{S}_0$  and  ${}^3\text{P}_1 m_J=0$  in the model, and the Hamiltonian is given by:

$$\begin{aligned} H = & \hbar\omega_c a^\dagger a + \sum_{j=1}^N \hbar\omega_e^j \sigma_{ee}^j + \sum_{k=1}^{N_f} \hbar\omega_f^k f_k^\dagger f_k + \frac{1}{2}\hbar\eta \left( ae^{-i\omega_d t} + a^\dagger e^{i\omega_d t} \right) \\ & + \sum_{j=1}^N \hbar g^j(\mathbf{r}_j) (\sigma_{ge}^j + \sigma_{eg}^j) (a + a^\dagger) + \sum_{k=1}^{N_f} \hbar g_f (a + a^\dagger) (f_k + f_k^\dagger). \end{aligned} \quad (7.1)$$

Using the method and notation of Chapter 2, the following equations were derived in a reference frame fixed to the driving laser frequency  $\omega_d$  (which will generally be assumed to be equal to  $\omega_c$ ):

$$\begin{aligned} \langle \dot{a} \rangle = & -i\frac{\eta}{2} - i \sum_{j=1}^N g_j \langle \sigma_{ge}^j \rangle - \left( \frac{\kappa}{2} + i\delta_{cd} \right) \langle a \rangle \\ \langle \dot{\sigma}_{ee}^j \rangle = & ig_j (\langle \sigma_{ge}^j \rangle \langle a \rangle^* - \langle \sigma_{eg}^j \rangle \langle a \rangle) - \gamma_{eg} \langle \sigma_{ee}^j \rangle \\ \langle \dot{\sigma}_{ge}^j \rangle = & ig_j (\langle \sigma_{ee}^j \rangle - \langle \sigma_{gg}^j \rangle) \langle a \rangle - \left( \frac{\gamma_{eg}}{2} + i\delta_{ed}^j \right) \langle \sigma_{ge}^j \rangle \\ \langle \dot{f}_k \rangle = & -i\delta_{fd}^k \langle f_k \rangle - iG \langle a \rangle. \end{aligned} \quad (7.2)$$

### 7.1.1 Relativistic Doppler shifts

For atoms moving at hundreds of m/s, the effects of relativity become significant when we are interested in even small shifts in frequency relative to the unperturbed resonance. If we consider only the motion along the  $x$  axis (as  $v_y$  and  $v_z$  are two orders of magnitude lower than  $v_x$ ), then the relativistic Doppler effect arises purely from time dilation. Time progresses slower for a fast-moving atom in the lab (cavity) frame, red-shifting the resonance frequency by  $\nu_{lab} = \nu_0/\gamma$ , where  $\gamma$  is the Lorentz factor. This is known as the transverse Doppler shift. It is accounted for in the atomic resonance frequencies via the detunings  $\delta_{ed}^j$  of each shifted atomic resonance with respect to the reference frame at  $\omega_d$ :

$$\delta_{ed}^j = \omega_E/\gamma_j = \omega_E \sqrt{1 - (v_x^j/c)^2} - \omega_d = \omega_E \left( \sqrt{1 - (v_x^j/c)^2} - 1 \right) - \delta_{dE}. \quad (7.3)$$

Fig. 7.1 shows the velocity distribution of  $v_x$  according to Eq. 6.1 in panel (a) for two different beam temperatures. Note these beam temperatures do not correspond directly to oven temperatures due to the influence of the oven nozzle. The distributions are instead based on measurements of the atomic beam under expected operating conditions. These velocity distributions in turn result in the distributions of transverse Doppler shifts shown in panel (b). Here  $\delta_e^p$  indicates the shift at the most probable  $v_x$ .

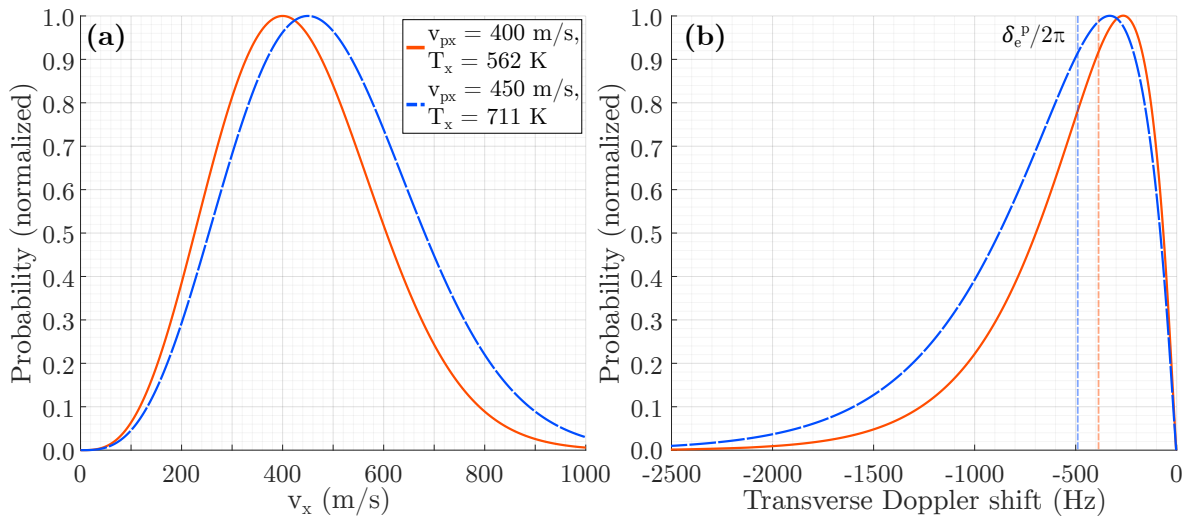


Figure 7.1: Velocity distribution (Eq. 6.1) and resulting transverse Doppler shifts (Eq. 7.3) for two different beam temperatures. The shifts at  $v_x = v_{px}$  are marked with vertical lines.

For atoms traveling at 400 m/s the shift is on the order of 400 Hz, but there is a significant tail of Doppler shifts up to a few kHz because of how  $\gamma$  scales with velocity.

### 7.1.2 Lasing dynamics in the hot beam system

An illustration of atomic dynamics in a numerical simulation is shown in Fig. 7.2, here for a flux of  $\Phi = 10^{13} \text{ s}^{-1}$ . The atoms are represented by dots colored according to their state, and here they start in  ${}^3P_1$  (red) if  $|v_z| < \lambda v_{px}/4W$ , otherwise  ${}^1S_0$  (blue). The atoms subsequently change state depending on their trajectory through the cavity waist and velocity - the cavity leaves a "trail" of  ${}^1S_0$  atoms in the atomic beam, with a size along  $y$  that depends on the cavity photon number.

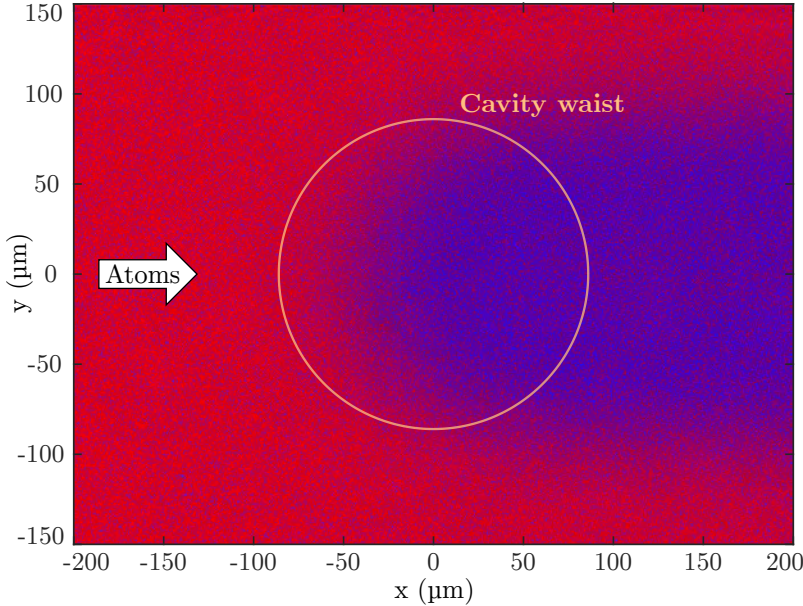


Figure 7.2: Simulation of atoms in the hot beam system as they traverse the cavity mode. The atoms are color-coded according to their state. Red:  ${}^3P_1$ , blue:  ${}^1S_0$ , purple: mixed. Figure adapted from [84].

A number of atoms (depending on the atom flux) are placed at  $x = -2.5W$  every tenth timestep in the simulations, relative to the cavity center. To reach steady state, the atoms must first propagate through the cavity, which takes on the order of 1 μs. In Eq. 7.2 the atoms

will not emit into the cavity if the cavity field and atomic coherences are zero. Therefore we set  $\eta = \kappa/\sqrt{2}$  during the first 1  $\mu\text{s}$  to mimic the effect of spontaneous emission (in steady state with no atoms it would result in a cavity field population of 1/2, but a well-defined phase). This initiates the dynamics and  $\eta$  is subsequently set to zero. More time is then needed for the atom-cavity dynamics to reach steady state behavior - typically on the order of  $\mu\text{s}$ , but very near the lasing threshold, it can take tens of  $\mu\text{s}$ . The steady state parameters can then be determined from the subsequent dynamics. In simulations presented here, on the order of 200  $\mu\text{s}$  is typically evaluated. Furthermore the cavity detuning is generally chosen to be  $\delta_{cE}/2\pi = 100$  kHz. A detuning of this magnitude enables us to determine the output power near resonance simultaneously with an approximate cavity pulling coefficient. An example of the behavior of the cavity output power during the first 100  $\mu\text{s}$  after initiating a simulation is shown in Fig. 7.3.

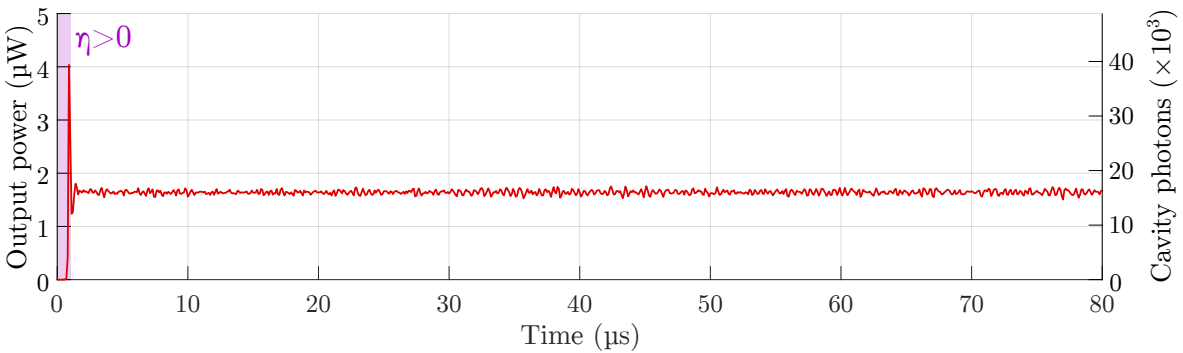


Figure 7.3: Time evolution of the total cavity output power (and photon number) in a simulation with  $\Phi = 10^{13} \text{ s}^{-1}$ ,  $v_{px} = 400 \text{ m/s}$  and no velocity selection. During the first 1  $\mu\text{s}$ ,  $\eta > 0$  to initiate the dynamics. Quantities such as output power are evaluated in steady state, e.g. for  $t > 10 \mu\text{s}$ .

### 7.1.3 Atom group approximation

Throughout the simulations presented in this chapter, the atom grouping approximation mentioned in Sec. 2.7 is used, with  $N_{pg} = 100$  atoms per group. In the continuous regime this does not affect mean values systematically, but fluctuations in e.g. power and instantaneous frequency over time scale with  $\sqrt{N_{pg}}$ , as seen in Fig. 7.4. Continuous mean values are evaluated over hundreds of  $\mu\text{s}$  after steady state is reached, so the random fluctuations over time also increase the random fluctuations in the evaluated mean values slightly.

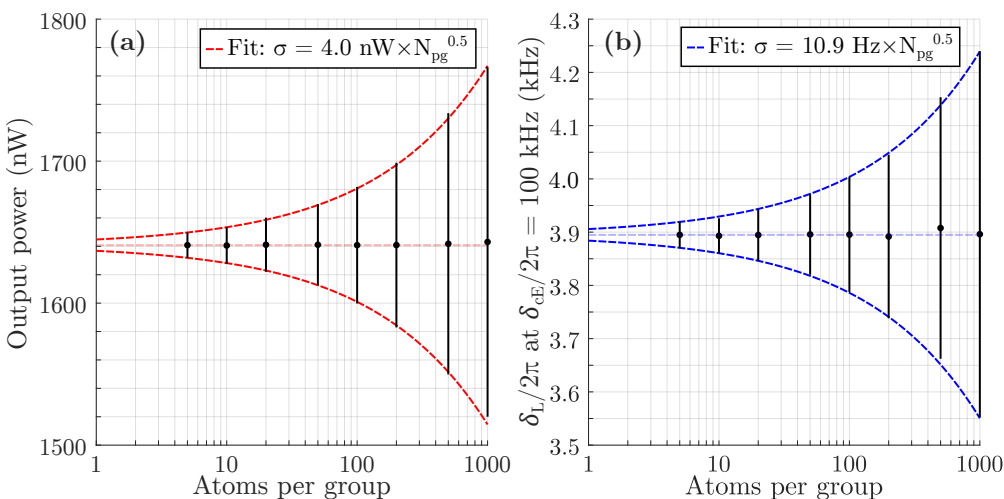


Figure 7.4: Scaling of mean values and fluctuations with  $N_{pg}$  in simulations during a time interval of 190  $\mu\text{s}$  for  $\Phi = 10^{13} \text{ s}^{-1}$ ,  $v_{px} = 400 \text{ m/s}$  and no velocity selection. (a) Cavity output power, (b) instantaneous lasing frequency. There is no systematic bias in the mean values in the continuous regime, but fluctuations scale with  $\sqrt{N_{pg}}$ .

## 7.2 Performance of the SRLM

Simulations were run using the cavity parameters in Tab. 6.1 to determine the expected output power from the SRLM. The results are presented in Fig. 7.5 in five different situations. Two sets of simulations assume either of the velocity distributions in Fig. 7.1(a). Within each set, one simulation assumes there is no velocity selection, with all atoms starting in  ${}^3\text{P}_1$ . Another simulation within each set assumes velocity selection is active, based on the criterium  $|v_z| < \lambda v_{px}/4W$ . Finally, one additional simulation is included for  $v_{px} = 400$  m/s, marked V2. Here the simulations use the specific population and temperature distributions obtained from the numerical simulations of velocity selection in Fig. 6.15, which may represent the effect of velocity selection more accurately, rather than the simple cutoff criterium.

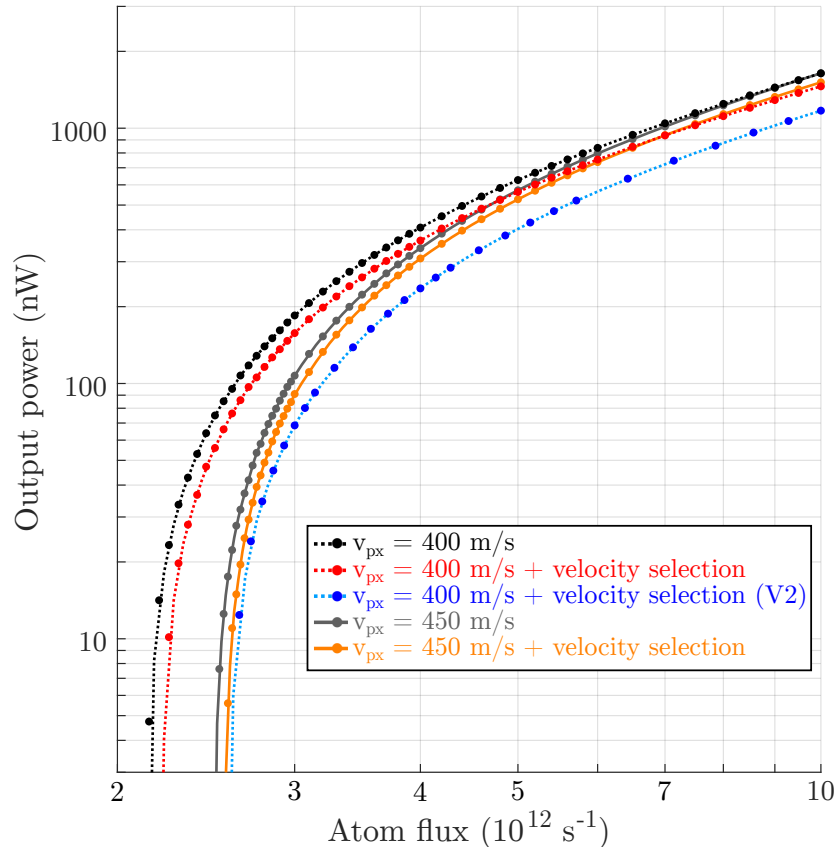


Figure 7.5: The cavity output power for varying atom flux according to simulations of the SRLM. Five different situations are investigated; the two velocity distributions in Fig. 7.1(a) with and without velocity selection. Velocity selection increases the lasing threshold slightly, and leads to a small reduction in output power. The lines show a moving mean with a span of two points. Figure adapted from [84].

We see that the threshold atom flux is approximately  $2.5 \cdot 10^{12} \text{ s}^{-1}$ , depending on  $v_{px}$ . Considering that the density decreases for higher  $v_{px}$ , we have  $\{3.71, 3.28\} \cdot 10^6$  atoms within the cavity waist for  $\Phi = 10^{13} \text{ s}^{-1}$  and  $v_{px} = \{400, 450\} \text{ m/s}$ , respectively. Accounting for this, the threshold is reached between 8 and  $8.5 \cdot 10^5$  atoms within the cavity waist, with a much smaller dependency on  $v_{px}$  for the atom number threshold.

In the simulations we see that the lasing threshold is slightly increased by the velocity selection scheme based on the cutoff criterium, and well above threshold the output power is lowered on the order of 10%. This is largely due to the reduction of the excited population. In the two cases  $v_{px} = \{400, 450\} \text{ m/s}$ , this velocity selection criterium results in  $\{17\%, 13\%\}$  of atoms starting in  ${}^1\text{S}_0$ . The drop in output power is not quite as high because the atoms with largest  $v_z$  also emit less efficiently when interacting with the cavity field, which has a

frequency closer to the resonance of the slow atoms. In the V2 case, 30% of atoms start in  $^1S_0$ , and the velocity distribution is not sharply cut off, resulting in a higher threshold and lower output power.

Once the threshold is reached, the output power increases rapidly. For e.g.  $v_{px} = 400$  m/s and with no velocity selection, the output power is zero for  $\Phi = 2.1 \cdot 10^{12}$  s $^{-1}$  but increases to 5 nW for  $\Phi = 2.15 \cdot 10^{12}$  s $^{-1}$ , which is already an easily detectable power. At  $\Phi = 7 \cdot 10^{12}$  s $^{-1}$  the output power reaches 1  $\mu$ W. Beyond this flux the power scales approximately linearly with the atom flux, as each atom emits on the order of one photon.

The cavity pulling characteristics are shown in Fig. 7.6 for a cavity detuning of  $\delta_{cE} = 2 \pi \cdot 100$  kHz and the same five situations as in Fig. 7.5.

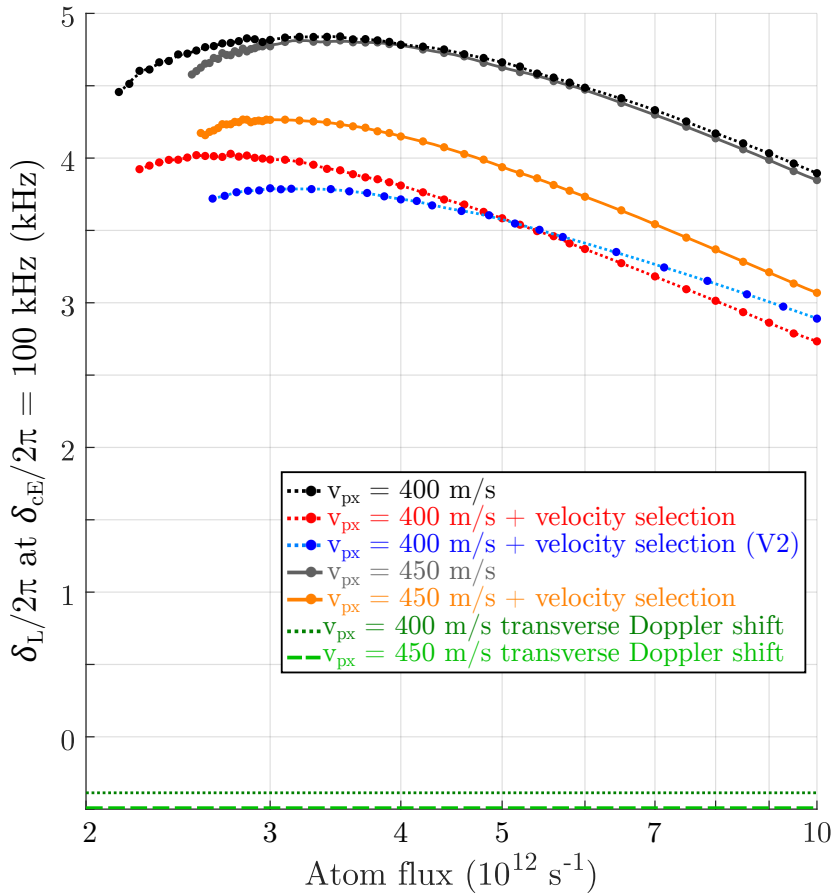


Figure 7.6: *Dependency of the lasing frequency shift on the atom flux for the same five situations as in Fig. 7.5. The cavity pulling coefficient can be considered approximately relative to the transverse Doppler shift for a given  $v_{px}$  (bottom lines). The simulations predict  $c_{\text{pull}}$  on the order of 0.03 to 0.06 and an 10-25% improvement from velocity selection. Lines show a moving mean with span of two points. Figure adapted from [84].*

First it is worth considering the impact of the relativistic Doppler shifts. The fact that the atomic resonance frequencies are distributed according to the asymmetric distribution in Fig. 7.1(b) means that it is non-trivial at which cavity resonance frequency,  $\omega_c$ , that the emitted lasing frequency  $\omega_L$  equals  $\omega_c$ . This should occur for a detuning on the order of the Doppler shift at  $v_x = v_{px}$ ,  $\delta_e^p$ , of -400 to -500 Hz - possibly shifted somewhat due to the peak at smaller values and large tail. In this situation the frequency where  $\omega_L = \omega_c = \omega_c^L$  provides the most logical reference point for defining the cavity pulling coefficient, instead of the unperturbed atomic resonance ( $\omega_E$ ):

$$c_{\text{pull}} = \frac{\omega_L - \omega_c^L}{\omega_c - \omega_c^L} = \frac{\delta_L - \delta_0}{\delta_{cE} - \delta_0}, \quad (7.4)$$

defining  $\delta_0 = \omega_c^L - \omega_E$  as the shift in ensemble resonance frequency due to the transverse Doppler shifts. Since we consider a cavity detuning of 100 kHz here, two orders of magnitude greater than the shifts, the denominator can be approximated by the cavity detuning,  $\delta_{cE}$ , as in the usual definition. But the shift in the ensemble resonance frequency caused by the Doppler shifts is not insignificant compared to  $\delta_L$ , so to obtain an approximate expression that does not rely on numerically determining  $\delta_0$ ,  $\delta_e^p$  can be used in its place. These values are indicated by the dashed green lines at the bottom of the figure. The value of  $c_{pull}$  is then given by the distance between these lines and the curves for the corresponding  $v_{px}$ .

We see that without velocity selection, the cavity pulling coefficients are on the order of 0.05 around the lasing threshold, with a maximum a bit above the threshold, and then a subsequent decrease to about 0.043 within the flux range considered here. Extrema in the cavity pulling coefficient are experimentally beneficial because they imply a local immunity to experimental fluctuations - at the cavity pulling maximum, small fluctuations in atom flux would not disturb the lasing frequency to first order, as it would elsewhere.

Such maxima are also visible for the curves with velocity selection included. The cutoff-based velocity selection reduces cavity pulling notably by 10-25 %, with  $c_{pull}$  in the range of 0.031 to 0.044 and 0.036 to 0.047 for  $v_{px}$  of 400 and 450 m/s, respectively. In the criterium  $|v_z| < \lambda v_{px}/4W$ , a higher  $v_{px}$  implies that the velocity selection scheme will have a smaller impact, as more atoms fulfill the criterium at a given  $T_z$ . The velocity selection based on simulated distributions, V2, shows a larger reduction in cavity pulling than the cutoff for low atom flux, but smaller reduction above  $\Phi = 5 \cdot 10^{12} \text{ s}^{-1}$ . This is due to the difference between the 2 mK velocity distribution from Fig. 6.15(d) used in V2 and the 3.6 mK distribution with a cutoff.

As we saw in Fig. 7.5 the emitted output power well above threshold is still at easily detectable levels in all cases. Therefore a more aggressive velocity selection criterium could also be set than in the examples shown here, if a high flux is obtained, to improve cavity pulling further at the expense of the output power.

### 7.2.1 Velocity selection requirements

In Sec. 6.4 we saw that shifting the velocity of atoms on the order of several m/s is realistic, so in this section we will investigate how the velocity shift affects the superradiant lasing signal. Here we assume  $\Phi = 10^{13} \text{ s}^{-1}$ ,  $v_{px} = 400 \text{ m/s}$ , and that all atoms for which  $|v_z| < \lambda v_{px}/4W$  is not obeyed (17%) start in  ${}^1\text{S}_0$ . For these  ${}^1\text{S}_0$  atoms,  $v_z$  is then fixed to one value at the beginning of a simulation to determine the impact of the different velocity classes. The results are shown in Fig. 7.7 for different velocity shifts. As other simulations with velocity selection also include a spread in the shifted velocities of  $T_z = 5 \text{ mK}$ , a data point at  $v_{shift} = 3 \text{ m/s}$  (green) is also included for this case. This has a minuscule impact compared to the case with a uniform shift of this magnitude.

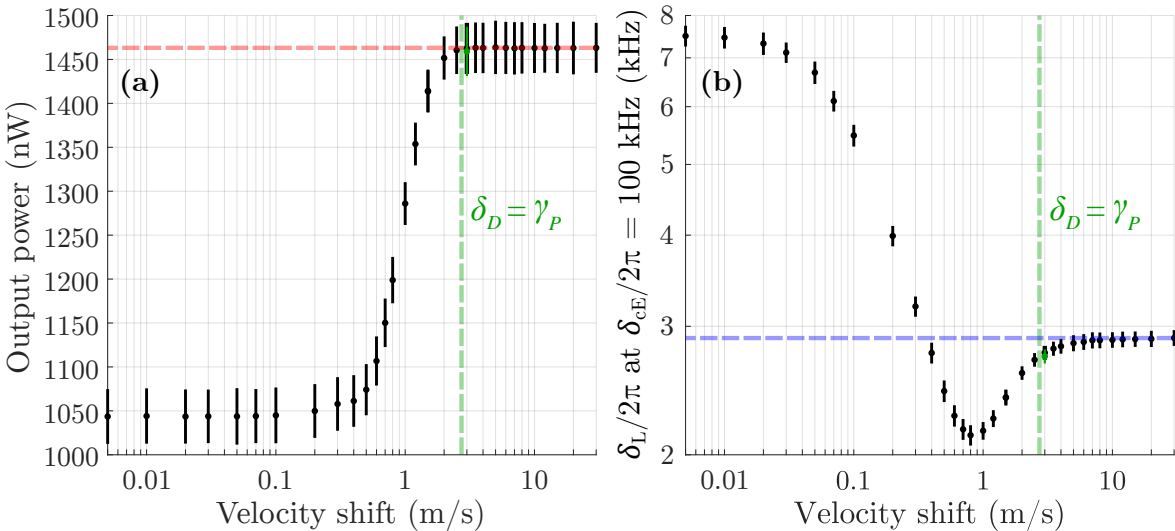


Figure 7.7: *Output power (a) and lasing frequency shift at 100 kHz cavity detuning (b) as function of velocity shift of rejected atoms in a velocity selection scheme. The atomic beam parameters are  $\Phi = 10^{13} \text{ s}^{-1}$  and  $v_{px} = 400 \text{ m/s}$ . Dashed horizontal lines show the values for  $v_{shift} = 30 \text{ m/s}$  for reference. Dashed vertical lines are based on Eq. 6.7. For the green data points at  $v_{shift} = 3 \text{ m/s}$ ,  $T_z = 5 \text{ mK}$  for the shifted atoms.*

We see that the output power is reduced due to absorption when the velocity shift is shifted less than 3 m/s. The shift in lasing frequency is sensitive to the velocity shifts over a broader range due to dispersive interactions. For a velocity shift of 3 m/s the deviation is less than 5 % of the frequency shift for 30 m/s. For comparison Eq. 6.7 suggests the velocity shift should be greater than 2.7 m/s given the single side output power of 730 nW and the SRLM cavity parameters.

### 7.2.2 Variations with atom temperature

The fact that velocity selection reduces cavity pulling is a result of the finite temperature, so reducing the temperature can similarly be advantageous. This is depicted in Fig. 7.8, where the temperature along the cavity axis is varied, with  $\Phi = 10^{13} \text{ s}^{-1}$ ,  $v_{px} = 400 \text{ m/s}$  and no velocity selection scheme. The green lines indicate  $T_z = 3.6 \text{ mK}$ , which was achieved during optimization of the SRLM and is used in the other simulations.

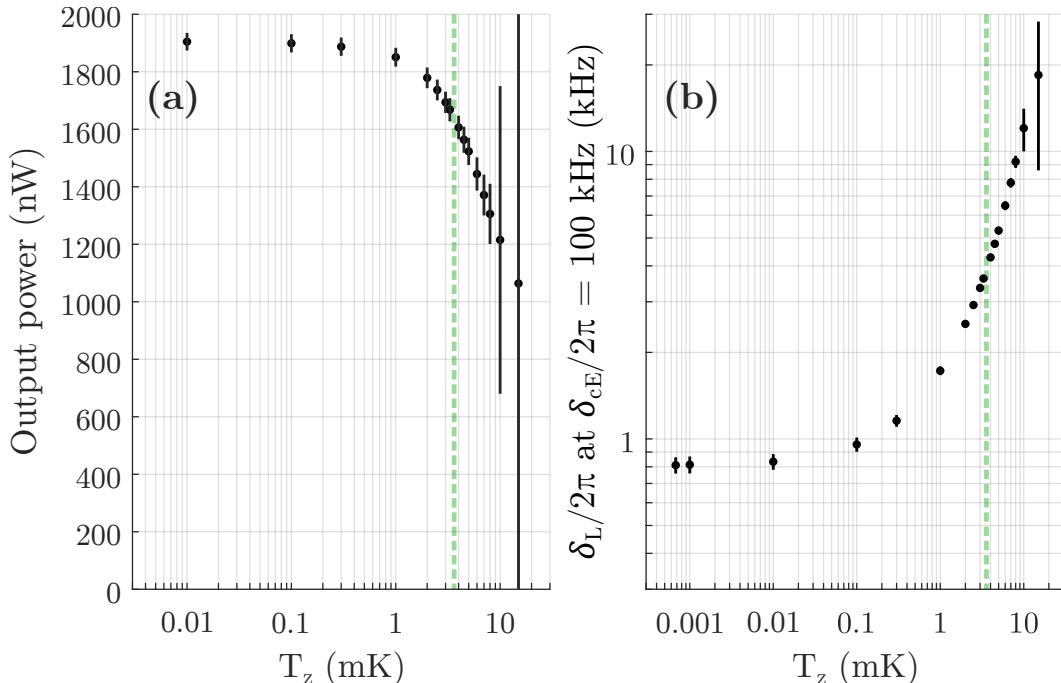


Figure 7.8: *Dependency of output power (a) and lasing frequency shift (b) on the atom temperature  $T_z$  along the cavity axis. The atomic beam parameters are  $\Phi = 10^{13} \text{ s}^{-1}$  and  $v_{px} = 400 \text{ m/s}$ . Dashed vertical lines indicate  $T_z = 3.6 \text{ mK}$  as used in other simulations.*

We find that the output power is sensitive to the temperature down to about 1 mK, below which it remains steady. At this point the Doppler shifts begin to become less significant compared to the Rabi frequency in this output power regime (again considering Eq. 6.7). In panel (b) we see that the cavity pulling can be influenced by the temperature over a wider range down to about 10  $\mu\text{K}$ , where cavity pulling has reduced to about 1/3 of its value at 3.6 mK (taking into account the relativistic Doppler shift). This suggests cavity pulling may be reduced significantly with an aggressive velocity selection scheme that leaves only the very slowest atoms, if the atom flux is high enough that lasing can still be maintained.

In the opposite regime above 8-10 mK, the standard deviations of output power and instantaneous lasing frequency increase significantly. Here oscillations in the output power become pronounced. A similar transition from stable to bistable superradiant lasing was found in [89], where the atomic beam was slanted with respect to the cavity axis. The bistable regime emerged when the atoms traversed more than half a wavelength along the cavity axis during their transit through the waist. For a high enough temperature in the SRLM, most atoms will similarly fulfill this criterium. In [87] similar transitions to a multi-component regime were found for a thermal distribution, which is more similar to our system. In Fig. 7.9 the dynamics are illustrated for  $T_z = 15 \text{ mK}$ , showing power oscillations and multiple frequency components arising in the spectrum, similar to the multi-component superradiant (MCSR) regime found in [87].

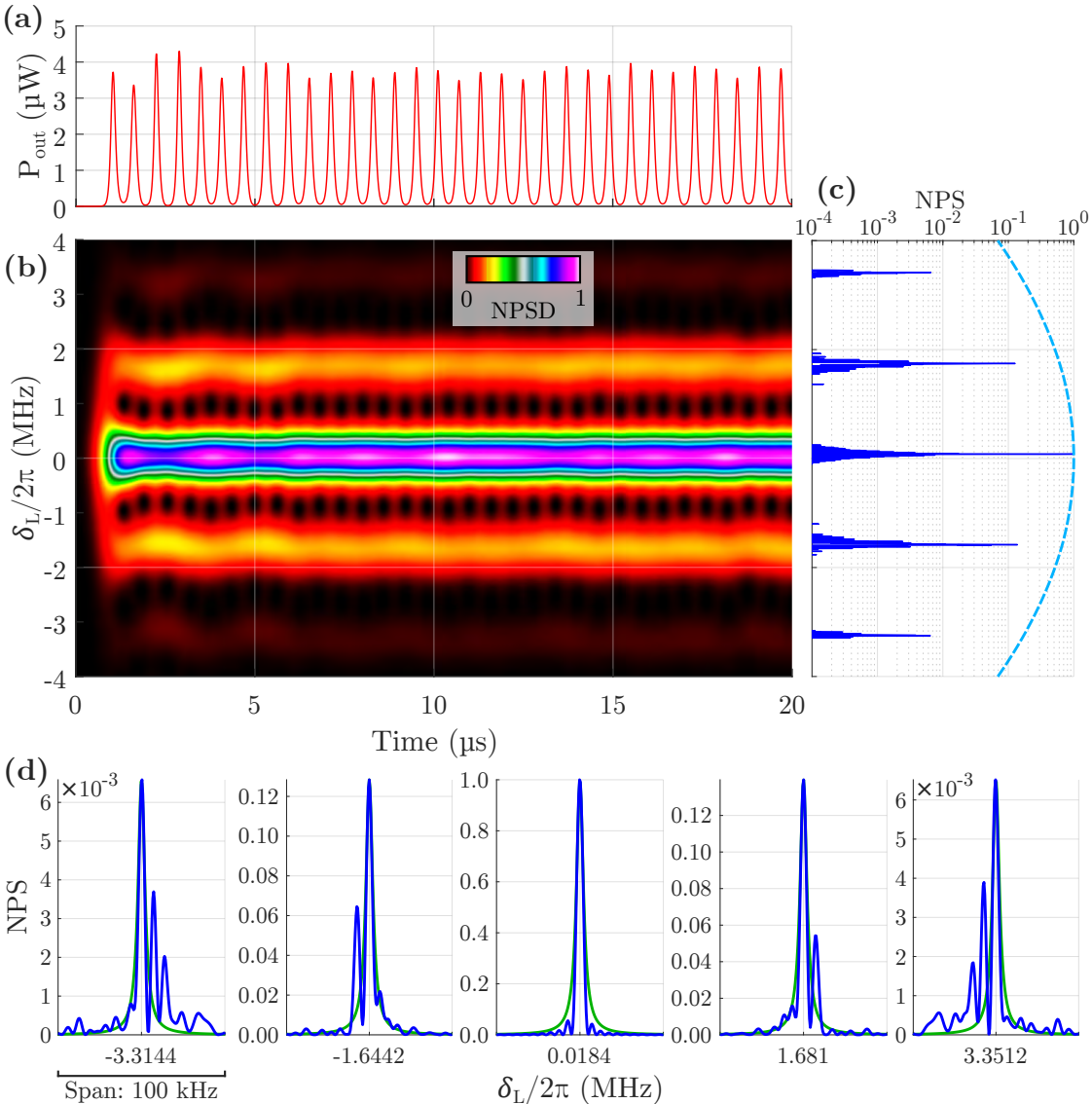


Figure 7.9: Multi-component lasing for  $T_z = 15 \text{ mK}$  and  $v_{px} = 400 \text{ m/s}$ . (a) The output power shows large oscillations with a frequency of  $1.66 \text{ MHz}$ . (b) Normalized power spectral density (NPSD) in a spectrogram with a window width of  $392 \text{ ns}$ , showing the frequency components in the emitted light. (c) The power spectrum after  $200 \mu\text{s}$ . The dashed curve shows a normalized Doppler shift distribution at  $15 \text{ mK}$  for comparison. (d) The individual peaks of panel (c), green curves indicate the  $5 \text{ kHz}$  Lorentzian Fourier width for comparison.

In this regime there is still a central component in the spectrum (panel (c)) from the atoms with lowest  $v_z$ , peaked  $18.4 \text{ kHz}$  from the atom transition frequency (corresponding to the point in Fig. 7.8(b)). Furthermore there are two peaks at  $\pm 1.66 \text{ MHz}$  from the central component, and another pair with slightly more than twice the separation. The five peaks in Fig. 7.8(c) are shown in more detail in panel (d).

We can consider how the observed splitting relates to relevant frequencies in the system. Two frequencies which are of the same order of magnitude are the Rabi frequency,  $2g\sqrt{n}/2\pi$ , and the transit time broadening,  $\Gamma_T/2\pi = 2v_{px}/\pi\sqrt{\pi}W$ . This definition of  $\Gamma_T$  is based on averaging over the transverse Gaussian profiles experienced by different atoms [85, p. 349] [149, p. 1663]. As it accounts for this, it is a bit lower than the Doppler shift required to traverse a full wavelength during transit through the center of the cavity waist,  $v_{px}/2W = 2.3 \text{ MHz}$ . Determining the exact scaling of the splitting frequencies would require simulations in several different regimes, and here we will consider just a few different examples. In one other case for  $T_z = 10 \text{ mK}$  and  $v_{px} = 350 \text{ m/s}$ , the dynamics are qualitatively similar to in Fig. 7.9

but with the five peak frequencies at  $\delta_L/2\pi = \{-3.53, -1.76, 0.0145, 1.79, 3.56\}$  MHz, giving a spacing of 1.77 MHz.

For the Rabi frequency,  $n$  oscillates between almost 0 and  $10^4$  in the 15 mK case, so a Rabi frequency may be attributed using  $\langle \sqrt{n} \rangle = 86$  and the maximum coupling  $g_0$ , giving a maximum average Rabi frequency of 1.94 MHz. For the 10 mK case we get 2.32 MHz. These frequencies are not related to the found splittings in an obvious way, but there is at least qualitative agreement of them increasing with the Rabi frequency. For the transit time broadening we get  $\Gamma_T/2\pi = 1.67$  MHz for the 15 mK example, but for the 10 mK case we get  $\Gamma_T/2\pi = 1.46$  MHz, indicating that the splittings do not scale with  $\Gamma_T$ .

We can also consider a case for  $T_z = 15$  mK and a slower atomic beam with  $v_{px} = 350$  m/s. In this regime the atoms traverse a bigger fraction of a wavelength during transit, and the lasing dynamics become chaotic, as seen in Fig. 7.10.

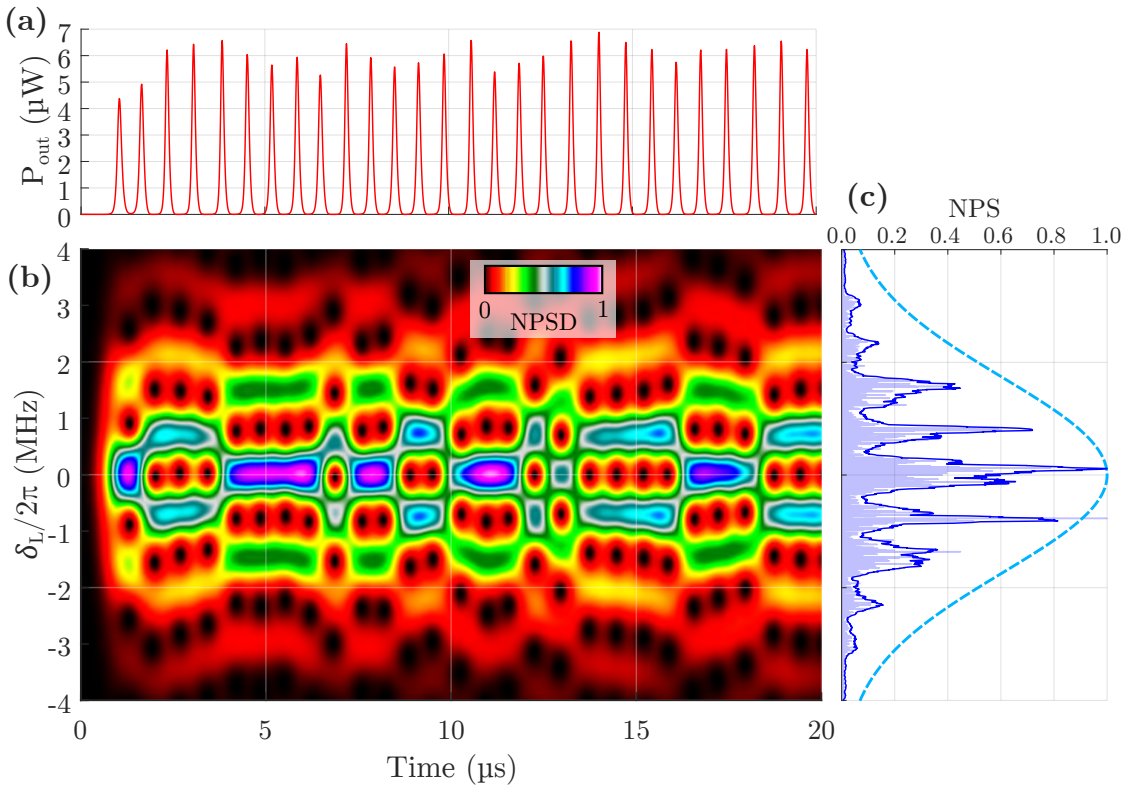


Figure 7.10: *Chaotic lasing for  $T_z = 15$  mK and  $v_{px} = 350$  m/s.* (a) The output power shows large, irregular fluctuations. (b) Spectrogram with a window width of 392 ns. (c) The power spectrum (light blue background) and its renormalized moving mean with a span of 100 kHz (dark blue) after 200  $\mu\text{s}$ . The dashed curve shows a normalized Doppler shift distribution at 15 mK for comparison.

The mean output power is just 3 % higher than for  $v_{px} = 400$  m/s, but the power fluctuations are bigger. In the spectrogram in panel (b) we see there are jumps between an "odd" regime with one main peak and sidebands like in Fig. 7.9 and another "even" regime with no central peak, but an even number of peaks symmetric around  $\delta_L \approx 0$ . The odd configuration has peaks near approximately  $\delta_L/2\pi = \{-1.47, 0.12, 1.58\}$  MHz, giving a span of 1.5 MHz, while the even configuration has peaks near  $\{-0.79, 0.81\}$  MHz, giving a span of 1.6 MHz. In [87, p. 12] such a chaotic, unstable regime is found between an odd regime for relatively low Doppler widths within MCSR, and even regime for larger widths.

Finally, we can also consider the behavior closer to the lasing threshold. In another simulation for the parameters in Fig. 7.9 but with half the atom flux, the main peak is on the order of

$10^4$  times larger than the sidebands, which also have a smaller splitting of 0.9 MHz. Here  $\langle\sqrt{n}\rangle = 44$ , giving  $2g_0\sqrt{n}/2\pi = 980$  kHz, in agreement with the splitting scaling with  $g\sqrt{n}$ . If we think of each of the peaks as originating from atoms within certain velocity ranges and neglect interactions between them, the atoms contributing the sidebands require a higher atom flux before reaching their lasing threshold than the ones contributing the main peak, because they are less abundant in the thermal distribution. From this we can expect regular sidebands to disappear near the lasing threshold of the whole system, especially at lower temperatures.

### 7.2.3 Impact of decoherence from stray light

Some stray light will inevitably reach the atoms within the cavity, and our main concern is scattered light from the transverse cooling beams and the 461 nm beam in Stage 2 of the pumping scheme. Considering this light as an incoherent pumping source from  $|g\rangle = ^1S_0$  to  $|c\rangle = ^1P_1$ , near the angular transition frequency  $\omega_C$ , we may approximate the transverse decay rate on the lasing transition  $\gamma_T$  as half the pumping rate  $w$ , using equations from Sec. 2.3:

$$\frac{\gamma_T}{\gamma_{eg}} \approx \frac{1}{2} + \frac{12\pi c^2 I}{\hbar\omega_C^3 \gamma_{eg}} = \frac{1}{2} + 10 \frac{W^{-1}}{m^{-2}} \cdot I. \quad (7.5)$$

This assumes that all the stray light reaching the atoms in the cavity has ideal polarization and frequency to drive one of the  $^1P_1$  Zeeman transitions. Any significant detuning relative to  $\gamma_{cg}/2\pi = 30$  MHz and any polarization imperfections would reduce it further. The simulated impact of an increase in  $\gamma_T$  on the superradiant laser emission is shown in Fig. 7.11.

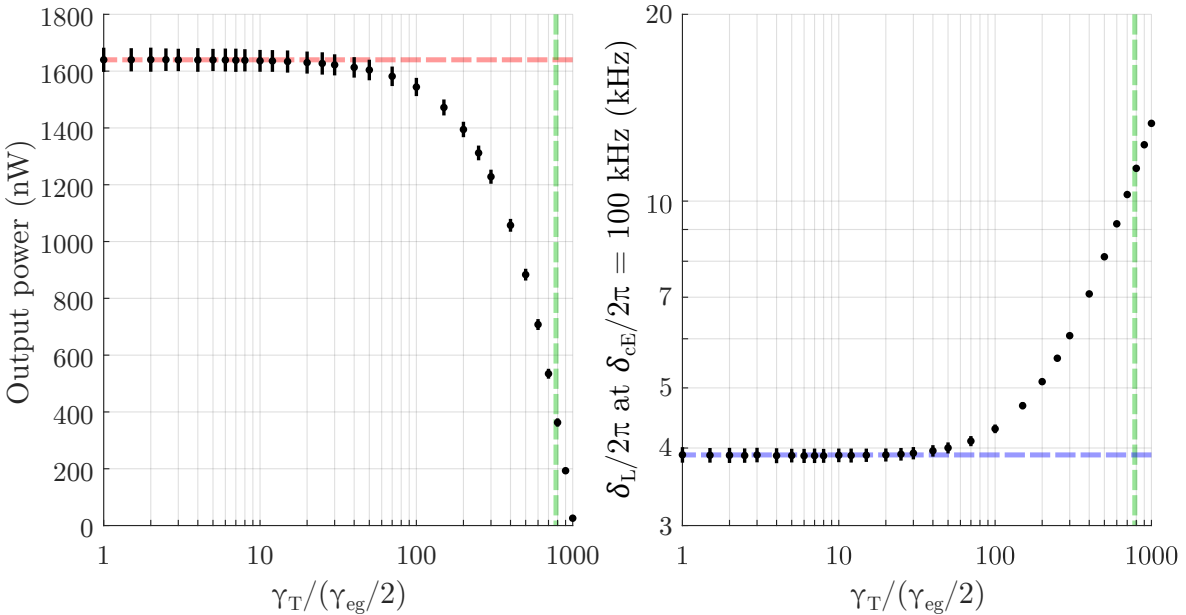


Figure 7.11: Dependency of output power (a) and lasing frequency shift (b) on the transverse decay rate  $\gamma_T$  in units of  $\gamma_{eg} = 2\pi \cdot 7.5$  kHz. Horizontal lines mark the ideal values with no additional decoherence. Vertical lines indicate where  $\gamma_T = 2g_0\sqrt{n}$  (using the photon number for  $\gamma_T = \gamma_{eg}/2$ ).

The drop in output power and increase in cavity pulling starts to become significant near  $\gamma_T \approx 100\gamma_{eg}$ , for an intensity on the order of  $1 \text{ W/m}^2$ . One order of magnitude above, the power drops to zero. In general the impact of decoherence will be significant when it is on the order of the Rabi frequency of the atom-cavity interaction,  $2g\sqrt{n}$ , so for e.g. a lower atom flux, less decoherence can be tolerated. If we consider the example in Sec. 6.4.1, we can assume 30 % of atoms (the rejected  $^1S_0$  population) each scatter 500 photons from the push beam. As a crude approximation we can then consider this as a point source located 5 mm

from the cavity. For an atom flux of  $10^{13} \text{ s}^{-1}$  the scattered power is then  $650 \mu\text{W}$ , giving  $2.3 \text{ W/m}^2$  at the cavity location, which would severely impact the performance. However this estimate is extremely uncertain, given the high density of the atomic beam, which can cause many internal scattering events. We can consider the mean free path of a  $461 \text{ nm}$  photon, for which the scattering cross section [20, p. 142] is  $10^{-13} \text{ m}^{-2}$ , again assuming ideal polarization and detuning. If the atom flux is confined within  $1/4$  of the cavity length, we then get an atom density of  $10^{17} \text{ m}^{-3}$  and assuming  $30\%$  are in  ${}^1\text{S}_0$ , the mean-free path is  $300 \mu\text{m}$ . As such photons may experience several scattering events on the way to the cavity, possibly protecting the cavity atoms to a degree, and highlighting the big uncertainty of these simple estimates.

### 7.2.4 Expected linewidth

In simulations of the SRLM, the linewidth is Fourier-limited to  $5 \text{ Hz}$  after  $200 \text{ ms}$ , with no sign of broadening occurring within the numerical model. As described in Sec. 2.6.3, the linewidth may be broadened further due to the neglected spontaneous emission into the cavity mode. The simple estimate  $C\gamma_{eg}$  yields a linewidth of  $9.4 \text{ Hz}$ . For  $v_{px} = \{400, 450\} \text{ m/s}$  we get  $\delta_D\tau = \{1.06, 1.20\}$ , using the notation in [86, p. 3]. Here an increase in linewidth of about  $30$  to  $40\%$  beyond  $C\gamma_{eg}$  is seen for such parameters. Further cooling or velocity selection could improve this. The generalized Schawlow-Townes limit gives a lower limit of  $0.3 \text{ Hz}$  for  $\Phi = 10^{13} \text{ s}^{-1}$ ,  $v_{px} = 400 \text{ m/s}$  and assuming a perfect inversion. This limit only exceeds  $C\gamma_{eg}$  for output powers below  $60 \text{ nW}$ , very near the lasing threshold.

## 7.3 Sensitivity to cavity fluctuations

Here we will consider the sensitivity of the superradiant laser to changes in the cavity resonance frequency more generally. First we will consider the case where the cavity detuning is fixed, but at an arbitrary value. The variation of output power and lasing frequency with the cavity detuning in this regime is shown in Fig. 7.12 for  $\Phi = 10^{13} \text{ s}^{-1}$ ,  $v_{px} = 400 \text{ m/s}$  and with no velocity selection.

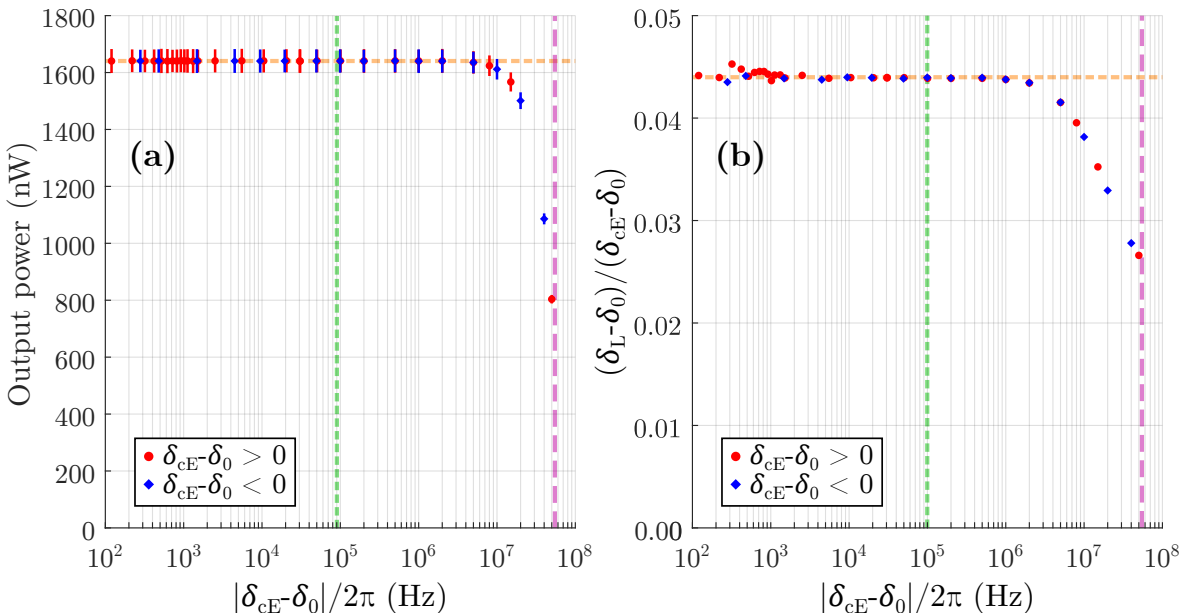


Figure 7.12: Dependency of output power (a) and lasing frequency shift  $\delta_L$  (b) on the cavity detuning,  $\delta_{cE}$ . The frequency axes are offset by the shift in ensemble resonance of  $\delta_0/2\pi = 520 \text{ Hz}$  due to the relativistic Doppler shifts. The detuning of  $100 \text{ kHz}$  used in other simulations is highlighted by the vertical green dashed line, and the vertical purple long dashed line indicates the magnitude of the cavity linewidth. The horizontal lines indicate the power and pulling coefficient for small detunings.

As seen in panel (a), the cavity output power is insensitive to changes in the cavity detuning that are small compared to the cavity linewidth of 53.9 MHz. From the data set in panel (b) we find  $\delta_0/2\pi = -520$  Hz for these parameters, somewhat larger than the transverse Doppler shift  $\delta_e^p/2\pi = -387$  Hz (seen in Fig. 7.1(b)) at the most probable  $v_x$ . This may be expected given the asymmetry of the distribution, and the variations in how the transit time matches  $1/2g\sqrt{n}$  for the different velocity classes. The detuning axes in Fig. 7.12 are therefore shifted by  $\delta_0$  to determine the cavity pulling coefficient over a wide range of cavity detunings, shown in panel (b). The pulling coefficient remains constant until the cavity detuning is on the order of the cavity linewidth, though the variation becomes apparent sooner than the variation in power. For large detunings the lasing frequency becomes even less sensitive to changes.

Frequency fluctuations vary significantly depending on the cavity detuning. This dependency is shown in Fig. 7.13 where we find a range of frequencies where the fluctuations, characterized by the standard deviation  $\sigma_{inst}$  in the instantaneous frequency, increase linearly with the cavity detuning. This occurs because of the random fluctuations in the atomic distribution over time, which cause small fluctuations in the cavity pulling coefficient. When the cavity is near resonance with the ensemble, a change in  $c_{pull}$  has little impact on the lasing frequency, but the larger the cavity detuning is, the more the lasing frequency will change due to a change in  $c_{pull}$ . Finally, these fluctuations also scale with the fluctuations in the ensemble distribution, which is affected by the atom group approximation as we saw in Fig. 7.4. This approximation has been accounted for in Fig. 7.13 by downscaling the fluctuations by a factor 10.

The linear relation does not hold for cavity detunings on the order of the cavity linewidth, which is to be expected as we saw that the cavity pulling coefficient also varies on this scale. There are also deviations below  $10^5$  Hz and an asymmetry with respect to  $|\delta_{cE} - \delta_0| = 0$ , in particular there is a minimum near  $\delta_{cE}/2\pi = 5.5$  kHz. At this cavity detuning the lasing frequency shift is  $\delta_L/2\pi = -250$  Hz, equal to the most probable transverse Doppler shift in Fig. 7.1(b). The minimum in fluctuations at this detuning is expected to arise from a combination of cavity pulling and the shape of the transverse Doppler shift distribution.

The nonlinear variation in cavity pulling or the increase of frequency fluctuations with detuning can in principle both be used for locking the cavity to the atomic transition. However a higher sensitivity may be obtained by beating the SRL output with light locked to the resonance of another mode of the cavity. Since the SRL output will approximately stay at the atom transition frequency if the cavity detuning changes, such a beat signal would change frequency approximately by the same amount as any shift in cavity detuning.

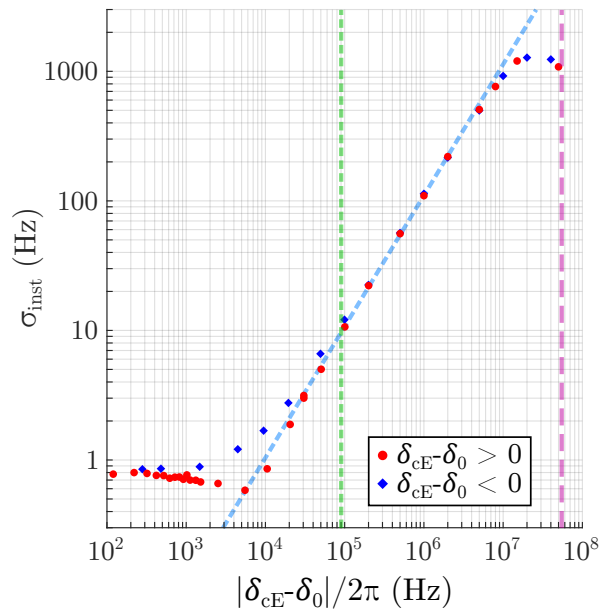


Figure 7.13: Standard deviation of the instantaneous frequency at different cavity detunings with respect to the ensemble resonance frequency. Vertical lines mark frequencies as in Fig. 7.12, and the blue dashed line highlights a linear regime.

### 7.3.1 Dynamic cavity pulling

Here we will investigate the impact of dynamic perturbations to the cavity resonance frequency, as this can be very different from the steady-state behavior. We will use the method described in Sec. 2.6.4, subjecting the system to sudden steps in cavity detuning and record the response of the instantaneous frequency. These steps are jumps away from zero detuning. The response is used to calculate the gain curves shown in Fig. 7.14, which can be interpreted as frequency-dependent cavity pulling coefficients. Below 100 kHz the response is approximately flat and corresponds to the static pulling coefficients  $(\delta_L - \delta_0)/(\delta_{cE} - \delta_0)$  in Fig. 7.12(b).

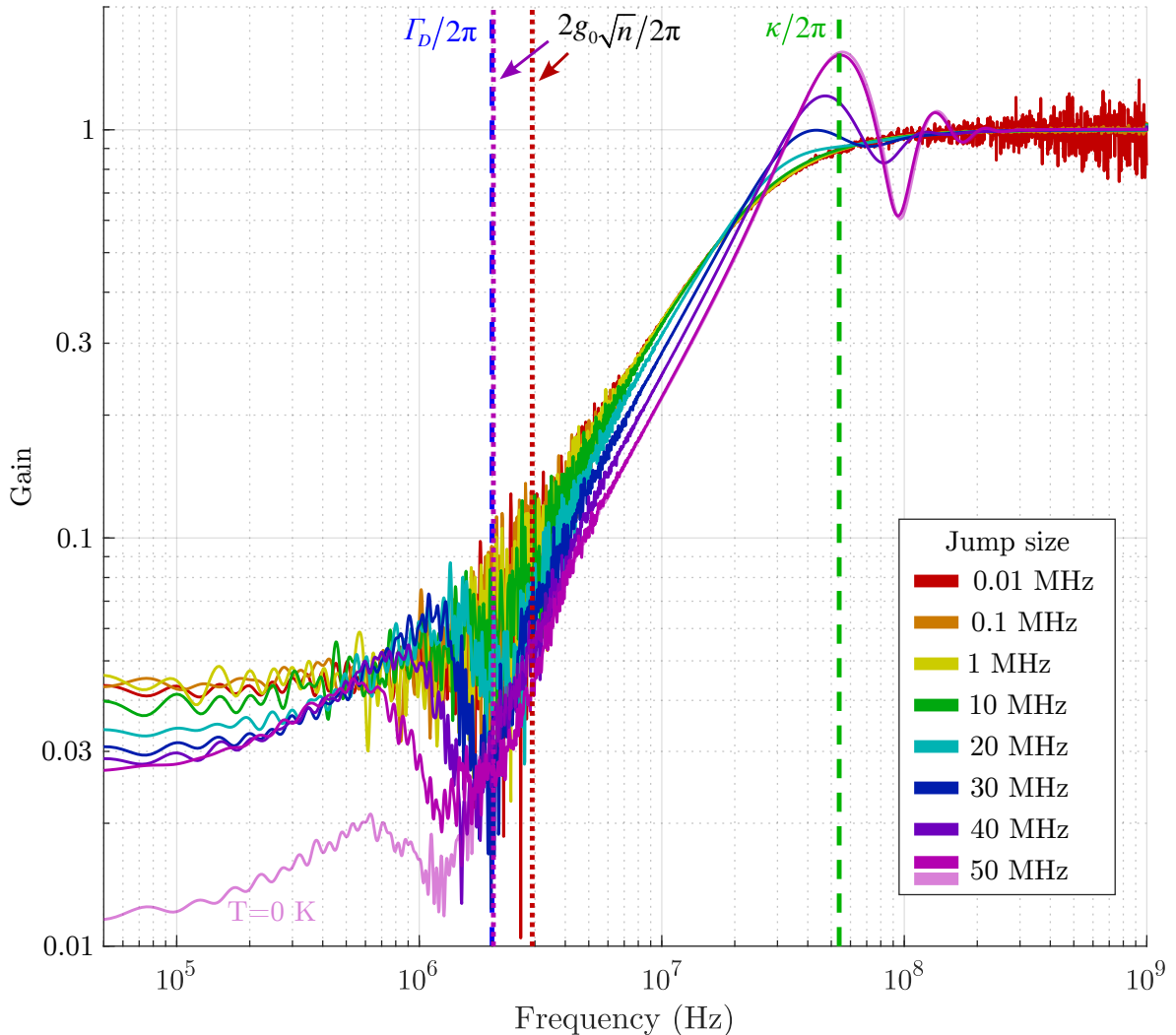


Figure 7.14: Frequency-dependent response of the instantaneous lasing frequency to instant jumps in the cavity detuning away from 0. The response is approximately flat below 100 kHz, corresponding to the static cavity pulling coefficient. Some characteristic frequencies in this regime are marked by vertical dashed lines.  $T_z = 3.6 \text{ mK}$  except for the curve marked with  $T_z = 0 \text{ K}$ , for comparison.

For small jump sizes, which are most likely to be encountered in the setup, the response curves are relatively smooth and increase from  $4 \cdot 10^{-2}$  to unity in the range of 1 to 100 MHz. This implies that very rapid changes in the cavity detuning would not be suppressed in the laser spectrum. In practice, the macroscopic motion of cavity mirrors is typically restricted below the MHz range. This motion may be caused by noise in the mirror piezo or mechanical disturbances, but will fall within the frequency range with significant suppression. There are also many sources of noise within mirrors and coatings themselves (see e.g. [150, Chap. 3]), for which the PSD generally decreases with frequency and as such these sources are also

suppressed in influencing the laser frequency. Therefore the most important result of Fig. 7.14 is that cavity pulling is more or less constant up to fluctuations of  $\sim 1$  MHz in this system.

For steps on the order of the cavity linewidth the curves become less smooth, and a peak forms at the cavity linewidth, showing that fluctuations on this order would actually be amplified in the lasing frequency shift, if they occurred on the timescale of the cavity lifetime. However this would require very extreme motion of the mirrors, unexpected in the physical setup.

Another dip feature appears in the curves near both the 3.6 mK Doppler width of the system and the Rabi frequencies, which are marked in the figure. Since the power becomes lower at large detunings as we saw in Fig. 7.12(a), the final Rabi frequency also lowers after these jumps. Thus the red vertical dashed line indicates the Rabi frequency for the 10 kHz jump, and the purple one indicates the smallest Rabi frequency for the 50 MHz jump.

One curve is included with a jump size of 50 MHz, but a temperature of 0 K for comparison. Here the power and Rabi frequency are a bit higher (2.5 MHz) than in the 3.6 mK case. The dip right below the Rabi frequency remains, but becomes less prominent. Additionally the cavity pulling is lowered for frequencies below the 3.6 mK Doppler width, instead approaching the steady-state value near 0.01 that we found for the lowest temperatures in Fig. 7.8(b).

Noise is visible near the Rabi frequency in the curves, and also at high frequencies when the jump size is small. This is introduced by the random fluctuations in the atom distribution over time, which affect the instantaneous frequency separately from the jump in detuning. As such the noise is not representative of actual changes in the response, but is simply a result of the other random effects in a simulation which are also causing fluctuations in the lasing frequency. This noise is further increased due to the atom group approximation and also increases with the analysis window length (20  $\mu$ s).

## 7.4 Absorption and driven lasing

Realizing superradiant lasing requires a sufficiently high atom flux to reach threshold and efficient atom pumping and cooling. Coupling resonant light into the cavity makes it possible to measure quantities that vary with the atom flux far below the threshold, which is useful for optimization. One tool is the absorption, where the atoms entering the cavity are left in  $^1S_0$  and the output power is monitored. A second tool is the amplification of light by  $^3P_1$  atoms. The scalings of these quantities relative to the cavity input power are shown in Fig. 7.15 for an input power of 1 nW,  $v_{px} = 400$  m/s and no velocity selection. Here the atom group approximation is omitted for  $\Phi \leq 10^{12}$  s $^{-1}$ .

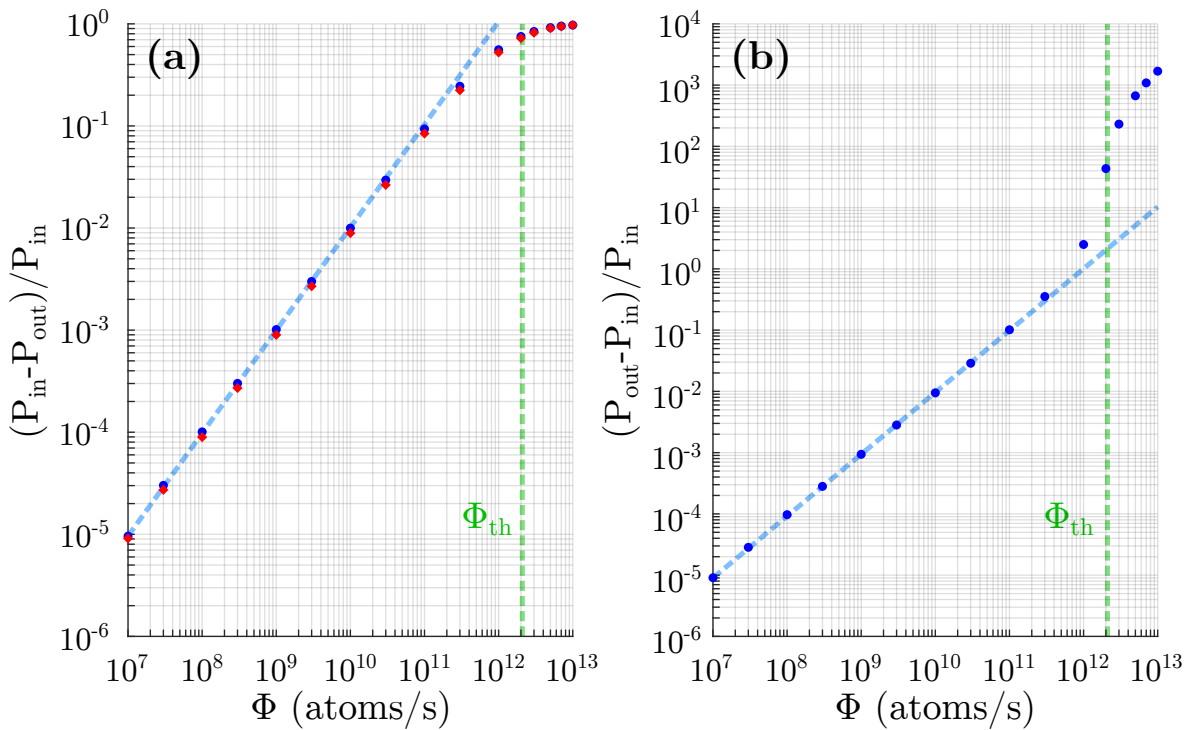


Figure 7.15: Possible signal amplitudes for (a) absorption measurements with atoms starting in  ${}^1S_0$ , or (b) amplification measurements with atoms starting in  ${}^3P_1$ .  $T_z = 3.6 \text{ mK}$  (blue circles) and  $5 \text{ mK}$  (red diamonds in panel (a)). The cavity input power is  $1 \text{ nW}$ , and  $v_{px} = 400 \text{ m/s}$ . The blue dashed line highlights the linear trend below the lasing threshold, and vertical green line indicates the threshold flux from Fig. 7.5 with no driving laser.

Far below the lasing threshold (indicated by vertical green lines), the potential signal amplitude is very low. Experimentally such signals may be detected by frequency-modulating some of the pumping stages to periodically shelve some of the atoms and vary the  ${}^1S_0$  or  ${}^3P_1$  populations. This would give an oscillating fingerprint in the output power which can more easily be distinguished from the constant background, e.g. on a spectrum analyzer.

The potential signal amplitudes are similar with either method far below the lasing threshold, but amplification measurements are much more sensitive near the threshold. As seen in panel (b), the power can increase by orders of magnitude within one magnitude in flux. On the other hand, the absorption signal becomes less sensitive to the atom flux, as seen in panel (a). These behaviors are also dependent on the cavity input power - amplifying  $1 \text{ nW}$  by a factor  $10^3$  yields an output power consistent with Fig. 7.5 above the threshold, but  $1 \mu\text{W}$  cannot be amplified to  $1 \text{ mW}$  as this would require far more energy than what can be released from the  ${}^3P_1-{}^1S_0$  transition into the cavity with these atom fluxes. On the other hand, a lower input power in an absorption measurement can result in complete absorption for a lower flux, making the signal insensitive at higher ranges of flux. With that in mind, a higher  $P_{in}$  is generally desirable if the sensitivity can be preserved, as this allows for a larger total signal amplitude.

As shown in Fig. 7.15(a), the signals are also sensitive to other parameters such as the temperature along the cavity axis - for  $T_z = 5 \text{ mK}$ , the absorption is reduced on the order of 10 % below threshold compared to  $3.6 \text{ mK}$ . As a result they can also be used to optimize the transverse cooling stage, and the amplification will be very sensitive to the efficiency of the later pumping stages as well, allowing for their optimization.



## Superradiant lasing from a cold atom beam

In this chapter we will use numerical simulations to explore continuous superradiant lasing in a potential system utilizing an ultracold atomic beam. The model and many of the results in this chapter have also been presented in [84]. The atom source is based on the cold atomic beam realized in [98], for which relevant parameters are listed in Table 8.1.

This architecture based on a cold atomic beam was initially considered during the design stage of the SRLM presented in Chapter 6, but the hot beam system proved to be advantageous. For comparison the flux in this cold beam system is about five orders of magnitude lower, the propagation velocities are over three orders of magnitude lower, and the temperature is in the low  $\mu\text{K}$  regime. The experimental setup required for generating such an atomic beam is also much more complex than the hot atomic beam. However the slow propagation velocity makes the relativistic Doppler shifts encountered in the hot beam system insignificant, and we also saw in Sec. 7.2.2 that the mK temperature is a limiting factor in reducing cavity pulling in the system. Furthermore the slow propagation velocities allow for repumping atoms within the cavity mode, such that each atom may emit multiple photons during transit.

Even though the hot beam system is advantageous for the kHz-wide  $^1\text{S}_0$ - $^3\text{P}_1$  transition in many aspects, realizing superradiant lasing on significantly narrower transitions with a hot beam requires unfeasible atom fluxes to reach lasing threshold. Therefore the physics and challenges of superradiant lasing using a cold atomic beam are not only of interest in the design of the SRLM, but also more generally for schemes using very narrow transitions.

Many of the behaviors in earlier chapters also apply to the cold beam system. At sufficiently high temperatures, multicomponent lasing can arise as for the repumped cloud in Chap. 5 and the hot beam system in Sec. 7.2.2. Variations in cavity pulling with cavity detuning variations in Sec. 7.3 similarly carry over qualitatively, even though the exact quantities are different. We will not go into detail with these aspects again, but instead focus on new effects appearing in the cold beam system.

Atom flux	$\Phi$	$3.25(14) \cdot 10^7 \text{ s}^{-1}$
Axial temperature	$T_x$	$29(2) \text{ } \mu\text{K}$
Radial temperature	$T_R$	$0.89(4) \text{ } \mu\text{K}$
Mean propagation velocity	$v_x$	$8.4(4) \text{ cm/s}$
Radial density parameter	$\sigma_R$	$23.3(4) \text{ } \mu\text{m}$
Radial trapping frequency	$\omega_t$	$2\pi \cdot 185(10) \text{ Hz}$

Table 8.1: *Parameters of the ultracold atomic beam source reported in [98] relevant for the simulations of continuous superradiant lasing. We will also consider higher atom fluxes, as further upgrades to the setup have made up to  $3 \cdot 10^8 \text{ s}^{-1}$  realistic [151].*

The system is illustrated in Fig. 8.1, looking along the cavity axis in panel (a), and the repumping axis in (b). Atoms arrive from the left, and it is assumed that they are shelved in the long-lived state  ${}^3P_0$ . When they arrive within the cavity waist, they are continuously repumped to  ${}^3P_1$   $m_J=0$ . This is done using the same transitions as in previous chapters, with a configuration of magnetic field and pump lasers similar to in Stage 3 of Fig. 6.13, but including also an 689 nm laser. The concrete schemes for the cold beam model here are illustrated in Fig. 8.1(c) and (d) for the shelving region and lasing region with continuous pumping, respectively. The atoms tend to eventually propagate away from the cavity region due to heating caused by repumping. The assumed cavity parameters are given in Table 8.2, where the waist size is chosen to ensure a good overlap with the atomic beam, and the linewidth is chosen to ensure a lasing threshold below the experimentally realized atom flux. The length is chosen to be comparable to the cavity in the hot beam machine. While a shorter length on the order of the atomic beam width would allow for better performance in simulations, it would also lead to technical drawbacks such as larger FSR and increased sensitivity to e.g. mirror fluctuations and piezo noise.

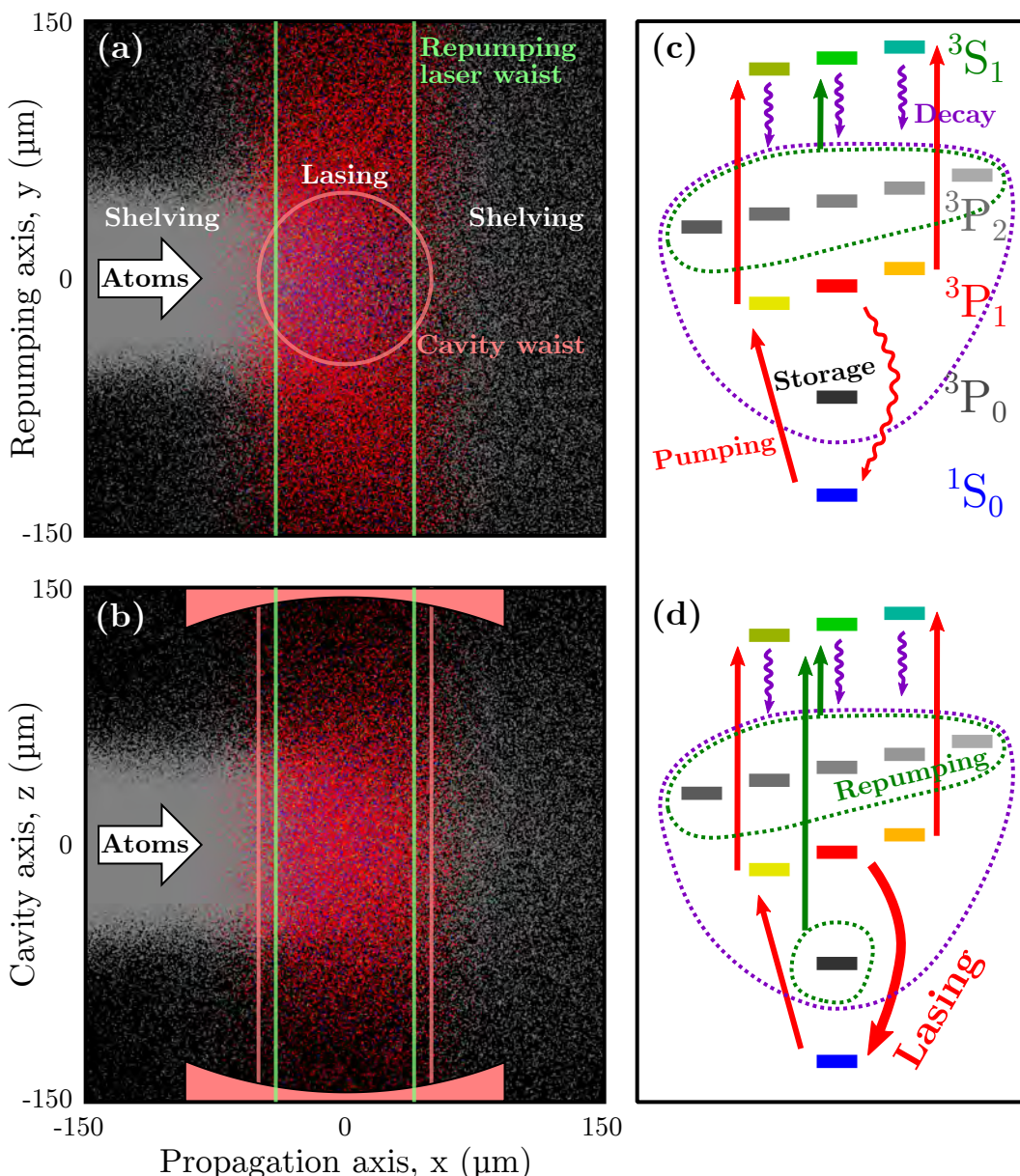


Figure 8.1: Illustration of the cold beam system for an atom flux of  $10^8 \text{ s}^{-1}$ . The spatial distribution of atoms is shown in (a) and (b). The atoms are color-coded by their state according to (c) and (d), without the variations in gray. The shelving scheme is shown in (c), and the repumping scheme within the lasing region is shown in (d). Adapted from [84].

Atom-cavity coupling	$g_0/2\pi$	20.29 kHz
Length	$L$	25 mm
Linewidth (FWHM)	$\kappa/2\pi$	20 MHz
Purcell rate	$(4g_0^2/\kappa)/2\pi$	82.33 Hz
Single-atom cooperativity	$C$	$1.103 \cdot 10^{-2}$
Waist radius	$W$	50 $\mu\text{m}$

Table 8.2: *Assumed parameters of the cavity in the cold beam superradiance simulations. The Purcell rate offers a simple estimate of the potential laser linewidth (see Sec. 2.6.3).*

## 8.1 Numerical model

Equations are derived for the cavity field and atomic states, using the methods in Chapter 2. Here we will drop angle brackets and use the same indices as in Sec. 6.4 to refer to the atomic states which are involved:

$$^1\text{S}_0: g, ^3\text{P}_0: n, ^3\text{P}_1: (i, e, u), ^3\text{S}_1: (x, y, z), ^3\text{P}_2: (p, q, r, s, t).$$

The Hamiltonian for the cold beam system describes the coherent dynamics involving the atom-cavity interaction at rates  $g^j$ , a driving laser at rate  $\eta$ , and filter cavities for calculating the spectrum. In addition to  $|g\rangle$  and  $|e\rangle$ , it also includes the states  $|i\rangle$  and  $|x\rangle$  for which the pumping interactions are treated coherently (with Rabi frequencies  $\chi_{li}^j$  from  $|g\rangle-|i\rangle$  and  $\chi_{lx}^j$  from  $|i\rangle-|x\rangle$ ):

$$\begin{aligned} H = & \hbar\omega_c a^\dagger a + \sum_{j=1}^N \hbar\omega_e^j \sigma_{ee}^j + \hbar\omega_i^j \sigma_{ii}^j + \hbar\omega_x^j \sigma_{xx}^j + \sum_{k=1}^{N_f} \hbar\omega_f^k f_k^\dagger f_k + \hbar\frac{\eta}{2} \left( ae^{-i\omega_d t} + a^\dagger e^{i\omega_d t} \right) \\ & + \sum_{j=1}^N \hbar\frac{\chi_{li}^j}{2} \left( \sigma_{gi}^j + \sigma_{ig}^j \right) \left( e^{ik_{li}r_j - i\omega_{li}t} + cc. \right) + \sum_{j=1}^N \hbar\frac{\chi_{lx}^j}{2} \left( \sigma_{ix}^j + \sigma_{xi}^j \right) \left( e^{ik_{lx}r_j - i\omega_{lx}t} + cc. \right) \\ & + \sum_{j=1}^N \hbar g^j(\mathbf{r}_j) \left( \sigma_{ge}^j + \sigma_{eg}^j \right) \left( a + a^\dagger \right) + \sum_{k=1}^{N_f} \hbar g_f \left( a + a^\dagger \right) \left( f_k + f_k^\dagger \right). \end{aligned} \quad (8.1)$$

Here  $\omega_{li}$  and  $\omega_{lx}$  are the laser frequencies, and we use notation such as  $k_{li}r_j$  for the dot product of the laser wavevector with the atomic position vector. From this Hamiltonian we can start by finding the time evolution of the expectation value of the filter cavity field annihilation operators,  $f_k$ :

$$\dot{f}_k = -i\delta_{fE}^k f_k - iG_a, \quad (8.2)$$

and the dynamics for the cavity field (including dissipation at the rate  $\kappa$ ):

$$\dot{a} = - \left( i\delta_{cE} + \frac{\kappa}{2} \right) a - i\frac{\eta}{2} e^{i\delta_{dE}t} - i \sum_{j=1}^N g^j \sigma_{ge}^j. \quad (8.3)$$

The detunings are relative to the unperturbed atomic lasing transition frequency,  $\omega_E$ , which is chosen as the rotating frame.  $a$  couples to the atomic coherences  $\sigma_{ge}^j$ . These, along with the other atomic coherences and populations, are treated within the stochastic master equation (SME) approach, as described in Sec. 2.2. We will continue to use  $\sigma$ -operator notation for the stochastic values (note  $\langle \rho_{eg}^j \rangle = \langle \sigma_{ge}^j \rangle$ ). Within the SME framework e.g.  $\sigma_{ge}^j$  and  $\sigma_{ee}^j$  do not decay continually, but instead have a probability within a time interval of  $p_j(dt) = \sigma_{ee}^j \gamma_{ge} dt$

to make a quantum jump to  $|g\rangle$ . This would lead to  $\sigma_{gg}^j = 1$  and all other populations and coherences being 0. In the time intervals where this does not occur,  $\sigma_{ge}^j$  evolves according to:

$$\begin{aligned}\dot{\sigma}_{ge}^j &= -i\delta_{eE}^j \sigma_{ge}^j + ig^j a (\sigma_{ee}^j - \sigma_{gg}^j) + i\frac{\chi_{li}^j}{2} \sigma_{ie}^j e^{-ik_{li}r_j + i\delta_{liI}t} \\ &\quad + \sigma_{ge}^j \left[ -\gamma_{eg} \left( \frac{1}{2} - \sigma_{ee}^j \right) + \gamma_{eg} \sigma_{ii}^j + \gamma_{xi} \sigma_{xx}^j \right].\end{aligned}\quad (8.4)$$

The atomic frequency shifts  $\delta_{eE}^j$  are generally 0, as there are no significant shifts in the lasing transition which are not accounted for by the coherent dynamics.  $\delta_{liI} = 0$  is the laser detuning from the Zeeman-shifted atomic transition frequency. The lower term is a renormalization from the SME. These equations for  $\dot{\sigma}_{ge}^j$  are eventually coupled to equations for the other populations and coherences. For the states treated with coherences, we get:

$$\begin{aligned}\dot{\sigma}_{gi}^j &= ig^j \sigma_{ei}^j a + i\frac{\chi_{li}^j}{2} (\sigma_{ii}^j - \sigma_{gg}^j) e^{-ik_{li}r_j + i\delta_{liI}t} - i\frac{\chi_{lx}^j}{2} \sigma_{gx}^j e^{ik_{lx}r_j - i\delta_{lxX}t} \\ &\quad + \sigma_{gi}^j \left[ \gamma_{eg} \sigma_{ee}^j - \gamma_{ig} \left( \frac{1}{2} - \sigma_{ii}^j \right) + \gamma_{xi} \sigma_{xx}^j \right]\end{aligned}\quad (8.5)$$

$$\begin{aligned}\dot{\sigma}_{ix}^j &= i\frac{\chi_{li}^j}{2} \sigma_{gx}^j e^{ik_{li}r_j - i\delta_{liI}t} + i\frac{\chi_{lx}^j}{2} (\sigma_{xx}^j - \sigma_{ii}^j) e^{-ik_{lx}r_j + i\delta_{lxX}t} \\ &\quad + \sigma_{ix}^j \left[ \gamma_{eg} \sigma_{ee}^j - \gamma_{ig} \left( \frac{1}{2} - \sigma_{ii}^j \right) - \gamma_{xi} \left( \frac{1}{2} - \sigma_{xx}^j \right) \right]\end{aligned}\quad (8.6)$$

$$\begin{aligned}\dot{\sigma}_{gx}^j &= ig^j \sigma_{ex}^j a + i\frac{\chi_{li}^j}{2} \sigma_{ix}^j e^{-ik_{li}r_j + i\delta_{liI}t} - i\frac{\chi_{lx}^j}{2} \sigma_{gi}^j e^{-ik_{lx}r_j + i\delta_{lxX}t} \\ &\quad + \sigma_{gx}^j \left[ \gamma_{eg} \sigma_{ee}^j + \gamma_{ig} \sigma_{ii}^j - \gamma_{xi} \left( \frac{1}{2} - \sigma_{xx}^j \right) \right]\end{aligned}\quad (8.7)$$

$$\begin{aligned}\dot{\sigma}_{ei}^j &= i\delta_{eE}^j \sigma_{ei}^j + ig^j \sigma_{gi}^j a^\dagger - i\frac{\chi_{li}^j}{2} \sigma_{eg}^j e^{-ik_{li}r_j + i\delta_{liI}t} - i\frac{\chi_{lx}^j}{2} \sigma_{ex}^j e^{ik_{lx}r_j - i\delta_{lxX}t} \\ &\quad + \sigma_{ei}^j \left[ -\gamma_{eg} \left( \frac{1}{2} - \sigma_{ee}^j \right) - \gamma_{ig} \left( \frac{1}{2} - \sigma_{ii}^j \right) + \gamma_{xi} \sigma_{xx}^j \right]\end{aligned}\quad (8.8)$$

$$\begin{aligned}\dot{\sigma}_{ex}^j &= i\delta_{eE}^j \sigma_{ex}^j + ig^j \sigma_{gx}^j a^\dagger - i\frac{\chi_{lx}^j}{2} \sigma_{ei}^j e^{-ik_{lx}r_j + i\delta_{lxX}t} \\ &\quad + \sigma_{ex}^j \left[ -\gamma_{eg} \left( \frac{1}{2} - \sigma_{ee}^j \right) + \gamma_{ig} \sigma_{ii}^j - \gamma_{xi} \left( \frac{1}{2} - \sigma_{xx}^j \right) \right].\end{aligned}\quad (8.9)$$

For the four related populations we get:

$$\begin{aligned}\dot{\sigma}_{gg}^j &= -ig^j (\sigma_{ge}^j a^\dagger - \sigma_{eg}^j a) - i\frac{\chi_{li}^j}{2} (\sigma_{gi}^j e^{ik_{li}r_j - i\delta_{liI}t} - \sigma_{ig}^j e^{-ik_{li}r_j + i\delta_{liI}t}) \\ &\quad + \sigma_{gg}^j \left[ \gamma_{eg} \sigma_{ee}^j + \gamma_{ig} \sigma_{ii}^j + \gamma_{xi} \sigma_{xx}^j \right]\end{aligned}\quad (8.10)$$

$$\dot{\sigma}_{ee}^j = ig^j (\sigma_{ge}^j a^\dagger - \sigma_{eg}^j a) + \sigma_{ee}^j \left[ -\gamma_{eg} (1 - \sigma_{ee}^j) + \gamma_{ig} \sigma_{ii}^j + \gamma_{xi} \sigma_{xx}^j \right]\quad (8.11)$$

$$\begin{aligned}\dot{\sigma}_{ii}^j &= i\frac{\chi_{li}^j}{2} (\sigma_{gi}^j e^{ik_{li}r_j - i\delta_{liI}t} - \sigma_{ig}^j e^{-ik_{li}r_j + i\delta_{liI}t}) \\ &\quad - i\frac{\chi_{lx}^j}{2} (\sigma_{ix}^j e^{ik_{lx}r_j - i\delta_{lxX}t} - \sigma_{xi}^j e^{-ik_{lx}r_j + i\delta_{lxX}t}) + \sigma_{ii}^j \left[ \gamma_{eg} \sigma_{ee}^j - \gamma_{ig} (1 - \sigma_{ii}^j) + \gamma_{xi} \sigma_{xx}^j \right]\end{aligned}\quad (8.12)$$

$$\begin{aligned}\dot{\sigma}_{xx}^j &= i\frac{\chi_{lx}^j}{2} (\sigma_{ix}^j e^{ik_{lx}r_j - i\delta_{lxX}t} - \sigma_{xi}^j e^{-ik_{lx}r_j + i\delta_{lxX}t}) \\ &\quad + \sigma_{xx}^j \left[ \gamma_{eg} \sigma_{ee}^j + \gamma_{ig} \sigma_{ii}^j + \gamma_{xi} (1 - \sigma_{xx}^j) \right].\end{aligned}\quad (8.13)$$

The decays ( $\gamma$ ) and incoherent pumping rates ( $w$ ) which determine the probability of quantum jumps into and out of these states correspond to rate equations given by:

$$\dot{\sigma}_{gg}^j = \gamma_{eg} (\sigma_{ii}^j + \sigma_{ee}^j + \sigma_{uu}^j) \quad (8.14)$$

$$\dot{\sigma}_{ee}^j = -\gamma_{eg}\sigma_{ee}^j + \frac{\gamma_{xe}}{2} (\sigma_{xx}^j + \sigma_{zz}^j) \quad (8.15)$$

$$\dot{\sigma}_{ii}^j = -\gamma_{ig}\sigma_{ii}^j + \frac{\gamma_{xi}}{2} (\sigma_{xx}^j + \sigma_{yy}^j) \quad (8.16)$$

$$\dot{\sigma}_{xx}^j = w_{nx}^j \sigma_{nn}^j + w_{px}^j \sigma_{pp}^j + w_{rx}^j \sigma_{rr}^j - \gamma_x \sigma_{xx}^j. \quad (8.17)$$

Here  $\gamma_x$  with a single subscript denotes the total decay rate from  $|x\rangle$ . All other states are treated neglecting coherences, using rate equations to determine the probabilities of discrete jumps both from decays and pumping laters. For  $|y\rangle$  and  $|z\rangle$  of  ${}^3P_1$  we get:

$$\dot{\sigma}_{yy}^j = w_{qy}^j \sigma_{qq}^j + w_{sy}^j \sigma_{ss}^j - \gamma_y \sigma_{yy}^j \quad (8.18)$$

$$\dot{\sigma}_{zz}^j = w_{nz}^j \sigma_{nn}^j + w_{uz}^j \sigma_{uu}^j + w_{rz}^j \sigma_{rr}^j + w_{tz}^j \sigma_{tt}^j - \gamma_z \sigma_{zz}^j. \quad (8.19)$$

For the remaining Zeeman levels of  ${}^3P_0$ ,  ${}^3P_2$ ,  $m_J=1$  of  ${}^3P_1$ , we get:

$$\dot{\sigma}_{nn}^j = -w_{nx}^j \sigma_{nn}^j - w_{nz}^j \sigma_{nn}^j + \gamma_{xn} (\sigma_{xx}^j + \sigma_{yy}^j + \sigma_{zz}^j) \quad (8.20)$$

$$\dot{\sigma}_{pp}^j = -w_{px}^j \sigma_{pp}^j + \frac{6}{10} \gamma_{xp} \sigma_{xx}^j \quad (8.21)$$

$$\dot{\sigma}_{qq}^j = -w_{qy}^j \sigma_{qq}^j + \frac{3}{10} \gamma_{xp} (\sigma_{xx}^j + \sigma_{yy}^j) \quad (8.22)$$

$$\dot{\sigma}_{rr}^j = -w_{rx}^j \sigma_{rr}^j - w_{rz}^j \sigma_{rr}^j + \gamma_{xp} \left( \frac{1}{10} \sigma_{xx}^j + \frac{4}{10} \sigma_{yy}^j + \frac{1}{10} \sigma_{zz}^j \right) \quad (8.23)$$

$$\dot{\sigma}_{ss}^j = -w_{sy}^j \sigma_{ss}^j + \frac{3}{10} \gamma_{xp} (\sigma_{yy}^j + \sigma_{zz}^j) \quad (8.24)$$

$$\dot{\sigma}_{tt}^j = -w_{tz}^j \sigma_{tt}^j + \frac{6}{10} \gamma_{xp} \sigma_{zz}^j \quad (8.25)$$

$$\dot{\sigma}_{uu}^j = -w_{uz}^j \sigma_{uu}^j - \gamma_{eg} \sigma_{uu}^j + \frac{\gamma_{xu}}{2} (\sigma_{yy}^j + \sigma_{zz}^j). \quad (8.26)$$

Parameters which we will generally use in the simulations are listed in Table 8.3. It takes a couple of milliseconds to reach steady state in simulations, so results are evaluated from the last millisecond of 5 ms simulations.

Magnetic field strength	$B$	47.6 $\mu\text{T}$
Zeeman splitting of ${}^3P_1$ ( $m_J=0$ to $m_J=1$ )		1 MHz
689 nm pump Rabi frequency	$\chi_{li}/2\pi$	100 kHz
688 nm pump Rabi frequency	$\chi_{lx}/2\pi$	1 MHz
679 nm pump rate (max)	$w_{nx}^0/2\pi$	1.73 MHz
707 nm pump rate (max)*		5 MHz
689 nm pump detuning from ${}^1S_0$ - ${}^3P_1$ $m_J=-1$		0
688, 679 and 707 nm pump detuning from unperturbed transitions		0
688 and 689 nm beam shape		Uniform
679 and 707 nm waist radius along x-axis	$W_p$	40 $\mu\text{m}$

Table 8.3: Pumping and magnetic field parameters chosen for the cold beam simulations of superradiance. \*The 707 pump rates driving the different transitions are further reduced by Clebsch-Gordan coefficients and Zeeman shifts, in addition to the intensity variation.

### 8.1.1 Light shifts

Here we will consider the effect of light shifts - primarily the effects of the dipole guide beam to be included in the model. The dipole guide is a far-detuned light beam and works by shifting the energy levels of the atoms to create an attractive potential energy landscape along the beam. The light shift in a state's energy can be calculated by the formula [152, p. 98]:

$$E_L = -\frac{\text{Re}(\alpha)I}{2\epsilon_0 c}. \quad (8.27)$$

The shift is proportional to the light intensity  $I$  and the polarizability of the atom  $\alpha$ , which for a given state (index  $i$ ) is given by [25] (see also: [152, p. 100], [153], [139, p. 159]):

$$\alpha_i = 6\pi c^3 \epsilon_0 \sum_{k,m_k} \frac{A_{Jki}(2J_k + 1)}{\omega_{Jki}^2(\omega_{Jki}^2 - \omega^2)} \begin{pmatrix} J_i & 1 & J_k \\ m_i & p & -m_k \end{pmatrix}^2 \quad (8.28)$$

The sum is over the states connected to state  $i$  via transitions. We see the contribution from each transition is proportional to the Einstein coefficient  $A_{Jki}$ , so strong transitions tend to give the largest contributions. However the denominator rapidly becomes small for larger detunings, so for certain frequencies, weak transitions can play a significant role. The final coefficient is the Wigner 3j-symbol (see e.g. more details at Eq. 2.44), which takes into account the angular momenta of the initial and final states involved in transitions, and the light polarization  $p$  ( $p = \pm 1$  drives  $\sigma^\pm$  transitions and  $p = 0$  drives  $\pi$ -transitions).

Light shifts should ideally be minimized on the lasing transition, especially if they are not uniform. This can be done by using a magic wavelength, where  $\alpha$  are the same for two states, so that the light shifts cancel out. Using the data in [25] (and [19, 15] for the small corrections from the  ${}^1S_0$ - ${}^3P_1$  transition), we can calculate the polarizability of the  ${}^1S_0$  and  ${}^3P_1$  Zeeman levels over a range of frequencies and for different light polarizations, shown in Fig. 8.2.

Here we see there are two magic wavelengths: one at 913.9 nm, which is magic for the  ${}^1S_0$ - ${}^3P_1$   $m_J=0$  transition, but only for light that drives  $\sigma^+$  or  $\sigma^-$  transitions. This is used for the dipole guide in the model of superradiance. There is also another magic wavelength at 1012 nm for transitions to  ${}^3P_1$   $m_J=1$  with  $\sigma^-$  light (and by symmetry,  $m_J=-1$  with  $\sigma^+$ ). Another factor that makes these magic wavelengths especially useful is that lasers with watts of power are available in this region. Finally, the slopes of  $\alpha(\omega)$  are relatively small such that the sensitivity to laser frequency deviations is relatively low. For these magic wavelengths  $\alpha > 0$  and thus atoms will be attracted to high-intensity regions, e.g. the center of a Gaussian waist, or the antinodes of an optical lattice. At shorter wavelengths additional magic wavelengths exist, including ones where  $\alpha < 0$  that can be used to repel atoms from high-intensity regions. A number of magic wavelengths for the narrow transitions in strontium are listed in e.g. [154, p. 51].

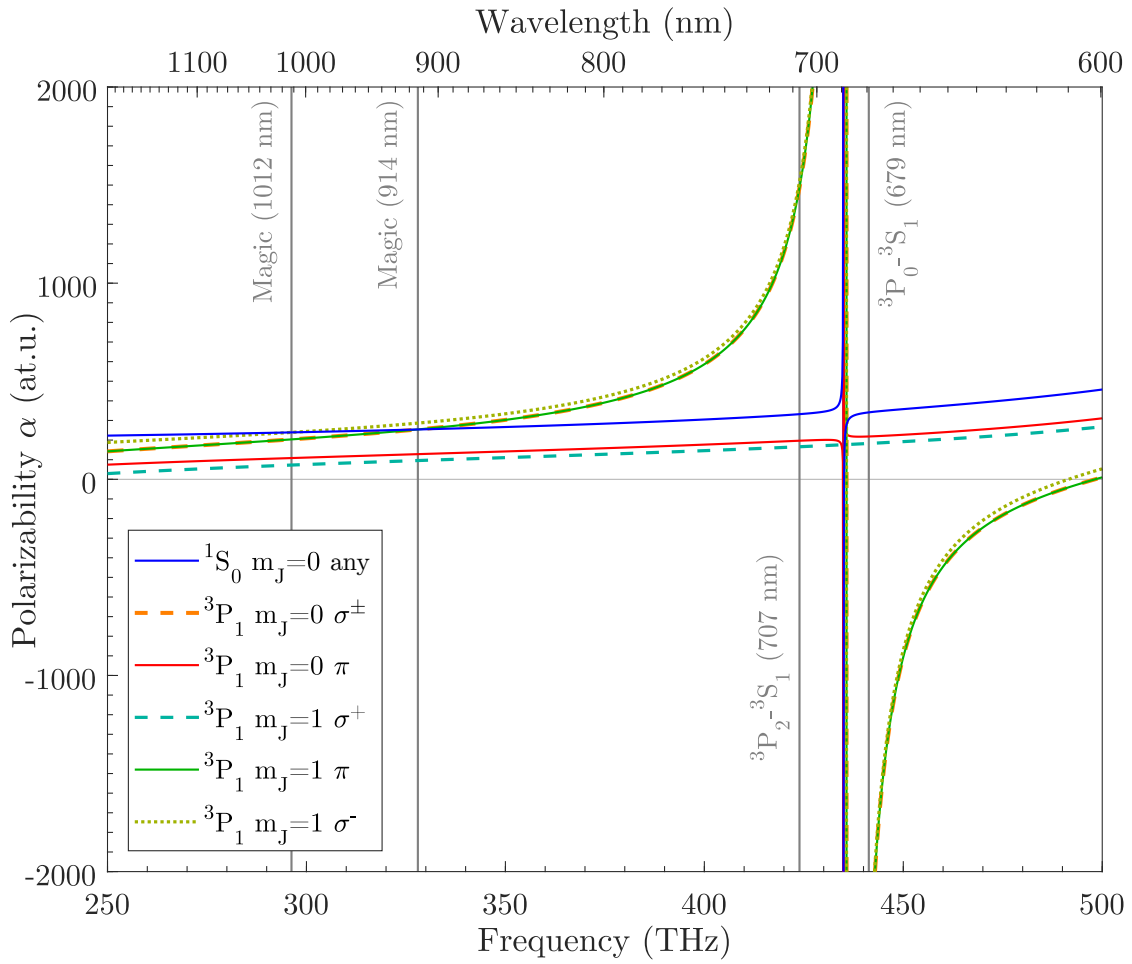


Figure 8.2: The polarizability of the  ${}^1S_0$  and  ${}^3P_1$  sublevels in atomic units ( $4\pi\epsilon_0 a_0^3$ , where  $a_0$  is the Bohr radius) for different light polarizations and zero magnetic field in the red and near-IR region. Some relevant transition and magic wavelengths marked. In some of the curves large features arise from the broad  ${}^3P_1$ - ${}^3S_1$  transition at 688 nm, and smaller features from the  ${}^1S_0$ - ${}^3P_1$  transition at 689 nm.

In addition to the magic wavelengths we also see that the repumper wavelengths of 679 and 707 nm are not magic. Due to the  ${}^3P_1$ - ${}^3S_1$  transition at 688 nm,  $\Delta\alpha < 0$  at 679 nm and  $\Delta\alpha > 0$  at 707 nm for  $\sigma^\pm$  light affecting the  ${}^1S_0$ - ${}^3P_1$   $m_J=0$  transition. This sets a requirement for the intensities of any repumping lasers if the  ${}^1S_0$ - ${}^3P_1$   $\pi$  transition is not to be light shifted. Assuming the repumpers drive  $\sigma^\pm$  transitions equally and are running waves, the intensity ratio must be approximately  $I_{679}/I_{707} = 2.55$  in order for the light shifts to cancel. The third repumper wavelength of 688 nm can also potentially cause a shift in the  ${}^1S_0$ - ${}^3P_1$  transition, but the the  $m_J=0$   $\pi$  transition between  ${}^3P_1$  and  ${}^3S_1$  is forbidden. Therefore large light shifts can be avoided by driving only the  $\pi$  transitions at 688 nm, for which the difference in  $\alpha$  is a factor 137 smaller than for the 679 nm repumper. With these driven transitions, a condition on intensity ratios for the light shifts of all three beams to cancel can be written as:

$$\begin{aligned} \alpha_{679} I_{679} + \alpha_{688} I_{688} + \alpha_{707} I_{707} &= 0 \implies \\ 137 \cdot I_{679} + I_{688} &= 53.7 \cdot I_{707}. \end{aligned} \quad (8.29)$$

Note that even if a magic intensity ratio is not chosen, these light shifts are still only on the order of 0.1 to 1 Hz for the 679 and 707 nm repumpers for realistic repumping intensities, and much less for the 688 nm repumper.

The pumping from level  ${}^1S_0$  to  ${}^3P_1$   $m_J=-1$  can also give rise to light shifts on the lasing transition. To illustrate how this affects different transitions we must account for the Zeeman

shift of the sublevels when calculating the polarizability. When the interaction between the atom and the magnetic field is weak compared to the spin-orbit interaction giving rise to fine structure, it can be treated as a perturbation to the fine structure levels, and the energy shift can be calculated by Eq. 1.1. To illustrate this we can consider a magnetic field strength of 4.76  $\mu\text{T}$ , for which the  $^3\text{P}_1$   $m_J=\pm 1$  levels are split by  $\pm 100$  kHz from  $m_J=0$ . The resulting polarizabilities of the lasing levels, averaging over  $\sigma^+$  and  $\sigma^-$  (corresponding to a laser with linear polarization orthogonal to the quantization axis), are shown in Fig. 8.3.

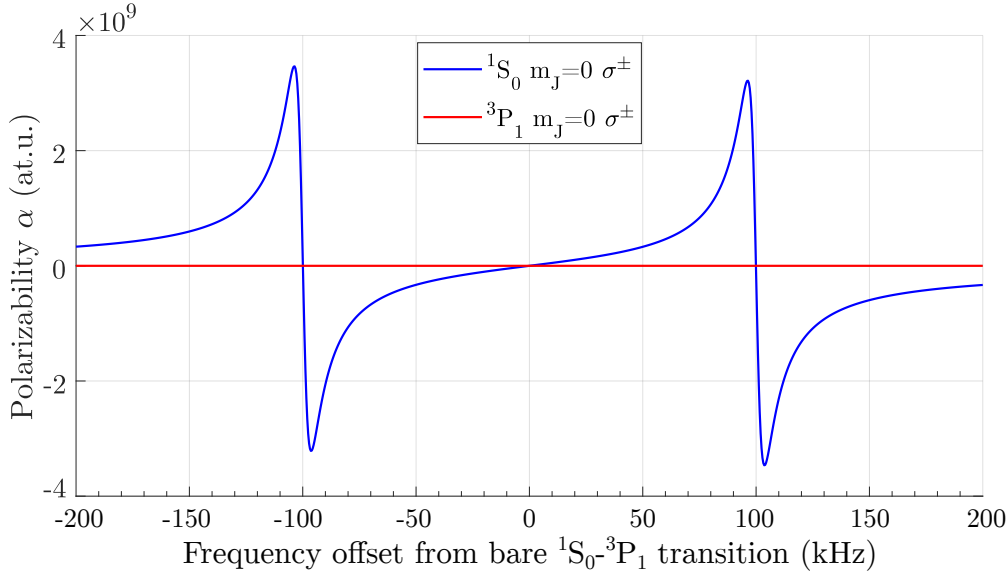


Figure 8.3: The polarizability of the  $^1\text{S}_0$  and  $^3\text{P}_1$   $m_J=0$  states for  $\sigma^\pm$  light and a magnetic field of 4.76  $\mu\text{T}$ , causing a Zeeman splitting of 100 kHz (a factor 10 less than in Table 8.3).

Since  $^1\text{S}_0$  can couple to  $^3\text{P}_1$   $m_J=+1$  and  $-1$  the dispersive feature appears around both of these resonances, which dominates compared to all other contributions, while  $^3\text{P}_1$   $m_J=0$  cannot couple to  $^1\text{S}_0$  via  $\sigma$  transitions. As both the 689 and 688 nm pumping lasers are treated as coherent interactions in the model, this enables us to account for the light shifts as well as other coherent effects.

### 8.1.2 Optical forces

Given the polarizability we can calculate the shift in an atom's energy when subjected to light at a certain wavelength according to Eq. 8.27. And since the force from a potential is given by the gradient of the potential energy, we can find the radial force from a running wave laser beam with a waist radius  $W_g$  and peak intensity  $I_0 = 2P/\pi W_g^2$ :

$$F = -\frac{d}{dr}E_L(r) = \frac{\alpha}{2\epsilon_0 c}\frac{d}{dr}I(r) = -\underbrace{\frac{2\alpha I_0}{\epsilon_0 c W_g}}_{ma_g}\frac{r}{W_g}\exp\left(-\frac{2r^2}{W_g^2}\right). \quad (8.30)$$

In [98] a 12 W dipole guide at 1070 nm was used. This was partially retroreflected, with different focus locations and waists ranging between 92 and 165  $\mu\text{m}$ . We will simply consider a Gaussian 15 W beam at 913.9 nm with waist radius of 165  $\mu\text{m}$ , which gives  $a_g = 46.1 \text{ m/s}^2$  for the  $^1\text{S}_0$  state and  $37.0 \text{ m/s}^2$  for the shelving state  $^3\text{P}_0$ .

In addition to a dipole guide, we will also consider the effect of an intracavity optical lattice at 913.9 nm. For an optical lattice the peak intensity in terms of the lattice power will be  $I_0 = 4P/\pi W_g^2$ . There will be both a radial force and a much stronger force from the

wavelength-scale lattice:

$$\begin{aligned} F = \frac{\alpha}{2\epsilon_0 c} \nabla I(r, z) &= \frac{\alpha I_0}{2\epsilon_0 c} \nabla \sin^2\left(\frac{\omega}{c}z\right) \exp\left(-\frac{2r^2}{W_g^2}\right) \Rightarrow \\ F &= -\frac{2\alpha I_0}{\epsilon_0 c W_g} \sin^2\left(\frac{\omega}{c}z\right) \frac{r}{W_g} \exp\left(-\frac{2r^2}{W_g^2}\right) \hat{r} + \frac{\alpha I_0 \omega}{2\epsilon_0 c^2} \sin\left(\frac{2\omega}{c}z\right) \exp\left(-\frac{2r^2}{W_g^2}\right) \hat{z}. \end{aligned} \quad (8.31)$$

These forces depend on the state of a given atom, as the polarizability varies. The polarizabilities at 913.9 nm are shown in Fig. 8.4. We see that the forces can vary on the order of 50%, depending on exactly which state an atom is in. For the  ${}^3S_1$  levels, the direction of any forces flip sign, so the atoms would become low-field seekers, but the rapid decay ( $\tau = 13$  ns) means this only happens intermittently. In a superradiant laser where repumping drives the atoms between all of these states, these variations of  $\alpha$  can lead to non-adiabatic motion. If an atom were for example brought from the  ${}^3P_J$  states to  ${}^3S_1$  while climbing up a lattice site, the potential hill would suddenly become a trough, the same effect responsible for Sisyphus-cooling. However cooling would require the pumping rate to be correlated both with the location of the atom in the lattice and the direction it is moving, for example with light and Doppler shifts, but would lead to many new requirements and complexities we will not consider here. Without these correlations, the changes in the potential landscape are most likely to cause heating. To give an idea of the order of magnitude of the light shifts with a lattice we can consider a cavity with waist radius of 50  $\mu\text{m}$  and an intra-cavity lattice of 1 W. In that case we would have the light shifts at the intensity maxima of 150 kHz on the  ${}^1S_0$ - ${}^3P_1$   $m_J=-1$  transition and  $\sim 1$  MHz on the  ${}^3P_J$ - ${}^3S_1$  transitions (see Appendix A.7).

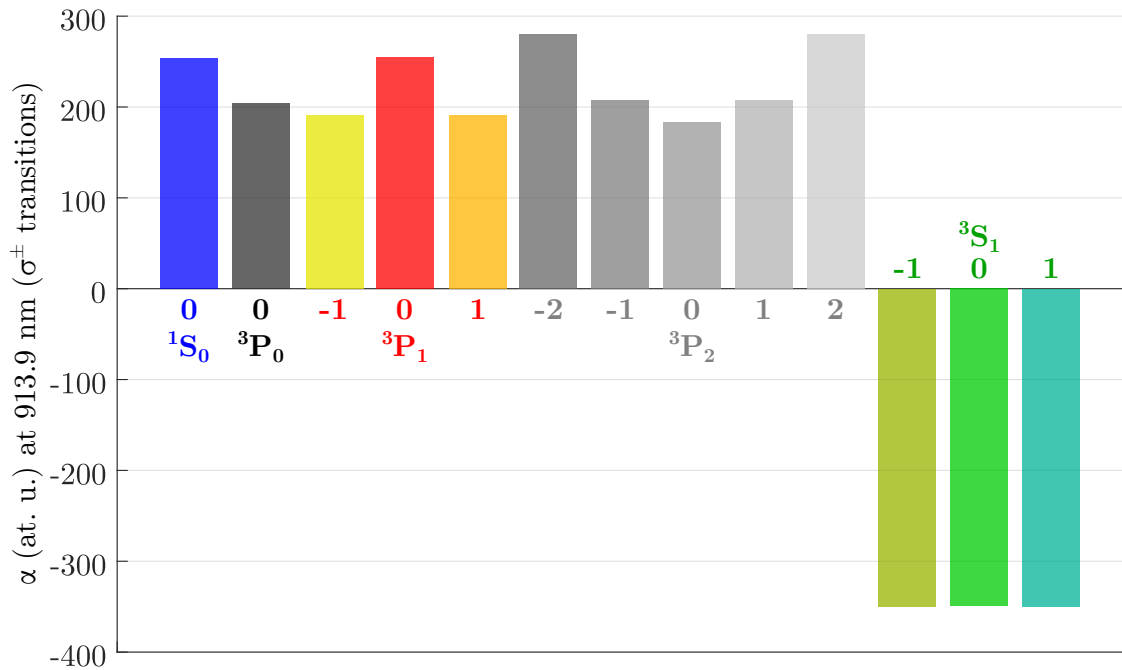


Figure 8.4: Polarizabilities  $\alpha$  of relevant states for a 913.9 nm laser driving  $\sigma^+$  and  $\sigma^-$  transitions equally. The dipole force is proportional to  $\alpha$ , and for  $\alpha > 0$  the atoms are low-field seekers, for  $\alpha < 0$ , high-field seekers.

Due to the recoils associated with repumping, the temperature of the atoms will increase along all dimensions to at the very least tens of  $\mu\text{K}$ , so that  $p \gg \hbar k$ . As a result we will consider the dipole guide forces classically.

## 8.2 Spatial variations in the lasing region

As we saw in the illustration in Fig. 8.1, the atoms do not follow the dipole guide through the cavity, but heat up significantly. In Fig. 8.5 the spatial variations along the  $x$ -axis are presented for the same simulation used for Fig. 8.1.

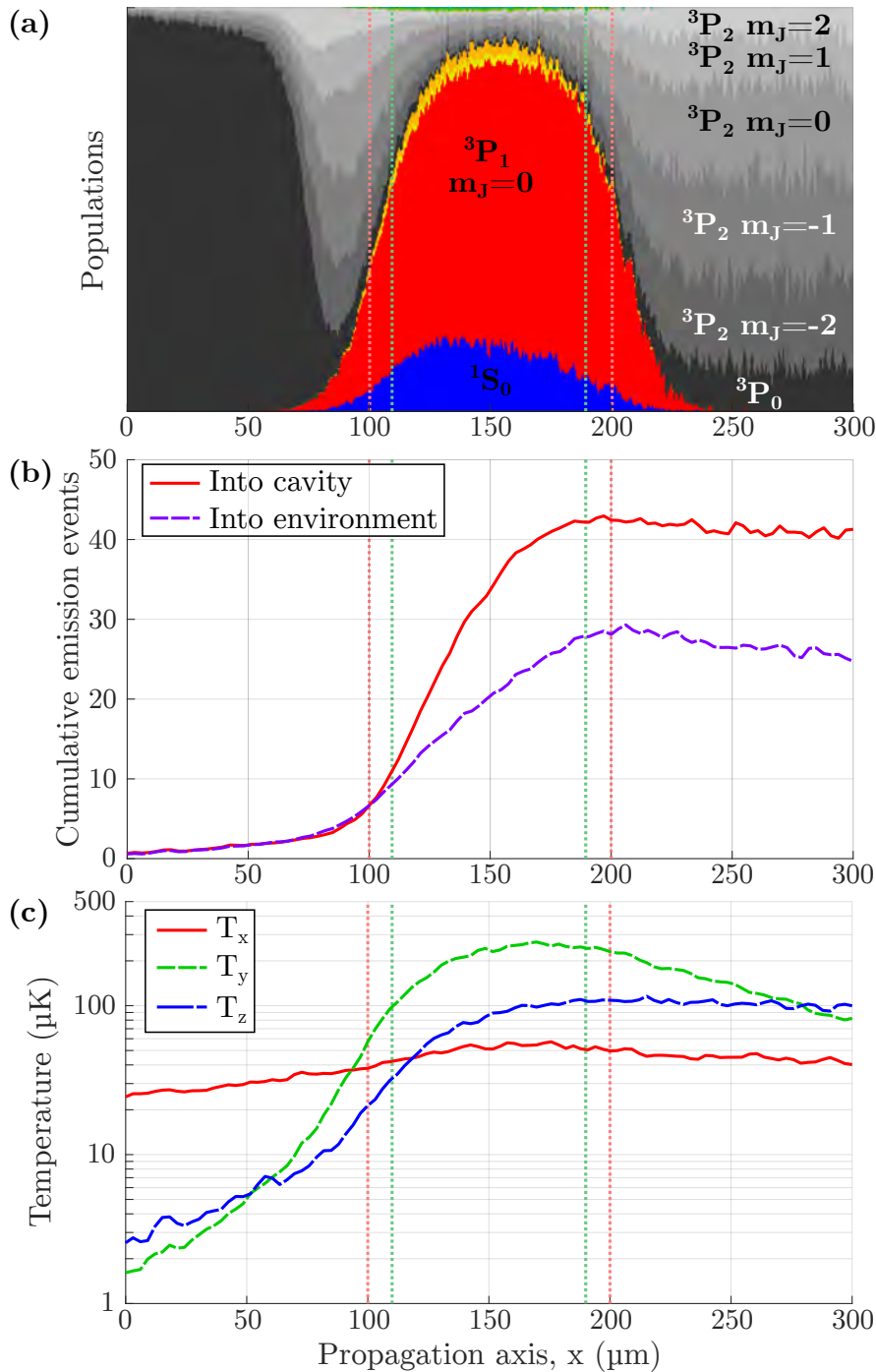


Figure 8.5: *Spatial variations within the atomic beam along the  $x$ -axis, as the atoms propagate through the repumping and lasing region.* (a) Histogram of populations, using the same color scheme as in e.g. Fig. 8.4. The inversion decreases slightly towards the exit side of the cavity region as the density decreases and temperature decreases. (b) Mean cumulative number of emission events from  $^3P_1 m_J=0$ . Atoms can emit on the order of 40 photons into the cavity before escaping. As some atoms diffuse back to  $x = 0$ , the number here is nonzero. (c) Atom temperatures along the three axes. Atoms heat up to  $100 \mu\text{K}$  along the cavity axis, and even more along the repumping axis. Figure adapted from [84].

Because of the Gaussian 679 and 707 nm repumper waists, the population of  ${}^3P_0$  (seen in panel (a)) gradually decreases towards the entry side of the cavity. The cavity coupling is low, so here excited atoms are about as likely to emit into the environment compared to the cavity, as seen in panel (b). But as atoms move within the cavity waist, the rate of emission into the cavity increases greatly. We saw in Fig. 5.3 that for the repumping scheme used here, an atom is subjected to 8 photon recoils from the pumping lasers (giving a recoil randomly along the  $y$  axis) and 7 from spontaneous emission (giving a fully randomly directed recoil). From the numbers in panel (b) where we see atoms emit on the order of  $\sim 65$  photons from the  ${}^3P_1 m_J=0$  state, this implies atoms are subjected to on the order of 1000 photon recoils. This largely explains the large increase in temperatures as atoms move into the cavity and then escape. However part of the increase in temperature also occurs due to the changes in state during repumping within the dipole guide. As we saw in Fig. 8.4, each state has a different polarizability, so the dipole guide potential has a different depth for each state. This changes the acceleration between each quantum jump, so the SME approach enables us to capture this effect. As the atoms end up being redirected from a simple trajectory along  $x$ , the quantities for large  $x$  mainly sample atoms starting with high initial  $x$ -velocities or which experience the most net recoils towards  $+x$ , which explains e.g. the lower  $T_y$  for large  $x$ .

The heating from repumping is sensitive to many different parameters. One is the atom flux - a higher flux increases the heating rate. This occurs because a higher atom flux leads to a larger the emission rate into the cavity will be  $(2g\sqrt{n})$ , which is the bottleneck in the repumping cycle (along with the spontaneous decay route). So when the atom flux increases, the emission rate into the cavity will also increase relative to the environment, and temperatures will increase more rapidly. The over-all motion in the dipole guide changes more from simply following the guide towards diffusing away from the cavity mode. The dipole guide waist and power affect the heating rate by determining how much the potential varies for the different states. A larger repumping waist and rate will obviously also increase the heating rate, assuming it is not so high that decoherence or high temperature causes  $2g\sqrt{n}$  to drop.

### 8.3 Output power, cavity pulling and linewidth

Fig. 8.6 shows the dependency of the cavity output power on atom flux. For the chosen cavity parameters, a lasing threshold is obtained near  $\sim 2 \cdot 10^7$  atoms/s. The power initially increases rapidly with flux - by two orders of magnitude from  $2 \cdot 10^7$  to  $10^8 \text{ s}^{-1}$ , where 1 nW is obtained. However the power does not scale as a simple polynomial, but increases ever more slowly for higher flux. This occurs because near the threshold, higher atom numbers increase the cavity interaction rate  $2g\sqrt{n}$  - the bottleneck in the repumping cycle - so each additional atom causes all atoms to emit more photons into the cavity on average. But as discussed in Sec. 8.2, a high atom flux eventually causes so much heating that atoms start to diffuse away from the cavity, or they may eventually move too quickly along the cavity axis to emit efficiently. Therefore the scaling at high flux could be expected to approach a polynomial  $P \propto N^a$ , with  $a$  probably a bit larger than 1.

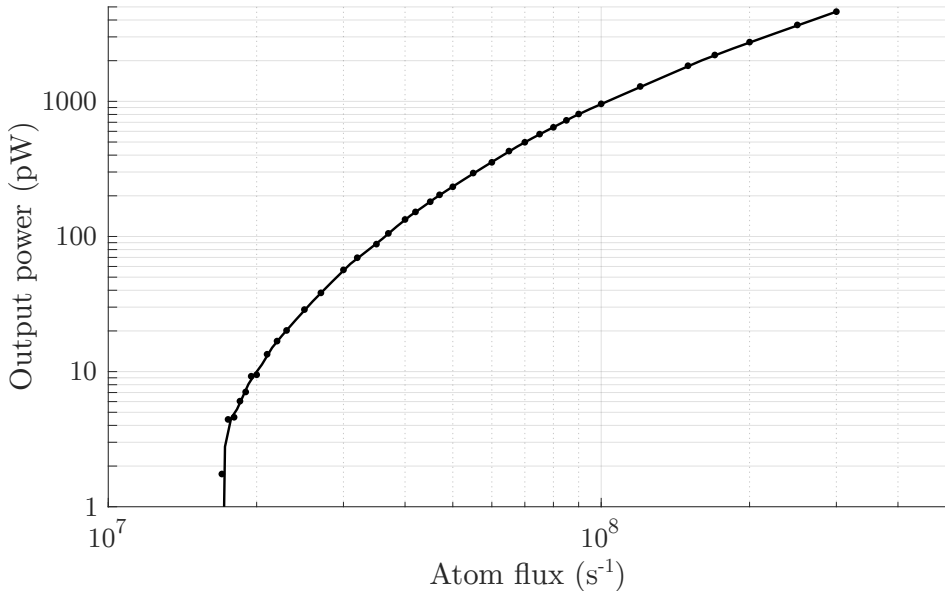


Figure 8.6: Total cavity output power for varying atom flux in the cold beam system. Lasing threshold is reached near  $2 \cdot 10^7$  atoms/s, and for  $10^8$  atoms/s, 1 nW can be achieved. Figure adapted from [84].

#### Cavity pulling

In Fig. 8.7 the lasing frequency shift  $\delta_L$  is shown within the same interval of atom fluxes, for three different cavity detunings  $\delta_{cE}$ . We will initially consider the standard parameters (dark curves). The coherent treatment of the 689 and 688 nm pumping interactions enable us to capture the impact of light shifts on the lasing frequency, which is the reason why the  $\delta_{cE} = 0$  curve does not follow  $\delta_L = 0$ . In this case we can determine the local cavity pulling coefficient from the distance between the curves. Near the threshold,  $c_{\text{pull}} \sim 0.01$ , and for  $2 \cdot 10^8$  atoms/s the atoms heat up to a mean  $T_z = 34 \mu\text{K}$  within the cavity waist. As the atom flux increases, the average temperature  $T_z$  along the cavity axis also increases, causing cavity pulling to increase until  $5 \cdot 10^7$  atoms/s, where  $T_z = 54 \mu\text{K}$ . At still higher flux, cavity pulling starts to decrease again, as the effect of higher atom numbers dominates (as is usually seen when superradiant lasers are considered) compared to heating. At  $3 \cdot 10^8 \text{ s}^{-1}$  we find  $T_z = 76 \mu\text{K}$ , but since the Doppler width scales with  $\sqrt{T}$ , the width does not increase so significantly with flux anymore.

As seen in the shape of the curve for  $\delta_{cE} = 0$ , the impact of light shifts appears to be non-trivial. It is sensitive to the inversion, which generally decreases for an increasing atom flux, but the effects considered in Sec. 8.2 makes the scaling with atom flux complicated. A

positive result is that there is a regime near  $8 \cdot 10^7 \text{ s}^{-1}$  where the net shift in lasing frequency is 0 for  $\delta_{cE} = 0$  simultaneously with it being independent of atom flux to first order. The bright curves in Fig. 8.7 show the behavior for a smaller pumping waist and lower 688 nm pumping rate for comparison. In this case the curves are more monotonic, with no plateau near  $8 \cdot 10^7$  atoms/s. This is because the smaller repumping waist causes less heating, so the effects from Sec. 8.2 give less prominent variations with the atom flux. From this we see that despite the complexity, they can also give rise to advantages like a regime where the lasing frequency has no net shift and is not sensitive to small variations in atom flux.

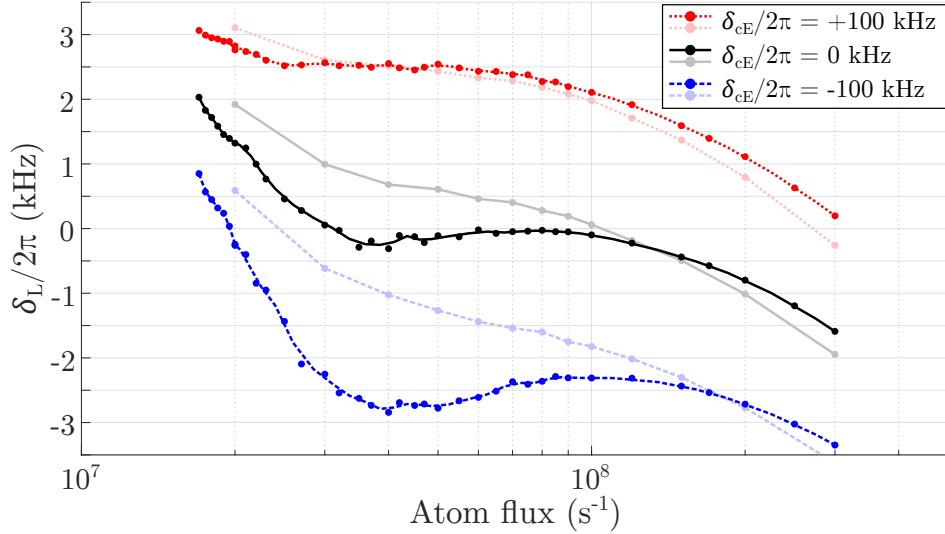


Figure 8.7: The shift in lasing frequency  $\delta_L$  for different atom flux at three different cavity detunings,  $\delta_{cE}$ . Standard parameters (Table 8.3) are shown in dark colors, while light variants are simulations with  $W_p = 30 \mu\text{m}$  and  $\chi_{lx}/2\pi = 0.8 \text{ MHz}$ . Cavity pulling can locally be characterized by the distance between the curves. Light shifts cause additional shifts in the curves. For a flux near  $8 \cdot 10^7 \text{ s}^{-1}$  there is no net shift in the lasing frequency at zero detuning, and here  $\delta_L$  is also insensitive to the atom flux to first order. Adapted from [84].

### Linewidth

Above threshold the simulations tend to predict linewidths that are simply Fourier-limited, which has been verified down to 25 Hz. As discussed in Sec. 2.6.3, the simulations may underestimate the linewidth. Some alternative estimates are shown in Fig. 8.8, based on the analytical equations from Sec. 2.6.3. The simple estimate based on the Purcell rate is indicated by the purple line. Other estimates are based on evaluating the parameters from simulations for the two different pumping waist sizes,  $W_p$ . Since the system operates within the superradiant crossover regime and is based on continuous repumping, Eq. 2.51 is shown (Tieri). These estimates are evaluated with  $T_2 = 1/\Gamma_D$  based on the average temperature along the cavity axis of atoms inside the waist, and also for  $T_2 = 0$  for comparison. This suggests a significant broadening due to heating. Finally, the generalized

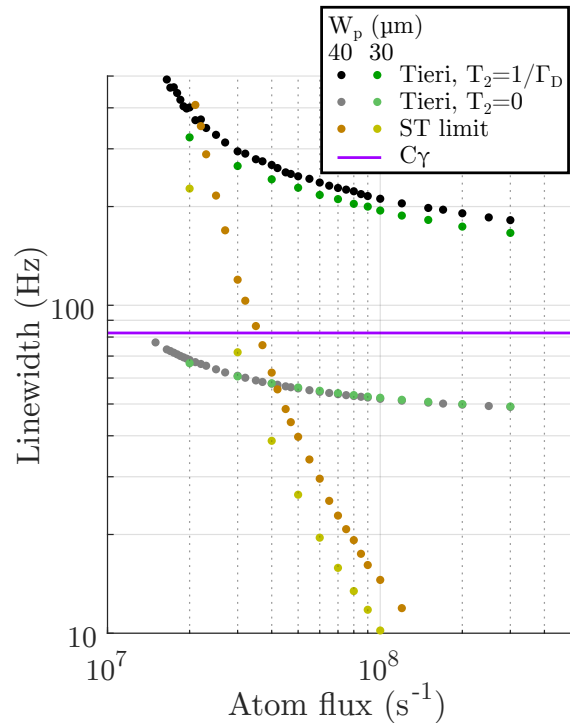


Figure 8.8: Laser linewidth estimates and limits of the cold beam system according to analytical equations, depending on flux and  $W_p$ .

Schawlow-Townes limit (Eq. 2.52) is shown, which may limit the linewidth near the lasing threshold.

These estimates of the linewidth are inferior compared to the hot beam system, and may not justify building a machine with such a complexity, though we here have only investigated a small fraction of a large parameter space. The linewidth may be improved with different cavity parameters at the cost of a higher lasing threshold, with different pumping parameters, and thermal effects may be reduced by an optical lattice.

## 8.4 Sensitivity to repumping laser variations

Even if the superradiant laser is not very sensitive to the cavity resonance frequency, it is not of much use if the repumping lasers disturb the frequency significantly, as they might then need to have their frequencies stabilized to the same level that is desired for the superradiant laser. As we saw in Sec. 8.1.1 our main concern is the ladder from  $|g\rangle - |i\rangle$  and  $|i\rangle - |x\rangle$  driven by the 689 and 688 nm lasers. In addition to nominal light shifts that depend on the power and frequency of the repumping lasers, these repumping parameters can also affect the total repumping rate and inversion. This would also have a range of effects on the dynamics and lasing frequency, considering the dynamics in Sec. 8.2. However this should not be significant for frequency shifts that are small compared to the power-broadened linewidths of the transitions. The standard parameters (Table 8.3) used in simulations assume the 689 nm pump laser is on resonance with the Zeeman-shifted  $m_J=-1$  level of  ${}^3P_1$ , while the 688 nm laser is still tuned to the unperturbed resonance of  ${}^3P_1-{}^3S_1$ , giving a nominal detuning of  $\delta_{lx}^0/2\pi = -333$  kHz from  $|i\rangle$  to  $|x\rangle$  (the same magnitude as for the  $|y\rangle-|z\rangle$  transition, which is treated incoherently as  $|g\rangle - |i\rangle$  is not driven). These are of course just one combination out of endless options that may lead to different sensitivities to the repumper laser frequencies, but one working combination is all that is needed.

### 8.4.1 Repumper frequencies

In Table 8.4 the shifts in lasing frequency are shown for an atom flux of  $8 \cdot 10^7$  s $^{-1}$ , zero cavity detuning, and with the repumping frequencies varied from the nominal values. The finite simulation time leads to random variations in the peak lasing frequency from the random atom variations during each realization, which are on the order of tens of Hz (these are also visible in some of the close neighboring points in Fig. 8.7). The crucial result is that the shifts in lasing frequency are several orders of magnitude smaller than the shifts in repumping laser frequencies. This allows the superradiant laser to have a significantly more stable frequency than the repumping lasers.

$\Delta\delta_{li}/2\pi$	$\delta_L/2\pi$	$\Delta\delta_{lx}/2\pi$	$\delta_L/2\pi$
-100 kHz	-570 Hz	-100 kHz	-40 Hz
-10 kHz	-97 Hz	-10 kHz	-65 Hz
-1 kHz	-66 Hz	-1 kHz	-65 Hz
0 Hz	-27 Hz	0 Hz	-26 Hz
1 kHz	-25 Hz	1 kHz	-37 Hz
10 kHz	+66 Hz	10 kHz	-2 Hz
100 kHz	+476 Hz	100 kHz	-55 Hz

Table 8.4: *Shifts in the peak lasing frequency  $\delta_L$  when either the 689 nm pump laser is detuned from its nominal value (left columns,  $\Delta\delta_{li}$ ), or the 688 nm pump laser (right columns,  $\Delta\delta_{lx}$ ). Note random variations within the finite evaluation time are also on the order of tens of Hz.*

### 8.4.2 Repumper intensities

Fig. 8.9 shows how lasing parameters depend on the Rabi frequencies from the 689 and 688 nm repumping lasers, for an atom flux of  $10^8 \text{ s}^{-1}$ . The lasing frequency is sensitive to the power of the repumpers, so they must be power-stabilized to achieve a good frequency stability.

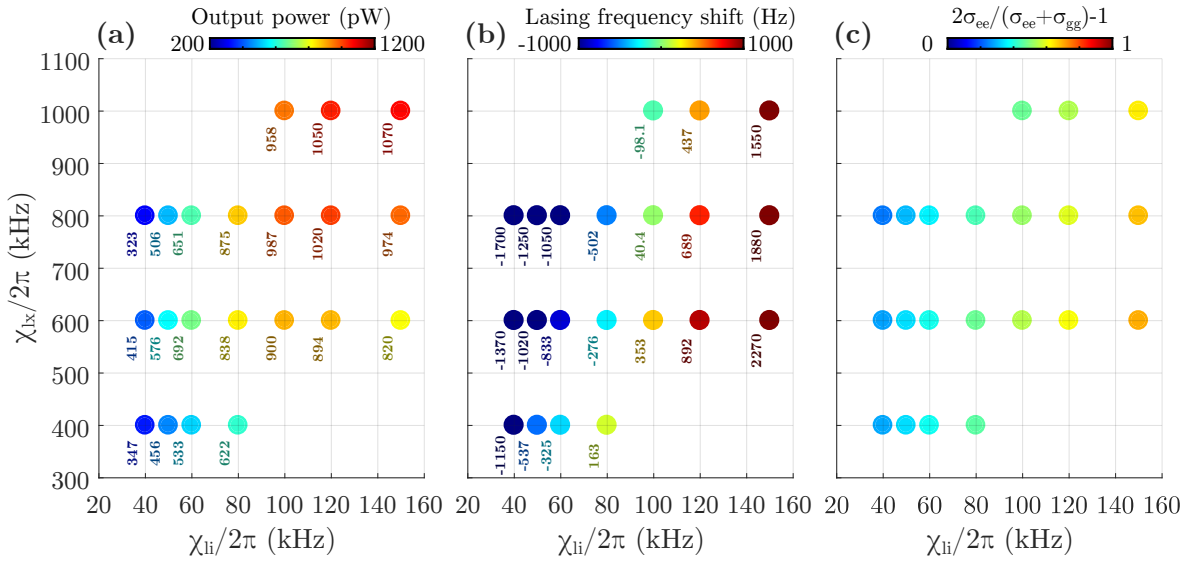


Figure 8.9: Lasing parameters in simulations with an atom flux of  $10^8 \text{ s}^{-1}$  and zero cavity detuning. (a) Cavity output power, (b) peak lasing frequency shift, (c) inversion on the lasing transition. Some values are listed next to the data points.

## 8.5 Optical lattice

Here we will consider the effect of an intracavity optical lattice at the magic wavelength. Such a lattice will result in large intensity variations on the wavelength scale within the cavity, unlike for the guided beam (with an 165  $\mu\text{m}$  waist). As considered in Appendix A.7, this could be problematic for the repumping scheme if the lattice power is on the order of watts. If the repumper frequencies are not modulated, the repumping rates will be spatially dependent. The modulation does not necessarily need to cover the full span in light shifts, as low repumping rates may be acceptable near the crests of the optical potential, from which atoms are repelled. Here we will not account for these variations in light shifts on the repumping transitions but simply consider the prospects if these challenges are overcome. The system in the presence of an optical lattice is depicted in Fig. 8.10, and the impact on different lasing parameters is shown in Fig. 8.11.

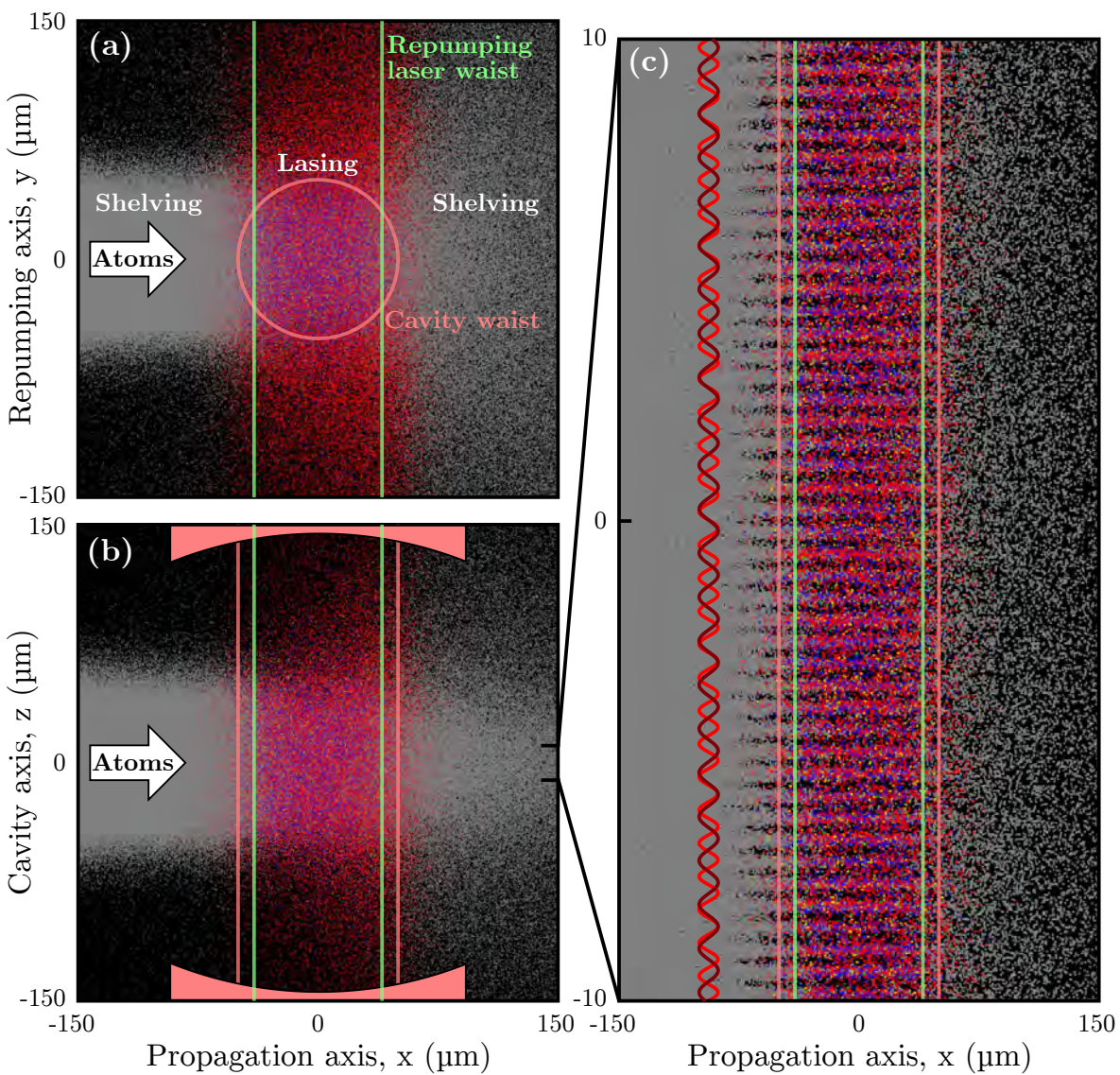


Figure 8.10: Illustration of the cold beam system, as in Fig. 8.1, here for an atom flux of  $3 \cdot 10^8 \text{ s}^{-1}$  and with an 10 W intra-cavity optical lattice. (a) Distribution and states of atoms in the  $xy$ -plane, (b)  $xz$ -plane and (c)  $xz$ -plane zoomed in along the  $z$  axis, showing the effect of the lattice on the motion of atoms. The variation in  $g$  (red sine) and lattice  $E$ -field (dark red sine) on the wavelength scale is illustrated.

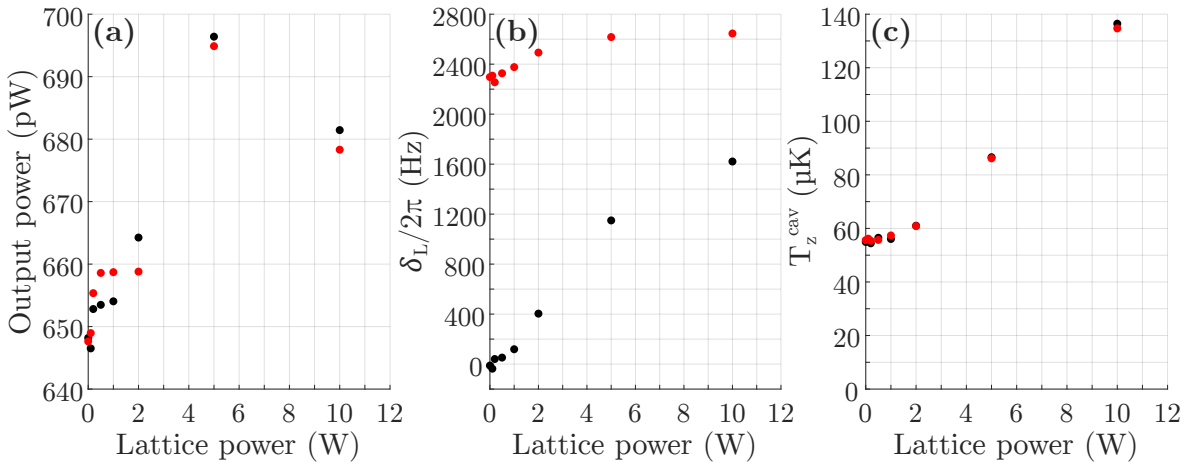


Figure 8.11: *Lasing parameters from simulations with an atom flux of  $8 \cdot 10^7 \text{ s}^{-1}$  and cavity detunings of 0 (black) or 100 kHz (red).* (a) Total cavity output power, (b) shift in lasing peak frequency and (c) mean temperature along the cavity axis for atoms within the cavity waist.

Both the radial and axial forces of the lattice (Eqs. in Sec. 8.1.2) influence the atoms. The radial force accelerates the atoms from the guided beam towards the center of the cavity waist. This has the advantage of increasing the atom density in the region with high cavity coupling rates, but also generally increases the propagation speed through the cavity. If this becomes too high, the density again decreases, and atoms will not have enough time to emit as many photons as for a lower lattice power. As a result the output power increases until about 5 W for the parameters in Fig. 8.11, and decreases again for a higher lattice power.

The radial force of the lattice similarly accelerates the atoms towards the center of the lattice antinodes, but this force also gradually increases as atoms get closer to the center of the cavity waist (see Fig. 8.10(c)). This causes the atomic motion to oscillate along the cavity axis. It causes the temperature  $T_z^{cav}$  to increase, but the effects considered in Sec. 8.2 also play a role in this. One is the lattice's impact on the number of repumping cycles, which scales roughly with the output power. In addition the larger changes in polarizability encountered within the lattice can lead to faster heating during repumping, compared to the variations within the dipole guide. Despite the increase in  $T_z^{cav}$ , we find in Fig. 8.11(b) that the cavity pulling coefficient gradually decreases from 0.024 to 0.01 for 10 W. Part of the reduction can be attributed to the fact that despite the increase in temperature, the movement is still confined to less than half the magic wavelength. Therefore the atoms do not experience the variations in  $g$  which lead to increased cavity pulling for ballistic motion at higher temperatures. Note the atoms in Fig. 8.10(c) which are in-between the lattice sites may have moved outside the cavity waist along the  $y$ -axis - as seen in Fig. 8.10(a), those are more likely to be in  ${}^3\text{P}_1$   $m_J=1$ .

Finally, we see that the net shift in lasing frequency at  $\delta_{cE} = 0$  also depends on the lattice power. This can be expected, as the lattice affects the dynamics in so many different ways which in the end changes the inversion and light shift. The attractive potential towards the cavity axis can also lead to even more complex motion, for example causing some atoms to orbit the cavity axis if they experience the right sequence of random recoils, or enter the cavity from the right distance along the  $y$ -axis.



## Conclusion and outlook

### Numerical models

In this thesis we have explored superradiant lasing in a variety of different settings, all with the common feature of using the kHz-wide  $^1\text{S}_0$ - $^3\text{P}_1$  transition in  $^{88}\text{Sr}$ . A significant part of the thesis is devoted to numerical simulations of these systems. The models treat atoms in small groups or fully individually, coupled to the common cavity mode. This allows us to account for variations of many conditions within the ensemble, such as cavity-coupling, pumping intensities, energy shifts and optical forces. As the atoms move around with different velocities, this approach also captures the effects of a finite temperature. We have used a few approaches to account for heating effects as well, in the settings where this is relevant.

The main parameters which we can predict are the power, phase and spectrum of the light emitted by the superradiant lasers, and as a result also how they are affected by variations in the cavity resonance frequency. One of the main drawbacks of the numerical approach presented here is the complexity of the dynamics and calculations. Exploring large parameter spaces can require weeks of calculations, at least on a single GPU. And with many different parameters which can have similar impacts, the scope is limited to examples, making it hard to extrapolate general relations. The advantage is that by accounting for the different effects, we can expect a better agreement than simplified models. As a result we have also seen good agreement between simulations and experiments of superradiant pulses. In the future it will be interesting to see how well the simulations describe the continuous regimes which are currently pursued experimentally.

Another important limitation of the model is that it does not include quantum noise in the treatment of the cavity mode. This limits the ability to predict the linewidth of superradiant lasers in the continuous regimes. It could be interesting to include this in the model, but for the performance it is at the same time critical that the linear scaling of the number of equations with atoms is preserved. Alternatively, the atom group approximation could be used to a much greater extent. As we saw this can distort phase and power fluctuations, it may also distort the predicted linewidth, however.

## Superradiant laser pulses and setups at UCPH

At the University of Copenhagen (UCPH), lasing pulses from a coherently pumped ensemble have been characterized in detail in the mK regime. The experiments and numerical model have complemented each other, with the numerical simulations showing good agreement and offering insight into dynamics that are not readily accessible in experiments, such as the varying behavior of atoms with different velocities. We have seen that in the superradiant crossover regime with coherent pumping, even despite a Doppler width  $\sim 4$  times greater than the cavity linewidth, cavity pulling can be suppressed by up to a factor 4 when considering the center of mass of the spectrum. In addition we saw that the frequency of the most prominent peak can even be immune to local changes in cavity detuning, when operating within certain ranges.

Experimental approaches and upgrades were presented which enabled us to trap ensembles with tens of millions of atoms at  $\mu\text{K}$  temperatures. This allowed us to realize superradiant crossover pulses where the Doppler width is now  $\sim 10$  times narrower than the cavity linewidth, and atoms with different velocities synchronize to a much greater extent. As a result, cavity pulling is also strongly reduced, now by a factor 56 when considering the center of mass of the spectrum. The  $\mu\text{s}$  pulse duration and associated broad linewidth makes this system based on coherent pumping of limited metrological interest in itself. But as a proof of principle system, it can give insight into the physics that may play a role in frequency references in the future. For example experiments are now underway to demonstrate a proposal for utilizing superradiant pulses in a Ramsey scheme [140].

A new regime that allows for much narrower linewidths is realized by incoherently repumping the atoms. Here we have presented simulations of such lasing pulses at both  $\mu\text{K}$  and mK temperatures, and investigated thermal effects of the repumping scheme. The pulse duration can be extended to the order of several ms, but changes in density and temperature lead to changes in cavity pulling during the pulse emission. We have seen how this can broaden many spectral features, but also a few examples where features can remain steady even despite large changes in the atom cloud parameters. Reaching linewidths at the Fourier limit of a few hundred Hz may be possible in a regime near zero cavity detuning and/or by controlling the cloud from an initial offset to keep the cavity pulling coefficient more steady. These quasi-continuous pulses are already being investigated in the lab at the time of writing, so we can look forward to more details from them in the future.

Still, fully continuous superradiant lasing is of much greater metrological interest, as even narrower linewidths can be obtained and dead-time can be eliminated. We have considered the temperature and atom number requirements for realizing continuous superradiance in the UCPH machine, finding that on the order of  $10^9$  atoms/s are required according to simulations. Experimentally this would be much more challenging than the quasi-continuous setting we have considered so far. One possibility is that the atoms are slowed, trapped and cooled with an offset from the cavity, before being directed through it. A second possibility is that superradiant lasing co-exists with the disturbances from MOT lasers within the cavity mode. In [155] lasing was considered in a driven V-level configuration, such as lasing in with a blue MOT cloud. Though coherent effects were shown to enable inversion on the lasing transition, the light from the broad transition also caused the system to behave as a good-cavity laser. A third possibility might be a cooling and trapping region next to, or surrounding the cavity mode, from which atoms can migrate into the lasing region. One advantage of such an approach is that a lower atom flux could be needed compared to the atomic beam systems we have considered, if the atoms tend to get recycled. Operating a MOT within the cavity, using transitions encountered during repumping, could allow for even further cooling and confinement with fewer disturbances of lasing compared to the  ${}^1\text{S}_0 - {}^1\text{P}_1$  transition, if they can be fed from an initial trapping stage.

Outside the realm of superradiant lasing, other directions can also be pursued in the upgraded machine at UCPH. One possibility is passive interrogation of atoms, in line with previous research [156, 157]. This may now be pursued in colder or more continuous settings, and has simpler requirements compared to overcoming the lasing threshold. The numerical models presented in the thesis can also readily be used to describe these settings, requiring only minor adaptations.

Continuous spectroscopy and potentially superradiance is also pursued in the "Sr2" machine at UCPH (also described in [121]). This has an architecture that produces a Zeeman-slowed continuous atomic beam, which is deflected towards an optical cavity. Simulations to determine the requirements for continuous lasing in this machine are presented in Appendix A.8, assuming a pre-pumped setting similar to the hot beam system. But since the propagation velocities in the atomic beam can be adjusted on the order of tens of m/s, lasing may also be considered in a continuously repumped setting similar to the model in Chapter 8, which could be an advantage for low velocities.

### Continuous superradiance based on machines at UvA and elsewhere

The purpose-built hot beam machine at the University of Amsterdam (UvA) is a promising platform for realizing continuous superradiance much further in the bad-cavity regime than the machines at UCPH. In this thesis we have described some key components of this machine from the assembly phase, including the science cavity, transverse cooling and cavity-coupling optics. We have also presented numerical simulations of the pumping stages in the machine to find the impact of different laser parameters on pumping and a velocity selection stage. The simulations suggest the velocity selection scheme can be used to reduce the temperature of atoms along the cavity axis from 3.6 mK down to e.g.  $\sim$ 2 mK by sacrificing 30% of the atoms.

Superradiant lasing in this system has also been investigated using numerical simulations, where we find a lasing threshold for  $\sim 2.5 \cdot 10^{12}$  atoms/s. The expected output power is tens to hundreds of nW, which is a great advantage compared to other proposals for continuous superradiance which require more complex machinery. The cavity pulling coefficient found in simulations is on the order of 0.03 to 0.06, with the lower range depending on realizing the velocity selection scheme, which may give an improvement on the order of  $\sim$ 25%. The high propagation velocities of atoms in the beam give rise to an asymmetric distribution of relativistic Doppler shifts with a peak on the order of hundreds of Hz, which are included in the numerical model. These cause a shift in the lasing frequency of the same order, and additionally have an impact on the frequency fluctuations arising from the random fluctuations in the atom distribution. The simulations have also been used to determine how the emitted power and spectrum is affected by the finite temperature, increased decoherence, and cavity resonance fluctuations at different frequencies and amplitudes. A simple estimate for the linewidth suggests this system can reach 9.4 Hz.

Finally, we have presented a numerical model and simulations of continuous superradiance in a regime with  $\mu\text{K}$  atoms, based on an atom source realized at UvA. In this system we assume atoms are continually repumped when they are near the center of the cavity waist, such that each atom can emit tens of photons into the cavity. This allows for an output power on the order of hundreds of pW. All states involved in the repumping scheme are included in the model, with the 689 and 688 nm repumping interactions modeled coherently. A stochastic master equation (SME) is used to model atomic decays as discrete quantum jumps. Forces from an optical dipole guide at a magic wavelength are also included in the model. These forces depend on the state of atoms, and the SME approach enables us to quantify how this affects the temperature of the atoms. The temperature is also affected directly by recoils from the pumping lasers and spontaneous emission. As a result it quickly grows to several tens of  $\mu\text{K}$  along the cavity axis, from the  $\sim 1 \mu\text{K}$  temperature in the atomic beam.

Cavity pulling coefficients in the system are on the order of 0.01-0.02. While light shifts from pumping can cause net shifts in the lasing frequency, we find certain parameter regimes where the net shift can simultaneously be zero and independent of the atom flux to first order. An intra-cavity optical lattice may reduce cavity pulling even further, provided the challenges of light shifts on pumping transitions can be overcome. On the other hand, the linewidth of 82 Hz based on a simple estimate, is inferior compared to the hot beam system, and may not justify the experimental complexity required to build such a system.

Other machines are also under development which are promising candidates for realizing continuous superradiance. At UvA, a second machine is under development for realizing continuous superradiance on the mHz-transition [99], and at JILA, continuous superradiance is also being pursued in strontium [129, p. 201].

# Appendices

## A.1 Tapered Amplifier power

The recorded power over time of the original TA (EYP-TPA-0690-00500-2003-CMT02-0000, setup described in [103, p. 56-57]) and the pump pulse power (total in the -1 order out of the Pump AOM) is shown in Fig. A.1. The power varies with optimization from day to day, but a degrading trend over the course of months is also visible.

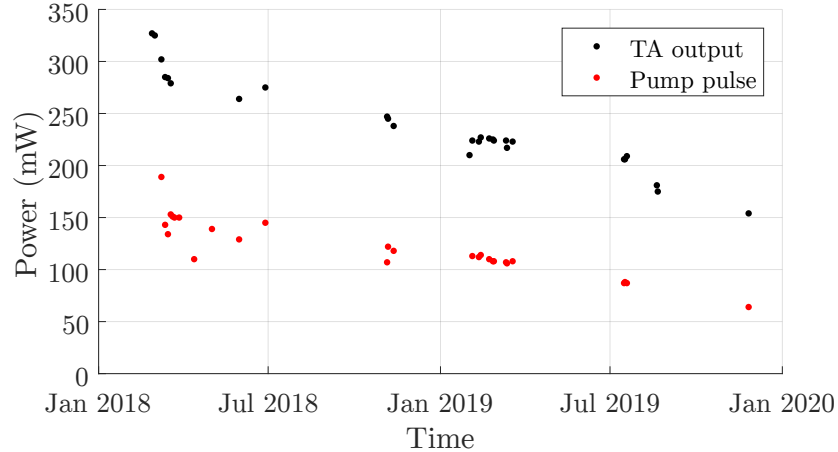


Figure A.1: *Degradation of the TA output power over time, with approximately 20 mW input power.*

## A.2 Beam profile for pumping mK atom cloud

In Fig. A.2 the beam profile of the pump pulse is shown which was used in experiments with the mK atom cloud. Gaussian fits are shown for an approximate quantitative description. The beam profile deviates heavily from a Gaussian after amplification by a tapered amplifier.

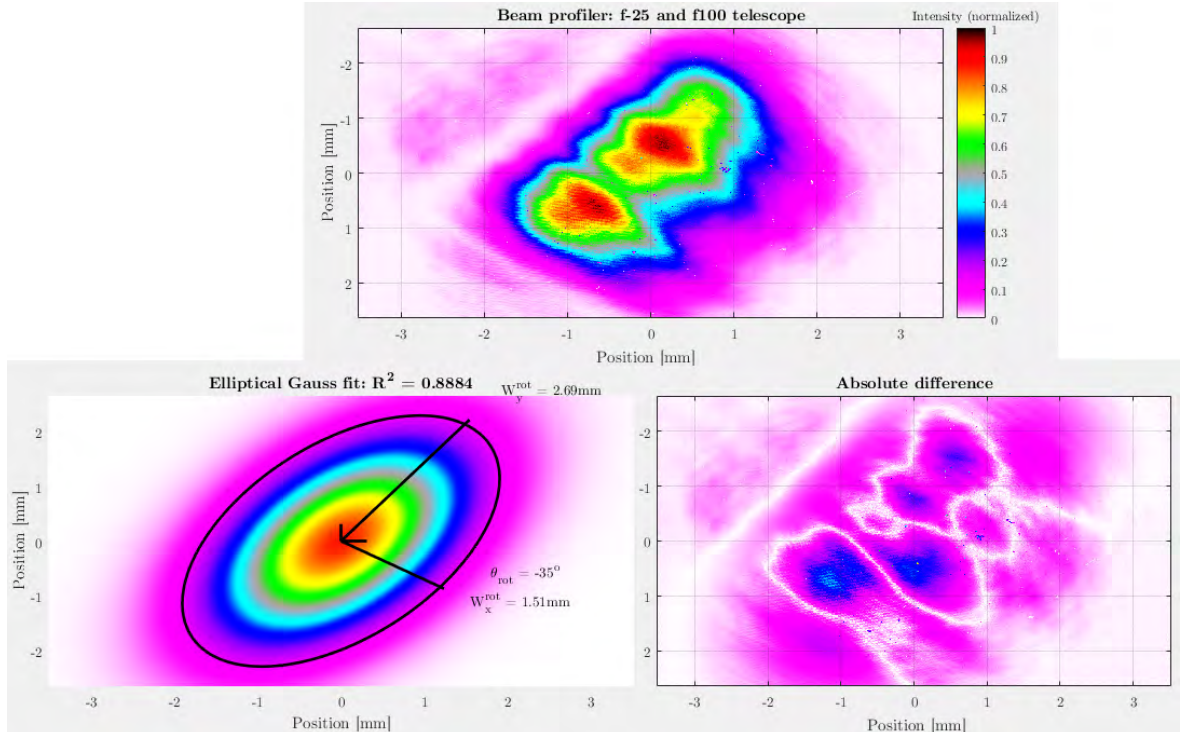


Figure A.2: *Top: Intensity distribution of the pump pulse recorded by a beam profiler. Left: 2D gaussian fit. Right: Absolute difference between the profile and fit.*

### A.3 Crossover pulses in mK ensembles for high atom numbers

Here simulations are shown for the parameters in Fig. 4.4, spanning atom numbers beyond what could be achieved in the experiments.

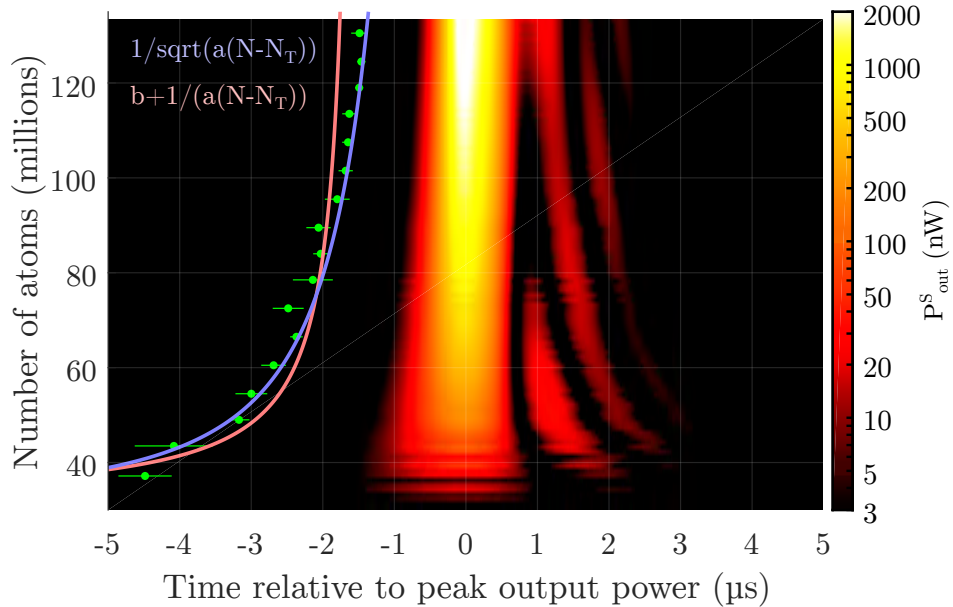


Figure A.3: Simulated single side cavity output power, as in Fig. 4.4, extended up to  $N = 1.33 \cdot 10^8$ . An  $1/\sqrt{a(N - N_{th})}$  fit to the lasing delay shows good agreement in the extended range, while  $b + 1/(a(N - N_{th}))$  shows poor agreement.

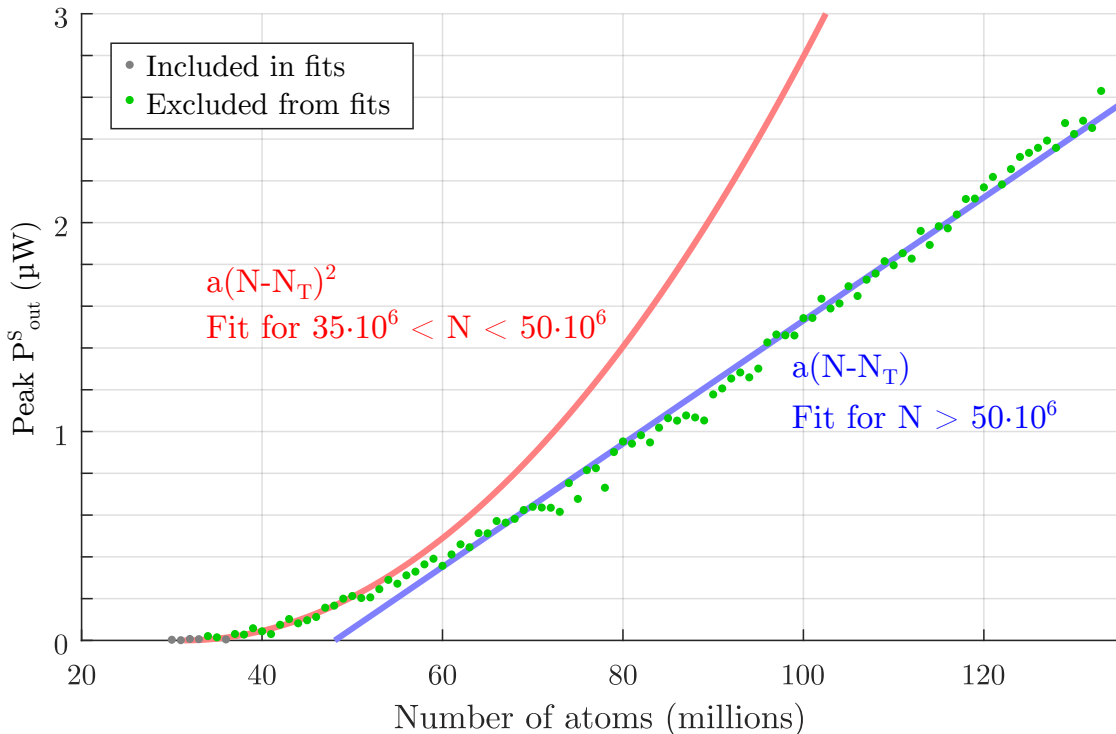


Figure A.4: Peak cavity output power from the simulations in Fig. A.3, and fits indicating regimes with  $N^2$ - and  $N$ -scaling. This behavior is similar to in [58, Fig. 4].

## A.4 Pulse spectrum dependency on cloud temperature

In Fig. A.5 the time evolution of the cavity field amplitude spectrum is shown, using an expanding Heaviside window starting at  $t = 0$ . The frequency axis is with respect to the pump pulse, which is equal to the atomic transition frequency. Note that a different color scale is used than in Fig. 4.9, and that the amplitude spectrum is shown rather than the power spectrum. The qualitative result to note is that at lower temperatures the multi-peaked background becomes less prominent in the spectrum, as expected from the fact that there are fewer atoms with high velocities.

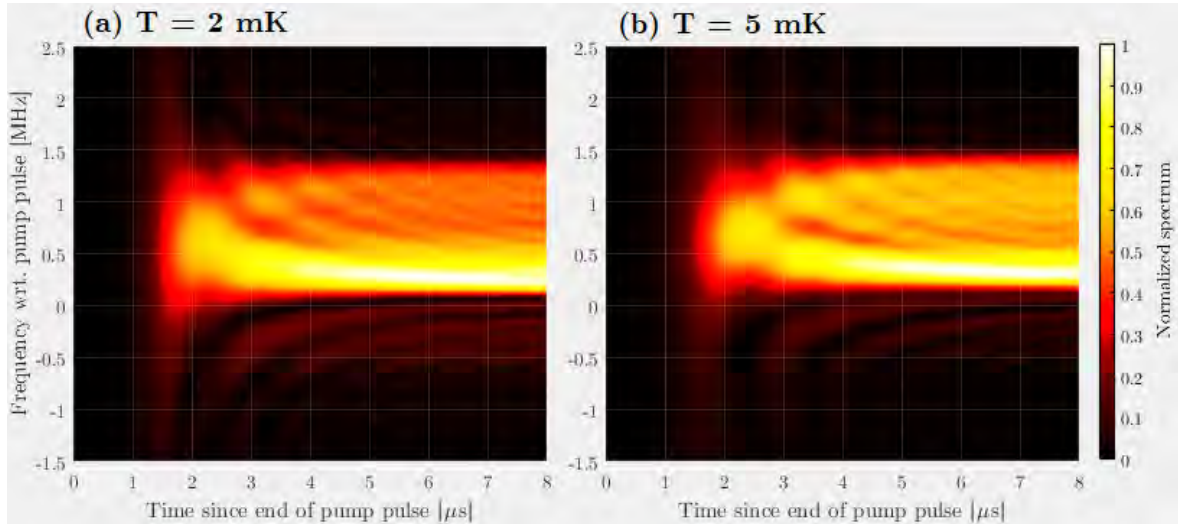


Figure A.5: (a) Normalized cavity field amplitude spectrum for  $N = 7 \cdot 10^7$  atoms,  $\delta_{cE}/2\pi = 1$  MHz and  $T = 2 \text{ mK}$  from a simulated lasing pulse. (b) Results with  $T = 5 \text{ mK}$  instead.

## A.5 Beam profile for pumping μK atom cloud

In Fig. A.6 the beam profile of the pump pulse used for the μK atom cloud is shown, along with a Gaussian fit and residuals. Unlike the mK pump pulse, the beam profile achieved here is a result from fiber-coupling the beam from a tapered amplifier.

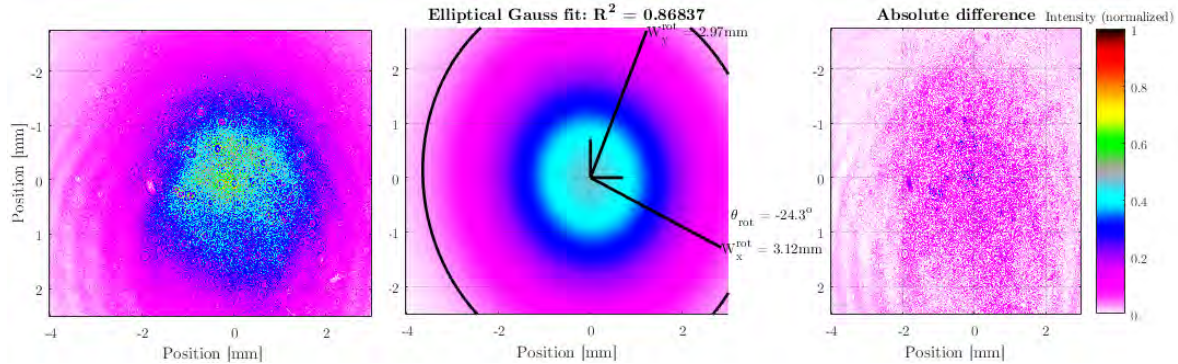


Figure A.6: Left: Intensity distribution of the pump pulse recorded by a beam profiler located at a distance from relevant optics that gives the same propagation distance as to the atom cloud. Center: 2D gaussian fit. Right: Absolute difference between the profile and fit.

## A.6 Pure and crossover pulses in the μK regime

In Fig. A.7 the dependency of the output power dynamics and power spectrum on cavity detuning are shown for three different atom numbers  $N$  and pump pulse durations  $T_p$ . The

temperature here is 40  $\mu\text{K}$ , the atom cloud radius is 250  $\mu\text{m}$  along all axes and the pump pulse power is 200 mW in these examples while assuming the beam profile in Appendix A.2.

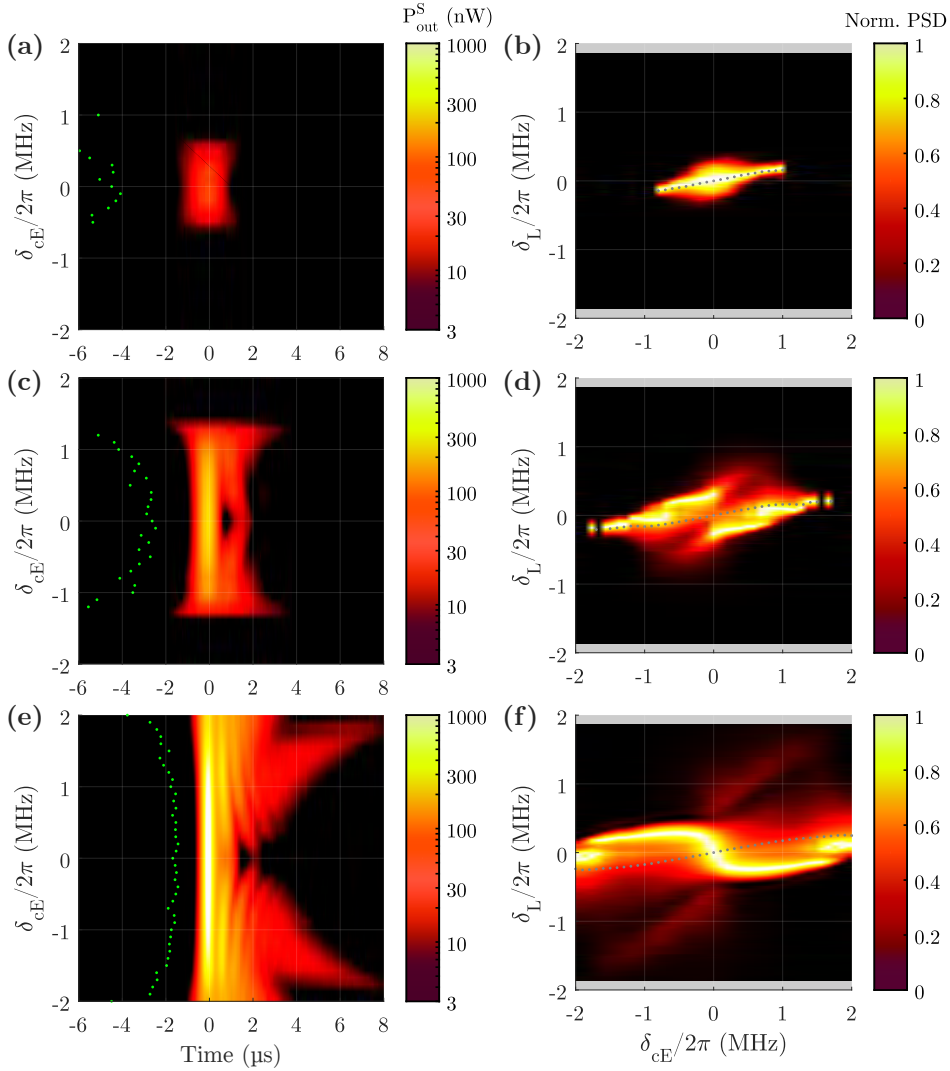


Figure A.7: Simulations of (a,c,e) output power dynamics and (b,d,f) power spectra for (a-b)  $N = 2 \cdot 10^6$  and  $T_p=110$  ns (shorter than a  $\pi$  pulse), (c-d)  $N = 4 \cdot 10^6$  and  $T_p=140$  ns (a  $\pi$  pulse) and (e-f)  $N = 10^7$  and  $T_p=140$  ns. Green dots indicate the end of pumping pulses, and gray dots show the intensity-weighted center of the spectra.

In panels (a) and (b) the atom number and excitation is low enough to realize a single pulse near the transition to the pure superradiant regime, giving also a simple spectrum with a single peak. In the lower panels we go into the crossover regime by increasing the number of excitations. Though the pulses in Sec. 5.1 are realized with slightly different parameters, the main difference is the even higher atom number compared to these examples.

## A.7 Light shifts on pumping transitions from optical lattice

The maximum variation in light shifts are shown in Table A.1 for an  $P = 1$  W intra-cavity optical lattice, using Eq. 8.27:

$$I_{\text{lat}}^{\text{max}} = \frac{4P}{\pi w_0^2} = 5.09 \cdot 10^8 \text{ W/m}^2, \quad \Delta\nu_{\text{max}} = -\frac{\text{Re}(\Delta\alpha) I_{\text{lat}}^{\text{max}}}{2\hbar\epsilon_0 c}. \quad (\text{A.1})$$

Wavelength	Transition	$\Delta\nu_{max}$ (kHz)
689 nm	$^1S_0$ to $^3P_1$ $m_J=-1$	150
679 nm	$^3P_0$ to $^3S_1$ $m_J=-1$	1319
688 nm	$^3P_1$ $m_J=-1$ to $^3S_1$ $m_J=-1$	1288
707 nm	$^3P_2$ $m_J=-2$ to $^3S_1$ $m_J=-1$	1502
707 nm	$^3P_2$ $m_J=-1$ to $^3S_1$ $m_J=0$	1327
707 nm	$^3P_2$ $m_J=0$ to $^3S_1$ $m_J=1$	1270

Table A.1: Maximum light shifts on some pumping transitions for a lattice power of 1 W.

## A.8 Simulations of lasing in the Sr2 Machine at UCPH

The "Sr2" machine at UCPH is based on a beam of atoms traversing an optical cavity, similarly to the hot beam machine at UvA, but uses a Zeeman slower and deflecting 2D MOT, enabling slower and more uniform propagation velocities. Using the hot beam model in Chapter 7 we can determine the atom flux requirement to realize lasing in this machine. Here we also assume an uniform beam, but simply assume the atoms start at the cavity axis,  $x = -W_c$ , in the excited state, and propagate with uniform velocities of  $v_x = 40$  m/s. The radial atomic beam temperature is assumed to be 4  $\mu$ K, and the relevant cavity parameters are  $\kappa/2\pi = 180$  kHz,  $L = 37$  mm and  $W_c = 250$   $\mu$ m. Here the lasing threshold occurs near  $2 \cdot 10^8$  atoms/s. The fast decay time of  $^3P_1$  sets a lower limit on the required propagation velocity on the order of tens of m/s to achieve inversion within the cavity waist, when the atoms are pumped before entry. For low propagation velocities a continuous repumping scheme could potentially enable more power from each atom.

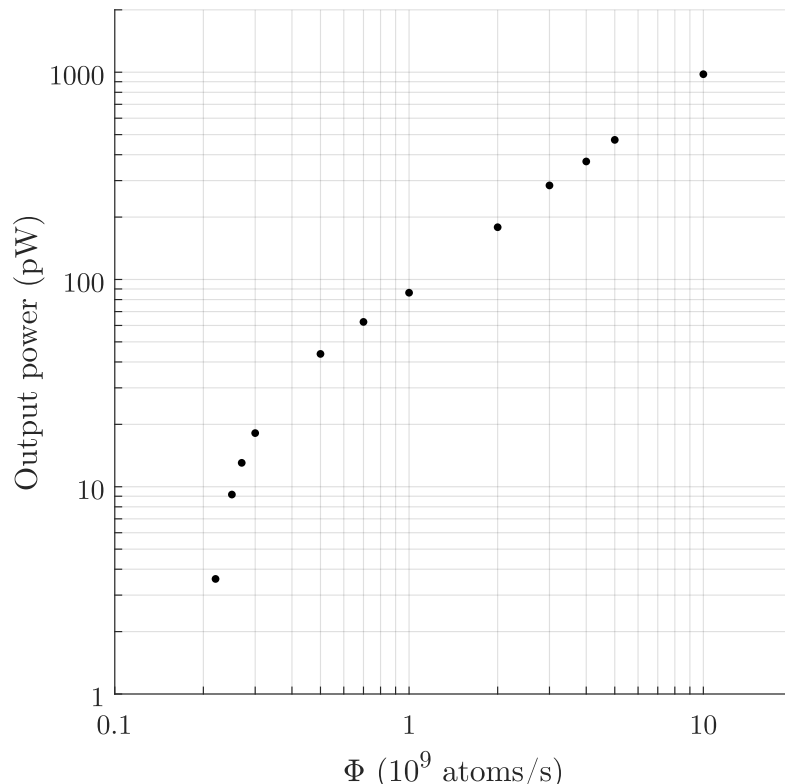


Figure A.8: Total cavity output power for different atom flux values in the "Sr2" system, according to simulations with a temperature of 4  $\mu$ K along the cavity axis.

# List of Figures

1.1	Strontium levels and transitions . . . . .	3
1.2	Example of a passive atomic clock . . . . .	5
1.3	Superradiant vs good-cavity laser . . . . .	6
1.4	Pulsed superradiance regimes . . . . .	8
1.5	Lasing pulse peak power scaling regimes . . . . .	8
1.6	Continuous superradiant laser architectures . . . . .	10
2.1	Numerical modeling of the time evolution of a superradiant laser . . . . .	13
2.2	Interaction and dissipation rates in a superradiant laser model . . . . .	16
2.3	Dynamics according to the SME and OBE . . . . .	24
2.4	Dynamics of OBE vs rate equations . . . . .	26
2.5	Clebsch-Gordan coefficients of relevant Zeeman levels in Sr . . . . .	27
2.6	Filter cavities for modeling laser spectra . . . . .	30
2.7	GPU vs CPU performance scalings . . . . .	33
2.8	Numerical simulation monitoring example . . . . .	34
3.1	Overview of the UCPH atom cloud machine . . . . .	35
3.2	Overview of laser systems for the UCPH cloud machine . . . . .	37
3.3	Photo of the atom cloud machine setup . . . . .	38
3.4	Photo of repumper laser breadboard . . . . .	39
3.5	MOT coil configuration and impact on Zeeman levels . . . . .	40
3.6	Sigma transitions in a MOT . . . . .	41
3.7	Angular variation in driven Zeeman transitions . . . . .	42
3.8	Numerical simulation of a blue MOT cloud . . . . .	43
3.9	Numerical simulation of trapping and cooling a red MOT cloud . . . . .	45
3.10	Simulation of trapping a red MOT cloud with slow B-field ramping . . . . .	47
3.11	Circuit for fast control of the current in a MOT coil . . . . .	48
3.12	Photos of MOT coil switching electronics . . . . .	49
3.13	MOT coil current scaling with electronic reference signals . . . . .	50
3.14	Customized reference signal and parameters for controlling MOT coil currents . . . . .	51
3.15	The CameraGUI used for the UCPH atom cloud machine . . . . .	52
3.16	Photo of the atom cloud machine with the original MOT coils . . . . .	53
3.17	Model circuit of eddy currents in the original MOT coils . . . . .	53
3.18	Simulations of eddy currents in the original MOT coils . . . . .	54
3.19	Experimental test of ramping the original MOT coils quickly . . . . .	55
3.20	Photos of hollow wire MOT coils . . . . .	56
3.21	Water cooling test of hollow wire MOT coil . . . . .	57
3.22	Ramping time tests of hollow wire MOT coils . . . . .	58
3.23	Magnetic field offset from compensation coils . . . . .	59
3.24	Cavity transmission modes during incoupling alignment . . . . .	60
3.25	PDH signals and locking characteristics . . . . .	61
3.26	Impact of cavity photons on absorption images of a blue MOT cloud . . . . .	62
3.27	Photos of blue MOT clouds before and after experimental upgrades . . . . .	63
3.28	Fluorescence signature of a red MOT cloud . . . . .	64
3.29	Initial absorption image of a red MOT cloud . . . . .	64
3.30	Absorption images of red MOT clouds and the impact of cavity photons . . . . .	65
3.31	Impact of red MOT cloud on cavity transmission during scan . . . . .	65
3.32	Small, seeded superradiant pulse from a red MOT cloud . . . . .	66
4.1	UCPH setup for superradiant laser pulses . . . . .	67
4.2	Power and phase dynamics in superradiant laser pulses . . . . .	69
4.3	Pulse beat signal examples from simulations and experiments . . . . .	71
4.4	Variation of pulses with atom number in simulations and experiments . . . . .	72
4.5	Variation of peak output power and delay with atom number . . . . .	73
4.6	Pulse power and phase dynamics in a simulation with a detuned cavity . . . . .	75
4.7	Pulse beat signals in a simulation and experiment with a detuned cavity . . . . .	76
4.8	Experimental pulse beat signal and spectral dynamics in a detuned cavity . . . . .	77
4.9	Spectral dynamics in a simulation with a detuned cavity . . . . .	78
4.10	Velocity-dependent absorption and emission for 0 vs 1 MHz cavity detuning . . . . .	79
4.11	Pulse variations with cavity detuning in simulations and experiments . . . . .	80
4.12	Variation in pulse spectra with cavity detuning in simulations and experiments . . . . .	82
4.13	Velocity-dependent absorption and emission in regime with a cavity-immune peak . . . . .	83

4.14 Variations in peak lasing frequency at different cavity detunings . . . . .	84
5.1 Pulse variations with cavity detuning in simulations and experiments at $\mu\text{K}$ . . . . .	86
5.2 Variation in pulse spectra with cavity detuning in simulations at $\mu\text{K}$ . . . . .	87
5.3 Repumping transitions and statistics for continuous superradiance . . . . .	88
5.4 Quasi-continuous pulse dynamics in a red MOT cloud with a high repumping rate . . . . .	90
5.5 Quasi-continuous pulse dynamics in a red MOT cloud with a low repumping rate . . . . .	91
5.6 Quasi-continuous pulse dynamics in a blue MOT cloud . . . . .	92
5.7 Quasi-continuous pulse dynamics in a blue MOT cloud at different cavity detunings . . . . .	93
5.8 Output power dependency on atom flux, temperature and repumping rate . . . . .	94
6.1 Illustration of the hot beam SRLM at UvA . . . . .	95
6.2 Monitor cavities . . . . .	96
6.3 SRLM science cavity components . . . . .	97
6.4 Final mirror attachment to science cavity . . . . .	98
6.5 Glue curing for the science cavity . . . . .	99
6.6 Assembly of SRLM with science cavity . . . . .	100
6.7 Final SRLM assembly with strontium . . . . .	101
6.8 Transverse cooling system for the SRLM . . . . .	102
6.9 PDH signal for the SRLM science cavity lock . . . . .	103
6.10 Photo of EOM assembly . . . . .	103
6.11 Plan for optics around the SRLM science cavity . . . . .	104
6.13 Illustration of stages in the SRLM . . . . .	105
6.14 Transitions and detunings in numerical model of pumping . . . . .	107
6.15 Numerical simulation of pumping and velocity selection . . . . .	108
7.1 Atomic beam velocity distribution and relativistic Doppler shifts . . . . .	113
7.2 Illustration of atoms in the hot beam system . . . . .	113
7.3 Example of output power dynamics in hot beam simulations . . . . .	114
7.4 Impact of the atom group approximation in hot beam simulations . . . . .	114
7.5 Output power variation with atom flux in the hot beam system . . . . .	115
7.6 Cavity pulling in the hot beam system . . . . .	116
7.7 Velocity selection requirements for the hot beam system . . . . .	118
7.8 Impact of atom temperature on the hot beam system . . . . .	119
7.9 Multi-component superradiance at high temperature . . . . .	120
7.10 Unstable multi-component superradiance at high temperature . . . . .	121
7.11 Impact of stray light on the hot beam system . . . . .	122
7.12 Dependency of cavity pulling on the cavity detuning magnitude . . . . .	123
7.13 Variations in frequency fluctuations with cavity detuning . . . . .	124
7.14 Dynamic cavity pulling and relevant frequencies . . . . .	125
7.15 Absorption and amplification in the hot beam system . . . . .	127
8.1 Illustration of cold beam system and pumping . . . . .	130
8.2 $^1\text{S}_0$ and $^3\text{P}_1$ polarizabilities in red/near-IR domain . . . . .	135
8.3 Polarizability of $^1\text{S}_0$ and $^3\text{P}_1$ $m_J=0$ with Zeeman shift . . . . .	136
8.4 Polarizabilities of Zeeman sublevels at 914 nm . . . . .	137
8.5 Spatial variations during superradiance in the cold beam system . . . . .	138
8.6 Cavity output power in the cold beam system . . . . .	140
8.7 Cavity pulling in the cold beam system . . . . .	141
8.8 Calculated linewidths in cold beam system . . . . .	141
8.9 Variation in lasing frequency with repumper intensities . . . . .	143
8.10 The cold beam system with an intra-cavity optical lattice . . . . .	144
8.11 Impact of lattice power on lasing parameters . . . . .	145
A.1 TA power degradation . . . . .	151
A.2 Beam profile for pumping mK atom cloud . . . . .	151
A.3 Crossover pulses for high atom numbers at mK . . . . .	152
A.4 Peak output power for high atom numbers at mK . . . . .	152
A.5 Pulse spectrum evolution at 2 vs 5 mK . . . . .	153
A.6 Beam profile for pumping $\mu\text{K}$ atom cloud . . . . .	153
A.7 Variation of crossover laser pulses with atom number at $\mu\text{K}$ . . . . .	154
A.8 Output power in simulations of the Sr2 system . . . . .	155

# List of Tables

3.1	Science cavity paramers of the UCPH atom cloud machine . . . . .	36
3.2	Resistances of hollow wire MOT coils . . . . .	57
6.1	Science cavity paramers of the UvA hot beam SRLM . . . . .	100
6.2	Parameters for pumping simulations of the UvA hot beam SRLM . . . . .	107
8.1	Paramers of a cold atom source demonstrated at UvA . . . . .	129
8.2	Science cavity paramers assumed for the cold beam system . . . . .	131
8.3	Assumed pumping and magnetic field parameters for the cold beam system . . . . .	133
8.4	Frequency-pulling from repumpers in the cold beam system . . . . .	142
A.1	Light shift magnitudes from lattice in cold beam system . . . . .	155

# Bibliography

- [1] A. D. Ludlow, M. M. Boyd, J. Ye, E. Peik, and P. O. Schmidt, Optical atomic clocks, *Rev. Mod. Phys.* **87**, 637 (2015).  
DOI: [10.1103/RevModPhys.87.637](https://doi.org/10.1103/RevModPhys.87.637) (Retrieved October 25, 2022)
- [2] M. Abdel-Hafiz et al., Guidelines for developing optical clocks with  $10^{-18}$  fractional frequency uncertainty, *arXiv* (2019).  
DOI: [10.48550/arXiv.1906.11495](https://doi.org/10.48550/arXiv.1906.11495) (Retrieved October 27, 2022)
- [3] D. G. Matei, T. Legero, S. Häfner, C. Grebing, R. Weyrich, W. Zhang, L. Sonderhouse, J. M. Robinson, J. Ye, F. Riehle, and U. Sterr, 1.5  $\mu\text{m}$  Lasers with Sub-10 mHz Linewidth, *Phys. Rev. Lett.* **118**, 263202 (2017).  
DOI: [10.1103/PhysRevLett.118.263202](https://doi.org/10.1103/PhysRevLett.118.263202) (Retrieved October 25, 2022)
- [4] J. M. Robinson, E. Oelker, W. R. Milner, W. Zhang, T. Legero, D. G. Matei, F. Riehle, U. Sterr, J. Ye, Crystalline optical cavity at 4 K with thermal-noise-limited instability and ultralow drift, *Optica* **6**, 240 (2019).  
DOI: [10.1364/OPTICA.6.000240](https://doi.org/10.1364/OPTICA.6.000240) (Retrieved October 25, 2022)
- [5] W. Zhang, J. M. Robinson, L. Sonderhouse, E. Oelker, C. Benko, J. L. Hall, T. Legero, D. G. Matei, F. Riehle, U. Sterr, and J. Ye, Ultrastable Silicon Cavity in a Continuously Operating Closed-Cycle Cryostat at 4 K, *Phys. Rev. Lett.* **119**, 243601 (2017).  
DOI: [10.1103/PhysRevLett.119.243601](https://doi.org/10.1103/PhysRevLett.119.243601) (Retrieved October 25, 2022)
- [6] J. Ye and T. W. Lynn, Applications of Optical Cavities in Modern Atomic, Molecular, and Optical Physics, *Advances In Atomic, Molecular, and Optical Physics* **49**, 1-83 (2003).  
DOI: [10.1016/S1049-250X\(03\)80003-4](https://doi.org/10.1016/S1049-250X(03)80003-4) (Retrieved October 25, 2022)
- [7] B. P. Abbott et al., Observation of Gravitational Waves from a Binary Black Hole Merger, *Phys. Rev.* **116**, 6 (2016).  
DOI: [10.1103/PhysRevLett.116.061102](https://doi.org/10.1103/PhysRevLett.116.061102) (Retrieved October 25, 2022)
- [8] T. E. Mehlstäubler, G. Grosche, C. Lisdat, P. O. Schmidt, and H. Denker, Atomic clocks for geodesy, *Rep. Prog. Phys.* **81**, 064401 (2018).  
DOI: [10.1088/1361-6633/aab409](https://doi.org/10.1088/1361-6633/aab409) (Retrieved October 25, 2022)
- [9] W. F. McGrew, X. Zhang, R. J. Fasano, S. A. Schäffer, K. Beloy, D. Nicolodi, R. C. Brown, N. Hinkley, G. Milani, M. Schioppo, T. H. Yoon, and A. D. Ludlow, Atomic clock performance enabling geodesy below the centimetre level, *Nature* **564**, 87–90 (2018).  
DOI: [10.1038/s41586-018-0738-2](https://doi.org/10.1038/s41586-018-0738-2) (Retrieved October 25, 2022)
- [10] N. Ashby, Relativity and the Global Positioning System, *Physics Today* **55**, 41-47 (2002).  
DOI: [10.1063/1.1485583](https://doi.org/10.1063/1.1485583) (Retrieved October 25, 2022)
- [11] I. M. Georgescu, S. Ashhab, and F. Nori, Quantum simulation, *Rev. Mod. Phys.* **86**, 153 (2014).  
DOI: [10.1103/RevModPhys.86.153](https://doi.org/10.1103/RevModPhys.86.153) (Retrieved October 25, 2022)
- [12] A. Derevianko, K. Gibble, L. Hollberg, N. R. Newbury, Chris. Oates, M. S. Safronova, L. C. Sinclair, and N. Yu, Fundamental physics with a state-of-the-art optical clock in space, *Quantum Sci. Technol.* **7**, 044002 (2022).  
DOI: [10.1088/2058-9565/ac7df9](https://doi.org/10.1088/2058-9565/ac7df9) (Retrieved October 25, 2022)
- [13] D. Mitra, K. H. Leung, and T. Zelevinsky, Quantum control of molecules for fundamental physics, *Phys. Rev. A* **105**, 040101 (2022).  
DOI: [10.1103/PhysRevA.105.040101](https://doi.org/10.1103/PhysRevA.105.040101) (Retrieved October 25, 2022)

- [14] S. M. Brewer, J.-S. Chen, A. M. Hankin, E. R. Clements, C. W. Chou, D. J. Wineland, D. B. Hume, and D. R. Leibrandt,  $^{27}\text{Al}^+$  Quantum-Logic Clock with a Systematic Uncertainty below  $10^{-18}$ , Phys. Rev. Lett. **123**, 033201 (2019).  
DOI: [10.1103/PhysRevLett.123.033201](https://doi.org/10.1103/PhysRevLett.123.033201) (Retrieved October 25, 2022)
- [15] T. L. Nicholson, S. L. Campbell, R. B. Hutson, G. E. Marti, B. J. Bloom, R. L. McNally, W. Zhang, M. D. Barrett, M. S. Safronova, G. F. Strouse, W. L. Tew, and J. Ye, Systematic evaluation of an atomic clock at  $2 \times 10^{-18}$  total uncertainty, Nat. Commun. **6**, 6896 (2015).  
DOI: [10.1038/ncomms7896](https://doi.org/10.1038/ncomms7896) (Retrieved October 25, 2022)
- [16] N. Huntemann, C. Sanner, B. Lipphardt, C. Tamm, and E. Peik, Single-ion atomic clock with  $3 \times 10^{-18}$  systematic uncertainty. Phys. Rev. Lett. **116**, 063001 (2016).  
DOI: [10.1103/PhysRevLett.116.063001](https://doi.org/10.1103/PhysRevLett.116.063001) (Retrieved October 25, 2022)
- [17] M. Schioppo, R. C. Brown, W. F. McGrew, N. Hinkley, R. J. Fasano, K. Beloy, T. H. Yoon, G. Milani, D. Nicolodi, J. A. Sherman, N. B. Phillips, C. W. Oates, and A. D. Ludlow, Ultrastable optical clock with two cold-atom ensembles, Nat. Photon. **11**, 48–52 (2017).  
DOI: [10.1038/NPHOTON.2016.231](https://doi.org/10.1038/NPHOTON.2016.231) (Retrieved October 25, 2022)
- [18] T. Takano, M. Takamoto, I. Ushijima, N. Ohmae, T. Akatsuka, A. Yamaguchi, Y. Kuroishi, H. Munekane, B. Miyahara, and H. Katori, Geopotential measurements with synchronously linked optical lattice clocks, Nat. Photon. **10**, 662–666 (2016).  
DOI: [10.1038/NPHOTON.2016.159](https://doi.org/10.1038/NPHOTON.2016.159) (Retrieved October 25, 2022)
- [19] J. E. Sansonetti and G. Nave, Wavelengths, Transition Probabilities, and Energy Levels for the Spectrum of Neutral Strontium ( $\text{SrI}$ ), J. Phys. Chem. Ref. Data **39**, 033103 (2010).  
DOI: [10.1063/1.3449176](https://doi.org/10.1063/1.3449176) (Retrieved October 25, 2022)
- [20] C. J. Foot, *Atomic Physics*, Oxford University Press (2014).
- [21] J. A. Muniz, D. J. Young, J. R. K. Cline, and J. K. Thompson, Cavity-QED measurements of the  $^{87}\text{Sr}$  millihertz optical clock transition and determination of its natural linewidth, Phys. Rev. Research **3**, 023152 (2021).  
DOI: [10.1103/PhysRevResearch.3.023152](https://doi.org/10.1103/PhysRevResearch.3.023152) (Retrieved October 25, 2022)
- [22] T. Akatsuka, K. Hashiguchi, T. Takahashi, N. Ohmae, M. Takamoto, and H. Katori, Three-stage laser cooling of Sr atoms using the  $5\text{s}5\text{p}^3\text{P}_2$  metastable state below Doppler temperatures, Phys. Rev. A **103**, 023331 (2021).  
DOI: [10.1103/PhysRevA.103.023331](https://doi.org/10.1103/PhysRevA.103.023331) (Retrieved October 25, 2022)
- [23] S. B. Nagel, C. E. Simien, S. Laha, P. Gupta, V. S. Ashoka, and T. C. Killian, Magnetic trapping of metastable  $^3\text{P}_2$  atomic strontium, Phys. Rev. A **67**, 011401(R) (2003).  
DOI: [10.1103/PhysRevA.67.011401](https://doi.org/10.1103/PhysRevA.67.011401) (Retrieved October 25, 2022)
- [24] M. Yasuda, T. Kishimoto, M. Takamoto, and H. Katori, Photoassociation spectroscopy of  $^{88}\text{Sr}$ : Reconstruction of the wave function near the last node, Phys. Rev. A **73**, 011403(R) (2006).  
DOI: [10.1103/PhysRevA.73.011403](https://doi.org/10.1103/PhysRevA.73.011403) (Retrieved October 25, 2022)
- [25] X. Zhou, X. Xu, X. Chen, and J. Chen, Magic wavelengths for terahertz clock transitions, Phys. Rev. A **81**, 012115, 2010.  
DOI: [10.1103/PhysRevA.81.012115](https://doi.org/10.1103/PhysRevA.81.012115) (Retrieved October 25, 2022)
- [26] C. W. Bauschlicher Jr, S. R. Langhoff, and H. Partridge, The radiative lifetime of the  $^1\text{D}_2$  state of Ca and Sr: a core-valence treatment, J. Phys. B: Atom. Mol. Phys. **18**, 1523 (1985).  
DOI: [10.1088/0022-3700/18/8/011](https://doi.org/10.1088/0022-3700/18/8/011) (Retrieved October 25, 2022)
- [27] E. Peik, T. Schumm, M. S. Safronova, A. Pálffy, J. Weitenberg, and P. G. Thirolf, Nuclear clocks for testing fundamental physics, Quantum Sci. Technol. **6** 034002 (2021).  
DOI: [10.1088/2058-9565/abe9c2](https://doi.org/10.1088/2058-9565/abe9c2) (Retrieved October 25, 2022)

- [28] P. Gill, When should we change the definition of the second?, *Phil. Trans. R. Soc. A* **369**, 1953 (2011).  
DOI: [10.1098/rsta.2011.0237](https://doi.org/10.1098/rsta.2011.0237) (Retrieved October 25, 2022)
- [29] T. Bothwell, D. Kedar, E. Oelker, J. M. Robinson, S. L. Bromley, W. L. Tew, J. Ye, and C. J. Kennedy, JILA SrI optical lattice clock with uncertainty of  $2.0 \times 10^{-18}$ , *Metrologia* **56**, 065004 (2019).  
DOI: [10.1088/1681-7575/ab4089](https://doi.org/10.1088/1681-7575/ab4089) (Retrieved October 25, 2022)
- [30] D. V. Schroeder, *An Introduction to Thermal Physics*, Pearson Education Limited (2014).
- [31] A. Quessada, R. P. Kovacich, I. Courtillot, A. Clairon, G. Santarelli, and P. Lemonde, The Dick effect for an optical frequency standard, *J. Opt. B: Quantum Semiclass. Opt.* **5**, 150 (2003).  
DOI: [10.1088/1464-4266/5/2/373](https://doi.org/10.1088/1464-4266/5/2/373) (Retrieved October 25, 2022)
- [32] R. W. P. Drever, J. L. Hall, F. V. Kowalski, J. Hough, G. M. Ford, A. J. Munley, and H. Ward, Laser phase and frequency stabilization using an optical resonator, *Applied Physics B* **31**, 97-105 (1983).  
DOI: [10.1007/BF00702605](https://doi.org/10.1007/BF00702605) (Retrieved October 25, 2022)
- [33] K. Numata, A. Kemery, and J. Camp, Thermal-Noise Limit in the Frequency Stabilization of Lasers with Rigid Cavities, *Phys. Rev. Lett.* **93**, 250602 (2004).  
DOI: [10.1103/PhysRevLett.93.250602](https://doi.org/10.1103/PhysRevLett.93.250602) (Retrieved October 25, 2022)
- [34] G. D. Cole, W. Zhang, M. J. Martin, J. Ye, and M. Aspelmeier, Tenfold reduction of Brownian noise in high-reflectivity optical coatings, *Nature Photonics* **7**, 644 (2013).  
DOI: [10.1038/nphoton.2013.174](https://doi.org/10.1038/nphoton.2013.174) (Retrieved October 25, 2022)
- [35] H. M. Goldenberg, D. Kleppner, and N. F. Ramsey, Atomic Hydrogen Maser, *Phys. Rev. Lett.* **5**, 361 (1960).  
DOI: [10.1103/PhysRevLett.5.361](https://doi.org/10.1103/PhysRevLett.5.361) (Retrieved October 25, 2022)
- [36] R. H. Dicke, Coherence in Spontaneous Radiation Processes, *Phys. Rev.* **93**, 99 (1954).  
DOI: [10.1103/PhysRev.93.99](https://doi.org/10.1103/PhysRev.93.99) (Retrieved October 25, 2022)
- [37] V. Ernst and P. Stehle, Emission of Radiation from a System of Many Excited Atoms, *Phys. Rev.* **176**, 1456 (1968).  
DOI: [10.1103/PhysRev.176.1456](https://doi.org/10.1103/PhysRev.176.1456) (Retrieved October 25, 2022)
- [38] N. Skribanowitz, I. P. Herman, J. C. MacGillivray, and M. S. Feld, Observation of Dicke Superradiance in Optically Pumped HF Gas, *Phys. Rev. Lett.* **30**, 309 (1973).  
DOI: [10.1103/PhysRevLett.30.309](https://doi.org/10.1103/PhysRevLett.30.309) (Retrieved October 25, 2022)
- [39] M. F. H. Schuurmans, Q. H. F. Vrehen, D. Polder, and H. M. Gibbs, Superfluorescence, *Advances in Atomic and Molecular Physics* **17**, 167 (1981).  
DOI: [10.1016/S0065-2199\(08\)60069-X](https://doi.org/10.1016/S0065-2199(08)60069-X) (Retrieved October 25, 2022)
- [40] R. Bonifacio and L. A. Lugiato, Cooperative radiation processes in two-level systems: Superfluorescence, *Phys. Rev. A* **11**, 1507 (1975).  
DOI: [10.1103/PhysRevA.11.1507](https://doi.org/10.1103/PhysRevA.11.1507) (Retrieved October 25, 2022)
- [41] A. Kumarakrishnan and X. L. Han, Superfluorescence from optically trapped calcium atoms, *Phys. Rev. A* **58**, 4153 (1998).  
DOI: [10.1103/PhysRevA.58.4153](https://doi.org/10.1103/PhysRevA.58.4153) (Retrieved October 25, 2022)
- [42] M. Gross and S. Haroche, Superradiance: An essay on the theory of collective spontaneous emission, *Phys. Rep.* **93**, 301 (1982).  
DOI: [10.1016/0370-1573\(82\)90102-8](https://doi.org/10.1016/0370-1573(82)90102-8) (Retrieved October 25, 2022)

- [43] R. Bonifacio, P. Schwendimann and F. Haake, Quantum Statistical Theory of Superradiance. I, Phys. Rev. A **4**, 302 (1971).  
DOI: [10.1103/PhysRevA.4.302](https://doi.org/10.1103/PhysRevA.4.302) (Retrieved October 25, 2022)
- [44] F. T. Arrechi, Cooperative Phenomena in Resonant Electromagnetic Propagation, Phys. Rev. A **2**, 1730 (1970).  
DOI: [10.1103/PhysRevA.2.1730](https://doi.org/10.1103/PhysRevA.2.1730) (Retrieved October 25, 2022)
- [45] M. F. H. Schuurmans, Superfluorescence and amplified spontaneous emission in an inhomogeneously broadened medium, Opt. Commun. **34**, 185 (1980).  
DOI: [10.1016/0030-4018\(80\)90011-5](https://doi.org/10.1016/0030-4018(80)90011-5) (Retrieved October 25, 2022)
- [46] M. S. Malcuit, J. J. Maki, D. J. Simkin, and R. W. Boyd, Transition from Superfluorescence to Amplified Spontaneous Emission, Phys. Rev. Lett. **59**, 1189 (1987).  
DOI: [10.1103/PhysRevLett.59.1189](https://doi.org/10.1103/PhysRevLett.59.1189) (Retrieved October 25, 2022)
- [47] J. Okada, K. Ikeda, and M. Matsuoka, Streak camera investigation of superradiance development, Opt. Commun. **27**, 321 (1978).  
DOI: [10.1016/0030-4018\(78\)90390-5](https://doi.org/10.1016/0030-4018(78)90390-5) (Retrieved October 25, 2022)
- [48] L. Allen and G. I. Peters, Superradiance, Coherence Brightening and Amplified Spontaneous Emission, Phys. Lett. A **31**, 95 (1970).  
DOI: [10.1016/0375-9601\(70\)90168-4](https://doi.org/10.1016/0375-9601(70)90168-4) (Retrieved October 25, 2022)
- [49] G. I. Peters and L. Allen, Amplified spontaneous emission I. The threshold condition, J. Phys. A: Gen. Phys. **4**, 238 (1971).  
DOI: [10.1088/0305-4470/4/2/009](https://doi.org/10.1088/0305-4470/4/2/009) (Retrieved October 25, 2022)
- [50] G. Ferioli, A. Glicenstein, F. Robicheaux, R. T. Sutherland, A. Browaeys, and I. Ferrier-Barbut, Laser-Driven Superradiant Ensembles of Two-Level Atoms near Dicke Regime, Phys. Rev. Lett. **127**, 243602 (2021).  
DOI: [10.1103/PhysRevLett.127.243602](https://doi.org/10.1103/PhysRevLett.127.243602) (Retrieved November 5, 2022)
- [51] M. O. Araújo, I. Krešić, R. Kaiser, and W. Guerin, Superradiance in a Large and Dilute Cloud of Cold Atoms in the Linear-Optics Regime, Phys. Rev. Lett. **117**, 073002 (2016).  
DOI: [10.1103/PhysRevLett.117.073002](https://doi.org/10.1103/PhysRevLett.117.073002) (Retrieved November 5, 2022)
- [52] A. Glicenstein, G. Ferioli, A. Browaeys, and I. Ferrier-Barbut, From superradiance to subradiance: exploring the many-body Dicke ladder, Opt. Lett. **47**, 1541-1544 (2022).  
DOI: [10.1364/OL.451903](https://doi.org/10.1364/OL.451903) (Retrieved November 5, 2022)
- [53] G. Ferioli, A. Glicenstein, I. Ferrier - Barbut, and A. Browaeys, Observation of a non-equilibrium superradiant phase transition in free space, arXiv (2022).  
DOI: [10.48550/arXiv.2207.10361](https://doi.org/10.48550/arXiv.2207.10361) (Retrieved November 5, 2022)
- [54] S. A. Schäffer, M. Tang, M. R. Henriksen, A. A. Jørgensen, B. T. R. Christensen, and J. W. Thomsen, Lasing on a narrow transition in a cold thermal strontium ensemble, Phys. Rev. A **101**, 013819 (2020).  
DOI: [10.1103/PhysRevA.101.013819](https://doi.org/10.1103/PhysRevA.101.013819) (Retrieved October 25, 2022)  
arXiv DOI: [10.48550/arXiv.1903.12593](https://doi.org/10.48550/arXiv.1903.12593) (Retrieved November 2, 2022)
- [55] M. A. Norcia, M. N. Winchester, J. R. K. Cline, and J. K. Thompson, Superradiance on the millihertz linewidth strontium clock transition, Science Advances **2**, 10, e1601231 (2016).  
DOI: [10.1126/sciadv.1601231](https://doi.org/10.1126/sciadv.1601231) (Retrieved October 25, 2022)
- [56] M. A. Norcia, J. R. K. Cline, J. A. Muniz, J. M. Robinson, R. B. Hutson, A. Goban, G. E. Marti, J. Ye, Frequency Measurements of Superradiance from the Strontium Clock Transition, Phys. Rev. X **8**, 021036 (2018).  
DOI: [10.1103/PhysRevX.8.021036](https://doi.org/10.1103/PhysRevX.8.021036) (Retrieved October 25, 2022)

- [57] T. Laske, H. Winter, and A. Hemmerich, Pulse Delay Time Statistics in a Superradiant Laser with Calcium Atoms, *Phys. Rev. Lett.* **123**, 103601 (2019).  
DOI: [10.1103/PhysRevLett.123.103601](https://doi.org/10.1103/PhysRevLett.123.103601) (Retrieved October 25, 2022)
- [58] A. Gogyan, G. Kazakov, M. Bober, and M. Zawada, Characterisation and feasibility study for superradiant lasing in  $^{40}\text{Ca}$  atoms, *Opt. Express*, **28**, 6881-6892 (2020).  
DOI: [10.1364/OE.381991](https://doi.org/10.1364/OE.381991) (Retrieved October 25, 2022)
- [59] M. Tang, S. A. Schäffer, A. A. Jørgensen, M. R. Henriksen, B. T. R. Christensen, J. H. Müller, and J. W. Thomsen, Cavity-immune spectral features in the pulsed superradiant crossover regime, *Phys. Rev. R* **3**, 033258 (2021).  
DOI: [10.1103/PhysRevResearch.3.033258](https://doi.org/10.1103/PhysRevResearch.3.033258) (Retrieved October 25, 2022)  
arXiv DOI: [10.48550/arXiv.2104.13305](https://arxiv.org/abs/2104.13305) (Retrieved November 2, 2022)
- [60] M. A. Norcia, and J. K. Thompson, Cold-Strontium Laser in the Superradiant Crossover Regime, *Phys. Rev. X* **6**, 011025 (2016).  
DOI: [10.1103/PhysRevX.6.011025](https://doi.org/10.1103/PhysRevX.6.011025) (Retrieved October 25, 2022)
- [61] F. Haake, M. I. Kolobov, C. Fabre, E. Giacobino, and S. Reynaud, Superradiant laser, *Phys. Rev. Lett.* **71**, 995 (1993).  
DOI: [10.1103/PhysRevLett.71.995](https://doi.org/10.1103/PhysRevLett.71.995) (Retrieved October 25, 2022)
- [62] D. A. Tieri, Minghui Xu, D. Meiser, J. Cooper, and M. J. Holland, Theory of the crossover from lasing to steady state superradiance, arXiv (2017).  
DOI: [10.48550/arXiv.1702.04830](https://arxiv.org/abs/1702.04830) (Retrieved October 25, 2022)
- [63] J. G. Bohnet, Z. Chen, J. M. Weiner, K. C. Cox, and J. K. Thompson, Linear-response theory for superradiant lasers, *Phys. Rev. A* **89**, 013806 (2014).  
DOI: [10.1103/PhysRevA.89.013806](https://doi.org/10.1103/PhysRevA.89.013806) (Retrieved October 25, 2022)
- [64] K. Debnath, Y. Zhang, and K. Mølmer, Lasing in the superradiant crossover regime, *Phys. Rev. A* **98**, 063837 (2018).  
DOI: [10.1103/PhysRevA.98.063837](https://doi.org/10.1103/PhysRevA.98.063837) (Retrieved October 25, 2022)
- [65] G. A. Kazakov and T. Schumm, Active optical frequency standards using cold atoms: Perspectives and challenges, EFTF, Neuchatel, pp. 411-414 (2014).  
DOI: [10.1109/EFTF.2014.7331523](https://doi.org/10.1109/EFTF.2014.7331523), [10.48550/arXiv.1503.03998](https://arxiv.org/abs/1503.03998) (Retrieved October 25, 2022)
- [66] D. Meiser and M. J. Holland, Steady-state superradiance with alkaline-earth-metal atoms, *Phys. Rev. A* **81**, 033847 (2010).  
DOI: [10.1103/PhysRevA.81.033847](https://doi.org/10.1103/PhysRevA.81.033847) (Retrieved October 25, 2022)
- [67] M. Xu, D. A. Tieri, E. C. Fine, J. K. Thompson, and M. J. Holland, Synchronization of Two Ensembles of Atoms, *Phys. Rev. Lett.* **113**, 154101 (2014).  
DOI: [10.1103/PhysRevLett.113.154101](https://doi.org/10.1103/PhysRevLett.113.154101) (Retrieved October 25, 2022)
- [68] C. Hotter, D. Plankensteiner, G. Kazakov, and H. Ritsch, Continuous multi-step pumping of the optical clock transition in alkaline-earth atoms with minimal perturbation, *Opt. Express* **30**, 5553-5568 (2022).  
DOI: [10.1364/OE.445976](https://doi.org/10.1364/OE.445976) (Retrieved October 25, 2022)
- [69] D. Pan, B. Arora,<sup>2</sup> Y. Yu, B. K. Sahoo, and J. Chen, Optical-lattice-based Cs active clock with a continual superradiant lasing signal, *Phys. Rev. A* **102**, 041101(R) (2020).  
DOI: [10.1103/PhysRevA.102.041101](https://doi.org/10.1103/PhysRevA.102.041101) (Retrieved October 25, 2022)
- [70] J. Chen, X. Chen, Optical lattice laser, Proceedings of the 2005 IEEE International Frequency Control Symposium and Exposition (2005).  
DOI: [10.1109/FREQ.2005.1574003](https://doi.org/10.1109/FREQ.2005.1574003) (Retrieved October 25, 2022)

- [71] Y. Wang, and J. Chen, Superradiant Laser with Ultra-Narrow Linewidth Based on  $^{40}\text{Ca}$ , Chinese Phys. Lett. **29**, 073202 (2012).  
DOI: [10.1088/0256-307X/29/7/073202](https://doi.org/10.1088/0256-307X/29/7/073202) (Retrieved October 25, 2022)
- [72] D. Meiser, J. Ye, D. R. Carlson, and M. J. Holland, Prospects for a Millihertz-Linewidth Laser, Phys. Rev. Lett. **102**, 163601 (2009).  
DOI: [10.1103/PhysRevLett.102.163601](https://doi.org/10.1103/PhysRevLett.102.163601) (Retrieved October 25, 2022)
- [73] P. Domokos and H. Ritsch, Collective Cooling and Self-Organization of Atoms in a Cavity, Phys. Rev. Lett. **89**, 253003 (2002).  
DOI: [10.1103/PhysRevLett.89.253003](https://doi.org/10.1103/PhysRevLett.89.253003) (Retrieved October 25, 2022)
- [74] M. Xu, S. B. Jäger, S. Schütz, J. Cooper, G. Morigi, and M. J. Holland, Supercooling of Atoms in an Optical Resonator, Phys. Rev. Lett. **116**, 153002 (2016).  
DOI: [10.1103/PhysRevLett.116.153002](https://doi.org/10.1103/PhysRevLett.116.153002) (Retrieved October 25, 2022)
- [75] C. Hotter, D. Plankensteiner, L. Ostermann, and H. Ritsch, Superradiant cooling, trapping, and lasing of dipole-interacting clock atoms, Optics Express **27**, 31193-31206 (2019).  
DOI: [10.1364/OE.27.031193](https://doi.org/10.1364/OE.27.031193) (Retrieved October 25, 2022)
- [76] S. B. Jäger, J. Cooper, M. J. Holland, and G. Morigi, Dynamical Phase Transitions to Optomechanical Superradiance, Phys. Rev. Lett. **123**, 053601 (2019).  
DOI: [10.1103/PhysRevLett.123.053601](https://doi.org/10.1103/PhysRevLett.123.053601) (Retrieved October 25, 2022)
- [77] S. B. Jäger, M. J. Holland, and G. Morigi, Superradiant optomechanical phases of cold atomic gases in optical resonators, Phys. Rev. A **101**, 023616 (2020).  
DOI: [10.1103/PhysRevA.101.023616](https://doi.org/10.1103/PhysRevA.101.023616) (Retrieved October 25, 2022)
- [78] T. Maier, S. Kraemer, L. Ostermann, and H. Ritsch, A superradiant clock laser on a magic wavelength optical lattice, Optics Express **22**, 13269 (2014).  
DOI: [10.1364/OE.22.013269](https://doi.org/10.1364/OE.22.013269) (Retrieved October 25, 2022)
- [79] Y. Zhang, C. Shan, and K. Mølmer, Ultranarrow Superradiant Lasing by Dark Atom-Photon Dressed States, Phys. Rev. Lett. **126**, 123602 (2021).  
DOI: [10.1103/PhysRevLett.126.123602](https://doi.org/10.1103/PhysRevLett.126.123602) (Retrieved October 25, 2022)
- [80] G. W. Harmon, J. T. Reilly, M. J. Holland, and S. B. Jäger, Mean-field Floquet theory for a three-level cold-atom laser, Phys. Rev. A **106**, 013706 (2022).  
DOI: [10.1103/PhysRevA.106.013706](https://doi.org/10.1103/PhysRevA.106.013706) (Retrieved October 25, 2022)
- [81] M. Takamoto, F. L. Hong, R. Higashi, and H. Katori, An optical lattice clock, Nature **435**, 321 (2005).  
DOI: [10.1038/nature03541](https://doi.org/10.1038/nature03541) (Retrieved October 25, 2022)
- [82] H. Katori, M. Takamoto, V. G. Pal'chikov, and V. D. Ovsiannikov, Ultrastable Optical Clock with Neutral Atoms in an Engineered Light Shift Trap, Phys. Rev. Lett. **91**, 173005 (2003).  
DOI: [10.1103/PhysRevLett.91.173005](https://doi.org/10.1103/PhysRevLett.91.173005) (Retrieved October 25, 2022)
- [83] G. A. Kazakov and T. Schumm, Active optical frequency standard using sequential coupling of atomic ensembles, Phys. Rev. A **87**, 013821 (2013).  
DOI: [10.1103/PhysRevA.87.013821](https://doi.org/10.1103/PhysRevA.87.013821) (Retrieved October 25, 2022)
- [84] M. Tang, S. A. Schäffer, and J. H. Müller, Prospects of a superradiant laser based on a thermal or guided beam of Sr-88, arXiv (2022).  
DOI: [10.48550/arXiv.2112.15420](https://doi.org/10.48550/arXiv.2112.15420) (Retrieved October 25, 2022)  
arXiv DOI: [10.48550/arXiv.2104.13305](https://doi.org/10.48550/arXiv.2104.13305) (Retrieved November 2, 2022)
- [85] J. Chen, Active Optical Clock, Chinese Science Bulletin **54**, 348-352 (2009).  
DOI: [10.1007/s11434-009-0073-y](https://doi.org/10.1007/s11434-009-0073-y) (Retrieved October 25, 2022)

- [86] H. Liu, S. B. Jäger, X. Yu, S. Touzard, A. Shankar, M. J. Holland, T. L. Nicholson, Rugged mHz-Linewidth Superradiant Laser Driven by a Hot Atomic Beam, *Phys. Rev. Lett.* **125**, 253602 (2020).  
DOI: [10.1103/PhysRevLett.125.253602](https://doi.org/10.1103/PhysRevLett.125.253602) (Retrieved October 25, 2022)
- [87] S. B. Jäger, H. Liu, J. Cooper, T. L. Nicholson, and M. J. Holland, Superradiant emission of a thermal atomic beam into an optical cavity, *Phys. Rev. A* **104**, 033711 (2021).  
DOI: [10.1103/PhysRevA.104.033711](https://doi.org/10.1103/PhysRevA.104.033711) (Retrieved October 25, 2022)
- [88] S. B. Jäger, H. Liu, J. Cooper, and M. J. Holland, Collective emission of an atomic beam into an off-resonant cavity mode, *Phys. Rev. A* **104**, 053705 (2021).  
DOI: [10.1103/PhysRevA.104.053705](https://doi.org/10.1103/PhysRevA.104.053705) (Retrieved October 25, 2022)
- [89] S. B. Jäger, H. Liu, A. Shankar, J. Cooper, and M. J. Holland, Regular and bistable steady-state superradiant phases of an atomic beam traversing an optical cavity, *Phys. Rev. A* **103**, 013720 (2021).  
DOI: [10.1103/PhysRevA.103.013720](https://doi.org/10.1103/PhysRevA.103.013720) (Retrieved October 25, 2022)
- [90] A. Bychek, C. Hotter, D. Plankensteiner, and H. Ritsch, Superradiant lasing in inhomogeneously broadened ensembles with spatially varying coupling, *Open Research Europe*, **1**:73 (2021).  
DOI: [10.12688/openresearcheurope.13781.2](https://doi.org/10.12688/openresearcheurope.13781.2) (Retrieved October 25, 2022)
- [91] G. A. Kazakov and T. Schumm, Stability analysis for bad cavity lasers using inhomogeneously broadened spin-1/2 atoms as a gain medium, *Phys. Rev. A* **95**, 023839 (2017).  
DOI: [10.1103/PhysRevA.95.023839](https://doi.org/10.1103/PhysRevA.95.023839) (Retrieved October 25, 2022)
- [92] D. Yu and J. Chen, Laser theory with finite atom-field interacting time, *Phys. Rev. A* **78**, 013846 (2008).  
DOI: [10.1103/PhysRevA.78.013846](https://doi.org/10.1103/PhysRevA.78.013846) (Retrieved October 25, 2022)
- [93] T. Shi, J. Miao, J. Zhang, and J. Chen, Active optical clock lasing on the Cs  $^7\text{S}_{1/2}$ - $^6\text{P}_{3/2}$  transition under a weak magnetic field, *Front. Phys.* **10**:967255 (2022).  
DOI: [10.3389/fphy.2022.967255](https://doi.org/10.3389/fphy.2022.967255) (Retrieved October 25, 2022)
- [94] J. G. Bohnet, Z. Chen, J. M. Weiner, D. Meiser, M. J. Holland, and J. K. Thompson, A steady-state superradiant laser with less than one intracavity photon, *Nature*, **484**, 78-81 (2012).  
DOI: [10.1038/nature10920](https://doi.org/10.1038/nature10920) (Retrieved October 25, 2022)
- [95] J. G. Bohnet, Z. Chen, J. M. Weiner, K. C. Cox, and J. K. Thompson, Relaxation Oscillations, Stability, and Cavity Feedback in a Superradiant Raman Laser, *Phys. Rev. Lett.* **109**, 253602 (2012).  
DOI: [10.1103/PhysRevLett.109.253602](https://doi.org/10.1103/PhysRevLett.109.253602) (Retrieved October 25, 2022)
- [96] J. M. Weiner, K. C. Cox, J. G. Bohnet, and J. K. Thompson, Phase synchronization inside a superradiant laser, *Phys. Rev. A* **95**, 033808 (2017).  
DOI: [10.1103/PhysRevA.95.033808](https://doi.org/10.1103/PhysRevA.95.033808) (Retrieved October 25, 2022)
- [97] C.-C. Chen, R. G. Escudero, J. Minář, B. Pasquiou, S. Bennetts, and F. Schreck, Continuous Bose-Einstein condensation, *Nature* **606**, 683 (2022).  
DOI: [10.1038/s41586-022-04731-z](https://doi.org/10.1038/s41586-022-04731-z) (Retrieved October 25, 2022)
- [98] C.-C. Chen, S. Bennetts, R. G. Escudero, B. Pasquiou, and F. Schreck, Continuous Guided Strontium Beam with High Phase-Space Density, *Phys. Rev. Applied*, **12**, 044014 (2019).  
DOI: [10.1103/PhysRevApplied.12.044014](https://doi.org/10.1103/PhysRevApplied.12.044014) (Retrieved October 25, 2022)
- [99] C. B. Silva, F. Famà, S. Zhou, S. A. Schäffer, G. A. Kazakov, B. Pasquiou, S. Bennetts, and F. Schreck, Towards a continuous superradiant laser on the strontium  $^1\text{S}_0$ - $^3\text{P}_0$  transition, *Bulletin of the American Physical Society*, (2021).  
Link: [meetings.aps.org/Meeting/DAMOP21/Session/V01.134](https://meetings.aps.org/Meeting/DAMOP21/Session/V01.134) (Retrieved October 25, 2022)

- [100] M. Barbiero, M. G. Tarallo, D. Calonico, F. Levi, G. Lamporesi, and G. Ferrari, Sideband-Enhanced Cold Atomic Source for Optical Clocks, *Phys. Rev. Applied* **13**, 014013 (2020).  
DOI: [10.1103/PhysRevApplied.13.014013](https://doi.org/10.1103/PhysRevApplied.13.014013) (Retrieved October 25, 2022)
- [101] I. Nosske, L. Couturier, F. Hu, C. Tan, C. Qiao, J. Blume, Y. H. Jiang, P. Chen, and M. Weidmüller, Two-dimensional magneto-optical trap as a source for cold strontium atoms, *Phys. Rev. A* **96**, 053415 (2017).  
DOI: [10.1103/PhysRevA.96.053415](https://doi.org/10.1103/PhysRevA.96.053415) (Retrieved October 25, 2022)
- [102] J. Li, K. Lim, S. Das, T. Zanon-Willette, C. -H. Feng, P. Robert, A. Bertoldi, P. Bouyer, C. C. Kwong, S. -Y. Lan, and D. Wilkowski, Bi-color atomic beam slower and magnetic field compensation for ultracold gases, *arXiv* (2022).  
DOI: [10.48550/arXiv.2209.08479](https://doi.org/10.48550/arXiv.2209.08479) (Retrieved October 25, 2022)
- [103] M. Tang, *Modeling lasing in a thermal strontium ensemble*, MSc thesis, Niels Bohr Institute, University of Copenhagen (2018)  
Link: [soeg.kb.dk/permalink/45KBDK\\_KGL/a5h4it/alma99124202594505763](https://soeg.kb.dk/permalink/45KBDK_KGL/a5h4it/alma99124202594505763) (Retrieved October 25, 2022).
- [104] Daniel A. Steck, *Quantum and Atom Optics*, available online at [steck.us/teaching](http://steck.us/teaching) (revision 0.12.0, 16 May 2017).
- [105] C. Gerry and P. Knight, *Introductory Quantum Optics*, Cambridge University Press (2008).
- [106] H. Bruus and K. Flensberg, *Many-Body Quantum Theory in Condensed Matter Physics - An Introduction*, Oxford Graduate Texts (2016).
- [107] D. Plankensteiner, C. Hotter, and H. Ritsch, QuantumCumulants.jl: A Julia framework for generalized mean-field equations in open quantum systems, *Quantum* **6**, p. 617 (2022).  
DOI: [10.22331/q-2022-01-04-617](https://doi.org/10.22331/q-2022-01-04-617) (Retrieved October 25, 2022)
- [108] Quantum Cumulants on Github: <https://github.com/qojulia/QuantumCumulants.jl> (Retrieved October 25, 2022)
- [109] R. Kubo, Generalized Cumulant Expansion Method, *Journal of the Physical Society of Japan* **17**, 1100-1120 (1962).  
DOI: [10.1143/JPSJ.17.1100](https://doi.org/10.1143/JPSJ.17.1100) (Retrieved October 25, 2022)
- [110] K. Debnath, Y. Zhang, and K. Mølmer, Collective dynamics of inhomogeneously broadened emitters coupled to an optical cavity with narrow linewidth, *Phys. Rev. A* **100**, 053821 (2019).  
DOI: [10.1103/PhysRevA.100.053821](https://doi.org/10.1103/PhysRevA.100.053821) (Retrieved October 25, 2022)
- [111] P. Kirton, M. M. Roses, J. Keeling, and E. G. Dalla Torre, Introduction to the Dicke Model: From Equilibrium to Nonequilibrium, and Vice Versa, *Advanced Quantum Technologies* **2**: 1800043 (2019).  
DOI: [10.1002/quate.201800043](https://doi.org/10.1002/quate.201800043) (Retrieved October 25, 2022)
- [112] P. Milonni and J. Eberly, *Laser Physics*, John Wiley & Sons (2010).
- [113] Clebsch-Gordan coefficients at Wolfram Demonstrations:  
<https://demonstrations.wolfram.com/ClebschGordanCoefficients/> (Retrieved October 25, 2022)
- [114] Daniel A. Steck, Rubidium 87 D Line Data, <https://steck.us/alkalidata/> (Retrieved January 27, 2022)
- [115] Wigner 3j-symbol at Wolfram Mathworld:  
<https://mathworld.wolfram.com/Wigner3j-Symbol.html> (Retrieved January 12, 2022)

- [116] R. K. Hanley, P. Huillery, N. C. Keegan, A. D. Bounds, D. Boddy, R. Faoro, and M. P. A. Jones, Quantitative simulation of a magneto-optical trap operating near the photon recoil limit, *Journal of Modern Optics*, **65:5-6**, 667-676 (2018).  
DOI: [10.1080/09500340.2017.1401679](https://doi.org/10.1080/09500340.2017.1401679) (Retrieved October 25, 2022)
- [117] V. S. Letokhov and V. G. Minogin, Laser Radiation Pressure on Free Atoms, *Physics Reports* **73**, 1-65 (1981).  
DOI: [10.1016/0370-1573\(81\)90116-2](https://doi.org/10.1016/0370-1573(81)90116-2) (Retrieved October 25, 2022)
- [118] S. J. M. Kuppens, M. P. van Exter, J. P. Woerdman, and M. I. Kolobov, Observation of the effect of spectrally inhomogeneous gain on the quantum-limited laser linewidth, *Optics Communications* **126**, 79-84 (1996).  
DOI: [10.1016/0030-4018\(96\)00034-X](https://doi.org/10.1016/0030-4018(96)00034-X) (Retrieved October 25, 2022)
- [119] B. T. R. Christensen, *Laser Stabilization With Laser Cooled Strontium*, PhD Thesis, Niels Bohr Institute, University of Copenhagen (2016).  
Link: [nbi.ku.dk/english/research/quantum-optics-and-photonics/quantum-metrology](https://nbi.ku.dk/english/research/quantum-optics-and-photonics/quantum-metrology) (Retrieved October 25, 2022)
- [120] M. R. Henriksen, *Cavity Enhanced Spectroscopy on Ultra Cold Atoms*, MSc thesis, Niels Bohr Institute, University of Copenhagen (2014).  
Link: [nbi.ku.dk/english/research/quantum-optics-and-photonics/quantum-metrology](https://nbi.ku.dk/english/research/quantum-optics-and-photonics/quantum-metrology) (Retrieved October 30, 2022)
- [121] S. A. Schäffer, *Cavity-enhanced optical clocks*, PhD thesis, Niels Bohr Institute, University of Copenhagen (2019).  
Link: [nbi.ku.dk/english/research/quantum-optics-and-photonics/quantum-metrology](https://nbi.ku.dk/english/research/quantum-optics-and-photonics/quantum-metrology) (Retrieved October 25, 2022)
- [122] M. R. Henriksen, *Optical Frequency References*, PhD thesis, Niels Bohr Institute, University of Copenhagen (2019).  
Link: [nbi.ku.dk/english/research/quantum-optics-and-photonics/quantum-metrology](https://nbi.ku.dk/english/research/quantum-optics-and-photonics/quantum-metrology) (Retrieved October 25, 2022)
- [123] M. Ambroza, *Investigation of superradiant effects in thermally cold Sr ensembles*, MSc thesis, Niels Bohr Institute, University of Copenhagen (2020).  
Link: [nbi.ku.dk/english/research/quantum-optics-and-photonics/quantum-metrology](https://nbi.ku.dk/english/research/quantum-optics-and-photonics/quantum-metrology) (Retrieved October 25, 2022)
- [124] D. Świerad et al, Ultra-stable clock laser system development towards space applications, *Sci. Rep.* **6**, 33973 (2016).  
DOI: [10.1038/srep33973](https://doi.org/10.1038/srep33973) (Retrieved October 25, 2022)
- [125] T. Walker, D. Sesko, and C. Wieman, Collective Behavior of Optically Trapped Neutral Atoms, *Phys. Rev. Lett.* **64**, 408 (1990).  
DOI: [10.1103/PhysRevLett.64.408](https://doi.org/10.1103/PhysRevLett.64.408) (Retrieved October 25, 2022)
- [126] K. Jooya, N. Musterer, K. W. Madison, and J. L. Booth, Photon-scattering-rate measurement of atoms in a magneto-optical trap, *Phys. Rev. A* **88**, 063401 (2013).  
DOI: [10.1103/PhysRevA.88.063401](https://doi.org/10.1103/PhysRevA.88.063401) (Retrieved October 25, 2022)
- [127] T. H. Loftus, T. Ido, M. M. Boyd, A. D. Ludlow, and J. Ye, Narrow line cooling and momentum-space crystals, *Phys. Rev. A* **70**, 063413 (2004).  
DOI: [10.1103/PhysRevA.70.063413](https://doi.org/10.1103/PhysRevA.70.063413) (Retrieved October 25, 2022)
- [128] X. Xu, T. H. Loftus, J. L. Hall, A. Gallagher, and J. Ye, Cooling and trapping of atomic strontium, *J. Opt. Soc. Am. B* **20**, 968-976 (2003).  
DOI: [10.1364/JOSAB.20.000968](https://doi.org/10.1364/JOSAB.20.000968) (Retrieved October 25, 2022)

- [129] M. A. Norcia, *New tools for precision measurement and quantum science with narrow linewidth optical transitions*, PhD thesis, University of Colorado Boulder (2017).  
Link: [scholar.colorado.edu/concern/graduate\\_thesis\\_or\\_dissertations/t435gc985](https://scholar.colorado.edu/concern/graduate_thesis_or_dissertations/t435gc985) (Retrieved October 25, 2022)
- [130] J. A. Muniz, M. A. Norcia, J. R. K. Cline, and J. K. Thompson, A Robust Narrow-Line Magneto-Optical Trap using Adiabatic Transfer, arXiv (2018).  
DOI: [10.48550/arXiv.1806.00838](https://doi.org/10.48550/arXiv.1806.00838) (Retrieved October 25, 2022)
- [131] M. A. Norcia, J. R. K. Cline, J. P. Bartolotta, M. J. Holland, and J. K. Thompson, Narrow-line laser cooling by adiabatic transfer, *New J. Phys.* **20**, 023021 (2018).  
DOI: [10.1088/1367-2630/aaa950](https://doi.org/10.1088/1367-2630/aaa950) (Retrieved October 25, 2022)
- [132] S. Snigirev, A. J. Park, A. Heinz, I. Bloch, and S. Blatt, Fast and dense magneto-optical traps for strontium, *Phys. Rev. A* **99**, 063421 (2019).  
DOI: [10.1103/PhysRevA.99.063421](https://doi.org/10.1103/PhysRevA.99.063421) (Retrieved October 25, 2022)
- [133] Daniel A. Steck, *Analog and Digital Electronics*, available online at [steck.us/teaching](http://steck.us/teaching) (revision 1.0.4, 1 August 2019).
- [134] H. J. Lewandowski, D. M. Harber, D. L. Whitaker, and E. A. Cornell, Simplified System for Creating a Bose-Einstein Condensate, *Journal of Low Temperature Physics* **132**, 309-367 (2003).  
DOI: [10.1023/A:1024800600621](https://doi.org/10.1023/A:1024800600621) (Retrieved October 25, 2022)
- [135] T. Pyragius, Developing and building an absorption imaging system for Ultracold Atoms, arXiv (2012).  
DOI: [10.48550/arXiv.1209.3408](https://doi.org/10.48550/arXiv.1209.3408) (Retrieved October 25, 2022)
- [136] H. D. Young, R. A. Freedman et al, *University Physics*, Pearson Education (2014).
- [137] K. F. Riley and M. P. Hobson, *Essential Mathematical Methods for the Physical Sciences*, Cambridge University Press (2011).
- [138] C. J. Dedman, K. G. H. Baldwin, and M. Colla, Fast switching of magnetic fields in a magneto-optic trap, *Review of Scientific Instruments* **72**, 4055 (2001).  
DOI: [10.1063/1.1408935](https://doi.org/10.1063/1.1408935) (Retrieved October 25, 2022)
- [139] F. Riehle, *Frequency Standards*, Wiley (2004).
- [140] C. Hotter, L. Ostermann, and H. Ritsch, Cavity sub- and superradiance enhanced Ramsey spectroscopy, arXiv (2022).  
DOI: [10.48550/arXiv.2201.09731](https://doi.org/10.48550/arXiv.2201.09731) (Retrieved October 25, 2022)
- [141] R. Brecha, L. A. Orozco, M. G. Raizen, M. Xiao, and H. J. Kimble, Observation of oscillatory energy exchange in a coupled-atom–cavity system, *J. Opt. Soc. Am. B* **12**, 2329-2339 (1995).  
DOI: [10.1364/JOSAB.12.002329](https://doi.org/10.1364/JOSAB.12.002329) (Retrieved October 25, 2022)
- [142] J. Bochmann, M. Mücke, G. Langfahl-Klabes, C. Erbel, B. Weber, H. P. Specht, D. L. Moehring, and G. Rempe, Fast Excitation and Photon Emission of a Single-Atom-Cavity System, *Phys. Rev. Lett.* **101**, 223601 (2008).  
DOI: [10.1103/PhysRevLett.101.223601](https://doi.org/10.1103/PhysRevLett.101.223601) (Retrieved October 25, 2022)
- [143] K. Durak, C. H. Nguyen, V. Leong, S. Straupe, and C. Kurtsiefer, Diffraction-limited Fabry–Perot cavity in the near concentric regime, *New J. Phys.* **16**, 103002 (2014).  
DOI: [10.1088/1367-2630/16/10/103002](https://doi.org/10.1088/1367-2630/16/10/103002) (Retrieved October 25, 2022)
- [144] Epotek ND353 specifications.  
Link: <https://www.epotek.com/docs/en/Datasheet/353ND.pdf> (Retrieved March 22, 2022)

- [145] Private communications with Stefan A. Schäffer.
- [146] Y. D. Chong, Li Ge, Hui Cao, and A. D. Stone, Coherent Perfect Absorbers: Time-Reversed Lasers, *Phys. Rev. Lett.* **105**, 053901 (2010).  
DOI: [10.1103/PhysRevLett.105.053901](https://doi.org/10.1103/PhysRevLett.105.053901) (Retrieved October 25, 2022)
- [147] D. Yang, Sh. Oh, J. Han, G. Son, J. Kim, J. Kim, M. Lee and K. An, Realization of superabsorption by time reversal of superradiance, *Nat. Photonics* **15**, 272–276 (2021).  
DOI: <https://doi.org/10.1038/s41566-021-00770-6> (Retrieved October 25, 2022)
- [148] H. J. Metcalf and P. van der Straten, *Laser Cooling and Trapping*, Springer (1999).
- [149] K. An and M. S. Feld, Semiclassical four-level single-atom laser, *Phys. Rev. A* **56**, 1662 (1997).  
DOI: [10.1103/PhysRevA.56.1662](https://doi.org/10.1103/PhysRevA.56.1662) (Retrieved October 25, 2022)
- [150] G. Harry, T. P. Bodiya, and R. DeSalvo, *Optical Coatings and Thermal Noise in Precision Measurement*, Cambridge University Press (2012).
- [151] Private communications with Shayne Bennetts.
- [152] R. Grimm, M. Weidemüller, and Y. B. Ovchinnikov, Optical dipole traps for neutral atoms, *Adv. At. Mol. Opt. Phys.* **42**, 95, (2000).  
DOI: [10.1016/s1049-250x\(08\)60186-x](https://doi.org/10.1016/s1049-250x(08)60186-x) (Retrieved October 25, 2022)
- [153] F. Le Kien, P. Schneeweiss, and A. Rauschenbeutel, Dynamical polarizability of atoms in arbitrary light fields: general theory and application to cesium, *Eur. Phys. J. D* **67**, 92, (2013). DOI: [10.1140/epjd/e2013-30729-x](https://doi.org/10.1140/epjd/e2013-30729-x) (Retrieved October 25, 2022)
- [154] S. Bennetts, *1000 times closer to a continuous atom laser: Steady-state strontium with unity phase-space density*, PhD thesis, University of Amsterdam (2019).  
Link: [strontiumbec.com](http://strontiumbec.com) (Retrieved October 25, 2022)
- [155] C. Hotter, D. Plankensteiner, and H. Ritsch, Continuous narrowband lasing with coherently driven V-level atoms, *New J. Phys* **22**, 113021 (2020)  
DOI: [10.1088/1367-2630/abc70c](https://doi.org/10.1088/1367-2630/abc70c) (Retrieved October 24, 2022)
- [156] P. G. Westergaard, B. T. R. Christensen, D. Tieri, R. Matin, J. Cooper, M. Holland, J. Ye, and J. W. Thomsen, Observation of Motion-Dependent Nonlinear Dispersion with Narrow-Linewidth Atoms in an Optical Cavity, *Phys. Rev. Lett.* **114**, 093002 (2015)  
DOI: [10.1103/PhysRevLett.114.093002](https://doi.org/10.1103/PhysRevLett.114.093002) (Retrieved October 27, 2022)
- [157] B. T. R. Christensen, M. R. Henriksen, S. A. Schäffer, P. G. Westergaard, D. Tieri, J. Ye, M. J. Holland, and J. W. Thomsen, Nonlinear spectroscopy of Sr atoms in an optical cavity for laser stabilization, *Phys. Rev. A* **92**, 053820 (2015)  
DOI: [10.1103/PhysRevA.92.053820](https://doi.org/10.1103/PhysRevA.92.053820) (Retrieved October 24, 2022)